

**High Resolution Numerical Simulations of Dust Devils in the
Convective Boundary Layer – Effects of Detailed Process
Representation on Vortex Development and Dust Release**

Von der Fakultät für Mathematik und Physik

der Gottfried Wilhelm Leibniz Universität Hannover zur Erlangung des Grades

Doktor der Naturwissenschaften

Dr. rer. nat.

genehmigte Dissertation von

M. Sc. Sebastian Giersch

2024

Referent: Prof. Dr. Siegfried Raasch

1. Korreferent: Prof. Dr. Björn Maronga

2. Korreferent: Prof. Dr. Peter Knippertz

Tag der Promotion: 06.12.2023

Abstract

Dust Devils (DDs) are convective whirlwinds that frequently occur in the atmospheric Convective Boundary Layer (CBL) of arid regions during daytime. If strong enough, they transport soil particles into the atmosphere. These aerosols alter cloud microphysics and the Earth's radiation budget. Existing quantifications of the particle release and estimates of the contribution of DDs to the local, regional, and global dust cycle are highly uncertain. Good knowledge about the DD statistics and dynamics would help to improve them. A better understanding of DDs is also beneficial for investigations of other vortex types like tornadoes or waterspouts. This thesis presents results from numerical investigations of DD-like vortices that occur in CBLs. The simulations are carried out with the turbulence-resolving PALM model system.

The first study investigates the effects of the grid spacing, background wind, and surface heat flux heterogeneities on the DD characteristics with a focus on the vortex strength. It is shown that grid spacings of 2 m, a striped pattern of heat flux heterogeneities, and moderate background winds significantly increase the vortex strength in Large-Eddy Simulation (LES) of the atmospheric CBL. These are the first numerical simulations that have ever produced DD-like vortices of observed intensity.

In the second study, DD-like vortices are investigated in Direct Numerical Simulation (DNS) of Rayleigh-Bénard convection for Rayleigh numbers up to 10^{11} for the first time. The model domain's aspect ratio, the velocity boundary condition, and the Rayleigh number are the main control parameters that are varied. It is shown that a minimum Rayleigh number of 10^7 is necessary for the development of DD-like vortices, which is much less than a typical atmospheric value of 10^{18} . While the aspect ratio shows only minor effects on the vortices, the Rayleigh number and surface friction are critical parameters for nearly all vortex properties. The results also reveal that the three-dimensional structure of the DDs is very similar to the one in LES of the atmospheric boundary layer, indicating that subfilter-scale models and parameterizations of the surface-atmosphere exchange in LES have a negligible influence on the vortices.

A grid convergence study of the DD statistics, where the grid spacing is gradually decreased from 10 to 0.625 m, is conducted in the third study of this thesis. Grid spacings of 1 m or less have never been used before for the analysis of DDs that develop in atmospheric LES while capturing the large-scale cellular pattern of the CBL. It is demonstrated that the derivation of meaningful quantitative vortex features requires a resolution of approximately 1 m or less. At this resolution, mean quantities averaged over all detected DDs are converged. However, maxima show no convergence, which is mainly attributed to the detachment of the vertically thin super-adiabatic layer in the vortex core from the near-surface region. This layer needs very fine grid spacings of less than 1 m to be sufficiently resolved. A comparison with measurements indicates that a grid spacing of just less than 0.5 m might be adequate for a convergence of the maximum values. For a qualitative investigation on the DD flow structure, a resolution of 2.5 m or smaller is recommended.

In the final study, the surface particle emission, the near-surface particle transport in vertical direction, and the particle concentration of DDs are investigated in LES of the at-

mospheric CBL. The focus is on dust-sized particles. It is found that DDs cause peak dust emission fluxes and dust mass concentrations of up to $50 \text{ mg m}^{-2} \text{ s}^{-1}$ and 10 mg m^{-3} , respectively, which is 1–2 orders of magnitude larger than previous numerical estimates. On average, the dust transport at 10 m height is five times larger than the surface dust emission, making DDs an important phenomenon for air quality and visibility. The DD's contribution to the total dust emission in desert-like regions reveals a mean of 5 %, which is almost one order of magnitude less compared to other measurement-based studies. The small contribution is attributed to large-scale patterns of relatively high dust emission, which follow the cellular flow pattern of the CBL and which are the dominant mechanism for the saltation-based dust release.

Keywords: dust devils, turbulence-resolving simulations, convective boundary layers.

Kurzzusammenfassung

Staubteufel (ST) sind atmosphärische konvektive Wirbel, die tagsüber in der konvektiven Grenzschicht arider Gebiete auftreten. Sind sie stark genug, transportieren ST Bodenpartikel in die Atmosphäre. Diese Aerosole verändern die Wolkenmikrophysik und den Strahlungshaushalt der Erde. Bestehende Quantifizierungen der Partikelfreisetzung und Schätzungen des Beitrags von ST zum lokalen, regionalen und globalen atmosphärischen Staubgehalt sind äußerst unsicher. Gute Kenntnisse über die Statistik und Dynamik von ST würden dazu beitragen diese Quantifizierungen und Schätzungen zu verbessern. Ein gutes Verständnis der ST Dynamik ist auch für Untersuchungen anderer Wirbeltypen wie Tornados oder Wasserhosen nützlich. In dieser Arbeit werden Ergebnisse numerischer Untersuchungen von ST-ähnlichen Wirbeln vorgestellt, die in konvektiven Grenzschichten auftreten. Die Simulationen werden mit dem turbulenzauflösenden Modell PALM durchgeführt.

Die erste Studie untersucht die Auswirkungen des Gitterabstandes, des Hintergrundwindes und der Heterogenität im Oberflächenwärmestrom auf die Eigenschaften der ST. Der Fokus liegt dabei auf der Wirbelstärke. Es zeigt sich, dass Gitterabstände von 2 m, ein streifenförmiges Muster von Wärmestromheterogenitäten und moderate Hintergrundwinde die Wirbelstärke in Grobstruktursimulationen der atmosphärischen konvektiven Grenzschicht signifikant erhöhen. Dies sind die ersten numerischen Simulationen, die jemals ST-ähnliche Wirbel in beobachtbarer Intensität erzeugt haben.

In der zweiten Studie werden erstmals ST-artige Wirbel in direkten numerischen Simulationen turbulenter Rayleigh-Bénard-Konvektion für Rayleigh-Zahlen bis zu 10^{11} untersucht. Das Aspektverhältnis der Modelldomäne, die Geschwindigkeitsrandbedingung und die Rayleigh-Zahl sind die wichtigsten Kontrollparameter, die variiert werden. Die Ergebnisse verdeutlichen, dass für die Entwicklung von ST-ähnlichen Wirbeln eine minimale Rayleigh-Zahl von 10^7 notwendig ist, die noch weit unter dem typischen atmosphärischen Wert von 10^{18} liegt. Während das Aspektverhältnis nur geringe Auswirkungen auf die Wirbel hat, sind die Rayleigh-Zahl und die Oberflächenreibung entscheidende Parameter für fast alle Wirbeleigenschaften. Die Ergebnisse zeigen auch, dass die dreidimensionale Struktur der simulierten ST derjenigen in Grobstruktursimulationen der atmosphärischen Grenzschicht sehr ähnlich ist, was darauf hindeutet, dass Modelle für die Subfilterskala und Parametrisierungen des Austausches zwischen Erdoberfläche und Atmosphäre in LES vermutlich nur einen geringen Einfluss auf die Wirbel haben.

Das Konvergenzverhalten der ST-Statistik bezüglich des numerischen Gitters wird in der dritten Studie dieser Arbeit für Gitterabstände zwischen 10 und 0,625 m untersucht. Auflösungen von 1 m oder weniger wurden bisher noch nie für die Analyse von ST verwendet, welche sich in atmosphärischer LES entwickeln bei der das großräumige zelluläre Konvektionsmuster der konvektiven Grenzschicht erfasst wird. Es wird deutlich, dass die Bestimmung von aussagekräftigen quantitativen Wirbeleigenschaften eine Auflösung von etwa 1 m oder weniger erfordert. Während die über alle detektierten ST gemittelten Größen bei dieser Auflösung konvergieren, zeigen die Maxima keine Konvergenz. Dies ist hauptsächlich auf die bodennahe Ablösung der vertikal sehr dünnen superadiabatischen Schicht im Wirbelkern zurückzuführen. Eine angemessene Auflösung dieser Schicht erfordert Gitterweiten

von weniger als 1 m. Ein Vergleich mit Messungen verdeutlicht, dass zur Konvergenz der Maximalwerte ein Gitterabstand von knapp unter 0,5 m ausreichend sein dürfte. Wenn eine rein qualitative Sichtweise auf die Strömungsstruktur der ST ausreicht, ist eine Auflösung von 2,5 m oder kleiner zu empfehlen.

In der finalen Studie werden die Partikelfreisetzung von der Erdoberfläche, der oberflächennahe Partikeltransport in vertikaler Richtung und die Partikelkonzentration von ST in Grobstruktursimulationen der atmosphärischen konvektiven Grenzschicht untersucht. Der Schwerpunkt liegt dabei auf staubgroßen Partikeln. Es zeigt sich, dass ST Spitzenwerte der Staubemissionsflüsse und der Staubmassenkonzentrationen von bis zu $50 \text{ mg m}^{-2} \text{ s}^{-1}$ beziehungsweise 10 mg m^{-3} verursachen, was 1 bis 2 Größenordnungen größer ist als frühere numerische Schätzungen. Im Durchschnitt ist der Staubtransport in 10 m Höhe fünfmal größer als die Staubemission an der Oberfläche, was ST zu einem wichtigen lokalen Phänomen für die Luftqualität und die Sichtweite macht. Der Beitrag von ST zur Gesamtstaubemission in wüstenähnlichen Regionen liegt im Mittel bei 5 %. Dies ist im Vergleich zu anderen messbasierten Studien fast eine Größenordnung geringer. Der reduzierte Beitrag wird großräumigen Mustern mit relativ hoher Staubemission zugeschrieben, die dem zellulären Strömungsmuster der konvektiven Grenzschicht folgen und den dominanten Mechanismus für die auf Saltation basierende Staubbefreiung darstellen.

Schlagwörter: Staubeufel, turbulenzauflösende Simulationen, konvektive Grenzschichten.

Contents

Abstract	III
Kurzzusammenfassung	V
List of Abbreviations	IX
List of Symbols	XI
1 Introduction	1
1.1 Motivation for Studying Dust Devils	2
1.2 Current State of Research	3
1.2.1 Dust Devil Formation	4
1.2.2 Dust Devil Characteristics	7
1.2.3 Dust Devil Dynamics	8
1.3 Numerical Simulation of Turbulent Flows	14
1.4 Numerical Simulation of Dust Devils	19
1.5 Objectives and Structure of the Thesis	22
2 Methods	27
2.1 The PALM Model System	27
2.2 Dust Devil Identification	31
2.2.1 Detection of Vortex Centers	33
2.2.2 Formation of Vortex Tracks	35
2.3 Statistical Analysis of Dust Devils	37
2.4 Tracking of Individual Dust Devils	39
3 Large-Eddy Simulations of Dust Devils of Observed Intensity	41
3.1 Declaration of Contributions	41
3.2 Research Article	41
4 Dust Devil-Like Vortices in Turbulent Rayleigh-Bénard Convection	65
4.1 Declaration of Contributions	65
4.2 Research Article	65
5 Grid Convergence Study of Dust Devil-Like Vortices	103
5.1 Declaration of Contributions	103
5.2 Research Article	103
6 Saltation-Induced Dust Emission of Dust Devils	145
6.1 Declaration of Contributions	145
6.2 Research Article	145

7	Conclusions	175
7.1	Summary and Discussion	175
7.2	Outlook	179
	Acknowledgements	183
	Bibliography	185
	Declaration	199
	Curriculum Vitae	201

List of Abbreviations

CBL	Convective Boundary Layer
CFD	Computational Fluid Dynamics
DD	Dust Devil
DNS	Direct Numerical Simulation
FFT	Fast Fourier Transform
LES	Large-Eddy Simulation
MOST	Monin-Obukhov Similarity Theory
MPI	Message Passing Interface
RANS	Reynolds-Averaged Navier-Stokes
SFS	Subfilter-Scale
SGS	Subgrid-Scale
TKE	Turbulence Kinetic Energy
URANS	Unsteady Reynolds-Averaged Navier-Stokes
VLES	Very Large-Eddy Simulation

List of Symbols

Greek Symbols

γ	Fraction of total dissipation of mechanical energy consumed by friction near the surface
δ_{ij}	Kronecker-Delta, $i, j \in \{1, 2, 3\}$
Δ	Grid spacing
Δp	Pressure drop
$\Delta x, \Delta y, \Delta z, \Delta x_i$	Grid spacings in x -, y -, and z -direction, $i \in \{1, 2, 3\}$
ε	Viscous dissipation rate of TKE per unit mass
ε_{ijk}	Levi-Civita symbol, $i, j, k \in \{1, 2, 3\}$
ζ	Vertical vorticity
η	Thermal efficiency
θ	Potential temperature
ν_m	Momentum diffusivity of air
ν_h	Thermal diffusivity of air
π	Number pi
π^*	Modified perturbation pressure
ρ	Air density
τ_{ij}^r	Deviatoric stress tensor
ϕ	Geographical latitude
Φ	Azimuthal direction
χ_s	Source or sink term of passive scalar
Ψ	Arbitrary variable
$\vec{\omega}$	Vorticity vector
Ω	Angular velocity of the Earth
$\vec{\Omega}$	Rotation vector of the Earth

Latin Symbols

C	Circulation
C_k	Kolmogorov constant
c_p	Specific heat capacity of air at constant pressure
e	Subgrid-scale TKE
$\vec{e}_r, \vec{e}_\Phi, \vec{e}_z$	Cylindrical unit vectors
E	Power spectral density of the TKE
f^*, f, f_j	Coriolis parameters, $j \in \{2, 3\}$
g	Gravitational acceleration
G	Low-pass filter function

i, j, k, n	Running indices
k	Wave number
\vec{k}	Cartesian unit vector in vertical direction
K_h	Subgrid-scale eddy diffusivity of heat
K_m	Subgrid-scale eddy diffusivity of momentum
N	Total number of flow realizations
p	Air pressure
p^*	Perturbation pressure
r	Radial direction
R	Gas constant of air
r_c	Vortex core radius
s	Arbitrary passive scalar
S	Surface
t	Time
T	Absolute Temperature
u, v, w, u_i	Components of the wind vector, $i \in \{1, 2, 3\}$
$u_g, v_g, u_{g,j}$	Components of the geostrophic wind vector, $j \in \{1, 2\}$
v_r, v_ϕ, v_z	Velocities in radial, azimuthal, and vertical direction in a cylindrical coordinate system
\vec{v}	Velocity vector in Cartesian coordinates
\vec{v}_{cyl}	Velocity vector in cylindrical coordinates
\vec{v}_h	Horizontal velocity vector in Cartesian coordinates
V	Characteristic tangential velocity
\vec{x}	Location vector in Cartesian coordinates
x, y, z, x_i	Cartesian Coordinates, $i \in \{1, 2, 3\}$
z_i	Boundary layer depth

Averages, Filters, and Indices Applied to the Variable Ψ

Ψ_0	Basic state in hydrostatic equilibrium
Ψ_∞	Values far away from a vortex center
Ψ_c	Values at the center of a vortex
Ψ^*	Deviation from the basic state
$\bar{\Psi}$	Reynolds average
Ψ'	Deviation from the Reynolds average
$\tilde{\Psi}$	Spatially filtered quantity
Ψ''	Deviation from the spatially filtered quantity

Operators

∇	Nabla operator
∇_{cyl}	Nabla operator in cylindrical coordinates
∇_{h}	Nabla operator in horizontal direction
\times	Cross product
d/dt	Total derivative
∂	Partial differential operator
$\partial/\partial t$	Local time derivative
$\partial/\partial x_i$	Local spatial derivative
\int	Indefinite integral
\int_a^b	Definite integral with limits a and b
Σ	Sigma sign for summation

Chapter 1

Introduction

Dust Devils (DDs) are dry atmospheric convective vortices with a vertical axis of rotation that occur in the terrestrial and martian planetary boundary layer during daytime when convection is present. If they are strong enough to lift soil particles such as dust or sand, they become visible (see Fig. 1.1). Like tornadoes, waterspouts, fire whirls, or steam devils, DDs belong to the class of small-scale concentrated vortices with a primarily columnar appearance (Kurgansky et al., 2016; Onishchenko et al., 2019). Several attempts have been made to define a DD (e.g., Cantor et al., 2006; Oke et al., 2007; Lorenz and Jackson, 2016; Oncley et al., 2016). However, no universally accepted definition exists so far because DDs show a diverse morphology (e.g., columnar, v-shaped or disordered), consist of different materials (e.g., sand, dust, or straw), and have characteristics that extend over several orders of magnitude (e.g., diameters between 1 m and more than 100 m, Murphy et al., 2016). A key difference to most of the other types of small-scale atmospheric vortices is the unimportance of wet thermodynamic processes for DD development (Kurgansky et al., 2016).



Figure 1.1: Image of a DD in the Atacama desert, Chile. Credit: Rita Nogherotto (distributed via imagedo.egu.eu).

Figure 1.1 reveals why DDs are regarded as an impressive and dynamically interesting phenomenon that can release dust or other soil particles into the atmosphere. Due to this release, DDs provide a natural source for atmospheric aerosols and affect air quality as well

as visibility. However, despite nearly a century of DD research (Lorenz et al., 2016), many uncertainties still exist. For example, possible mechanisms for their formation (e.g., Spiga et al., 2016) or the amount of their dust release (e.g., Klose et al., 2016) are controversially discussed. The general objective of this thesis is to improve the knowledge and understanding of DDs and related processes by using Computational Fluid Dynamics (CFD) modeling approaches. The focus is on basic characteristics, the dynamics, and the particle release of DDs. In addition, a generic approach for their technical extraction from CFD data is presented and numerical requirements for an appropriate simulation of DDs are discussed. This discussion will form the basis for future CFD studies of DDs.

The remainder of this chapter motivates the research of DDs, presents state-of-the-art results, which are of importance for the subsequent chapters, highlights the fundamentals and characteristics of DDs, and illustrates how they have been studied so far. A special focus is on turbulence-resolving numerical simulation techniques that are used in the following for the study of DDs. The concluding section of this chapter introduces the main research questions and the topics that continue this thesis.

1.1 Motivation for Studying Dust Devils

The interest in terrestrial DDs and convective whirlwinds in general goes back to the antiquity and was mainly caused by their fascinating appearance and dynamics as well as the damage and discomfort due to these whirlwinds (Lorenz et al., 2016). Although in most cases DDs are not dangerous, several reports exist where these vortices were responsible for structural damages, injuries, and even deaths due to twirling objects or collapsing accommodations (Lorenz and Myers, 2005; Lorenz et al., 2016). According to Onishchenko et al. (2019), DDs are the most common vortex structure in the Earth's atmosphere and the understanding of their properties, structure and formation mechanisms can improve the current knowledge of other concentrated whirlwinds like tornadoes. DDs are also regarded as a potentially important mechanism for transporting heat and sediments like dust into the atmosphere (Rennó et al., 2004; Klose et al., 2016). Once dust is lifted, it contributes to the atmospheric amount of aerosols and can affect the Earth climate in the long term by scattering and absorbing both solar and long-wave radiation (e.g., Miller et al., 2014; Chaibou et al., 2020) or by modifying cloud microphysics (e.g., DeMott et al., 2003; Bangert et al., 2012). For an overview of dust impacts on the climate, the reader is referred to Schepanski (2018). The investigation of the lifted amount of soil particles by dust devils is also relevant for the vortices themselves. Dust has a potentially positive feedback on the vortex intensity caused by direct solar heating of the whirling dust column, which maintains or even enhances buoyancy and, finally, increases the particle load (Fuerstenau, 2006). This radiative effect might be especially large for dust devils in the late afternoon, when the sun is low and the rays are nearly perpendicular to the dust column (Kurgansky, 2006). Additionally, the lifted dust interacts with nutrient, carbon, and water cycles of different ecosystems (e.g., Bristow et al., 2010; Shao et al., 2011; Schepanski, 2018), contributes to the transport of viable microorganisms or chemical pollutants that affect, for example, the coral reefs (e.g., Shinn et al., 2000; Garrison et al., 2003), and influences human and animal health by allergens and pathogens that are carried with the dust (e.g., Kellogg and Griffin, 2006). Reduced visibility is another effect of dust entrainment by DDs (e.g., Hall, 1981). Therefore, the role and significance of DDs compared to other dust release processes need to be studied.

Electric fields in a swirling DD, which are created by the triboelectric charging of dust

grains and a separation of heavy coarse-grained sand particles at the bottom from lighter fine dust at the top, are also of interest (e.g., Farrell et al., 2004). The electrification can cause radio interference in the microwave range and is capable to affect the particle transport within the vortex (Onishchenko et al., 2019). Electrical forces can even significantly increase the initial particle emission with direct consequences for the total amount of lifted dust (Kok and Renno, 2006; Esposito et al., 2016). Because the electrified particles are moving, a magnetic field is also created (Farrell et al., 2004), which might have consequences for future vortex detection methods and communication equipment (Thorne et al., 2022).

Martian DDs are particularly studied because they are thought to significantly contribute to the atmosphere's background haze (e.g., Kahre et al., 2006). According to Balme and Greeley (2006), they are the main mechanism of day-to-day dust injection and probably account for several tens of percent of the atmospheric dust budget (Fenton et al., 2016). They also significantly change the local and regional surface albedo by forming so-called dust devil tracks (e.g., Geissler, 2005; Reiss et al., 2016). Both the lifted soil particles and the tracks affect the radiative budget and, consequently, might even modify the weather patterns and climate on a local, regional, and global scale (Klose et al., 2016; Reiss et al., 2016). Robotic and human Mars explorations also need to take into account DDs due to their potential effects on landers or rover solar panels through the electric and magnetic fields or wind extremes during descent and landing phases (Balme and Greeley, 2006; Lorenz et al., 2016). The main differences between Martian and terrestrial dust devils are their larger spatial dimensions and higher rotational wind speeds on Mars (e.g., Balme and Greeley, 2006; Murphy et al., 2016). However, this thesis focuses on terrestrial DDs but results are partly applicable to Martian DDs as well because they are alike in many ways (Balme and Greeley, 2006).

1.2 Current State of Research

To date, DDs have been studied in the field (e.g., Murphy et al., 2016), in the laboratory (e.g., Mullen and Maxworthy, 1977), and by numerical simulations (e.g., Kanak, 2006). Visual field observations in the middle of the 20th century are considered as the first scientific investigations of DDs on Earth (e.g., Ives, 1947; Williams, 1948). Later on, in situ measurements were provided with the help of fixed or mobile instruments (e.g., Wyett, 1954; Sinclair, 1964; Lamberth, 1966). Nowadays, the advances in drone technology enable further mobile in situ measurements to collect time-series data (Jackson et al., 2018). Since the late 20th century, landers equipped with meteorological instruments like the Viking landers or mobile robots have been used to study DDs on Mars (Ryan and Lucich, 1983; Greeley et al., 2006). With the advances in satellite technology, orbital observations became another tool for monitoring Martian DD activity, especially through their tracks (e.g., Fisher et al., 2005). Orbital observations of terrestrial DDs are an exception (e.g., Reiss, 2016). Instead, ground-based remote sensing instruments are applied in terrestrial field studies. Bluestein et al. (2004) used a Doppler radar system to quantify DD characteristics, whereas the Doppler lidar technology was applied by Fujiwara et al. (2011). A quite novel approach to investigate the characteristics of DD-like vortices is the use of thermal image velocimetry, which provides a two-dimensional, horizontal velocity distribution with high spatial and temporal resolution by tracking brightness temperature images (Inagaki and Kanda, 2022). Field observations, however, suffer from the erratic occurrence of DDs and the limited area that can be reliably monitored. This drawback can partly be avoided by laboratory experiences (e.g., Mullen and

Maxworthy, 1977) or, since the late 1990s, by numerical simulations (e.g., Kanak, 2006), where convective vortices are studied under well-controlled initial and boundary conditions. Another essential advantage of numerical simulations is that all relevant properties of the vortices (e.g., wind speed, pressure, and temperature) are directly accessible without much effort. Before some numerical simulation techniques are discussed in detail, some fundamentals of DDs are presented that could be derived in the past from visual field observations, measurements, laboratory investigations, CFD results, and theoretical considerations. The information that is given facilitates the understanding and interpretation of the research articles presented in the Chapters 3, 4, 5, and 6.

1.2.1 Dust Devil Formation

DDs are very common on Mars (e.g., Cantor et al., 2006; Ellehoj et al., 2010; Steakley and Murphy, 2016) and usually occur in arid or semi-arid regions on Earth from late morning to late afternoon during the summer (e.g., Oke et al., 2007; Jemmett-Smith et al., 2015; Tang et al., 2018). Australia, East Africa, South America, and the Middle East are typical examples that show a high frequency of occurrence (Klose et al., 2016). In these regions, the conditions for DD development are often fulfilled, which especially includes (Ives, 1947; Williams, 1948; Hess and Spillane, 1990; Balme and Greeley, 2006):

- C1. a sky with no or only a few clouds that favors strong insolation and, consequently, large super-adiabatic lapse rates near the surface,
- C2. light to moderate background winds, and
- C3. mostly dry and flat or gently sloping terrain with loose surface material (to make the convective vortex visible) and only little or no surface vegetation.

Although these conditions are well-known, exact quantitative values for the required lapse rates or background winds are uncertain. Observed surface and 2-m air temperatures by Ansmann et al. (2009) indicated a minimum required lapse rate for DD formation of $8.5\text{--}10\text{ K m}^{-1}$. Between 1 and 2 m height, they identified much lower gradients of $0.9\text{--}1\text{ K m}^{-1}$ that are needed for the development of a DD. Oke et al. (2007) determined a value of 0.9 K m^{-1} , measured between 0.12 and 2.52 m above the surface. Similar to Oke et al. (2007), Broersen (2013) stated that temperature lapse rates of at least 0.76 K m^{-1} (between 0.1 and 2.5 m above the ground) are required for DD formation. Field data by Ryan (1972) suggested much smaller values of $\sim 0.1\text{ K m}^{-1}$ in a layer between 0.3 and 10 m. Thus, reported lapse rates vary between two orders of magnitude ($0.1\text{--}10\text{ K m}^{-1}$). Regarding the background wind, Oke et al. (2007) found DD activity only in a range of $1.5\text{--}7.7\text{ m s}^{-1}$, with a peak at 3 m s^{-1} (no measurement height for the wind was given). During the field campaign of Balme et al. (2003), light winds below 5 m s^{-1} (at 2 m height) were present while DDs were forming. Kurgansky et al. (2011) noted an upper threshold for DD occurrence of 8 m s^{-1} (2-m wind speed) and enhanced activity for moderate winds between 2 and 8 m s^{-1} . Similar 2-m wind speeds were obtained by Broersen (2013), who detected DDs in the range of $0.1\text{--}7.5\text{ m s}^{-1}$, with the highest activity between $2\text{--}3\text{ m s}^{-1}$. Field observations also suggested that no minimum wind threshold for DD occurrence exists (Kurgansky et al., 2011). Lapse rates and background winds are further discussed in the articles of Chapters 3 and 5.

The conditions C1 and C2 enable the development of a well-mixed Convective Boundary Layer (CBL), in which convection dominates and mean wind shear is unimportant. The CBL can be divided into three sublayers: the surface layer, the mixed layer, and the entrainment zone (Stull, 1988). DDs, as a ground-level phenomenon, develop within the surface layer, which accounts for 5 to 10 % of the whole CBL, that is, approximately the first 5 to 10 decameters. Large DDs or the large-scale thermal updrafts of the CBL to which DDs are often connected (Ryan and Carroll, 1970; Zhao et al., 2004; Raasch and Franke, 2011; Sullivan and Patton, 2011) extend up to the CBL top (~ 1000 m). In addition to the vertical structure of the lower atmosphere, the horizontal pattern of the CBL also determines the regions of preferential DD formation. In the CBL, large-scale convective cells with a polygonal (often hexagonal) structure show narrow branches and vertices with strong updrafts and a broad downward motion in the center (e.g., Schmidt and Schumann, 1989). This structure is shown in Fig. 1.2. DD occurrence is strongly connected to these branches and vertices. The cellular pattern disappears if the planetary boundary layer is dominated by wind shear (see also Kanak et al., 2000; Kanak, 2005; Raasch and Franke, 2011). The relation between DD occurrence and the polygonal convective pattern is systematically addressed in Chapter 3 of this thesis. Parameters that can be used to describe the convective pattern and, thus, potential DD occurrence are the ratio of the convective velocity scale w_* and the friction velocity u_* or, equivalently, the ratio between the convective boundary layer height h and the Obukhov length L (Hess et al., 1988). The convective velocity scale, friction velocity, and the Obukhov length characterize the typical updraft speed in convective thermals, the mean wind shear in the surface layer, and the turbulence condition in the surface layer, respectively. The ratios are sometimes applied in regional and global simulation models to quantify the frequency of DD occurrence (Klose et al., 2016). Hess et al. (1988) and Hess and Spillane (1990) suggested a value of $-h/L \geq 50$ and Hess et al. (1988) and Lyons et al. (2008) a value of $w_*/u_* > 5$ as a necessary condition for the formation of DDs. In Chapter 5, the ratio w_*/u_* is discussed.

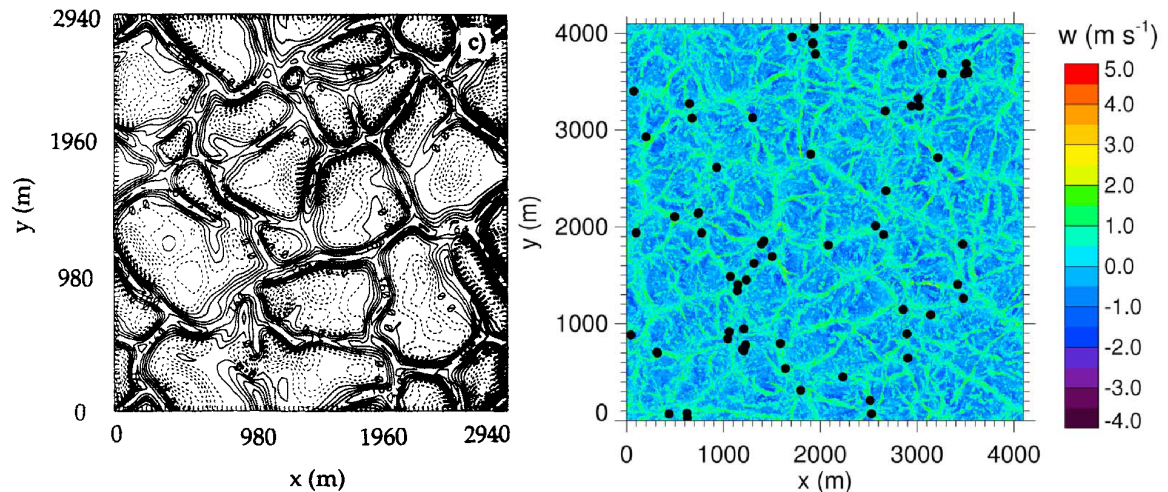


Figure 1.2: Snapshots of horizontal cross sections of the vertical velocity derived from LES data. Visualizations are taken from Kanak et al. (2000) (left, contours from -0.36 to 0.28 with interval 0.04 m s^{-1}) and Raasch and Franke (2011) (right). Black dots on the right indicate vortex centers detected at this snapshot. Reproduced with permission from John Wiley & Sons.

The terrain (C3) is even more favorable for DD development if surface heterogeneities like a different heating or surface roughness are taken into account (e.g., Sinclair, 1969; Rennó et al., 2004; Rafkin et al., 2016). Williams (1948) and Sinclair (1969) emphasized the potential importance of obstacles in the generation of whirls and, subsequently, DDs. The initiation of vortices is also favored by wind gustiness, that is, the variation of wind velocity on short timescales (Newman et al., 2002), which might be attributed to abrupt changes in the surface roughness (Kurgansky et al., 2011). Rennó et al. (2004) highlighted large horizontal temperature gradients caused by irrigated fields that have the potential of producing more intense convective circulations and a larger number of convective vortices compared to homogeneous surfaces. Chapter 3 examines a differential heating of surfaces and its effect on DDs.

Convective vortices can even form in the absence of mean background winds, surface inhomogeneities, or other imposed sources of angular momentum (Kanak et al., 2000). Several studies have proposed mechanisms for the initial DD development in such idealized cases. Kanak et al. (2000) and Raasch and Franke (2011) proposed frameworks for the local generation at the cell vertices of the convective flow pattern. Because of flow asymmetries along convergence lines that merge at the cell vertices and because of convective tilting of near-surface horizontal vorticity, vertical vortices are inevitably generated. Instead, Ito et al. (2013) argued that the necessary circulation for DDs originate from the baroclinically generated horizontal vorticity in the middle of the mixed layer that is transported to the surface by downdrafts. Additionally, Rennó et al. (2004) and Kanak (2005) suggested the so-called hairpin mechanism, in which loops of horizontal rotation are lifted by the updrafts along the cell branches where the flow converges. This lifting creates two counter-rotating vertical vortices of which one remains. All these initial formation mechanism are discussed in Chapter 4.

However, not only heterogeneities in the surface roughness (or surface friction) can influence the vortex formation and, subsequently, its characteristics. The general level of the roughness is also an important factor, even when it is assumed to be homogeneous. In their laboratory study, Wilkins et al. (1975) found broader and weaker vortices when friction is present. Similar results were obtained by Neakrase and Greeley (2010), who stated that an increase in roughness causes an increase in vortex size but a decrease in tangential velocity (see also Zhao et al., 2004). However, a low level of roughness makes the vortex more concentrated compared to frictionless cases due to the enhanced near-surface air convergence and, thus, due to stronger updrafts in the vortex core. For a medium or high roughness, the previously mentioned tendencies described by Wilkins et al. (1975) and Neakrase and Greeley (2010) might dominate (Kurgansky et al., 2016). Numerical simulations by Zhao et al. (2004) showed a weak and stable flow in the vortex over a free-slip surface (no friction) but a violent and turbulent flow over a no-slip surface (with friction). Their results also indicated that surface friction has no effect on the pressure distribution around the vortex. Gu et al. (2008) showed that surface roughness significantly affects the morphology of DDs, changing from a column-like vortex on a very smooth surface to an upside-down cone-like DD on rougher surfaces. Consequently, there is no general agreement and diverse perspective on how the roughness affects the flow near the ground and, thus, contributes to the development of DDs (see also Kurgansky et al., 2016). Therefore, Chapter 4 highlights the effects of surface friction on DDs. Another effect of surface friction is that it makes the flow more turbulent, causing more effective mixing (Wilkins et al., 1975; Leslie, 1977), which smooths sharp gradients of the flow variables. Such sharp gradients are especially

present in DDs, suggesting that a strong turbulent flow accelerates the collapse of DD-like vortices and reduces their lifetimes. The effects of the flow's general turbulence level on convective vortices are also studied in Chapter 4.

1.2.2 Dust Devil Characteristics

Once formed, DDs show distinct features that are listed in Table 1.1. All parameters for which there is sufficient data and which are relevant for this thesis are shown. The values are rounded to the nearest order of magnitude and represent typical features for terrestrial vortices. The cited literature in the third column mostly refers to review papers and articles that either focused on the specific parameter of the first column or summarized results from different studies. In this way, the given typical values do not rely on single dust devil measurements only.

Common lifetimes of DDs are between 1 and 10 min but also shorter times less than a minute and longer times up to several hours have been reported. Larger dust devils tend to have longer lifetimes. Diameters range from 1 to 100 m with a strongly right-skewed (positively skewed) distribution, which means that small-scale DDs between 1 and 10 m are much more frequent and diameters of 100 m are rare. DDs typically reach heights of 10 to 100 m. In extreme cases, even several kilometers are possible. Horizontal wind speeds often amount to $5\text{--}10\text{ m s}^{-1}$ with peak values of up to 25 m s^{-1} . If the horizontal wind is divided into a tangential and radial component like in Tratt et al. (2003) or Inagaki and Kanda (2022), the tangential velocity is typically higher than the radial component. Vertical winds ($1\text{--}10\text{ m s}^{-1}$) are usually smaller than the horizontal component. The translation speed of DDs, that is, the speed at which dust devils move, is mostly comparable to the near-surface background wind of the CBL. In general, they move 10–20 % faster than the wind at 10 m height. Because dust devil occurrence is strongly suppressed above approximately $7\text{--}8\text{ m s}^{-1}$ but triggered for low to moderate background winds (see Subsection 1.2.1), the typical translation speed is between $1\text{--}10\text{ m s}^{-1}$. The DD strength expressed by the pressure drop in the vortex core mostly amounts to several hundred pascals. However, fixed monitoring stations often measure smaller values less than 100 Pa because they do not necessarily detect the actual center of the vortex, where the pressure drop is strongest, and they do not distinguish between a dust-free or dust-laden vortex (Lorenz, 2014). The latter usually shows stronger pressure drops during its lifetime in order to enable particle lifting (e.g., Balme and Hagermann, 2006; Lorenz and Jackson, 2015). Beside the pressure drop, also the vertical vorticity is sometimes used to measure the vortex strength. The vorticity in three dimensions is defined as the local spinning motion at some point in the fluid and is mathematically determined by the curl of the velocity field. Therefore, it is a microscopic measure of the rotation. In case of dust devils, usually the third component (vertical vorticity) is calculated. Remote sensing data suggest typical values between $0.1\text{--}1\text{ s}^{-1}$ for this quantity. DDs also show higher core temperatures of typically several degrees compared to the surroundings due to the continuous, near-surface inflow of warm air heated by the ground (see also Subsect. 1.2.3). The most variable parameters are the particle mass concentration with a range of $1\text{--}1000\text{ mg m}^{-3}$ and the particle flux with characteristic values between 1 and $1000\text{ mg m}^{-2}\text{ s}^{-1}$. The high variability is mainly caused by methodological difficulties in the determination of these parameters and their inherent large variation within DDs. Finally, DD statistics show a similar number of clockwise and counterclockwise rotating vortices.

There are no general guidelines on how to conduct dust devil studies in the field. This

is why many different types of observations, measurement techniques, and data analysis tools complicate an identification of "typical" dust devil characteristics (Lorenz and Jackson, 2016). Electric fields and the morphology are other parameters of interest (e.g., Jackson and Farrell, 2006; Murphy et al., 2016). However, they are not a subject of this thesis.

Table 1.1: Typical dust devil characteristics reported from field studies.

Parameter	Measurements and observations	Literature
Lifetime	1–10 min	Lorenz (2013) Murphy et al. (2016)
Diameter	1–10 m	Mortan (1966), Kurgansky (2006) Lorenz (2011)
Height	10–100 m	Cooley (1971), Murphy et al. (2016)
Wind speeds	5–10 m s ⁻¹ (horizontal), 1–10 m s ⁻¹ (vertical)	Balme and Greeley (2006), Cantor et al. (2006), Murphy et al. (2016)
Translation speed	110–120 % of the ambient wind, 1–10 m s ⁻¹	Crozier (1970), Balme et al. (2012)
Pressure drop	100–1000 Pa	Lamberth (1966), Kanak (2006), Murphy et al. (2016)
Vertical vorticity	0.1–1 s ⁻¹	Fujiwara et al. (2011), Bluestein et al. (2004), Inagaki and Kanda (2022)
Temperature increase	1–10 K	Balme and Greeley (2006), Kanak (2006)
Particle loading	1–1000 mg m ⁻³	Rennó et al. (2004), Metzger et al. (2011), Murphy et al. (2016)
Particle fluxes	1–1000 mg m ⁻² s ⁻¹	Klose et al. (2016)
Sense of rotation	No preferred direction	Carroll and Ryan (1970), Kanak (2006)

1.2.3 Dust Devil Dynamics

Steady-state DDs in their mature and well-developed stage are shown in Fig. 1.3. In many cases, DDs are located within rising plumes and characterized by an expanding core with height (Fig. 1.3c). They are often tilted in the same direction as the mean background wind and, thus, in the direction of motion (Fig. 1.3a). It is this horizontal motion that sustain the DDs for a longer time. Otherwise, the supply of warm surrounding air would be soon interrupted (Kurgansky et al., 2016). Near the region around the low-pressure center a column of hot rising air is present. Together with the tangential velocity, this rising air forms the swirling helical structure that can often be observed in nature. In some DDs, the upward swirling flow might occur throughout the whole DD (Fig. 1.3a), while in some other cases

a reversal in flow (downward flow) might appear at considerable height above the surface (Fig. 1.3b), which is sometimes termed as a vortex breakdown (see also Fig. 1.4a). Kurgansky et al. (2016) suggested that updraft motion predominates in tightly organized rope-like vortices. If a downward flow is present, it is normally weaker and cooler compared to the central updrafts and can even exist at ground level, penetrating the whole DD. In this case, the downdraft is often surrounded by an annular region of strong radial shear in the tangential and axial velocity component, representing a two-cell vortex state (Fig. 1.4b). In this state, the highest near-surface upward wind velocities are typically located slightly outside the core and decrease rapidly with radius from the point where the maximum is reached. In general, the vertical movement of air is controlled by the buoyancy and axial pressure gradient force. Especially in the lower part of the vortex, the flow converges in radial direction due to the low pressure in the core and reduced angular momentum induced by surface friction. The radial inflow region of near-surface warm air (only a few meters thick) forces the convective behavior and often reaches its maximum just outside the visible dust column. Within the column, the radial component is almost zero or might even point out of the center. The outward flow arises when the radial inflow in the surface layer is strong enough to trigger a so-called overshooting of this rapid inflow, resulting in intense outward-leaning updrafts at the edge of the DD several meters above ground (Fig. 1.3b). This effect can be observed in nature when DDs appear as inverse cones. However, for idealized frictionless cases, these outward-leaning updrafts do not occur due to the much smaller radial inflow. This is why inverse cone-like DDs are probably more frequent on rough than on smooth grounds. Neglecting viscous forces and surface friction, the radial velocity is controlled by the centrifugal force (the rotation) and the radial pressure gradient. The tangential velocity typically peaks at the border of the dust column at a considerable height above the Earth's surface and is almost zero at the core along the vertical axis. From an analytical point of view, the radial distribution of the tangential velocity often follows to a first approximation the Rankine vortex model (see below). The region outside the DD is typically characterized by cooler air that sinks down (Sinclair, 1973; Zhao et al., 2004; Balme and Greeley, 2006; Kurgansky et al., 2016).

In summary, a DD resembles a one-cell vortex with a vortex breakdown. During its most intense and persistent state, a transition to a doubled-celled vortex is possible (see also Mullen and Maxworthy, 1977; Spiga et al., 2016). This state is mainly characterized by a downward flow in the core with strong spiral updrafts around, a rapidly increasing toroidal movement toward the border of the dust column and strong near-surface radial inflow in the surrounding region. Background winds, subvortices, and local gusts or obstacles contribute to the variability in flow structure and the deviation from an axisymmetric behavior. DDs can also be divided spatially into characteristic flow regions or temporally into different stages of development (e.g., Sinclair, 1973; Zhao et al., 2004). The flow regions are addressed in Chapter 6. A detailed explanation of the life cycle is beyond the scope of this thesis. The basic dynamics of DD-like vortices described above play an important role in the understanding of the numerical results that will follow.

A common way to approach vortex dynamics is the vorticity equation, which describes the temporal evolution of the three-dimensional vorticity vector $\vec{\omega} = \nabla \times \vec{v}$, in which $\vec{v} = u_i = (u, v, w)$ is the velocity vector in a Cartesian coordinate system with the index $i \in \{1, 2, 3\}$ and $\nabla = (\partial/\partial x, \partial/\partial y, \partial/\partial z)$ is the respective nabla operator with the location vector $\vec{x} = x_i = (x, y, z)$. The vorticity equation can be derived by taking the curl of the Navier-Stokes momentum equation and using several vector calculus identities. The Navier-Stokes equa-

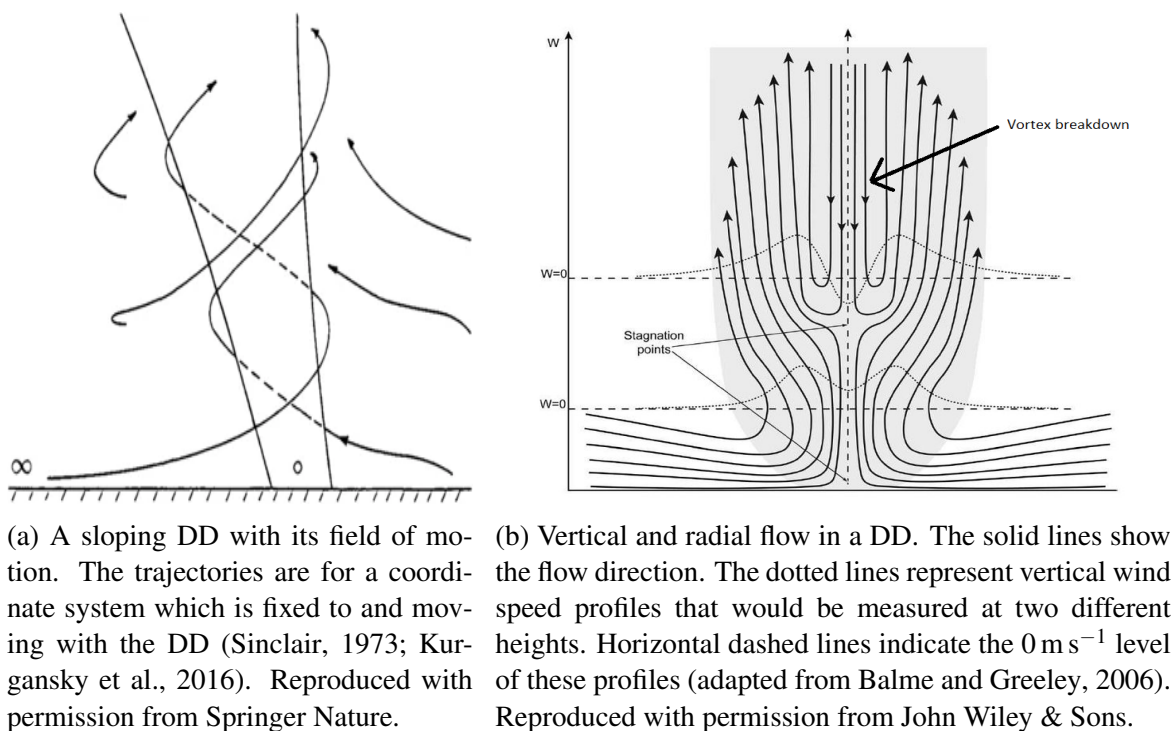
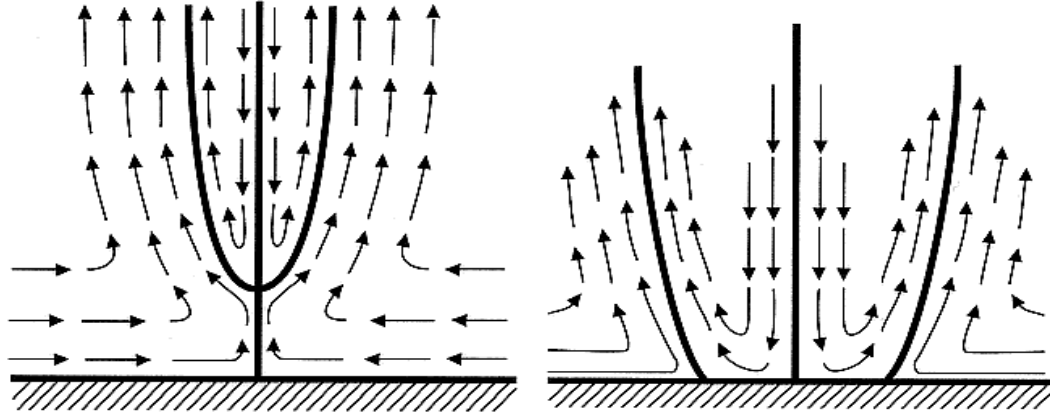


Figure 1.3: Different sketches of the typical flow around DDs in a vertical plane.

tions in general are able to predict the future state of a Newtonian turbulent fluid from an Eulerian perspective and include equations for the conservation of momentum, energy, and mass. Some authors restrict the Navier-Stokes equations only to the conservation of momentum (e.g., Pope, 2000). The vorticity equation reads for a rotating frame of reference under the reasonable assumptions of a constant Earth-rotation vector $\vec{\Omega} = (0, f^*/2, f/2)$ and incompressibility of air:

$$\frac{\partial \vec{\omega}}{\partial t} + (\vec{v} \cdot \nabla)(\vec{\omega}) = [(\vec{\omega} + 2\vec{\Omega}) \cdot \nabla] \vec{v} + \frac{1}{\rho^2} \nabla \rho \times \nabla p + \nu_m \nabla^2 \vec{\omega}, \quad (1.1)$$

where t is the time, ρ is the air density, p is the air pressure, and ν_m is the kinematic viscosity (sometimes also called the momentum diffusivity) of air. The Coriolis parameters f^* and f are defined as $2\Omega \cos(\phi)$ and $2\Omega \sin(\phi)$, respectively, with $\Omega = 7.29 \times 10^{-5} \text{ rad s}^{-1}$ being



(a) A single-celled below and doubled-celled above vortex with vortex breakdown for a medium swirl ratio. (b) Two-cell vortex with a central downward motion through the whole vortex for a higher swirl ratio than in (a).

Figure 1.4: Vortex models depending on the swirl ratio, which describes the ratio of angular to radial momentum (adapted from Wakimoto and Liu, 1998). At large ratios (not shown), the flow indicates multiple vortices and becomes highly asymmetric (see also Kurgansky et al., 2016). ©American Meteorological Society. Used with permission.

the Earth's angular velocity and ϕ being the geographical latitude. The Coriolis force can be neglected for DDs due to Rossby numbers that are orders of magnitude larger than one (Balme and Greeley, 2006). The Rossby number describes the ratio of inertial to Coriolis forces. Usually, it is the vertical vorticity $\zeta = \vec{k} \cdot \vec{\omega}$ (\vec{k} is the unit vector in z -direction) which is of interest in case of a DD (e.g., Raasch and Franke, 2011; Ito et al., 2013; Onishchenko et al., 2019). From Equation (1.1) it follows (see also Rafkin et al., 2016):

$$\frac{d\zeta}{dt} = \underbrace{-\zeta(\nabla_{\mathbf{h}} \cdot \vec{v}_{\mathbf{h}})}_{\text{divergence term}} - \underbrace{\left(\frac{\partial w}{\partial x} \frac{\partial v}{\partial z} - \frac{\partial w}{\partial y} \frac{\partial u}{\partial z} \right)}_{\text{twisting term}} - \underbrace{\frac{1}{\rho^2} \vec{k} \cdot (\nabla_{\mathbf{h}} p \times \nabla_{\mathbf{h}} \rho)}_{\text{solenoidal term}} + \underbrace{v_{\mathbf{m}} \nabla^2 \zeta}_{\text{diffusion term}}. \quad (1.2)$$

The subscript h marks the horizontal components, where the vertical direction is assumed to be zero. In fact, only the solenoidal term is able to create vertical vorticity from an initially non-rotating flow. It describes the baroclinity, that is, the misalignment of surfaces of constant pressure and constant density. If the density is replaced with the temperature by using the ideal gas law, it can be shown that baroclinity also describes the misalignment of surfaces of constant pressure and constant temperature. In a baroclinic atmosphere, there is a temperature gradient on a constant pressure surface, which would create a circulation and thus vorticity. Mathematically, the circulation can be regarded as the averaged vorticity for a specific area. The solenoidal term can further be interpreted as a contribution to the horizontal shear of the horizontal velocity because $(\partial \rho / \partial x)(\partial p / \partial y)$ creates $\partial v / \partial x$ and $(\partial \rho / \partial y)(\partial p / \partial x)$ creates $\partial u / \partial y$ or in words, a horizontal pressure gradient accelerates lighter air parcels faster than heavier ones. The horizontal divergence and diffusion term already require existing vertical vorticity to be nonzero. A converging flow decreases the radius of air parcels that circulate in a vortex tube. This necessarily increase the vorticity in accordance with the Kelvin's circulation theorem, which says that in a barotropic ($\nabla p \times \nabla \rho = 0$), inviscid fluid the circulation is constant. In incompressible flows, $\nabla_{\mathbf{h}} \cdot \vec{v}_{\mathbf{h}}$ can be replaced with $-\partial w / \partial z$ due to the conservation of mass. Therefore, the divergence

term is also described as the stretching term because the ends of a vertical vortex tube are being pulled apart in case of positive vertical gradients of w . Such gradients would stretch and thin the vortex tube, resulting in higher vorticity. The molecular diffusion (often neglected in turbulent flows) tries to unify the vorticity field. It removes vorticity where it is high and increases vorticity where it is low, although counter-gradient diffusion is theoretically possible (Rafkin et al., 2016). The twisting term produces vertical vorticity through the product of horizontal gradients of w and the vertical shear of the horizontal wind, that is, horizontally orientated vortex tubes will be tilted into vertical direction.

In this thesis, a Boussinesq-approximated form of the Navier-Stokes equations without viscous forces is used for the numerical simulations (see Chapter 2.1). In such a system, baroclinic processes can not directly generate vertical vorticity because the solenoidal term described above is zero for this component (see also Cao, 1999; Ito et al., 2013). Instead, processes like vortex stretching, tilting, advection, and the (subgrid-scale) turbulent diffusion can locally modify vertical vorticity (see also Kanak, 2006). If the baroclinic term of the three-dimensional vorticity equation (second term on the right hand side of Eq. (1.1)) is split into

$$\frac{1}{\rho^2} \nabla \rho \times \nabla p = \frac{1}{\rho^2} \left(\nabla_h \rho \times \nabla_h p + \nabla_h \rho \times \frac{\partial p}{\partial z} \vec{k} + \frac{\partial \rho}{\partial z} \vec{k} \times \nabla_h p \right), \quad (1.3)$$

it can be shown that only the horizontal component (second term on the right-hand side of Eq. (1.3)) is retained under the Boussinesq approximation because of

$$\frac{1}{\rho^2} \nabla_h \rho \times \frac{\partial p}{\partial z} \vec{k} = -\frac{g}{\theta_0} \vec{k} \times \nabla_h \theta^* \quad (1.4)$$

Here, θ is the potential temperature, g is the gravitational acceleration, a subscript 0 denotes the so-called basic state in hydrostatic equilibrium and an asterisk marks deviations from this state so that all thermodynamic variables Ψ such as the pressure, density, or (potential) temperature can be written as $\Psi(x, y, z, t) = \Psi_0(z) + \Psi^*(x, y, z, t)$. In the original primitive equation model, the baroclinic term has both horizontal and vertical components (Cao and Cho, 1995; Cao, 1999). The first and last term of Eq. (1.3) (both zero in a Boussinesq flow) arise out of the flow inertia and are completely independent from gravitational forces. The second term (active in a Boussinesq flow) describes the generation of horizontal vorticity through the buoyancy force that acts on displaced air parcels from their unperturbed position (see again Eq. (1.4)). However, because baroclinic effects are unable to generate vertical vorticity under the Boussinesq approximation, it must be initially created by the twisting term so that a vertical vortex can form (see also Heifetz et al., 2019). Flow convergence or, equivalent, the stretching term might then increase existing vertical vorticity and a persistent DD might be generated. The above information is important to better understand the remarks on vortex development in the subsequent chapters.

Some analytical vortex models have frequently applied to describe DD dynamics. This especially includes the Rankine (Rankine, 1868), Burgers-Rott (Burgers, 1948; Rott, 1958) and Vattistas (Vattistas et al., 1991) vortex models. For example, Kanak (2005) and Nishizawa et al. (2016) applied the Rankine and Burgers-Rott model to their numerically simulated DD-like vortices. The analysis of Kanak (2005) showed that the Burgers-Rott model is more precise for the convective vortices that spontaneously arise in numerical simulations of the CBL. However, also the Rankine model gave satisfying results. Sinclair (1973), Tratt et al. (2003), and Bluestein et al. (2004) only used the Rankine vortex to analytically describe the

radial distribution of the tangential velocity of measured DDs. For a similar purpose, Lorenz (2014) and Jackson et al. (2021) used the Vatisstas model. Also more complex approaches have been discussed in literature to model DD dynamics like an exact solution of the Euler equations for an incompressible non-dissipative medium by Onishchenko et al. (2021). Such approaches are rarely used in practice, probably because of their more difficult application. In the following Chapters 3 and 4, the Rankine vortex model is applied, which is why it is briefly introduced. The Rankine vortex model neglects the radial and vertical velocity components and assumes a solid body rotation inside a finite round core of radius r_c with constant vorticity (forced vortex) followed by a potential or free vortex with zero vorticity everywhere. In such a structure, the piecewise-continuous tangential velocity profile v_Φ in radial direction r is determined by

$$v_\Phi(r) = \begin{cases} Vr/r_c & \text{for } r \leq r_c, \\ Vr_c/r & \text{for } r > r_c, \end{cases} \quad (1.5)$$

which describes a linear velocity increase with radial distance in the core up to a characteristic or maximum value V and a subsequent decrease with r^{-1} in the outer region. The point where V is reached (at r_c) is often described as the vortex wall radius (e.g. Kurgansky et al., 2016; Lorenz, 2016). As mentioned above, the vorticity is constant in the core and is generally given by

$$\nabla_{\text{cyl}} \times \vec{v}_{\text{cyl}} = \left(\frac{1}{r} \frac{\partial v_z}{\partial \Phi} - \frac{\partial v_\Phi}{\partial z} \right) \vec{e}_r + \left(\frac{\partial v_r}{\partial z} - \frac{\partial v_z}{\partial r} \right) \vec{e}_\Phi + \frac{1}{r} \left(\frac{\partial}{\partial r} (rv_\Phi) - \frac{\partial v_r}{\partial \Phi} \right) \vec{e}_z, \quad (1.6)$$

where ∇_{cyl} and v_{cyl} are the nabla operator and velocity vector in cylindrical coordinates (r, Φ, z) , respectively, and $\vec{e}_{r, \Phi, z}$ describes the cylindrical unit vectors. Eq. (1.6) yields a vertical vorticity ζ of $2V/r_c$ (angular velocity of V/r_c) if the tangential velocity profile from Eq. (1.5) is assumed and v_r and v_r are neglected. Another important physical parameter for the analysis of vortices is the circulation C , which describes the macroscopic rotation for a finite two-dimensional area of the fluid. It can be determined by the surface integral of the curl of the velocity field. If the surface normal direction points in the direction of the vertical unit vector, the circulation around a Rankine vortex with constant vorticity amounts to

$$C = \int \int_S \zeta dS = 2\pi V r_c, \quad (1.7)$$

in which S describes the surface. Also the pressure drop Δp can be derived from the Euler equations in polar coordinates under the assumption of axial symmetry (e.g., Alekseenko et al., 2007). It is given by

$$\Delta p = \rho V^2. \quad (1.8)$$

The pressure reduction at the core boundary, where also the maximum tangential velocity V is reached (see above), is given by $\Delta p/2$. This result is often used to define the vortex radius if a visible dust column is absent (e.g., Lorenz, 2014; Lorenz and Lanagan, 2014; Lorenz and Jackson, 2016; Kahanpää et al., 2016). In spite of its simplicity, the Rankine combined vortex model performs well for various of applications (Kurgansky et al., 2016).

Another approach to theoretically understand and describe steady-state vortex dynamics is the thermodynamic framework proposed by Rennó et al. (1998) in which DDs are

regarded as convective heat engines in cyclostrophic balance, that is, centrifugal forces are balanced by pressure gradient forces. The theory is able to predict the pressure drop as well as the wind speed (horizontal and vertical) of convective vortices and was successfully validated against real DDs (Rennó et al., 2000). It is used in Chapter 5 for a theoretical evaluation of the numerical results. Therefore, it is shortly described below. Rennó et al. (1998) derived the following equation to get the order of magnitude for the pressure drop across a dust devil:

$$\Delta p = p_\infty - p_c = p_\infty \left\{ 1 - \exp \left[\left(\frac{\gamma \eta}{\gamma \eta - 1} \right) \left(\frac{c_p}{R} \right) \left(\frac{T_c - T_\infty}{T_\infty} \right) \right] \right\}. \quad (1.9)$$

Here, p_c , T_c , p_∞ , and T_∞ are the pressure and temperature at the vortex center (subscript c) and at a large radial distance from the center (subscript ∞), respectively. The variable R is the gas constant of air, and γ is the fraction of the total dissipation of mechanical energy consumed by friction near the surface with a value between 0.5 and 1.0 (Rennó et al., 1998). The thermal efficiency η defines the fraction of the heat input that is turned into work. The Carnot efficiency represents an upper bound for η . In practice, η can be estimated as $gz_i/c_p T_\infty$ with z_i the boundary layer depth and c_p the specific heat capacity at constant pressure (Souza et al., 2000; Kurgansky et al., 2016). Typical values are $\eta \approx 0.1$ (Rennó and Ingersoll, 1996; Rennó et al., 1998, 2000). Equation (1.9) predicts the maximum thermodynamic intensity of a convective vortex (Rennó et al., 2000). Consequently, Δp should be considered as an upper limit for DDs rather than a typical value. By using the ideal gas law and Eq. (1.9), an expression for the wind speed around a DD under cyclostrophic balance can be derived:

$$v_\Phi = \sqrt{RT_\infty \left\{ 1 - \exp \left[\left(\frac{\gamma \eta}{\gamma \eta - 1} \right) \left(\frac{c_p}{R} \right) \left(\frac{T_c - T_\infty}{T_\infty} \right) \right] \right\}}. \quad (1.10)$$

This tangential velocity estimate is usually interpreted as an upper bound to the observed values (Rennó and Ingersoll, 1996; Rennó et al., 2000; Souza et al., 2000). Equations (1.9) and (1.10) can be further simplified by using the assumptions $\gamma \eta - 1 \approx -1$ (Rennó et al., 1998) and $1 - \exp(-x) \approx x$ for an arbitrary number $x \ll 1$ (see also Kurgansky et al., 2016):

$$\Delta p = \frac{\gamma \eta c_p p_\infty (T_c - T_\infty)}{RT_\infty}, \quad (1.11)$$

$$v_\Phi = \sqrt{\gamma \eta c_p (T_c - T_\infty)}. \quad (1.12)$$

The Eqs. (1.11) and (1.12) are the equations used in this thesis.

1.3 Numerical Simulation of Turbulent Flows

In this thesis, turbulence-resolving flow simulations are performed. This section gives an overview of the physical and mathematical background regarding these numerical simulations. Based on the given information, requirements for the numerical simulation of DDs are subsequently introduced (Section 1.4).

A fluid can be treated as a continuous medium instead of studying the movement of individual molecules. In such a medium, two different states regarding the fluid's flow are distinguished: a laminar state, where streamlines appear mostly parallel, and a turbulent

state, where streamlines are very irregular. To determine whether a flow is turbulent or laminar, the Reynolds number can be calculated, which is a dimensionless quantity that describes the ratio of inertial forces to viscous forces. The critical value above which the flow is considered turbulent varies, for example, with the specific geometry. For a pipe flow, a typical critical value is 2300 (Schlichting and Gersten, 2006). Above this value, the smallest disturbance would be sufficient to cause a turbulent state. The vast majority of engineering and geophysical flows are turbulent, which especially includes atmospheric boundary layer flows with typical Reynolds numbers of 10^8 (e.g., Wyngaard, 2010). Such flows are extremely sensitive regarding initial and boundary conditions and are characterized by many eddies of different spatial and temporal scales that interact with each other and exchange energy. In addition, turbulent motions are three-dimensional, anisotropic, nonlinear, unsteady and irregular. Consequently, flow quantities like the velocity or the temperature vary significantly with position and time, which is why they appear mostly random and chaotic. Therefore, turbulence is usually described by its statistical properties. An exact prediction of the state of a turbulent flow is impossible because no general, continuously differentiable, analytical solution of the Navier-Stokes equations exist. In case of very idealized and simplified conditions like for homogeneous, stationary, isotropic, and/or incompressible turbulent flows, the Navier-Stokes equations can be solved analytically. One of the most important feature of turbulence is the ability to mix and redistribute the fluid's matter, heat, or momentum much more effectively than a laminar flow, where only the molecular diffusion is responsible for mixing. Finally, turbulent flows are characterized by a high rate of energy dissipation due to the enhanced frictional forces between fluid elements. Thus, a continuous energy supply is necessary to sustain a turbulent state. Typical examples of turbulent flows are wind turbine wakes, rivers, boundary layer flows, or exhaust plumes from chimneys. For a comprehensive overview about the key properties of turbulence, the reader is referred to Tsinober (2009).

Figure 1.5 schematically visualize the wave-number-dependent kinetic energy distribution $E(k)$ of a typical atmospheric turbulence spectrum as a log-log graph. It can be interpreted as a representation of the size-dependent eddy strength and plays a crucial role in the understanding of the different modeling approaches for turbulent flows (see next paragraph). The turbulence spectrum is typically derived from the power spectral density of the turbulent velocity field. Its integral is equal to the variance of this velocity (see also Wyngaard, 2010). The region adjacent to the peak value and the leftmost side of the spectrum belong to the energy containing or production range, where Turbulence Kinetic Energy (TKE) is added to the flow by the extraction of energy from the mean flow. The production range covers the largest (small wave numbers), energy containing, and highly anisotropic eddies of the spectrum, where viscous effects are negligible. The middle area is known as the inertial subrange, where TKE approximately follows the Kolmogorov $-5/3$ power law scaling. Here, energy is transferred from larger to smaller scales (without loss or production) caused by the nonlinear interactions between the eddies and the decay of vortices. Strictly speaking, this is only true on average. An instantaneous and local energy transfer is also possible from small to large eddies, which is known as the backscatter of TKE. The turbulent motions in the inertial subrange are still dominated by inertial forces and not significantly influenced by the viscosity of the fluid. At the smallest scales of the spectrum close to the Kolmogorov length scale, which is about 10^{-3} m in the atmospheric boundary layer and describes the characteristic length scale of the dissipative and much more isotropic eddies, the energy is converted into heat due to viscous forces. This region controls the rate at which TKE is

extracted from the flow. The whole process of energy transfer from the production range to the dissipation range is called energy cascade, which is fundamental for the understanding of turbulence. It implies that under equilibrium conditions the dissipation rate is completely controlled by the production rate because in between (in the inertial subrange) there are no sources or sinks of TKE and energy is just transferred to smaller scales as explained above.

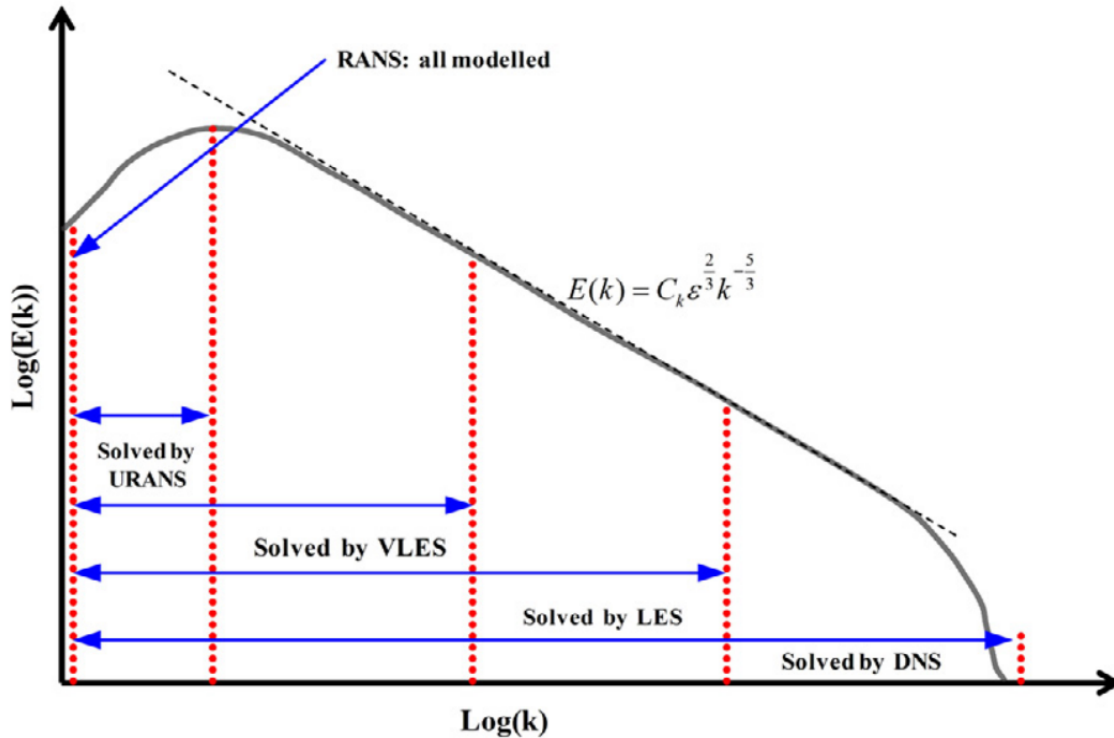


Figure 1.5: Schematic view of the turbulence energy spectrum (solid line) and the portions that are explicitly solved by different simulation approaches for turbulent flows (blue arrows). Vertical dotted lines show the upper limits of the resolved spectrum in terms of the wave number. The black dashed line indicates Kolmogorov's $k^{-5/3}$ power law with ϵ the viscous dissipation rate of TKE per unit mass, k the wave number, and C_k the Kolmogorov constant (Argyropoulos and Markatos, 2015). Reproduced with permission from Elsevier.

As already indicated at the beginning of this section, no tools are currently available to approach the whole complexity of turbulence analytically. Instead, laboratory and field experiments (e.g., wind tunnel experiments or scintillometer measurements) as well as CFD simulations are frequently used. Due to the constant increase in computing power (e.g., García-Risueño and Ibáñez, 2012) and the advances in numerical techniques for solving differential equations, turbulence is nowadays often studied numerically. In general, turbulence simulation approaches try to numerically integrate the atmospheric fluid dynamics equations, that is, the fully compressible or incompressible, non-hydrostatic Navier-Stokes equations, in a four-dimensional way (all three spatial directions plus the temporal dimension). Usually, three different approaches are distinguished. Two of them, the Direct Numerical Simulation (DNS) and Large-Eddy Simulation (LES) technique, try to solve the governing equations to get a three-dimensional, time-dependent, turbulent flow field for one specific realization of the flow. A realization represents one specific member of an ensemble of different repetitions of the same flow scenario. These simulations are called turbulence-resolving. Conceptually, DNS is the simplest approach. It solves the Navier-Stokes equa-

tions directly without any simplifying assumption or approximation apart from the inevitable approximations for solving differential equations numerically. From a physical point of view, this implies that all turbulent length (time) scales, from the largest (longest) down to the smallest (shortest), are resolved, which is why it is considered as the most precise way to simulate a turbulent flow. Because DNS resolves all the scales without the usage of any turbulence parameterization, it requires a lot of computational resources, that is, the required number of floating-point operations is usually very high. The computational resources scale with the third power of the Reynolds number (e.g., Pope, 2000). The Reynolds number is also a measure of the scale separation between the largest and smallest flow structures. High values indicate a large difference between their dimensions (e.g., Wyngaard, 2010). Therefore, DNS is restricted to flows with low or moderate Reynolds numbers typically less than 10^4 (e.g., Mellado et al., 2018). It is often suitable for academic research, for example to study the fundamentals of turbulence, but not practical for atmospheric or industrial applications.

LES can be regarded as an intermediate stage between DNS and Reynolds-Averaged Navier-Stokes (RANS) – the third approach to simulate turbulent flows. In LES, only the largest energy-containing eddies of the flow are explicitly simulated that account for 80-90 % of the turbulent transport (e.g., Spiga et al., 2016). The smaller ones are just parameterized by using Subfilter-Scale (SFS) models, which try to capture the influence of the smaller-scale motions on the resolved flow by modeling the so-called SFS stresses. Typically, these stresses are modeled via certain relationships to the resolved flow quantities. Famous approaches are the classical Smagorinsky model (Smagorinsky, 1963; Lilly, 1966) or the eddy-viscosity model by Deardorff (1980), which solves a prognostic equation for the SFS-TKE. For high Reynolds numbers like those of the atmospheric CBL, near-surface turbulent interactions and exchanges must still be completely modeled, even in LES. This so-called near-wall modeled LES is a consequence of the reduced eddy size of the energy-carrying eddies when approaching the surface. For an explicit resolution of these eddies much finer grid spacings compared to the bulk region of the flow must be applied, which is often computationally too expensive. Only for moderate Reynolds numbers, near-wall resolved LES is an appropriate tool. To realize the scale separation in LES mathematically, the Navier-Stokes equations are solved for spatially filtered flow quantities, which are representative for the larger-scale turbulent motions. Through the filtering, the aforementioned SFS stresses arise due to the nonlinearity of the Navier-Stokes equations. The filtering can be realized either by an explicit analytical filter (e.g. a Gaussian or box filter) or by an implicit filtering, where the discretization on a numerical grid with a certain characteristic grid spacing works as the low-pass filter (e.g., Schumann, 1975). In case of implicit filtering, scales less than the characteristic filter width are often named as the Subgrid-Scale (SGS) instead of the more general term SFS. For both explicit and implicit filtering, the characteristic filter width must be located within the inertial subrange of the turbulence spectrum. Otherwise, either the modeled part of the spectrum will be too large for achieving reasonable results or the computational costs will exceed the available resources. Formally, the decomposition of a turbulent quantity, for example the velocity component u , into a spatially filtered (resolved) part $\tilde{u}(\vec{x}, t)$ and a residual (SFS) part $u''(\vec{x}, t)$ so that

$$u(\vec{x}, t) = \tilde{u}(\vec{x}, t) + u''(\vec{x}, t) \quad (1.13)$$

is typically introduced by the explicit application of a low-pass filter function G according

to the formula

$$\tilde{u}(\vec{x}, t) = \int \int \int_{-\infty}^{\infty} G(\vec{x} - \vec{x}') u(\vec{x}', t) dx'_1 dx'_2 dx'_3 \quad (1.14)$$

with \vec{x}' being the variable to be integrated. The quantity $\tilde{u}(\vec{x}, t)$ is still a turbulent field because only a portion of the turbulence spectrum is filtered out. The scale separation enables LES to be computationally less expensive than DNS but it still requires more computational resources than RANS with the advantage of an increased accuracy and reliability. Additionally, LES provides information about the flow that RANS is not able to supply, like high-frequency turbulent time series that can directly be measured in reality. The increasing computing power during the recent decades has led to a frequent usage of LES also in many engineering applications (e.g., Sarkar, 2020).

Finally, RANS models parameterize all the turbulent scales and the governing equations are solved for the mean quantities with the help of turbulence models (e.g., eddy viscosity models) that account for the effects of the turbulent scales on the mean flow via the closure of the unknown Reynolds stress terms. These terms arise from the averaging of the Navier-Stokes equations and represent the mean transfer of, for example, momentum and heat, caused by the whole spectrum of turbulence. Turbulence models are often less universal and require more model tuning compared to their counterpart in LES – the SFS models. The latter must only take care of the small turbulent scales, which contain much less energy and which tend to be similar in many physical setups. Instead, turbulence models must capture the whole range of eddies, also the large energy-containing and anisotropic ones. This makes the turbulence models an important model component for the final flow solution despite the fact that they are subject to large uncertainties. The averaging operation in RANS usually corresponds to an ensemble average or, in case of stationary turbulence, to a temporal average. Each turbulent quantity, for example the velocity component u , can be decomposed into a mean value $\bar{u}(\vec{x}, t)$ and a deviation $u'(\vec{x}, t)$ from it:

$$u(\vec{x}, t) = \bar{u}(\vec{x}, t) + u'(\vec{x}, t). \quad (1.15)$$

The ensemble-averaged value $\bar{u}(\vec{x}, t)$ is defined as

$$\bar{u}(\vec{x}, t) = \lim_{N \rightarrow \infty} \frac{1}{N} \sum_{n=1}^N u(\vec{x}, t; n), \quad (1.16)$$

where the summation index n indicates each individual realization of the flow and N describes the total number of realizations. The ensemble average, also often referred to as the Reynolds average, is a linear operator that fulfills the commutative and distributive property. In addition, averaging \bar{u} again has no effects and an average of the fluctuating part is zero. If the turbulent quantity is stationary or homogeneous, the ensemble average is only a function of \vec{x} or t , respectively, and it can be replaced by a time or spatial average of a single realization (see also Wyngaard, 2010). RANS is less computationally expensive compared to a comparable realization of the physical setup with DNS or LES, which is why it is widely used in industrial applications. However, for investigating the characteristics of turbulence and turbulent phenomena like DDs, RANS is unsuitable (see also Section 1.4).

The basic ideas of the aforementioned methods for simulating a turbulent flow can be schematically incorporated into the energy cascade and the underlying turbulence spectrum. This is shown in Fig. 1.5 by the blue arrows, which mark the regions of the spectrum that are

explicitly solved by the respective CFD method. However, the methods mentioned so far are by far not complete. Further approaches have been developed like Unsteady Reynolds-Averaged Navier-Stokes (URANS), Very Large-Eddy Simulation (VLES), or hybrid RANS-LES that shall be mentioned here only for the sake of completeness (see also Fröhlich and von Terzi, 2008). In contrast to steady-state simulations, where the flow does not change with time, URANS also considers the large-scale unsteadiness of the flow but these simulations are still based on the RANS equations. Also VLES tries to explicitly simulate the larger-scale portion of the eddies but is based on the traditional LES approach that uses SFS models. In case of hybrid RANS-LES, the basic idea is to define three different regions: one, where RANS is applied and another one, where LES is applied with a transition region in between that is controlled by blending functions, which smoothly switches between the two model types. This approach tries to make use of the advantages of LES while keeping the efficiency of RANS models where LES would be too expensive. In this thesis, DNS (Chapter 4) and LES (Chapter 3, 5, and 6) are performed. In a next step, it is clarified how and under which constraints DDs, as a turbulent phenomenon in the CBL, can be numerically simulated.

1.4 Numerical Simulation of Dust Devils

One main motivation for studying DDs numerically is related to the much simpler generation of spatially and temporally high-resolution, three-dimensional data compared to field measurements. Regions of $\sim 10\text{ km}^2$ can be monitored in a simulation with high spatial and temporal resolution of several meters and a few tenths of a second, respectively (e.g., Raasch and Franke, 2011). So far, this is not possible with measurements. As soon as the resolution is high ($\sim 1\text{ m}$), the monitoring area gets rather small ($\sim 100\text{--}1000\text{ m}^2$) (e.g., Oncley et al., 2016; Inagaki and Kanda, 2022). In addition, nearly every DD feature can be derived from the numerical data without too much effort. Instead, measurements must often focus on a limited number of DD features, mostly the pressure drop (e.g., Lorenz, 2012) and the flow field with only some or all wind components included (e.g., Sinclair, 1973; Bluestein et al., 2004). Another aspect which motivates the numerical simulation of DDs is to find a parameterization for global and regional climate models that accounts for the effects of convective vortices on the dust cycle (see also Spiga et al., 2016). Only with numerical simulations, a large population of DDs, covering the whole range of different characteristics, can be determined under various environmental conditions. Using this population, a DD parameterization could be established.

The previous section has shown that turbulence-resolving numerical simulations are only possible with DNS and LES. Because DDs develop in the atmospheric CBL, which is a strong turbulent environment, and because DDs by themselves are considered to be a turbulent, coherent phenomenon with spatial and temporal scales of just a few meters and minutes (see again Subsection 1.2.2), an explicit resolution of at least some parts of the turbulence spectrum must be ensured to investigate these vortices. Thus, only DNS and LES are capable of adequately resolving DDs, at least if a sufficiently small grid spacing is chosen. Figure 1.6 illustrates what a sufficiently small grid spacing means in terms of the turbulence energy spectrum introduced one section before. Even if a resolution below 1 m is chosen, typical dust devils with diameters of 1–10 m (see Table 1.1) are still affected by the poorly resolved scales. An appropriate spatial resolution of a specific phenomenon typically requires at least 5–10 grid points (e.g., Xie and Castro, 2006; Spiga et al., 2016). Due to

an artificially increased dissipation by the numerical model's advection scheme and/or a too dissipative behavior of the SGS model, the simulated kinetic energy of scales of even several times the grid spacing significantly deviate from reality (see Fig. 1.6). Therefore, it is desirable to shift the poorly resolved wave numbers as far as possible toward high wave numbers away from the DD scale. A high resolution below 1 m must be chosen for DNS anyway to work appropriately for atmospheric flows with smallest scales of $\sim 10^{-3}$ m.

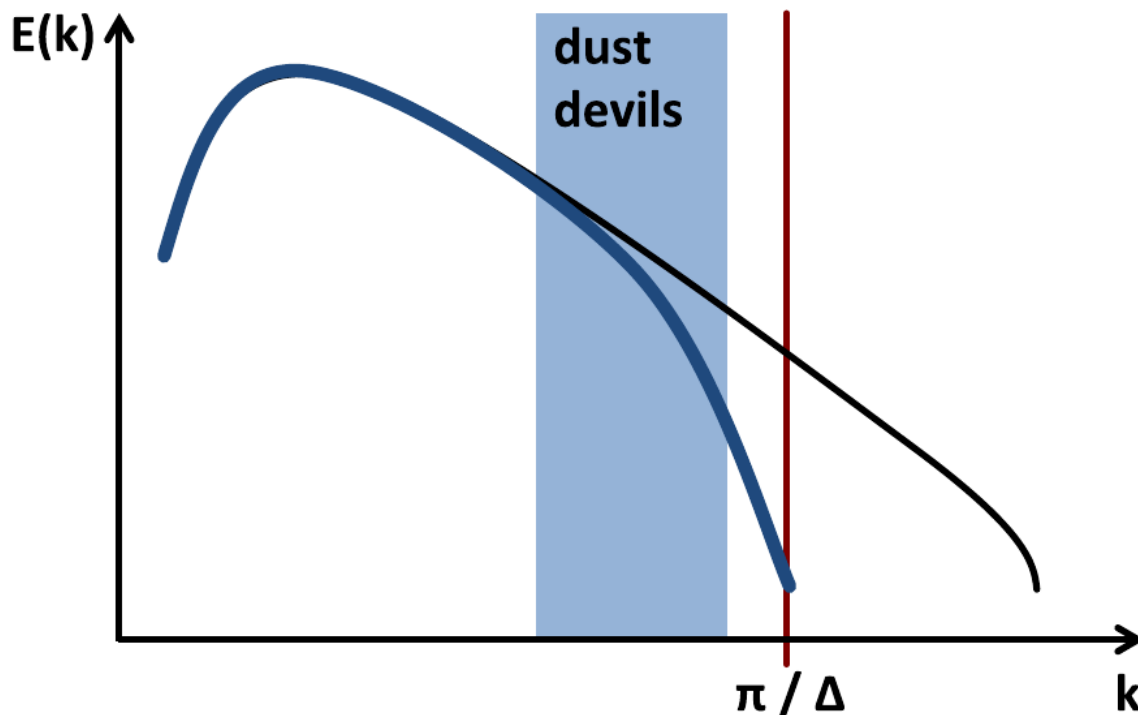


Figure 1.6: Idealized turbulence kinetic energy spectrum measured in the CBL (black line) or derived from LES (blue line). The wave number that belongs to the LES grid spacing Δ is indicated by the red line at π/Δ . The shaded area in blue indicates the typical horizontal size range of dust devils (Spiga et al., 2016). Reproduced with permission from Springer Nature.

Despite a relatively large grid spacing of several tens of meters, Mason (1989) and Kanak et al. (2000) were the first who present evidence of dust devil-like, convective whirlwinds in LES of the terrestrial CBL. Also Ito et al. (2010b) showed with a resolution of 50 m that the characteristic vortex structure can be at least qualitatively reproduced even in relatively coarse-resolution LES. However, results from high resolutions with grid spacings of a few meters are, of course, much closer to real DDs (Kanak, 2005; Raasch and Franke, 2011). Coarse-resolution LES probably resolve rather the larger-scale "parent-type" circulations, in which DDs are embedded, and not the actual DD-scale vortex (Kanak, 2006).

In addition to the resolution, the physical size of the simulation domain is a crucial issue. There is strong evidence that the existence of vertical vortices is connected to the larger-scale cellular flow pattern of the CBL and to the vertically deep convective plumes (see Subsections 1.2.1 and 1.2.3). The convective pattern shows a spatial horizontal scale of several times the boundary layer height, that is, several kilometers, whereas the depth of the big thermals directly scales with the boundary layer height (e.g., Mason, 1989; Kanak

et al., 2000). Both the pattern and the thermals must be resolved by a sufficiently large simulation domain to simulate the typical environment for dust devil formation realistically. A sufficiently large domain is only guaranteed if artificial flow effects caused by the domain boundaries and their conditions (usually periodic in LES of DDs) are minimized and do not affect the development of the cells or plumes. The resolution demand is not solely restricted to the convective thermals and cells but to the whole range of atmospheric phenomena, which might control the main features of the CBL such as secondary circulations. A similar statement was made by Spiga et al. (2016):

A proper representation of the fundamental boundary layer dynamics, i.e., the cellular pattern of convection, is as important as the highest possible resolution for the successful simulation of dust devil.

Therefore, the DNS approach fails here. The today's available computing power is not sufficient to fully resolve all the atmospheric scales from 10^{-3} m to 10^3 m. Nevertheless, DNS can be applied for simulations on a laboratory scale and, thus, for lower Reynolds numbers than in the atmosphere. In some DNS, convective vortices similar to DDs could already be observed in classical Rayleigh–Bénard convection or in unbounded free convection over a heated plate (e.g., Cortese and Balachandar, 1993; Fiedler and Kanak, 2001; Mellado, 2012). However, DNS has rarely been used so far for an investigation of DDs (see also Chapter 4) probably because no vortices similar to the real atmospheric scale can be simulated with this technique, at least within the medium air. Other gases or liquids with high fluid viscosities can be principally simulated with DNS on a larger scale than a few meters because a high fluid viscosity reduces the Reynolds number (see also Mellado et al., 2018). If DD-like vortices were detected in DNS simulations, they were only superficially investigated or these kind of vortices were only a side effect of the actual research topic. A comprehensive DNS investigation of the statistics of a large dust devil population and an analysis of the vortex dynamics with DNS are still missing.

When DDs are simulated with LES, the flow is affected by both the parameterization of the SFS mixing and the boundary conditions for the surface-atmosphere exchange. DDs originate in the surface layer, which is typically 10–100 m thick in the atmospheric CBL (e.g., Stull, 1988). Typical model resolutions in DD studies are of the order of 10 m (Kanak, 2006), that is, the surface layer is usually enclosed by a few grid points only. Thus, near-surface processes including DDs are often not well-resolved and the parameterization of the SFS as well as the numerical treatment of the ground surface might significantly affect the development of DDs. Common approaches to model the surface-atmosphere exchange of heat, momentum, and matter are bulk aerodynamic formula (e.g., Kanak, 2005) or boundary conditions based on Monin-Obukhov Similarity Theory (MOST) (e.g., Maronga et al., 2020b). However, no investigations on the effects of surface boundary conditions or SFS models on DDs exist so far, which is why this issue is addressed in Chapter 4.

Beside the uncertainties that arise from the SFS model and the boundary conditions, the flow solution is also affected by several simplifications that are frequently made in LES of terrestrial DDs. These simplifications are partly applied but also partly rejected in Chapters 3–6, depending on the specific research question. First, moisture and related phase changes are not considered (e.g., Gu et al., 2008; Ito et al., 2010b; Raasch and Franke, 2011) because they are insignificant for the arid and semi-arid regions where DD occur (see again Section 1.2.1). Second, no radiative processes are included in the numerical setups and a fixed sensible heat flux is imposed at the surface during runtime (e.g., Zhao et al., 2004; Kanak,

2005; Raasch and Franke, 2011; Klose and Shao, 2016). This is especially reasonable for LES simulations that have simulation times of several hours and want to capture a quasi-stationary state of the atmosphere during the afternoon of a typical sunny summer day. Also if the radiative forcing timescales are larger than the convective timescales, adequate simulation results can be expected even if radiative processes are not considered (Spiga et al., 2016). In addition, Kurgansky et al. (2016) mentioned that the radiative feedback caused by the radiation absorption of the lifted particles might be only important for very large martian DDs during the late afternoon. Third, several LES of DDs run without a prescribed background wind in the free convection regime (e.g., Kanak et al., 2000; Kanak, 2005; Gheynani and Taylor, 2010; Ohno and Takemi, 2010a). However, Subsection 1.2.2 has indicated a potentially large effect of a background wind on the DD formation, which would be completely neglected in such idealized setups. Finally, the explicit simulation of airborne particles is rarely part of the simulation because the focus is mostly on the dynamics and basic statistics of DDs. The publications of Zhao et al. (2004), Gu et al. (2006), Ito et al. (2010a), and Klose and Shao (2016) are the only exceptions for terrestrial investigations. Zhao et al. (2004) and Gu et al. (2006) considered the transport of sand particles of different size (40–160 μm and 100–300 μm , respectively) based on a Lagrangian coordinate system and artificially injected the particles into the simulation domain without a physics-based dust emission scheme. Ito et al. (2010a) used an Eulerian approach to model the dust concentrations for four different grain sizes (1, 3, 6, and 10 μm) and applied an experimental formula for the dust release. In fact, Klose and Shao (2016) were the first who incorporated a physics-based and size-resolved dust emission, transport and deposition scheme into their LES, focusing on DDs. If neither dust release nor dust transport mechanisms are included in the simulations, real DDs can not be simulated as soon as the visibility of the vortex is a mandatory criterion to be considered as a DD. This is why LES studies of DDs normally focus on vertically oriented, coherent, columnar whirlwinds and not on visible vortices. These whirlwinds are very common in simulations of the CBL. They are sometimes called dust devil-like vortices in the absence of visible tracers, which is legitimate because no universal theoretical or mathematical dust devil definition exists and the basic dynamics are the same (see also Kanak, 2006; Oncley et al., 2016; Spiga et al., 2016). If not otherwise stated, this thesis does not distinguish between a dust-laden vortex and an invisible one (see also Section 2.2). The terms (convective) vortex, whirlwind, dust devil, and dust devil-like vortex are used as synonyms. Also note that the focus of this thesis is not on numerical simulations of individual vertical vortices, which are triggered by an appropriate selection of initial and boundary conditions (e.g., Zhao et al., 2004; Gu et al., 2008). Instead, the attention is on CBL-scale simulations, where convective vortices spontaneously occur as in nature.

1.5 Objectives and Structure of the Thesis

In the following, the main research focus of this thesis is clarified based on the previously mentioned research areas related to terrestrial DDs. However, the focus of each single study and the motivation for it (Chapter 3, 4, 5, and 6) is comprehensively explained in the respective article. Here, the basic context of all four studies is highlighted.

Different LES studies noticed a significant quantitative discrepancy between features of numerically simulated DDs and observed ones, although from a purely qualitative perspective a high level of agreement was found, for example for the overall flow structure. Kurgansky et al. (2016) stated that there is a smaller vertical vorticity in numerical simulations

compared to observed DDs and that LES of the atmospheric CBL typically produces many low-intense DD-like vortices instead of a few very intense ones. Even in high-resolution LES of Kanak (2005), central pressure deficits were about one order of magnitude smaller (~ 10 Pa instead of ~ 100 Pa) and diameters larger (~ 10 – 100 m instead of ~ 1 – 10 m) than observations suggested. Similar, Spiga et al. (2016) came to the conclusion that differences from observations were especially noted in the vortex intensity in terms of the central pressure drop with weaker values in simulated vortices. Therefore, a main question of this thesis is:

1. What causes the quantitative discrepancy between simulated and observed DD-like vortices and how can realistic values be reproduced in LES?

In other words, this study tries to determine which control parameters are appropriate to reproduce realistic DDs and how different vortex features depend on these parameters. Section 1.4 highlighted the importance of the model resolution on the DD characteristics. Therefore, the effects of the grid spacing need to be studied. Investigations regarding a varying resolution were already made, for example by Raasch and Franke (2011), who found out that vortices are more numerous and intense for higher resolutions. However, it is unclear if refining the resolution is enough to obtain realistic dust-devil-like vortices (Spiga et al., 2016). The observational data from Subsection 1.2.1 showed that background winds and heterogeneities are crucial environmental conditions for the DD development, which is why their effects are also studied in the following. Only the background wind has been addressed in other LES studies before. For example, Ohno and Takemi (2010b) showed that vortices are preferentially generated under moderate wind conditions in terms of their number and intensity. Furthermore, shorter lifetimes were determined if the mean wind speed was increased. Results from Raasch and Franke (2011) indicated that the vortex strength and number heavily depend on the background wind and that for mean winds larger than 5 m s^{-1} vortex generation is significantly reduced. Spiga et al. (2016) noted that in DD studies heterogeneities has not been considered yet although they must be included to make progress on the understanding of the variability of DD activity with environmental conditions and to improve the validity of comparative studies between LES and observations. The focus in this thesis is on heterogeneities of the surface heating because field observations by Rennó et al. (2004) indicated a significant influence of large horizontal temperature gradients created by differently heated surfaces on the generation of DDs. The results of the individual and integral effects of the grid spacing, background wind, and surface heterogeneities on the LES of DDs are presented in Chapter 3.

LES has some conceptual disadvantages compared to DNS, which especially includes the parameterization of SFS processes and the surface-atmosphere exchange. To overcome these shortcomings, DNS of turbulent Rayleigh-Bénard convection between two differently heated flat plates are performed in the study presented in Chapter 4. Two main research question are addressed in this context:

2. Is DNS able to generate DD samples for a comprehensive statistical analysis and if so what are the main control parameters in these setups?
3. What are differences and similarities between convective vortices in DNS of Rayleigh-Bénard convection and LES of the atmospheric CBL?

Apart from a comparison with LES, DNS results can also be compared to experimental data of Rayleigh-Bénard convection. For example, the Barrel of Ilmenau is an appropriate facility to study DD-like vortices (Loesch and du Puits, 2021). However, quantitative results

have only recently been published by Kaestner et al. (2023), which is why they are not incorporated in the following studies but addressed in the concluding Chapter 7. In Rayleigh-Bénard convection, flow properties and structures strongly depend on the aspect ratio of the model domain and the Rayleigh number (Bailon-Cuba et al., 2010; Pandey et al., 2018). The aspect ratio is especially important with respect to the large-scale thermal plumes and cellular convective pattern. Both should be captured by the domain, even if a broadening of structure size with simulation time is observed (e.g., von Hardenberg et al., 2008), which is sometimes also true in LES (Kanak, 2006). The Rayleigh number significantly controls the turbulent scale separation in the flow and the overall strength of the convection. Preliminary DNS investigations indicate that minimum Rayleigh numbers of 10^6 – 10^7 are necessary for a development of sufficiently strong swirling upward motions (Cortese and Balachandar, 1993; Fiedler and Kanak, 2001). Another control parameter which is examined in the following DNS simulations is the velocity boundary condition. As shown in Subsection 1.2.1, surface friction affects the DDs significantly. In the following, it is distinguished between no-slip (zero velocities) and free-slip (zero velocity gradients) boundary conditions, which represent situations with and without friction, respectively. Cortese and Balachandar (1993), who focused on the vertical vorticity in the flow under free-slip conditions, noted that swirling plumes are also present in thermal convection with no-slip boundary conditions but at higher Rayleigh numbers than those required for the free-slip conditions. This hypothesis still needs clarification. A last question that is addressed in the following DNS study is related to the formation and maintenance of DDs:

4. Do DD-like vortices in DNS of Rayleigh-Bénard convection preferentially occur at the vertices and branches of the polygonal convective cells like it can be expected from LES and if so, what are possible mechanisms for their formation and maintenance?

As mentioned in Subsection 1.2.1, these mechanisms are not yet fully understood and the close connection between the convective cellular pattern and the occurrence of DDs still needs to be verified for DNS simulations. To answer the above question, the vorticity budget equation, which was introduced in Subsection 1.2.3, is considered. The DNS investigations are discussed in Chapter 4 of this thesis.

The Chapters 3 and 4 will reveal again the previously mentioned strong dependence of DDs features on the model resolution, which is basically true for both DNS and LES. However, while the resolution in LES can be chosen much more flexibly from a theoretical point of view (somewhere in the inertial subrange), DNS already requires a resolution in the range of the Kolmogorov length scale. Therefore, a quite fundamental question arises:

5. What is the dependence of different DD features on the grid spacing and what is the required resolution in LES to capture the whole range of atmospheric DDs realistically?

This research focus is different from the grid spacing investigations of Chapter 3, where it is mostly on the vortex intensity and where no grid convergence study is conducted. Instead, the combined effects of different control parameters (grid spacing, background wind, heterogeneities) are of main interest and no suggestions for resolution requirements are developed. In fact, only two different grid spacings (2 and 10 m) are studied in Chapter 3 compared to a gradually decrease from 10 to 0.625 m in the grid convergence study of Chapter 5. An answer to the above Question 5 would help to better interpret results from differently resolved runs. Until now, grid spacings from approximately 1 to 100 m has been used in LES studies

about DDs (Kanak, 2006; Spiga et al., 2016). Even at relatively high resolutions of 3 m, the maximum wind locations that can be used to describe the size of the vortex core (see Rankine vortex model in Subsection 1.2.3) are usually only 1–2 horizontal grid points away from the center (Ohno and Takemi, 2010a). Thus, most DD cores are still poorly resolved with 3 m grid spacing. Spiga et al. (2016) claimed that there is a strong need to run LES at finer horizontal grid spacing while keeping the horizontal domain size similar to coarse-resolution LES. Only in this case, statistics of the numerous small DD-like vortices can be fully resolved and fine scales of the vortex structure can be assessed. The grid convergence study of Chapter 5 will also help to solve conflicting statements regarding resolution effects. Some authors have clearly proven a strong resolution dependence on, for example, the intensity and size (e.g., Raasch and Franke, 2011), while others like Ito et al. (2013) stated that vortex intensity in terms of the vorticity is left unchanged, even if the horizontal resolution is refined from 50 to 5 m.

The knowledge of resolution requirements for LES of DDs is especially beneficial for studies that try to derive quantitative estimates as precise as possible. Such estimations are obtained for rather simple, basic vortex features (e.g., the size or frequency of occurrence) but also for more complex quantities like particle fluxes and concentrations, where existing values are highly variable (see again Subsection 1.2.2). Within the last two decades, most authors have justified the importance of DDs by their potentially significant dust release and transport, although dust was not explicitly considered in their simulations (e.g., Farrell et al., 2004; Raasch and Franke, 2011; Oncley et al., 2016). The frequent usage of this justification highlights the importance to clarify the role of DDs for the local, regional, and global dust cycle. So far, the global contribution by DDs to the total mineral dust emission is estimated between 3.4 % (Jemmett-Smith et al., 2015) and 35 % (Koch and Renno, 2005). Contributions of 38 % and 53 % are given for the regions of North Africa (Pan et al., 2021) and Western China (Han et al., 2016), respectively. However, the determination of these values mostly rely on the combination of measurements, weather forecasting models like WRF or the IFS developed at ECMWF, and DD theory. LES was not applied to derive these estimates. So far, the only estimate based on LES was derived by Klose and Shao (2016). They stated a regional contribution for Australia in the range of 0.03–0.19 % but used a rather coarse grid spacing of 10 m. Spiga et al. (2016) noted that the explicit treatment of the lifting and transport of dust in LES of terrestrial DDs is still a nascent area of research, which is why most LES are restricted to invisible convective vortices rather than real visible dust devils. In this thesis, particle fluxes and concentrations with respect to DDs are discussed in Chapter 6 in order to provide a valuable contribution to this nascent area of research and to the debate about the significance of the DDs sediment transport. Answers to the following question shall be given:

6. How much do DD-like vortices contribute to the particle release and transport in the atmospheric CBL and what are typical particle concentrations within these vortices?

The most up-to-date view on this issue is summarized in Klose et al. (2016). They state that the DD contribution to the continental or global dust budget on Earth seems to be small but on local and regional scales convective vortices can be a major dust event type with consequences for the visibility, cloud processes, topography, soil productivity, human as well as animal health, and atmospheric thermodynamic properties (see also Section 1.1).

The structure of this thesis results as follows: After a summary of the methods that are used to investigate DDs, three peer-reviewed research papers are presented in Chapters 3–5

that address the Questions 1–5 above. A fourth study about the amount of dust release and transport by DDs is presented in Chapter 6. This study is still under review. It concludes the result section. Finally, conclusions of the whole thesis are given that summarize and discuss the main achievements and that give a future perspective on different topics related to DDs.

Chapter 2

Methods

This chapter introduces the basics about the methods that are frequently applied in this thesis. One of these methods is the numerical flow simulation with the PALM model system (Raasch and Schröter, 2001; Maronga et al., 2015, 2020a), which has been developed at the Institute of Meteorology and Climatology in Hanover since the 1990s. The model is introduced in Section 2.1 with all components and features that are relevant for the subsequent chapters. For a comprehensive overview of PALM, the reader is referred to Maronga et al. (2020a). The identification algorithm (Section 2.2) and the statistical analysis of convective vortices (Section 2.3) are further important components of this thesis. The last section of this chapter explains how instantaneous and time-averaged three-dimensional data of individual DDs are obtained. During the past five years of this research project, all methods were subjected to modifications either due to general improvements and additions or due to specifics of the investigated research questions. While the applied model components of PALM remained almost unchanged, the methods regarding the DD identification and statistical analysis underwent significant changes based on the observations that were made in each single study. This chapter aims to highlight the basic ideas and similarities of the methods. Details can be found in the respective articles. Also the user extensions to the PALM model code and the postprocessing scripts are linked there via the research data repository system of the Leibniz University Hannover (<https://data.uni-hannover.de/>). Therefore, the developed user code is not attached to this thesis.

2.1 The PALM Model System

The PALM model system, originally called the Parallelized Large-Eddy Simulation Model (PALM), is used for the DNS and LES simulations in this thesis. It is a Fortran-based model code specifically used for LES of different types of atmospheric and oceanic boundary layer flows (e.g., Noh et al., 2004; Kanda et al., 2013; Dörenkämper et al., 2015). PALM has been frequently applied to study characteristics of CBLs, for example, with respect to surface heterogeneities (Maronga and Raasch, 2013) or clouds (Gronemeier et al., 2017). First studies on DDs with PALM were performed by Raasch and Franke (2011). The subsequent investigations frequently refer to the main results of this study. The model code of PALM is optimized for the usage on massively parallel computer architectures. Parallelization is realized with the Message Passing Interface (MPI) (e.g., Gropp et al., 1999) through a two-dimensional domain decomposition along the horizontal directions with usually but not necessarily equally sized subdomains (a difference of one grid point is maximum allowed).

In its default state, PALM solves the non-hydrostatic, incompressible and Boussinesq-approximated form of the Navier-Stokes equations, where the density is treated as a constant. In LES mode, the equations are filtered by a spatial scale separation approach after

Schumann (1975), where the resolved quantities are defined as a spatial average over discrete Cartesian grid volumes. Thus, the separation of the resolved and unresolved scales is done implicitly via the numerical grid (see also Section 1.3). In total, six prognostic variables are solved on a staggered Arakawa C-grid (Harlow and Welch, 1965; Arakawa and Lamb, 1977): the Cartesian velocity components u , v , and w that are defined centrally at the faces of a grid box, the potential temperature θ , the SGS-TKE e (only in LES mode), and an arbitrary passive scalar s that are all defined at the grid box center. The final set of equations, which describes the conservation of momentum, mass, thermal internal energy, and any scalar quantity for a dry atmosphere can be written in continuous form with the help of the Einstein summation convention as

$$\frac{\partial \bar{u}_i}{\partial t} = -\frac{\partial \bar{u}_i \bar{u}_j}{\partial x_j} - \varepsilon_{ijk} f_j \bar{u}_k + \varepsilon_{i3j} f_3 u_{g,j} - \frac{1}{\rho} \frac{\partial \bar{\pi}^*}{\partial x_i} + g \frac{\bar{\theta} - \langle \theta \rangle}{\langle \theta \rangle} \delta_{i3} - \frac{\partial}{\partial x_j} \tau_{ij}^r, \quad (2.1)$$

$$\frac{\partial \bar{u}_j}{\partial x_j} = 0, \quad (2.2)$$

$$\frac{\partial \bar{\theta}}{\partial t} = -\frac{\partial \bar{u}_j \bar{\theta}}{\partial x_j} - \frac{\partial \overline{u_j'' \theta''}}{\partial x_j}, \quad (2.3)$$

$$\frac{\partial \bar{s}}{\partial t} = -\frac{\partial \bar{u}_j \bar{s}}{\partial x_j} - \frac{\partial \overline{u_j'' s''}}{\partial x_j} + \chi_s. \quad (2.4)$$

Here, $i, j, k \in \{1, 2, 3\}$, $f_j = (0, f^*, f)$, δ is the Kronecker delta, ε is the Levi-Civita symbol, $u_{g,j} = (u_g, v_g, 0)$ are the geostrophic wind speed components, $g = 9.81 \text{ m s}^{-2}$ is the gravitational acceleration, χ_s represents source/sink terms of s , and $\pi^* = p^* + 2/3 \rho e$ describes the modified perturbation pressure (also called dynamic pressure) with p^* being the perturbation pressure and $e = 0.5 \overline{u_k'' u_k''}$ the SGS-TKE. The deviatoric or reduced stress τ_{ij}^r is defined as

$$\tau_{ij}^r = \overline{u_i'' u_j''} - \frac{1}{3} \overline{u_k'' u_k''} \delta_{ij} = \overline{u_i'' u_j''} - \frac{2}{3} e \delta_{ij}. \quad (2.5)$$

An overbar is used here instead of a tilde as in Section 1.3 to indicate spatially filtered quantities because the spatial scale separation approach after Schumann (1975) acts like a Reynolds operator. Angular brackets mark a horizontal average. The terms in Eq. (2.1) represent from left to right the local change in time of the filtered velocity, the advection term in flux form, the Coriolis force, the large-scale pressure gradient term expressed by the geostrophic wind, the dynamic pressure gradient term, the buoyancy term, and gradients of the SGS turbulent transport. The isotropic term $2/3e$ of the dynamic pressure, which represents the hydrostatic or volumetric part of the total SGS stress tensor, is often omitted in incompressible model codes like PALM. This is because the pressure term in Eq. (2.1) is solely used to guarantee a velocity field free of divergence (see below). Spatial gradients of the hydrostatic part, however, would create such divergences, which would then have to be removed by the pressure term again. Therefore, these spatial gradients are not considered at all.

The above equations do not represent a closed system due to the SGS terms, which arises from the filtering and need to be parameterized (see also Section 1.3). In this thesis, the 1.5-order turbulence closure after Deardorff (1980) is used for the parameterization in a modified version based on Moeng and Wyngaard (1988) and Saiki et al. (2000). The closure

assumes that the transport by SGS eddies is proportional to the local gradients of the mean quantities. It reads

$$\tau_{ij}^r = -K_m \left(\frac{\partial \bar{u}_i}{\partial x_j} + \frac{\partial \bar{u}_j}{\partial x_i} \right), \quad (2.6)$$

$$\overline{u_j'' \theta''} = -K_h \frac{\partial \bar{\theta}}{\partial x_j}, \quad (2.7)$$

$$\overline{u_j'' s''} = -K_h \frac{\partial \bar{s}}{\partial x_j}, \quad (2.8)$$

with K_m and K_h being the local SGS eddy diffusivities of momentum and heat, respectively. The value for K_h is also used for any other scalar quantity apart from θ . The eddy diffusivities are proportional to the square root of e and to the SGS mixing length, which takes into account the thermal stratification. The SGS-TKE is calculated by an own prognostic equation. For more details regarding the turbulence closure, the reader is referred to Maronga et al. (2015).

With the above set of equations, PALM can also be used in DNS mode. Only the filtering is omitted and eddy diffusivities must be interpreted as spatially and temporally constant molecular values ν_m and ν_h . The variable ν_h describes the thermal diffusivity of the regarded fluid. When the diffusivities are set constant in PALM, no SGS-TKE is computed ($e = 0$) and the following nonhydrostatic and nonfiltered incompressible system of equations in Boussinesq-approximated form is solved:

$$\frac{\partial u_i}{\partial t} = -\frac{\partial u_i u_j}{\partial x_j} - \frac{1}{\rho} \frac{\partial p^*}{\partial x_i} + g \frac{\theta - \langle \theta \rangle}{\langle \theta \rangle} \delta_{i3} + \nu_m \frac{\partial^2 u_i}{\partial x_j^2}, \quad (2.9)$$

$$\frac{\partial u_j}{\partial x_j} = 0, \quad (2.10)$$

$$\frac{\partial \theta}{\partial t} = -\frac{\partial u_j \theta}{\partial x_j} + \nu_h \frac{\partial^2 \theta}{\partial x_j^2}, \quad (2.11)$$

$$\frac{\partial s}{\partial t} = -\frac{\partial u_j s}{\partial x_j} + \nu_h \frac{\partial^2 s}{\partial x_j^2} + \chi_s. \quad (2.12)$$

Here, no Coriolis and large-scale pressure gradient force are considered because they do not affect the flow in DNS of classical Rayleigh-Bénard convection, which is simulated in Chapter 4. In LES, however, these two forces might become important mainly due to the much larger temporal and spatial scales of the LES setups (see Chapter 3, 5, and 6).

The spatial discretization of the model domain is realized by finite differences with an equidistant grid spacing Δx and Δy in the horizontal directions. In the vertical direction, the grid can be stretched to a coarser or finer resolution. Typically, Δz is increased in the free atmosphere well above the boundary layer height to save computational costs. This procedure can not be applied to the atmospheric boundary layer because of much higher gradients, turbulence, and smaller temporal as well as spatial scales of the flow-controlling phenomena occurring in this region. The arrangement of the variables on a staggered Arakawa C-grid (see above) doubles the effective spatial resolution in comparison to non-staggered grids (Maronga et al., 2015). The default advection scheme in PALM is based on the flux formulation of the advection terms. They are discretized by an upwind fifth-order scheme of

Wicker and Skamarock (2002), which contains an artificially added numerical dissipation term to stabilize the numerical solution. Therefore, the scheme is known to be highly dissipative but gives in combination with the third-order Runge-Kutta time-stepping scheme (Williamson, 1980), which is used in PALM for the temporal discretization, the best results with respect to accuracy and algorithmic simplicity. If numerical dissipation shall be avoided, PALM offers the possibility to switch to a second-order scheme of Piacsek and Williams (1970) that, however, suffers from strong numerical dispersion. The Runge-Kutta time-stepping scheme divides the time integration into three intermediate steps. The final solution for the next time step is calculated from the weighted average of these substeps.

The Boussinesq-approximation requires incompressibility of the flow. However, the numerical integration of the governing equations automatically produces divergences, which must be removed. To achieve this, PALM uses a predictor–corrector method where a Poisson equation is solved for $\overline{p^*}$ at each Runge-Kutta substep (see also Patrinos and Kistler, 1977). The solution of the discrete Poisson equation is realized by a direct solver using a Fast Fourier Transform (FFT) algorithm, which computes the discrete Fourier transform of the Poisson equation in both horizontal directions. In this thesis, the external FFTW3 library (Frigo and Johnson, 2005) is used for the transformation. Its two-dimensional (along x and y) application creates systems of linear equations for each vertical grid column. Because these linear systems can be written as a matrix vector multiplication where the matrix has a tridiagonal shape, they are solved by using the tridiagonal matrix algorithm or Thomas algorithm (e.g., Sultanian, 2018). Afterwards, the horizontal dimensions of the resulting three-dimensional perturbation pressure field are transformed back from Fourier to Euclidean space by using the FFT algorithm again (see also Schumann and Sweet, 1988).

PALM is able to handle a variety of boundary conditions. In the following, Dirichlet and Neumann boundary conditions are used at the model top and bottom. The first condition sets the actual value of a specific quantity (e.g., the temperature at the surface), whereas a Neumann condition defines a value for the derivative in wall-normal direction (e.g., zero-gradient condition at the surface). In case of the horizontal velocities, a Dirichlet (Neumann) condition corresponds to a no-slip (free-slip) condition in PALM. Based on MOST, a constant flux layer is usually assumed between the surface and the first grid level above where scalars and horizontal velocities are defined. With this theory, local vertical momentum and heat fluxes are calculated at the bottom boundary if they are not prescribed by the user. Note, a constant flux layer does not allow for free-slip conditions at the surface. At all lateral domain boundaries (x - and y -direction), PALM’s option for cyclic boundary conditions is applied. Consequently, the horizontal domain can be interpreted as an infinitely wide plane. More information on the boundary conditions is given in the respective Chapters 3–6.

The initialization of the subsequent simulations is realized with horizontally constant but height-dependent velocity and potential temperature profiles. Details can be found in the studies of Chapters 3–6. To accelerate the onset of convection, PALM offers a mechanism that imposes random perturbations on the horizontal velocity components. This is done at each grid point from close to the surface until one third of the domain height. The perturbations represent uniformly distributed pseudo-random numbers with a user-defined maximum amplitude (0.25 m s^{-1} hereinafter). They are only imposed at the beginning of the simulation until a certain domain-averaged perturbation energy (or resolved-scale TKE) is exceeded. The threshold is set to $0.01 \text{ m}^2 \text{ s}^{-2}$ in the following. Note that due to these artificial flow disturbances and the physically unbalanced initialization, a model spin-up time must be considered in each simulation.

Another feature of PALM that is applied in this thesis is the self-nesting (Hellsten et al., 2021), which is used in vertical direction only. It enables simulations with very high spatial resolution up to several hundred meters above the surface while simultaneously simulating a sufficiently large horizontal domain, which would otherwise exceed the available computational resources. In this way, near-surface processes like DDs can be resolved much better and the large-scale cellular pattern of the CBL is still captured (see also Section 1.4). The basic idea of the vertical nesting is illustrated in Fig. 2.1. Two or more LES model domains with different vertical extents and grid resolutions run in parallel with a continuous communication between them (e.g., to exchange boundary conditions). The outermost domain with the coarsest resolution is called the root domain while the remaining model domains with a lower vertical extent and finer resolutions are called child domains. Because domains can recursively be nested into each other (see Fig. 2.1 right), child domains can also act as a so-called parent domain, which refers to the surrounding domain of each child. Thus, the root model is also a parent model that contains at least one child domain. The top boundary conditions for the child model are provided by interpolating the values from the coarse to the fine grid for all prognostic quantities (except e , where simple zero-gradient conditions are used). In the following, self-nesting is employed in a two-way mode, where parent models are also influenced by their child models. Everywhere where a parent domain overlaps with a child domain (except close to the nest boundaries), the original parent solution is replaced by the fine-resolution child solution based on the antinterpolation approach of Clark and Farley (1984), where a simple averaging over one parent domain grid volume around the parent grid node in question is executed. The inter-model communication to exchange information between the different domains is realized by using MPI, similar to the intra-model communication system, which enables PALM to efficiently run on massively parallel computer architectures (see first paragraph of this section).

Data handling in PALM is a crucial issue due to the huge amount of data that is easily created during computationally expensive (in terms of short time steps and the number of grid points) LES. Therefore, data operations like the calculation of an average are executed online whenever possible, that is, during the simulation. This significantly reduces, for example, the time-dependent output. In principle, PALM is able to provide time series, vertical profiles, two-dimensional cross sections, three-dimensional data, and masked output for a variety of quantities that might be either time-averaged or spatially averaged or both. The files are stored in netCDF format, which is an open, self-describing, and machine-independent format for array-oriented scientific data. The written file content follows the [UC]² data standard (Scherer et al., 2020). The data handling becomes even more important if user-defined output quantities are defined via the user interface, which offers the ability to extend the default code by own calculations. The user interface is used for the technical implementation of the DD identification and the determination of basic vortex properties like the instantaneous radius (see Section 2.2.1).

2.2 Dust Devil Identification

The identification of DD-like vortices can be split into two parts as visualized in Fig. 2.2: the detection of vortex centers (see Subsection 2.2.1) and the formation of so-called vortex tracks (see Subsection 2.2.2). A track is interpreted as a DD-like vortex if it fulfills certain requirements, for example regarding the track's lifetime. In general, numerical studies of DD-like vortices must use certain criteria to distinguish these vortices from the remaining

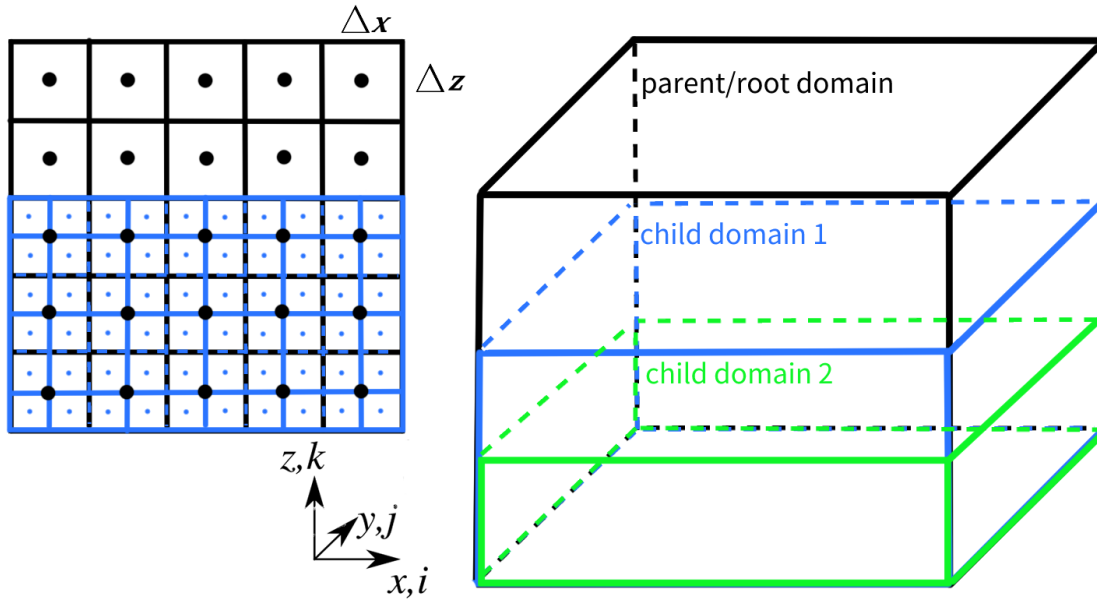


Figure 2.1: Schematic view on the vertical nesting. On the left, a two-dimensional (x - z -plane) sketch of the parent (black) and child (blue) grid structure is shown. Dots mark grid box centers, where scalar quantities are defined. On the right, a three-dimensional view of a configuration with two nested domains is shown. The first child domain acts as a parent for the second child domain and simultaneously as a child for the root domain.

flow structures and, thus, to be able to detect them. If dust is present in the simulation, a quantitative connection between optical properties like the atmospheric visibility, optical depth, or opacity and the suspended sediment load could be established for a detection, which is, however, difficult to implement (e.g., Metzger et al., 1999; Baddock et al., 2014; Luan et al., 2017). Because of that and because dust is rarely explicitly considered in numerical simulations (see also Section 1.3), DDs are usually not detected by their optical features. Kanak (2005) searched for high absolute vertical vorticity values (if not otherwise stated, only vorticity from now on) in combination with a well-developed rotating horizontal flow to identify single DD-like vortices. In a similar manner, Toigo et al. (2003) and Gheyhani and Taylor (2010) focused on time series of local vorticity extrema and their horizontal locations to find the most intense vertical vortices. However, these rather qualitative detection methods without concrete detection thresholds are not suitable to identify a meaningful sample of DD-like vortices but only selected examples. By analyzing times series of vorticity extrema at each height, Ito et al. (2010b) defined a threshold of 0.1 s^{-1} that must be exceeded by the vortices to be considered as a DD-like vortex. In addition, a vortex center was only identified if a pressure drop of more than 10 Pa near the surface was exceeded. The procedure to define a numerically simulated DD by a local pressure minimum and vorticity extremum that are larger than certain thresholds is probably the most common and robust approach to detect convective whirlwinds, why it is also used in this thesis (see Subsection 2.2.1). Ohno and Takemi (2010a), Raasch and Franke (2011), Klose and Shao (2016), and Nishizawa et al. (2016) are just a few examples that follow this procedure to derive meaningful DD statistics. However, the instantaneous detection of a (potential) DD center at a certain time by its pressure and vertical vorticity values is not necessarily connected to a

natural DD-like vortex. Further criteria must be established, for example with respect to the persistence of this center or its surrounding features. For this purpose, the detected centers are combined to vortex tracks, which is explained in Subsection 2.2.2. These vortex tracks are then filtered based on the available information about natural DDs.

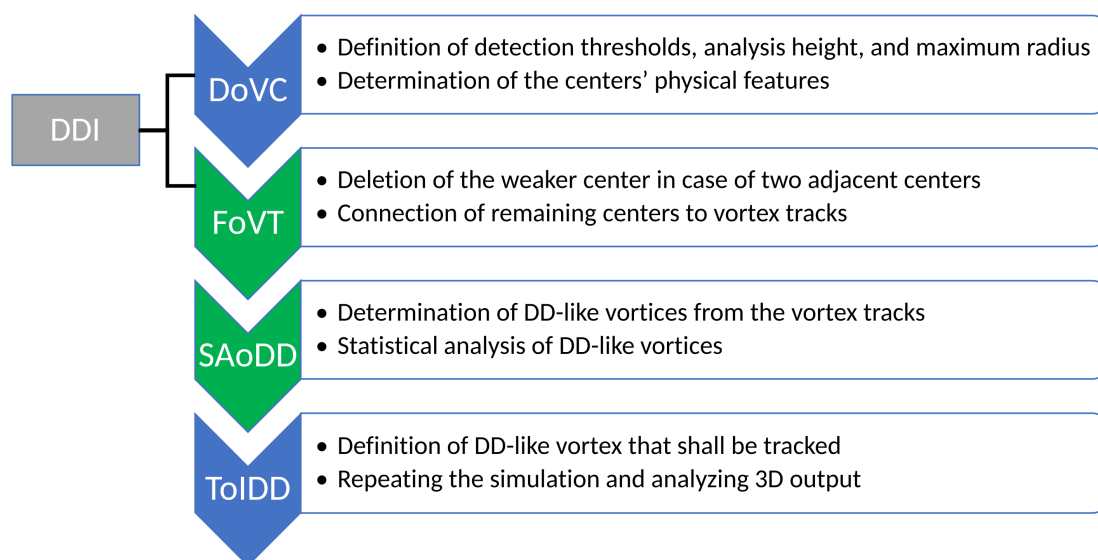


Figure 2.2: Flow chart of the different methods that are used to study dust devils. Processes that are performed during the simulation are highlighted in blue, like the detection of vortex centers (DoVC) and the tracking of individual dust devils (ToIDD), while processes that are carried out after a simulation are displayed in green, like the formation of vortex tracks (FoVT) and the statistical analysis of dust devils (SAoDD). DoVC and FoVT are summarized under the term dust devil identification (DDI). On the right side, the key points of each methodology are listed.

2.2.1 Detection of Vortex Centers

In this thesis, the term DD defines a thermally driven vortex, which rotates around the vertical axis and exceeds certain pressure drop and absolute vertical vorticity thresholds – two main characteristics of DDs (see Section 1.2.2). The (modified) perturbation pressure introduced in Section 2.1 is interpreted as the pressure drop (see also Kanak, 2005). To identify vortices during the simulation, the first step is to check at every time step whether there is a local pressure drop and vorticity extremum somewhere at the grid points of a predefined grid level near the surface. This grid level is referred to as the analysis height. If extrema are detected, they must exceed certain thresholds to be considered as DD-like vortex centers. These thresholds are not fixed values and differ between the publications or even change within the same study, depending on the specific research question and model resolution (e.g., Raasch and Franke, 2011; Klose and Shao, 2016). Usually, their exact values are determined based on deviations from some simulated mean values rather than from real DD characteristics because quantitative simulation results do not necessarily agree with reality

(see again Section 1.5). For example, if a poorly-resolved simulation underestimates the vortex strength significantly and thresholds are based on natural values, it might happen that no vortices are detected at all although DD-like vortices occur in the simulation. In the following, the standard deviation is taken as a statistical measure to quantify the deviations from the mean (background) values. It is derived from different snapshots of horizontal cross sections of p^* or ζ at analysis height and must be determined in a simulation before the actual detection run is performed. Thus, a numerical setup is executed at least twice, once for determining the thresholds and once for detecting the vortices. The following aspects should be additionally considered in the selection of the absolute values of the thresholds:

1. They should be large enough to filter out the random, non-coherent turbulence as much as possible.
2. They should be small enough to get enough data for analysis, that is, most of the vortex lifetime (from the genesis until the decay) should be captured.
3. The technical detection process should be independent of changes of the numerical setup. Otherwise, setup changes can easily create different DD statistics although the physics did not change.

The last point especially refers to the resolution. For example, if the general level of the vorticity and/or pressure drop increases due to a better resolution, the detection thresholds should also be increased accordingly to ensure a better comparability between the differently resolved runs. Otherwise, the same vortex before the resolution change is detected with a smaller lifetime than afterwards although the physics might not have changed at all. This is schematically visualized in Fig. 2.3 for the pressure drop. Only the (to a certain extent quite arbitrary) selection of constant thresholds would cause a DD sample with longer-lasting vortices for better resolutions, which should be avoided. Note, the location of a distinct pressure drop and absolute vorticity maximum do not necessarily coincide. This is especially true for high-resolution LES, as shown in Chapter 5. Therefore, an appropriate area must be defined for detection where both quantities show local extrema and exceed the selected thresholds. Additionally, it must be decided whether the pressure drop or the absolute vorticity maximum is considered as the actual position of the vortex center. Details can be found in Chapters 3–6.

As soon as a center is detected, basic features of the surrounding flow and the center itself are determined and stored during each simulation of the following studies. This includes the values of the pressure drop and absolute vorticity maximum at or around the center, the detection time and location, the central values of potential temperature and vertical velocity, the tangentially averaged maximum values of the radial, tangential, vertical, and horizontal velocities, and the distance from the center where the tangentially averaged pressure drop is just 50% of the core pressure drop. This distance is interpreted as the (instantaneous) radius of the vortex core (see also Subsection 1.2.3). The radial and tangential component are derived from a transformation of the horizontal Cartesian components u and v to a polar coordinate system. Further study-specific outputs are presented in the individual Chapters 3–6.

Beside the detection thresholds and the analysis height, the maximum allowed radius must be set previous to the simulation. The determination of grid point surrounding information often requires data transfer from one processor core to another due to the horizontal domain decomposition for parallelization (see Fig. 2.4). Because of memory requirements

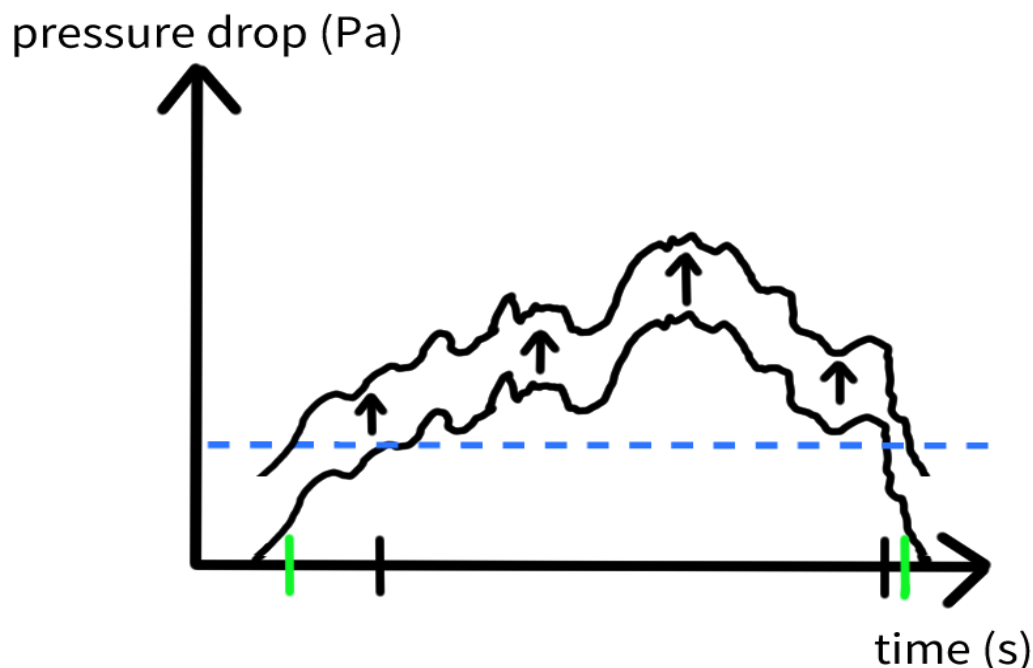


Figure 2.3: Sketch of a vortex's pressure drop signal with simulated time. The black line, vertically shifted in positive y -direction, describes the pressure drop of the same vortex, but resolved with a better resolution. The dashed blue line marks the detection threshold, which is assumed to be constant in both differently resolved simulations. Tick marks indicate the start and end time of the vortex's lifetime for the coarse (black) and fine (green) resolution.

and data transfer times, the data exchange must be limited. Therefore, the flow information that encloses a vortex center can only be studied up to a certain distance from the center, which limits the possible maximum radius of a DD-like vortex. The first technical realization of the detection algorithm did not allow for a data exchange radius of more than one subdomain size. In the course of time, this limit was extended to three subdomain sizes to allow for the usage of many processors and, consequently, small subdomains of only several tens of grid points while being able to capture also the larger-scale DDs. In the example shown in Fig. 2.4, the detected vortex and its flow characteristics are properly captured because the actual radius is less than the maximum possible value. For further information, the reader is referred to the Chapter 4, where this issue is addressed again. In Fig. 2.2, the key points of this section are summarized.

2.2.2 Formation of Vortex Tracks

After the simulation, the information about the detected centers is available in unsorted form. In a Fortran-based postprocessing script, the data is sorted with respect to the simulated time and filtered based on the spatial distance of simultaneously detected centers. If they are too close to each other, the weaker center is deleted (see Fig. 2.2, first bullet point of FoVT). This procedure avoids to count the same vortex twice or even more if it deviates strongly from a circular pattern or if it consists of multiple subvortices (e.g., Bluestein et al., 2004). In addition, the deletion takes care of the merging of vortex centers (e.g., Ohno and Takemi,

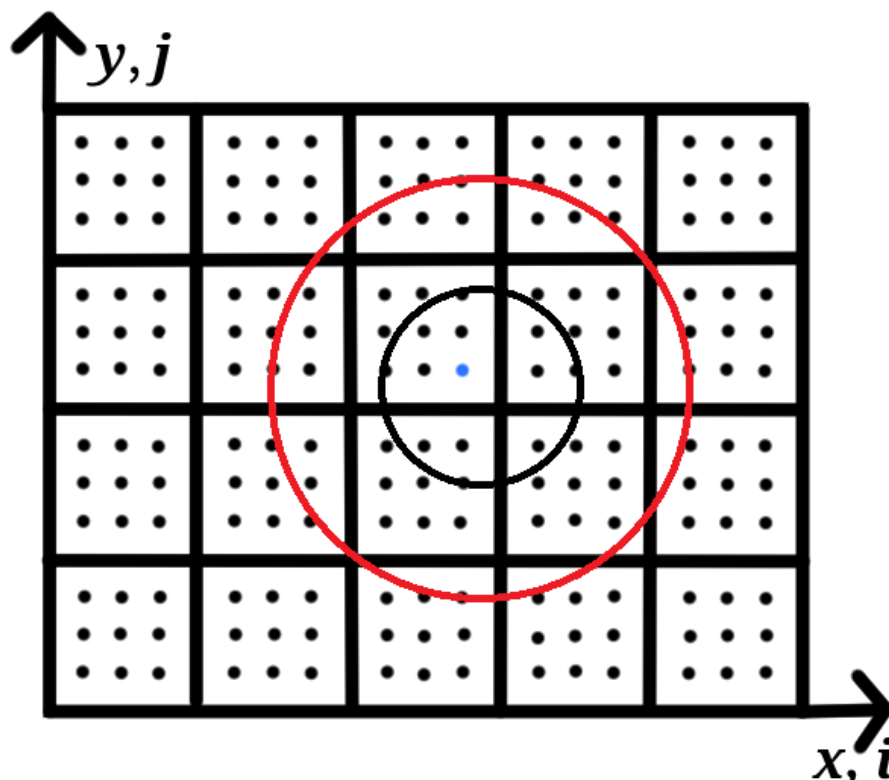


Figure 2.4: Example of a processor core topology due to the horizontal domain decomposition for parallelization. Each subdomain (5×4 in total) is assigned to one MPI process, which corresponds to one processor core. The red circle illustrates the maximum allowed area (radius of 4 grid points in this example) that is considered around the detected center (blue dot) during the calculation of various flow features (e.g., the maximum wind velocities). The black circle marks the actual extent of the vortex core (radius of 2 grid points) determined by the pressure criterion explained in the text.

2010a). The exact spatial distance, for which the filtering is applied, varies with the studies presented in this thesis (see Chapters 3–6).

Afterwards, a vortex center identified at a specific model time step is, whenever possible, connected to a vortex center at one of the following time steps to form DD tracks (see Fig. 2.2, second bullet point of FoVT). Several issues need to be considered in this process:

1. The next center to which the previous center is connected must occur within a reasonable amount of time. If this time is too large, centers might be combined that actually represent different vortices. If it is chosen too small, pressure drops and/or vorticities of a vortex that are just momentarily smaller than the detection thresholds would cause new DD tracks by mistake.
2. The maximum distance that a vortex is allowed to cover in a certain amount of time must also be limited. In other words, the maximum allowed horizontal translation velocity must be adequately chosen. Too large values are physically unrealistic and increase the probability to combine different vortices into just one. Too small values would prohibit the DD-like vortex to move forward realistically and two centers of

the same track might not be connected.

3. A natural DD does not change its rotation direction during lifetime. Therefore, it is reasonable to claim that the (area-averaged) vorticities of one single track must have the same sign. As it will be shown in Chapter 5, area-averaged vorticities represent the overall rotation much better than the local vorticity extremum that is used for detection, especially in high-resolution runs.
4. Another possible criterion for the connection of two vortex centers at different times is to restrict the pressure drop and vorticity change to a few percent between two consecutive detections. From a physical point of view, it is reasonable to assume that a vortex track does not show turbulent fluctuations of several ten percent or more just between two consecutive time steps with a typical temporal distance of 0.01–10 s in the following simulations.

With the help of the above information, different connection procedures are developed in the Chapters 3–6, depending on the specific research question and based on the knowledge of previous studies.

The combination of centers at different time steps to the same track is technically realized by assigning a so-called identification number to each detection. All detections that can be combined via the above Criteria 1–4 get the same number. After all detections are processed, the data is sorted with regard to the identification number. In this way, the final data file contains the tracks in sequential order starting with track number one. However, the sorting in terms of the identification number does not guarantee that within the same track, detections are also ordered regarding the simulated time, which is why each track must also be temporally sorted. Finally, an ASCII file is written with vortex tracks that are sorted according to the identification number and the simulated time. This significantly facilitates the subsequent statistical analysis of the DD-like vortices.

The sorting algorithm mentioned in the previous paragraph must be able to handle a lot of data (several hundred million lines with 10–20 entries per line) in a reasonable amount of time, especially because it is called several times. It is realized by a Fortran 95 implementation of the so-called quicksort algorithm, which is often the best practical choice for sorting because of its efficiency (Cormen et al., 2009). The algorithm sorts real numbers into ascending numerical order based on the divide-and-conquer paradigm.

2.3 Statistical Analysis of Dust Devils

In another postprocessing step, vortex features of the different tracks are calculated to determine the portion of the tracks that are DD-like. In addition, the statistical analysis of the DD-like vortices is performed (see Fig. 2.2 at SAoDD). All this is realized with a Python-based script. Python is used here instead of Fortran because it offers many and easy to handle predefined functions for calculating and plotting statistical data. In a first step, the script determines the track's lifetimes, translation speeds as well as the track's maximum and mean (lifetime-averaged) values of the instantaneous radii, pressure drops, potential temperatures, vorticities, and tangential, radial, vertical, and horizontal velocities introduced in Subsection 2.2.1. With this information, tracks with a lifetime below a critical value are deleted. In addition, the remaining vortices are only analyzed if they are persistent enough to enable an air parcel to circulate the vortex at least once, that is, the lifetime must be larger

than one turnaround time. The minimum allowed lifetime value for DD-like vortices varies in the following. Principally, it depends on the simulation technique (LES or DNS), the specific research question, comparability requirements between different simulations, and the knowledge about natural DD lifetimes. The time required for one circulation around a vortex is calculated as the quotient of the vortex circumference (computed with the lifetime-averaged radius) and the mean tangential velocity. Further requirements on the tracks to be considered as a DD-like vortex are conceivable. For example, in Chapter 5, the tracks additionally need a radius of at least 5 m to be considered in the statistical analysis in order to increase the compatibility between differently resolved runs.

In a last step, the remaining vortices are statistically analyzed. The calculated statistics from a single simulation are representative for a subset of an unknown DD population, which is usually described as a sample. The DD statistics include sample-averaged values, sample maxima, and minima for each vortex feature mentioned above. Also, the number of clockwise and counterclockwise DD-like vortices and correlations between different quantities are determined. To measure the variation of a specific vortex property within the sample, standard deviations and variances are computed. However, the correct interpretation of the statistical results is essential, which shall be illustrated by the following example: A dust devil population typically shows a strongly right-skewed (positive skewness) distribution of, for example, the pressure drop or the diameter, that is, very intense or very large vortices do rarely occur. Additionally, the capability of dust-lifting strongly depends on these vortex properties. Only the most intense, largest and most durable vortices lift a significant amount of dust. Thus, the averaged released dust amount derived from an entire DD population is mainly determined by extreme DD events and a DD with typical or mean characteristics contribute only to a small portion to it. Consequently, a typical (mean) DD does not lift a mean amount of dust but significantly less (see also Lorenz and Jackson, 2016).

Finally, a big challenge for each numerical simulation is to answer the question if the statistical results are realistic or not. This is partly related to the quality and resolution of comparative data from the field. Different measurement and observation techniques, various types of measuring sensors installed at different heights, differences in the definition of a DD, and spatial and/or temporal resolution discrepancies complicate a comparison, also between the measurements themselves (see also Lorenz and Jackson, 2016; Murphy et al., 2016). This is further enhanced by variable environmental conditions during the field campaigns and the huge difference in the number of DDs from which typical characteristics are derived. The statistical analysis of real DDs can be based on a few tens of DD-like vortices (e.g. Hess and Spillane, 1990) or several thousands (Snow and McClelland, 1990). In addition, DDs in the field are rarely tracked from their appearance until their decay due to the erratic occurrence in combination with the limitations of the mobile or fixed measurement system (e.g., Sinclair, 1964, 1973; Oncley et al., 2016; Inagaki and Kanda, 2022). Thus, measurements usually contain only a short part of the vortex life cycle. Lifetime-averaged or maximum values from these time series or from spatial data are not necessarily comparable to the maximum or mean values from numerically simulated vortices, where almost the entire life cycle is captured. Also Spiga et al. (2016) noticed that better and more complete observations are needed to validate the numerical results. Apart from that, the numerical DD statistics depend on the technical realization of the vortex identification in an unknown way (see also Section 2.2), which is why this dependence must be limited as much as possible. It must also be ensured that similar statistical quantities are compared. For example, a typical or mean DD feature can be derived in different ways. Averages over the entire detection

time of single vortices are just as conceivable as averages over a few snapshots of a large DD sample. The first approach ideally considers the whole life cycle but single vortices are not representative for a whole DD population. Instead, the second approach might consider all kinds of DDs but different phases of the life cycle are easily mixed up and snapshots might not represent a single vortex correctly. Double averages (over the entire detection time and sample size) are probably the most intuitive way to avoid these problems, which is why this approach is mostly applied in this study. Note, different stages of vortex development are not investigated in the following. The focus is on the mature state and representative values for the whole vortex lifetime.

2.4 Tracking of Individual Dust Devils

Several DD features like subvortices or tilted rotation axes (see Subsections 1.2.2 and 1.2.3) can not or only hardly be detected with the information at single grid points of a specific height. Instead, a time-dependent, three-dimensional study of the flow quantities around the DD center is needed. The technical procedure for conducting such studies is explained below (see also Fig. 2.2 at ToIDD). It is used in Chapters 4 and 5 for the derivation of instantaneous and time-averaged cross-sections through single DD-like vortices.

The technical realization of "chasing" vortices during the simulation is also realized via PALM's user interface (see Section 2.1). The basic idea is to consider a three-dimensional grid of a manageable size that originates in the vortex center at the lowest grid point of the simulation domain and moves with the vortex during its lifetime. The spatial resolution of this moving grid is the same as for the total domain so that both grids always overlap. Consequently, there is no need to define new grid points and the original PALM grid structure can be used to sample various variables on the vortex grid: the perturbation pressure, potential temperature, the three Cartesian velocity components, the vorticity, and vorticity budget terms like the divergence or twisting term. Similar to Raasch and Franke (2011), the vorticity budget terms are spatially averaged over a square around the vortex center and stored as time series. But also lifetime-averaged budget terms without any spatial average are calculated during the simulation. Other sampling data are stored as time-averaged values over the whole vortex life cycle and during each model time step where the vortex exists. The storage size of the time-dependent data can easily reach several terabytes, depending on the vortex lifetime and number of grid points of the moving grid. For the long-lasting DD-like vortices (~ 10 min), grids with approximately $100 \times 100 \times 100$ points are already challenging, especially if more than one vortex shall be considered. Furthermore, additional memory is necessary on each processor core to realize the data sampling during the run (see also Raasch and Franke, 2011). This memory demand scales with the number of grid points of the moving grid and the number of output quantities for which such a grid needs to be defined. The subsequent high-resolution simulations run with a moving grid of the order of 10^6 grid points and 10 additional 64-bit variables, resulting in approximately 100MB additional memory that is needed on each core. Nowadays, computer clusters typically have a maximum usable memory size of several gigabytes per processor core (e.g., the HLRN-IV-System of the North German Supercomputing Alliance), which is why an additional memory demand of less than 1 GB due to the sampling is reasonable. For the sake of simplicity, the current implementation of the tracking can handle just one DD simultaneously, which must be defined before the simulation starts (see last paragraph). Thus, vortices that overlap in time cannot be tracked in parallel.

A prerequisite for the online tracking of individual DD is the knowledge about their occurrence before the simulation starts. This information is extracted from the previous model run where the user code for the actual detection of vortex centers is active (see Subsection 2.2.1). If the tracking would start immediately with a certain detection, that is, within the same run, it would not be clear if this detection belongs to a DD-like vortex track (see Subsection 2.2.2) and how this detection relate to subsequently detected centers. Therefore, a three-dimensional investigation of the flow around a DD-like vortex requires to simulate the same physical setup three times. One simulation is needed for fixing the vortex detection thresholds, one for the detection itself, and one for tracking individual vortices.

Chapter 3

Toward Large-Eddy Simulations of Dust Devils of Observed Intensity: Effects of Grid Spacing, Background Wind, and Surface Heterogeneities

3.1 Declaration of Contributions

The author contributions are given on the left at the first page of the research article.

3.2 Research Article

Giersch, S., Brast, M., Hoffmann, F., and Raasch, S.: Toward Large-Eddy Simulations of Dust Devils of Observed Intensity: Effects of Grid Spacing, Background Wind, and Surface Heterogeneities, *J. Geophys. Res. Atmos.*, **124**, 7697–7718, doi:10.1029/2019JD030513, 2019.

©2019. The Authors. CC BY-NC-ND 4.0 License. Reproduced with permission from John Wiley & Sons.



RESEARCH ARTICLE

10.1029/2019JD030513

Toward Large-Eddy Simulations of Dust Devils of Observed Intensity: Effects of Grid Spacing, Background Wind, and Surface Heterogeneities

S. Giersch¹ , M. Brast^{1,2}, F. Hoffmann^{1,3,4} , and S. Raasch¹ 

¹Institute of Meteorology and Climatology, Leibniz University Hannover, Hannover, Germany, ²Now at METEK Meteorologische Messtechnik GmbH, Elmshorn, Germany, ³Now at Cooperative Institute for Research in Environmental Sciences (CIRES), University of Colorado Boulder, Boulder, CO, USA, ⁴Now at Chemical Sciences Division, NOAA Earth System Research Laboratory (ESRL), Boulder, CO, USA

Key Points:

- First numerical simulations producing dust devil-like vortices of observed intensity are presented
- Grid spacings of 2 m, heating heterogeneities, and moderate background winds increase the strength of simulated dust devils significantly
- Over heterogeneous surfaces, dust devil-like vortices cumulate at low-level convergence lines

Correspondence to:S. Raasch,
raasch@muk.uni-hannover.de**Citation:**

Giersch, S., Brast, M., Hoffmann, F., & Raasch, S. (2019). Toward large-eddy simulations of dust devils of observed intensity: Effects of grid spacing, background wind, and surface heterogeneities. *Journal of Geophysical Research: Atmospheres*, 124, 7697–7718. <https://doi.org/10.1029/2019JD030513>

Received 19 MAR 2019

Accepted 23 MAY 2019

Accepted article online 8 JUL 2019

Published online 29 JUL 2019

Author Contributions**Conceptualization:** S. Giersch, F. Hoffmann, S. Raasch**Data curation:** S. Giersch**Methodology:** S. Giersch, M. Brast, F. Hoffmann, S. Raasch**Software:** S. Giersch, M. Brast, F. Hoffmann**Validation:** S. Giersch**Writing - Original Draft:** S. Giersch, F. Hoffmann**Formal Analysis:** S. Giersch, F. Hoffmann**Investigation:** S. Giersch, F. Hoffmann**Project Administration:** S. Raasch**Resources:** M. Brast, F. Hoffmann

©2019. The Authors.

This is an open access article under the terms of the Creative Commons Attribution-NonCommercial-NoDerivs License, which permits use and distribution in any medium, provided the original work is properly cited, the use is non-commercial and no modifications or adaptations are made.

Abstract Dust devils are convective vortices with a vertical axis of rotation made visible by lifted soil particles. Currently, there is great uncertainty about the extent to which dust devils contribute to the atmospheric aerosol input and thereby influence Earth's radiation budget. Past efforts to quantify the aerosol transport and study their formation, maintenance, and statistics using large-eddy simulation (LES) have been of limited success. Therefore, some important features of dust devil-like vortices simulated with LES still do not compare well with those of observed ones. One major difference is the simulated value of the core pressure drop, which is almost 1 order of magnitude smaller compared to the observed range of 250 to 450 Pa. However, most of the existing numerical simulations are based on highly idealized setups and coarse grid spacings. In this study, we investigate the effects of various factors on the simulated vortex strength with high-resolution LES. For the first time, we are able to reproduce observed core pressures by using a high spatial resolution of 2 m, a model setup with moderate background wind and a spatially heterogeneous surface heat flux. It is found that vortices mainly appear at the lines of horizontal flow convergence above the centers of the strongly heated patches, which is in contrast to some older observations in which vortices seemed to be created along the patch edges.

1. Introduction

Dust devils are convective vortices with a vertical axis and the capability to lift dust. This capability makes dust devils not only an interesting optical phenomenon but also an important part of the climate system: Dust devils are known to increase the transport of dust from the surface to the atmosphere by several orders of magnitude compared to their background values of the dust flux (Renno et al., 2004). Therefore, dust devils have to be considered in the global dust budget with commensurate influences on cloud formation processes, the global radiation budget, or the water and carbon cycle (Shao et al., 2011). However, the contribution that dust devils have to the global dust budget is still under debate (e.g., Jemmett-Smith et al., 2015; Koch & Renno, 2005). To quantify the different effects of the aerosol transport through dust devils into the atmosphere, sufficient statistics on the occurrence and strength of dust devils are required. But the derivation of these statistics is rather difficult. First, observations suffer from the erratic occurrence of dust devils and the limited area, which can be reliably monitored (e.g., Lorenz, 2014). Second, numerical simulations, from which the deviation of these statistics would be straightforward, have not been able to reproduce dust devils of observed intensities (e.g., Kanak, 2006). In particular, the highest simulated core pressure drop of 72.4 Pa (Raasch & Franke, 2011) is still almost 1 order of magnitude smaller than typically observed values in the range of 250 to 450 Pa (Sinclair, 1973; Kanak, 2005, 2006). Thus, the main objective of this study is the identification of reasons for this deviation of numerical simulations from observations and, consequently, the simulation of dust devils of observed intensity.

Large-eddy simulation (LES) models are the most common method for simulating the development of dust devils in the convective boundary layer (CBL; e.g., Gheynani & Taylor, 2010; Kanak, 2005; Kanak et al., 2000; Ito et al., 2013; Raasch & Franke, 2011). For this task, the simulations have to fulfill two demands. First, they have to simulate a domain sufficiently large enough to represent the cellular pattern of convection,

Supervision: S. Raasch
Visualization: S. Giersch, F. Hoffmann
Writing - review & editing: S. Giersch, M. Brast, F. Hoffmann, S. Raasch

whose vertices are believed to be necessary for the generation of dust devils (e.g., Kanak, 2005; Raasch & Franke, 2011). And second, they have to resolve dust devils themselves by a sufficiently fine resolution. To cover both needs, a model domain of a couple of kilometers in each horizontal direction and a grid spacing in the order of tens of meters or less are necessary. In this way, however, a dust devil is resolved by a couple of grid points only. Structures on these scales are just partly resolved (e.g., Sagaut, 2006, Chapter 7), giving a possible explanation for the deviation between simulations and observations. Accordingly, this study will analyze how the grid spacing affects the intensity of simulated dust devils first.

Furthermore, the effect of the simulated environment in which the dust devils will develop is investigated. In past dust devil simulations, setups have been highly idealized, neglecting background winds and heterogeneous surface heating (e.g., Kanak et al., 2000; Ohno & Takemi, 2010). In fact, these are conditions rarely found in nature, and previous studies show that these parameters may affect the occurrence and strength of dust devils significantly. For instance, LES of Raasch and Franke (2011) showed that moderate background winds enhance and intensify the formation of dust devil-like vortices, whereas strong background winds decrease their occurrence in accordance with observations (Sinclair, 1969). Moreover, Sinclair (1969) and Renno et al. (2004) observed that heterogeneous surfaces, caused by different patterns of heating or surface roughness, affect the formation of dust devils, too. Rugged terrain, such as mountains, prevents dust devils from developing, while heterogeneous conditions, such as hills or dry riverbeds, can be favorable. Both effects, background winds and the pattern of surface heating, will be studied in the following.

All in all, this study will offer an overview of several factors affecting the strength of simulated dust devils, aiming the first simulation of dust devils of observed intensity. In addition, the first LES especially designed for investigating the impact of heterogeneities on the intensity of dust devils is introduced. In the following, the term dust devil refers to all convective vortices exceeding certain core pressure drop and vorticity thresholds (section 2.2). Furthermore, vortex, dust devil, and dust devil-like vortex are used as synonyms. The paper is structured as follows. The applied simulation setups and analysis methods are described in section 2. The results are presented in section 3. A summary concludes this study in section 4.

2. Methodology

All simulations are carried out with the Parallelized Large-Eddy Simulation Model (PALM; Maronga et al., 2015), which solves the nonhydrostatic, filtered, incompressible Navier-Stokes equations in Boussinesq-approximated form and an additional transport equation for potential temperature. Time stepping is based on a third-order Runge-Kutta scheme (Williamson, 1980); advection is approximated by a fifth-order scheme by Wicker and Skamarock (2002). In addition, subgrid-scale mixing is parameterized based on a 1.5th-order closure after Deardorff (1980). PALM uses the modified version of Moeng and Wyngaard (1988) and Saiki et al. (2000).

The application of the Boussinesq-approximation requires incompressibility of the flow, which is not satisfied by the numerical integration of the governing equation used in PALM. Hence, a predictor-corrector method (Patrinos & Kistler, 1977) is used, in which a Poisson equation for the so-called perturbation pressure is solved, guaranteeing the incompressibility of the flow. In case of horizontally homogeneous heating the absolute value of the perturbation pressure is interpreted as the pressure drop within dust devils as it is done similarly in studies of, for example, Kanak et al. (2000), Kanak (2005), and Raasch and Franke (2011). However, for the simulations with heterogeneous heating, where mean pressure gradients along the heterogeneity arise (see section 3.4), a different interpretation of the perturbation pressure is required. Instead of absolute values, relative values of the perturbation pressure with respect to the instantaneous average along the homogeneous direction are interpreted as the pressure drop (see section 2.2 for a more detailed explanation).

Due to their inherent errors, the application of a suitable advection scheme is mandatory to allow a sufficient development of small-scale phenomena like dust devils, covering only a couple of grid points. Usually, schemes of odd order of accuracy are dominated by numerical diffusion, damping small-scale features of the flow. Numerical dispersion is predominantly occurring for schemes of even order. It provokes instabilities (also known as wiggles) in the vicinity of strong gradients (Hirsch, 2007, Chapter 8; Durran, 2010, Chapter 3), being inherent features of dust devil centers. Therefore, an artificial increase of the collapse of dust devils through numerical dispersion has been observed in our simulations if a second-order advection scheme by Piacsek and Williams (1970) is used (not shown). To avoid this, high-order and less dispersive advec-

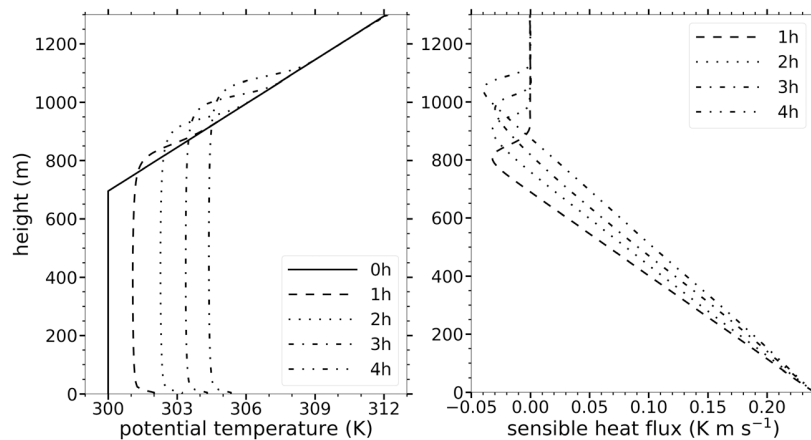


Figure 1. Horizontally and temporally averaged profiles of the potential temperature (left) and sensible heat flux (right) for four different simulation times derived from HO. The initial profile of the potential temperature is indicated by the solid line.

tion schemes are necessary, like the fifth-order scheme by Wicker and Skamarock (2002). It is based on an approximation of the advection term of even accuracy (viz., sixth order), which causes numerical dispersion. Due to the addition of an artificial dissipation term, the order of the scheme is reduced by one and the wiggles produced by the dispersion error are damped by numerical diffusion. Thus, a better representation of vortices and the associated strong gradients can be reached in comparison to the second-order scheme by Piacsek and Williams (1970), used in an earlier LES study on dust devils by Raasch and Franke (2011).

2.1. General Setup

For this study, several different simulations of a dry atmospheric boundary layer have been conducted. This subsection will give an overview of their initialization. In all simulations with homogeneous heating, a CBL is simulated by prescribing a constant sensible surface heat flux of $0.24 \text{ K}\cdot\text{m}\cdot\text{s}^{-1}$ (approximately $285 \text{ W}/\text{m}^2$), which is a typical value for clear-sky situations in the middle latitudes during the afternoon in spring and summer (e.g., Cellier et al., 1996; Parlow, 2003). For the heterogeneous simulation, this heat flux is split in two equally sized rectangles of $0.12 \text{ K}\cdot\text{m}\cdot\text{s}^{-1}$ ($140 \text{ W}/\text{m}^2$) and $0.36 \text{ K}\cdot\text{m}\cdot\text{s}^{-1}$ ($430 \text{ W}/\text{m}^2$), resulting in a domain-averaged flux of $0.24 \text{ K}\cdot\text{m}\cdot\text{s}^{-1}$ ($285 \text{ W}/\text{m}^2$) as applied in the homogeneous simulations. An idealized profile of potential temperature is specified at the beginning of the simulation featuring a constant value of 300 K up to 700 m followed by a capping inversion of $0.02 \text{ K}/\text{m}$ (see Figure 1). Well above the capping inversion a sponge layer is applied, where Rayleigh damping reduces spurious reflections of vertically propagating waves. The horizontal wind components are initialized by using a height-constant geostrophic wind, being a synonym for the background wind in the following. To trigger off the onset of convection, random perturbations are imposed on the horizontal velocity field at the beginning of the simulation.

At the bottom boundary, a no-slip condition is prescribed for the horizontal wind components. A free-slip condition is used at the top boundary. In addition, doubly periodic boundary conditions are used. For calculating the momentum flux at the surface, a constant flux layer is assumed as the boundary condition between the surface and the first grid level, using Monin-Obukhov similarity theory. This requires a value for the roughness length, which is set to 0.1 m (typical for rural areas). The Coriolis parameter is set to $1.26 \times 10^{-4} \text{ s}^{-1}$ corresponding to a latitude of 52° .

A quadratic model domain of $4 \times 4 \text{ km}^2$ is applied in the horizontal directions to resolve the pattern of convective cells adequately. As stated in section 1, this is necessary since the vertices of these cells are the primary source for the formation of dust devils and have to be resolved for a successful simulation of dust devils (e.g., Kanak, 2005; Raasch & Franke, 2011). The height of the model domain is located well above the inversion ($1,900\text{--}2,100 \text{ m}$) to not interact with the growing CBL. Above $1,200 \text{ m}$, the vertical grid spacing is stretched. Very high resolution LES of 2-m grid spacing are carried out for selected simulations. Most simulations, however, are conducted with a (still relatively high) resolution of 10 m as a compromise between resolution and computing costs. The simulated time is restricted to $14,400 \text{ s}$. This is a further compromise between compu-

Table 1
Summary of Characteristics of the Conducted Simulations

Simulation name	Domain size $L_x \times L_y \times L_z$ (m ³)	Number of grid points	Grid spacing (m)	Wind speed (m/s)	Wind direction	Heterogeneity (width in kilometers)
HO	4,000 × 4,000 × 1,950	400 × 400 × 144	10	0	—	no
HOhf	4,000 × 4,000 × 1,950	400 × 400 × 144	10	0	—	no
HOhr	4,000 × 4,000 × 1,782	2,000 × 2,000 × 640	2	0	—	no
HOu2.5	4,000 × 4,000 × 1,950	400 × 400 × 144	10	2.5	<i>x</i>	no
HOu5	4,000 × 4,000 × 1,950	400 × 400 × 144	10	5	<i>x</i>	no
HOu7.5	4,000 × 4,000 × 1,950	400 × 400 × 144	10	7.5	<i>x</i>	no
HOu10	4,000 × 4,000 × 1,950	400 × 400 × 144	10	10	<i>x</i>	no
HE	4,000 × 4,000 × 1,950	400 × 400 × 144	10	0	—	yes (4)
HE2	4,000 × 4,000 × 1,950	400 × 400 × 144	10	0	—	yes (2)
HE8	8,000 × 4,000 × 1,950	800 × 400 × 144	10	0	—	yes (8)
HE16	16,000 × 4,000 × 1,950	1,600 × 400 × 144	10	0	—	yes (16)
HEv5	4,000 × 4,000 × 1,950	400 × 400 × 144	10	2.5	<i>y</i>	yes (4)
HEv5hr	4,000 × 4,000 × 1,782	2,000 × 2000 × 640	2	5	<i>y</i>	yes (4)

Note. HE = heterogeneous; HO = homogeneous.

tational costs and providing sufficient dust devil statistics that heavily depends on the resolution, domain size, and simulated time.

An overview of all conducted simulations is given in Table 1, stating varied parameters: domain size, number of grid points, grid spacing, wind speed, wind direction, and pattern of heating (homogeneous/heterogeneous with different widths of the heterogeneity). Moreover, the table assigns a name to each simulation, which will be used as a reference in the following. The first part of the name indicates homogeneous (“HO”) or heterogeneous (“HE”) simulations. Then, if a background wind is imposed, the wind direction (“*u*” / “*v*” for the wind in *x* or *y* directions, respectively) and the absolute value of the wind speed (m/s) are given. If applicable, special characteristics of the simulation like an increased heat flux, different widths of the heterogeneity, or the resolution are indicated at the end of the name: “hr” stands for “high-resolution simulation” with a grid spacing of 2 m, “hf” stands for “high heat flux” with a sensible heat flux of 0.36 K·m·s^{−1}.

2.2. Vortex Detection and Analysis

For vortex detection, the same algorithm as developed and used by Raasch and Franke (2011) is applied. This subsection will briefly summarize this algorithm and mention changes and additions that have been necessary for this study. The reader is referred to Raasch and Franke (2011) for a more detailed description.

Vortices are detected at the first computational grid point above the surface by identifying local maxima (or relative maxima in case of heterogeneous simulations) of the absolute value of perturbation pressure drop $|p|$ and the absolute value of vorticity, which describes the vertical component of rotation of the velocity field

$$|\zeta| = \left| \frac{\partial v}{\partial x} - \frac{\partial u}{\partial y} \right|, \quad (1)$$

where *u* and *v* are the horizontal velocity components in *x* and *y* directions, respectively. For simulations with heterogeneous heating (see section 3.4), values of the perturbation pressure drop relative to the instantaneous average along *y* (homogeneous direction) are considered. This is due to the fact that with heterogeneous heating along *x* a secondary circulation parallel to the *x* axis develops, which is caused by a large-scale negative perturbation pressure drop over the stronger heated area and positive perturbation pressure drop over the less heated region. Thus, the mean reference perturbation pressure is not 0 anymore. Typical values for the mean reference perturbation pressure are several pascals (e.g., Letzel & Raasch, 2003).

For all simulations with a grid spacing of 10 m, a dust devil-like vortex is identified if $|\zeta| \geq 0.087 \text{ s}^{-1}$ and $|p| \geq 3.5 \text{ Pa}$, which would correspond to a tangential velocity at the dust devil’s wall of 1.7 m/s and a wall radius of 20 m (according to the Rankine vortex model, where the vortex wall corresponds with the maximum tangential velocity). At the same time, the pressure minimum needs to be located at the maximum of

the vorticity or at an adjacent grid point. This takes into account that the location of the pressure minimum and the axis of rotation can be slightly different. The applied thresholds correspond to 5 times the standard deviation of vorticity and 3 times the standard deviation of perturbation pressure. The standard deviation is calculated from HO (or HOhr for the high-resolution LES) using an instantaneous horizontal cross section taken from the analysis height after 4 hr of simulation time. This procedure is in good agreement with other dust devil detection algorithms (e.g., Nishizawa et al., 2016).

The used thresholds for detecting dust devils seems to be quite low compared to observational data. For example, a pressure value of at least 30 Pa is necessary to lift dust under ideal conditions (Lorenz, 2014). Low values, however, are necessary to record almost the entire life cycle of the vortex. Nevertheless, the very initial and very last phase of a dust devil's life cannot be recorded. The selection of the thresholds is also a compromise between getting a sufficiently large amount of data for analysis and eliminating the random noise of noncoherent turbulence as much as possible. Since the high-resolution LES (2-m grid spacing) tend to produce dust devils of higher intensity, the threshold values are $|\zeta| \geq 0.32 \text{ s}^{-1}$ (5 times the standard deviation) and $|p| \geq 3.5 \text{ Pa}$ (3 times the standard deviation) for these runs. The different thresholds for different grid spacings do not affect the comparability of the simulations since we are mainly interested in intense dust devils, which feature most of the time much higher values than the applied threshold values.

For dust devil track analysis, the vortex center identified at a certain model time step is connected to a vortex center at the following time step (or the time step after that) if the distance between both is less or equal than two grid points. Allowing the vortex to be not detected at the following (first) time step but at the time step thereafter (second time step) takes into account that the vorticity or the perturbation pressure could be momentarily just less than the threshold value. An additional criterion to avoid counting two different dust devil centers to the same track is that the vorticity have to have the same sign at any time step of the track. Sometimes several dust devil centers are detected in the vicinity of each other during one specific time step. This might be the case for dust devils deviating strongly from a circular pattern resulting in several local extrema that are erroneously identified as dust devil centers (or for the rare case of a dust devil consisting of several vortices, which have also been observed in nature; Bluestein et al., 2004). To avoid counting a single dust devil twice or more, the weaker vortex centers (rated by the core pressure drop) located within the dust devils radius are rejected before track analysis. The vortex radius is determined from the tangentially averaged pressure drop distribution around each center. The distance where the pressure drop is reduced to 50% of the core pressure drop is assumed to be the radius of the vortex. This radius criterion matches most of the common vortex models, which try to define the dust devil structure analytically (e.g., Lorenz, 2014).

3. Results

Before advancing to the analysis of several parameters affecting the intensity of simulated dust devils, the following subsection will give a general overview of the control simulation HO. Afterward, we will modify HO's setup systematically to test the effect of grid spacing, background wind, and heterogeneities to work out their individual impacts on the intensity of simulated dust devils.

3.1. Control Simulation HO

The general development of the CBL in HO can be generalized to all following simulations. Figure 1 displays horizontally and temporally averaged vertical profiles of the potential temperature and the vertical sensible heat flux at several points in time. In this study, time averaging will always refer to a period of 900 s before the respective output time. The profiles indicate a well-mixed boundary layer growing in time. Due to the heating from the surface, the lowest meters feature an unstable stratification, which is a necessary condition for the development of dust devils (e.g., Sinclair, 1969). The vertical profiles of the sensible heat flux exhibit the prescribed value of $0.24 \text{ K}\cdot\text{m}\cdot\text{s}^{-1}$ at the surface, which decreases monotonically throughout the boundary layer, indicating that the simulation has reached a quasi-stationary state after 1 hr. Earlier times ($<2,700 \text{ s}$) are considered as model spin-up and not analyzed.

The cellular pattern of the simulated CBL is visible in horizontal cross sections of the vertical velocity at different heights after 10,800-s simulated time (Figure 2). The cells are dominated by high positive velocities at the cell edges, whereas negative velocities cover the cell centers. For the applied horizontal domain size of $4 \times 4 \text{ km}^2$, about two to three dominant cells in each horizontal direction are represented (Figure 2, bottom). Above one third of the boundary layer height, the polygonal structure changes to a pattern consisting of

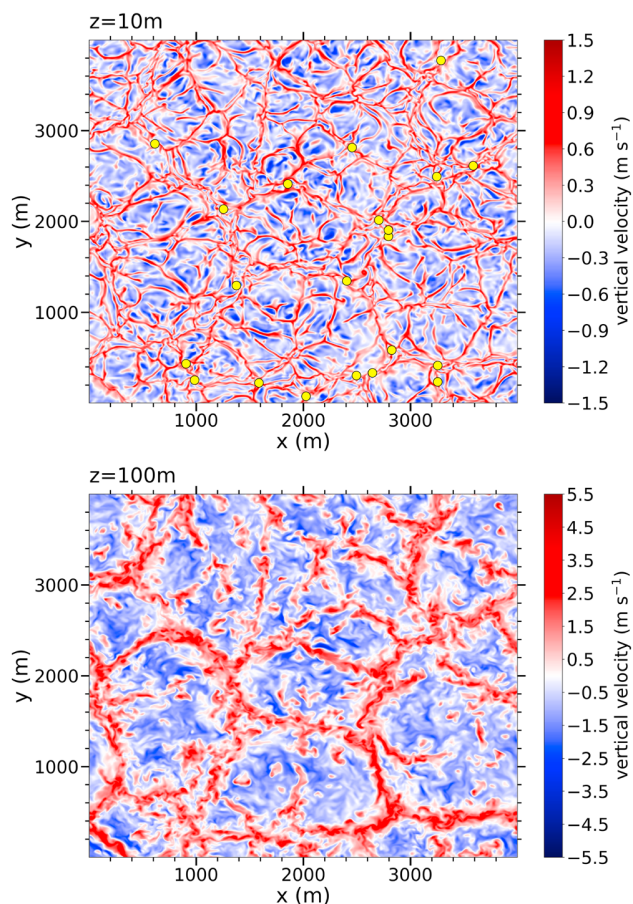


Figure 2. Horizontal cross sections of the instantaneous vertical velocity at 10 m (top) and 100 m (bottom) height after 10,800-s simulated time derived from simulation HO. Detected vortex centers are depicted as yellow dots.

several isolated plumes with strong updrafts and widespread downdrafts (not shown), which is a well-known behavior of the CBL (e.g., Schmidt & Schumann, 1989).

At 10-m height, the vertical velocity exhibits a finer cellular pattern than at higher levels. However, the locations of vortex centers (yellow dots) coincide well with the cell vertices where, due to the horizontal convergence, higher vertical velocities arise than in the cell centers and several convergence lines merge. This finding is in accordance with previous studies (e.g., Kanak, 2005; Raasch & Franke, 2011), which have elaborated that the cell edges and especially the vertices are the primary location of dust devil generation.

The significant contribution of cell vertices to the development of vertical vortices is also confirmed by the spatial distribution of dust devil tracks detected between 9,000 and 14,400 s (Figure 3): The tracks clearly resemble the pattern of convective cells due to their preferential occurrence at the cell vertices and edges. Overall, 1,952 vortex tracks were detected during this 1.5-hr period.

To further analyze how statistics change between the different simulations, some bulk characteristics are compiled in Table 2, which lists, from left to right, the number of detected dust devils N , averaged lifetime $\bar{\tau}$, translation or migration speed $\overline{v_{i,\text{mean}}}$, radius $\overline{r_{\text{mean}}}$, maximum core pressure drop $|p|_{\text{max}}$, maximum vorticity $|\zeta|_{\text{max}}$, and maximum tangential velocity $\langle u_{\text{tan}} \rangle_{\text{max}}$. The overbar describes an average over all N detected vortices, whereas the angle brackets refer to the maximum of a tangentially averaged value determined for each dust devil center. The index “max” refers to the maximum value during the whole lifetime of one specific vortex, and the index “mean” indicates a value averaged over the whole lifetime of a single vortex. Besides, the standard deviations and the overall maximum values are shown in Table 2. For all the following

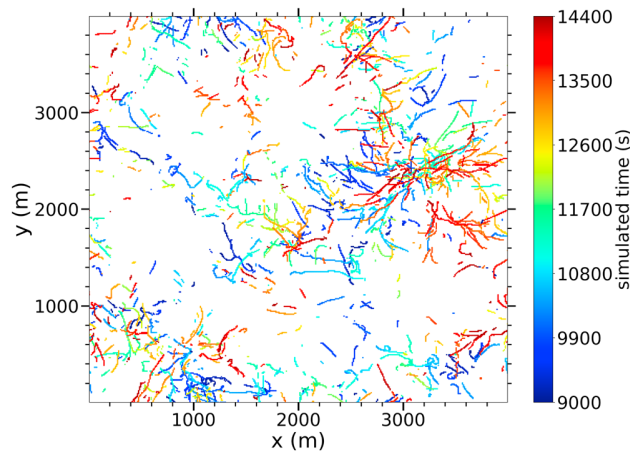


Figure 3. Spatial distribution of all 1,952 vortex tracks between 9,000 and 14,400 s derived from simulation HO. Each vortex center is represented by a dot. The color of the dot codes the simulated time at detection.

statistics, only vortices after the model spin-up (>2,700 s) with a lifetime of

$$\tau > \max \left(120 \text{ s}, \frac{2\pi r_{\text{mean}}}{\langle u_{\text{tan}} \rangle_{\text{mean}}} \right) \quad (2)$$

are considered. Equation (2) says that a vortex has to exist for at least 120 s and that an air parcel flowing with $\langle u_{\text{tan}} \rangle_{\text{mean}}$ can circulate the vortex once or more during its lifetime. This procedure restricts the statistics to the longer-lasting and thereby stronger dust devil-like vortices, which are much more relevant in the discussion of simulating realistic maximum core pressure drops. Nevertheless, for the presentation of the spatial distribution of dust devil-like vortices (e.g., Figure 3) each vortex track independent of its lifetime is considered.

It should be mentioned here that the main reason for listing bulk properties is to afford others a better comparison of their model results with this study. However, the focus of discussion and analysis is on the maximum core pressure drop. For the mean value of this parameter, the confidence interval with a confidence level of 95% is specified for each simulation in order to account for statistical significance. Simulation HO shows a confidence interval of [8.71 Pa, 9.30 Pa]. In addition, no linear correlation could be found between vortex radius and core pressure drop as well as between the vortex radius and its duration for each of the following simulations. This is indicated by Pearson correlation coefficients, which are around 0.2 or lower.

3.2. The Effect of Grid Spacing

To study the effect of grid resolution on the intensity of dust devils, the previously presented simulation HO has been repeated with a grid spacing of 2 m instead of 10 m. This simulation (named HOhr) is almost identical to the simulation comprehensively examined by Raasch and Franke (2011). The main differences are (i) the applied fifth-order advection scheme by Wicker and Skamarock (2002) instead of the second-order scheme by Piacsek and Williams (1970), and (ii) the extended simulation time from 1.5 to 4 hr.

Table 2
Dust Devil Characteristics Derived From Simulation HO

N	$\bar{\tau}$ (s)	$\overline{v_{\text{t}}}_{\text{mean}}$ (m/s)	\bar{r}_{mean} (m)	$\overline{ p }_{\text{max}}$ (Pa)	$\overline{ \zeta }_{\text{max}}$ (s ⁻¹)	$\overline{\langle u_{\text{tan}} \rangle}_{\text{max}}$ (m/s)
861	280 ± 184	0.94 ± 0.40	18.26 ± 3.45	9.01 ± 4.45	0.432 ± 0.094	2.31 ± 0.57
	1,496	2.53	44.55	44.03	0.934	5.54

Note. The second row represents the maximum values with respect to all 861 dust devils fulfilling equation (2). HO = homogeneous.

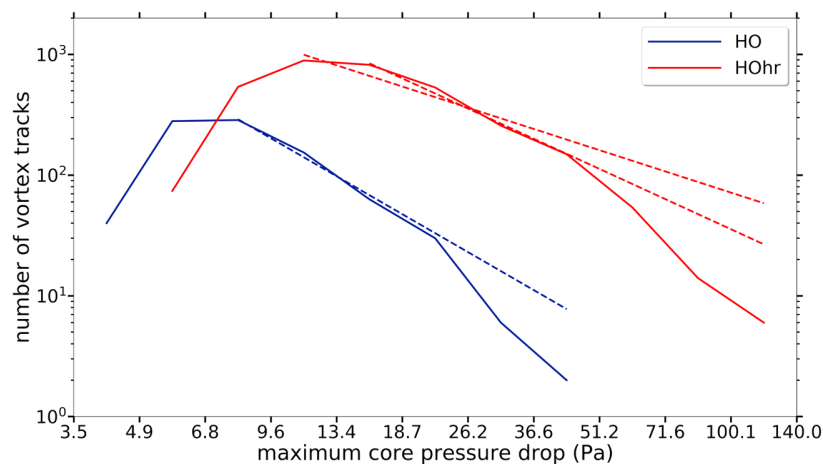


Figure 4. Number of vortex tracks as a function of each track's maximum core pressure drop for simulations HO (blue) and HOhr (red). The dashed lines indicate fitted power laws using nonlinear least squares analysis. For HOhr, two lines are shown, that indicate the different slopes of -1.72 and -1.21 mentioned in the text.

The general dynamics of the CBL, as described for HO, are also apparent in HOhr, including the cellular pattern of convection and the generation of dust devil-like vortices at cell vertices and edges. However, the vortices itself are much better resolved in HOhr, including their dynamics responsible for the generation of a higher core pressure drop. This is shown in Figure 4, which displays the number of vortex tracks (satisfying equation 2) as a function of each track's maximum core pressure drop for both simulations, HO and HOhr. The axes are logarithmically scaled with a bin size ratio of about $\sqrt{2}$ as suggested by Lorenz and Jackson (2016), who argued that this ratio is a good compromise between retaining enough data points to define the function shape while keeping enough counts in each bin to avoid large counting errors. The $\sqrt{2}$ ratio is kept constant in all subsequent plots using logarithmic binning. For HOhr, the most intense dust devils exhibit a factor of 3 higher core pressure drops than in HO, and the total number of dust devil tracks satisfying equation (2) increases by a factor of 4 (from 861 to 3,335). The increased number of vortices is purely related to the better resolution of the dynamics in the CBL and would be even higher if the same detection thresholds (3.5 Pa, 0.087 s^{-1}) had been used. The most intense vortex shows a pressure drop of 138.64 Pa.

The decreasing number of vortex tracks with increasing maximum core pressure drop can be described by a truncated power law starting from the bin with the highest number of detected vortex tracks (e.g., Lorenz & Jackson, 2016; Nishizawa et al., 2016). The power law has the form

$$f(x; a, k) = ax^k, \quad (3)$$

where a and k are constants and x describes the maximum core pressure drop. To fit the function f to the data and determine the coefficients, nonlinear least squares analysis has been used. The resulting curves are also illustrated in Figure 4 revealing a differential power law slope (k value) for the HO data of -2.16 and -1.21 for HOhr (-1.72 if the bin with the second highest number is used as a starting point), which correspond to the range of slopes derived from observational data (-1 to -3 ; Lorenz, 2014; Lorenz & Jackson, 2016). It has to be noted that the slope heavily depends on the selected starting point and the bin limits which vary from plot to plot to keep the bin ratio constant. If, for example, the maximum number of detected vortex tracks is not pronounced and therefore hard to define, several slopes are conceivable.

Table 3
Dust Devil Characteristics Derived From Simulation HOhr

N	$\bar{\tau}$ (s)	$\overline{v_{i,\text{mean}}}$ (m/s)	$\overline{r_{\text{mean}}}$ (m)	$\overline{ p _{\text{max}}}$ (Pa)	$\overline{ \zeta _{\text{max}}}$ (s^{-1})	$\overline{\langle u_{\text{tan}} \rangle_{\text{max}}}$ (m/s)
3,335	210 ± 105	1.08 ± 0.39	4.69 ± 1.52	17.70 ± 11.91	2.76 ± 0.78	3.03 ± 0.57
	995	2.75	26.06	138.64	7.76	9.0

Note. The second row represents the maximum values with respect to all 3,335 dust devils fulfilling equation (2).

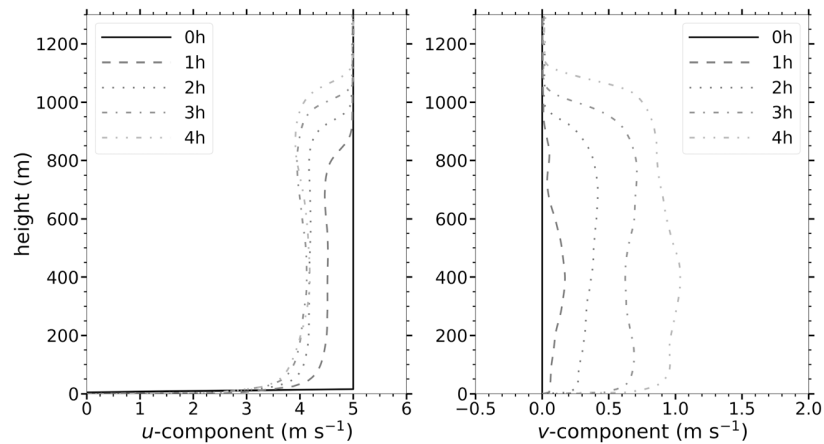


Figure 5. Horizontally and temporally averaged profiles of the horizontal velocity components u (left) and v (right) for five different simulation times derived from HOu5.

Table 3 lists the most important statistical quantities for simulation HOhr, showing much higher values of the averaged pressure drop maximum, vorticity maximum, and tangential velocity maximum compared to HO. This consistent behavior can be well described by theoretical models like the Rankine vortex or Burgers-Rott vortex model that put pressure drop, vorticity, and tangential velocity in relation (e.g., Alekseenko et al., 2007). The mean radius averaged over all detected vortices is much smaller compared to HO but can be still described with about two grid points. The changes in the mean translation speed are comparatively low, whereas the averaged lifetime of a dust devil decreases from 280 to 210, which can be attributed to the different detection thresholds in HO and HOhr as well as to the better resolution of small-scale, short-lived structures. Finally, the confidence interval of the averaged pressure drop maximum is [17.29 Pa, 18.10 Pa].

The comparison between HO and HOhr shows that it is mandatory to decrease the grid spacing for a successful simulation of dust devils. An even further reduction of the grid spacing might result in even higher core pressure drops. This claim is supported by analyzing power spectral densities of the perturbation pressure, potential temperature, and velocity components (not shown). The combination of the subgrid-scale model dissipation and the numerical dissipation of the advection scheme strongly damps spatial scales less than 4 times the grid spacing. Therefore, fluctuations on a scale of several meters are still heavily damped in simulations with 2-m grid spacing, which requires even finer resolutions for an accurate study of dust devils. For example, ultrahigh resolution dust devil simulations with a grid spacing of 0.1 m performed by Gu et al. (2008) reproduced core pressure drops of 200 Pa. However, these simulations are not able to cover the generation of dust devils by the dynamics of the boundary layer due to limited computing capabilities restricting the modeling domain to a couple of hundreds of meters horizontally. Also in our study, computing capabilities prohibit a further reduction of grid spacing (e.g., the HOhr simulation demands 23-hr CPU time on 6400 cores of a CRAY-XC40), and even a grid spacing of 2 m is too expensive for all simulations of this study. Accordingly, we will receive our main conclusions on the effects of background wind and heterogeneities on the strength of dust devils from simulations using a 10-m grid spacing, before we return to a 2-m grid spacing for the final simulation of our study.

3.3. The Effect of Background Wind

Previous studies suggest that light background winds are beneficial to dust devil formation in numerical models (e.g., Raasch & Franke, 2011) and in the real atmosphere (e.g., Rafkin et al., 2016). A further increase in background wind, however, turns the convective cells to a band-like pattern, therefore, inhibiting the formation of dust devils (Raasch & Franke, 2011; Sinclair, 1969). To quantify the effect of background wind on dust devil intensity, we impose different geostrophic winds of 2.5, 5.0, 7.5, and 10.0 m/s in x direction (simulations HOu2.5, HOu5, HOu7.5, and HOu10).

In Figure 5, the evolving horizontally and temporally averaged vertical profiles of the horizontal wind components are shown exemplarily for a geostrophic wind of 5.0 m/s.

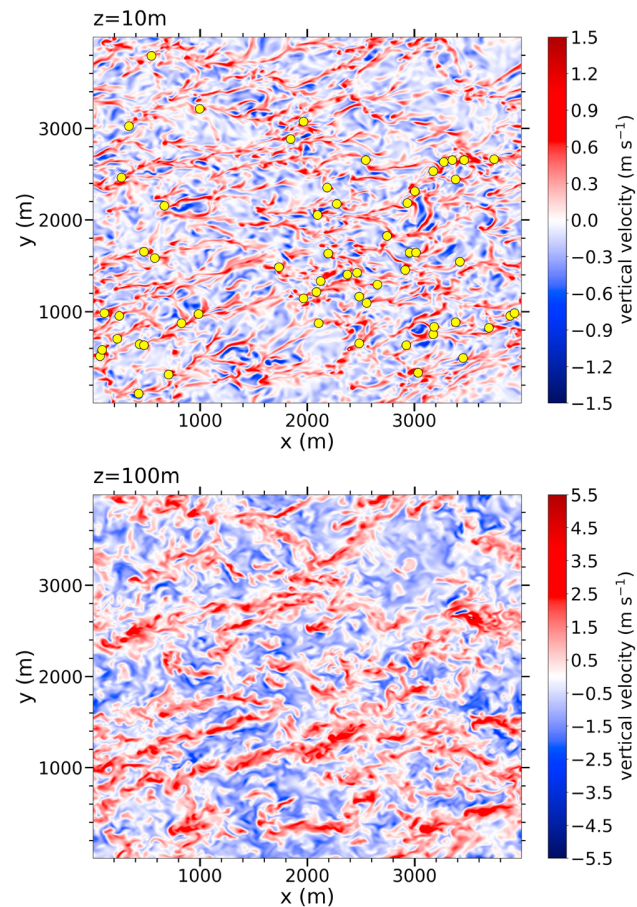


Figure 6. Horizontal cross sections of the instantaneous vertical velocity at 10 m (top) and 100 m (bottom) height after 10,800-s simulated time derived from simulation HOU7.5. Detected vortex centers are depicted as yellow dots.

The profiles indicate again a well-mixed boundary layer growing in time. Wind shear, known to significantly influence dust devil development (e.g., Balme et al., 2003), is mainly apparent close to the ground and in the entrainment zone near the inversion height. Above, the geostrophic balance is fulfilled. Furthermore, the wind direction changes according to the Ekman spiral from x axis parallel (270°) above the inversion height to roughly 255° close to the ground (after 4 hr). The profiles of HOU2.5, HOU7.5, and HOU10.0 show a similar behavior.

For a geostrophic wind of 5.0 m/s, the vertical velocity exhibits a similar convective cell pattern as shown in Figure 2 with vortex centers at the vertices and branches of the cells. For a weaker geostrophic wind of 2.5 m/s (simulation HOU2.5) the convective cell pattern is more pronounced than in simulation HOU5 (not shown), while for stronger geostrophic winds of 7.5 and 10.0 m/s the cell pattern is completely blurred and structures appear to be elongated along the x direction (Figure 6 for HOU7.5).

The vortices move approximately in the direction of the mean near-surface wind during the course of their lifetime. Thus, convective cells (well pronounced in Figure 3) are blurred here completely, which can be also seen from the spatial distribution of dust devil tracks derived from simulation HOU5 (Figure 7). The averaged translation direction is 253° . However, a single vortex can have deviations from the mean surface wind direction of more than 30° , with a standard deviation of migration

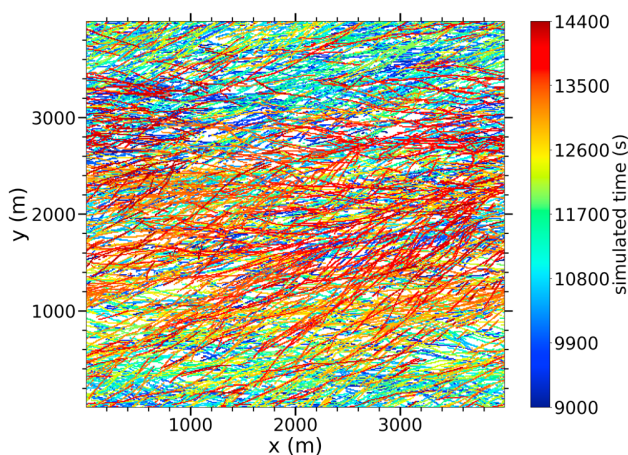


Figure 7. Spatial distribution of all 9,111 vortex tracks between 9,000 and 14,400 s derived from simulation HOU5. Each vortex center is represented by a dot. The color of the dot codes the simulated time at detection.

Table 4
 Dust Devil Characteristics Derived From Simulation HOu2.5, HOu5, HOu7.5, and HOu10

Simulation name	N	$\bar{\tau}$ (s)	$\overline{v_{\text{mean}}}$ (m/s)	$\overline{r_{\text{mean}}}$ (m)	$\overline{ p _{\text{max}}}$ (Pa)	$\overline{ \zeta _{\text{max}}}$ (s^{-1})	$\overline{\langle u_{\text{tan}} \rangle_{\text{max}}}$ (m/s)
HOu2.5	1,460	280 ± 190	2.1 ± 0.67	22.01 ± 5.50	10.18 ± 5.46	0.438 ± 0.106	2.40 ± 0.63
		1,656	4.37	55.10	52.15	0.944	5.71
HOu5	1,889	258 ± 150	3.94 ± 0.75	26.37 ± 6.79	11.61 ± 6.03	0.438 ± 0.107	2.54 ± 0.65
		1,398	6.11	81.20	51.06	0.947	5.78
HOu7.5	1,143	214 ± 98	5.73 ± 0.77	29.30 ± 7.38	12.55 ± 6.78	0.440 ± 0.111	2.63 ± 0.68
		889	9.33	70.0	54.57	0.933	5.61
HOu10	536	181 ± 61	7.21 ± 0.8	30.87 ± 9.28	14.25 ± 7.59	0.464 ± 0.118	2.85 ± 0.70
		593	9.81	71.85	51.42	0.910	5.59

Note. The second row of each conducted simulation represents the maximum values with respect to all N tracked dust devils fulfilling equation (2).

direction of 13.92° (HOu2.5), 8.20° (HOu5), 6.55° (HOu7.5), and 6.61° (HOu10). This agrees with observations of Lorenz (2016), who showed that dust devil migration directions follow the ambient wind but with a standard deviation described by $\arctan(R/U)$ with U being the ambient wind speed and R being a constant that depends on the regarded data set.

The total number of detected vortex tracks between 9,000 and 14,400 s is much higher for simulation HOu5 (9,111) than those for HO (1,952) and HOu2.5 (4,309) but still less than the number for HOu7.5 (14,226) or HOu10 (23,882) indicating that even stronger background winds trigger the development of vertical vortices. This is because of the increased near-surface wind shear, whereby additional horizontal vorticity is generated, which is then tilted into vertical vorticity via the twisting term (see Raasch & Franke, 2011). At the same time, vortices become more and more unstable due to higher turbulence that occur together with higher background winds. Further turbulence then favors the decay of coherent structures like dust devils, which results in shorter averaged lifetimes (see the bulk characteristics in Table 4). As explained by Raasch and Franke (2011), the decrease of longer-lasting, well-developed dust devils can be additionally explained by the more shear-dominated conditions, which inhibit persistent, convective cells essentially needed for the generation and maintenance of dust devils.

The interaction between reduced averaged lifetimes and increased total numbers of vortex tracks in case of higher background winds is illustrated in Figure 8, which shows the cumulative number of vortex tracks having a lifetime greater or equal to the respective value on the x axis. It can be seen that no- and low-wind

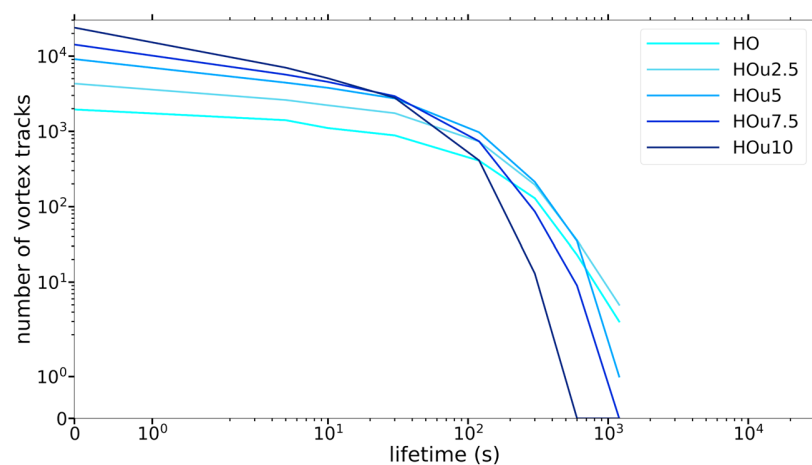


Figure 8. Cumulative number of vortex tracks between 9,000 and 14,400 s as a function of the vortices' lifetime for simulations HO, HOu2.5, HOu5, HOu7.5, and HOu10. The colors were chosen in a way that higher wind speeds have darker blue tones.

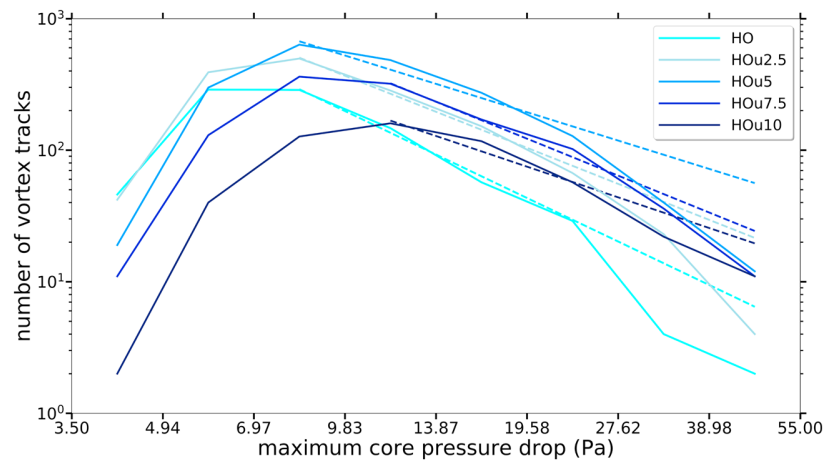


Figure 9. Number of vortex tracks as a function of each track's maximum core pressure drop for simulations HO, HOu2.5, HOu5, HOu7.5, and HOu10. The colors were chosen in a way that higher wind speeds have darker blue tones. The dashed lines indicate fitted power laws using nonlinear least squares analysis.

situations produce more longer-lasting vortices than under strong-wind conditions. For short-lived vortices, the exact opposite is the case.

Table 4 also shows that the impact of the background wind velocity on the number of detected vortex tracks satisfying equation (2) is less distinct. For a moderate increase of the background wind of 2.5 and 5.0 m/s the number of tracks (1,460 for HOu2.5 and 1,889 for HOu5) increases by a factor of about 2 in comparison to the windless simulation HO (861). For stronger background winds of 7.5 or 10.0 m/s the number of tracks decreases drastically to 1,143 and 536, respectively. This behavior is a consequence of both effects described above: an increasing total number of detected tracks accompanied by decreasing averaged lifetimes at higher background winds. For winds up to 5 m/s the increase of tracks is more pronounced in the statistically analyzed data than the decline in lifetime. Therefore, the number of tracks with a duration of at least 120 s increases, too. For geostrophic winds above 5 m/s, however, the overall increase of tracks is less pronounced than the decline in lifetime, which results in lower values for N .

The quantitative impact of different background winds on the maximum core pressure drop occurring during each track is presented in Figure 9 (for exact values see Table 4). The plots' average maximum core pressure drop increases from 9.01 to 10.18, 11.61, 12.55, and 14.25 Pa having confidence intervals of [8.71 Pa, 9.30 Pa], [9.90 Pa, 10.46 Pa], [11.34 Pa, 11.88 Pa], [12.16 Pa, 12.94 Pa], and [13.61 Pa, 14.89 Pa] for the simulations HO, HOu2.5, HOu5, HOu7.5, and HOu10, respectively. This shows that higher background winds result in more intense vortices, shifting the maximum number of detected vortex tracks to higher maximum core pressure drop values. The higher relative number of intense vortices can be explained by the increased near-surface shear due to stronger background winds, whereby the horizontal component of rota-

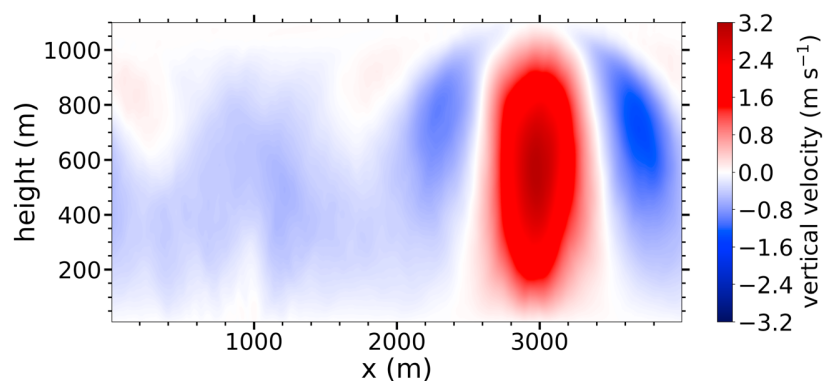


Figure 10. Vertical cross section of vertical velocity at 10,800 s, averaged along y and over the previous 900 s for simulation HE.

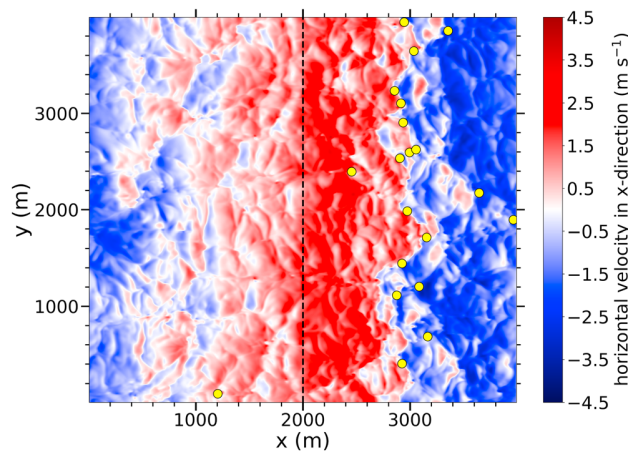


Figure 11. Horizontal cross section of the u component of the horizontal velocity at 5-m height and at 10,800-s simulated time for simulation heterogeneous. The dashed line represents the border between the differently heated areas (left: less heated, right: stronger heated). Detected vortex centers are depicted as yellow dots.

tion increases, which contributes via the twisting term to larger vorticity, dust devil tangential velocity, and pressure drop values (see Table 4 and Raasch & Franke, 2011). In addition, the total maximum core pressure drop increases compared to HO but does not change significantly with background wind. The combination of a nearly constant total maximum pressure drop with an increased number of intense vortices within the population results in less steep differential power law slopes of -2.21 (HO), -1.83 (HOu2.5), -1.44 (HOu5), -1.26 (HOu7.5), -1.88 if the bin with the second highest number is used as indicated in Figure 9), and -1.56 (HOu10). A meaningful comparison to observational data is still pending due to missing database.

All in all, high background winds are beneficial to the production of more intense vortices, but the number of long-living vortex tracks (several minutes) decreases drastically if a certain threshold velocity is exceeded. Therefore, light or moderate background winds, as they are typically present in regions of high dust devil occurrence (Jemmett-Smith et al., 2015), should be also included in future LES of dust devils to represent their observed intensity more accurately.

3.4. The Effect of Heterogeneities

To quantify the effect of heterogeneities on the intensity of dust devils, a striped pattern of heating is imposed in simulation HE: The left half of the model domain's surface ($0 \text{ m} \leq x < 2,000 \text{ m}$) is heated with a surface

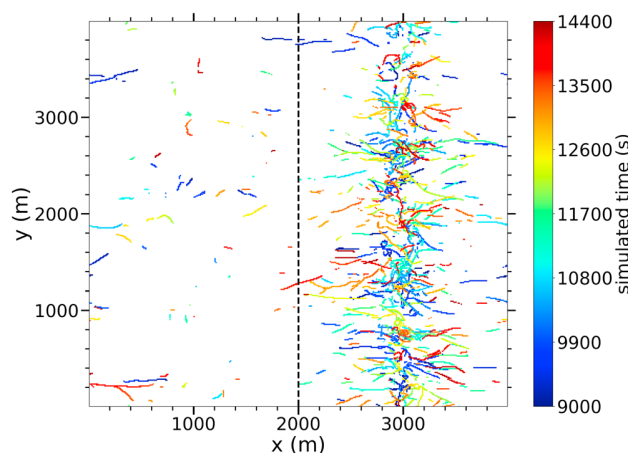


Figure 12. Spatial distribution of all 1,298 vortex tracks between 9,000 and 14,400 s derived from simulation HE. Each vortex center is represented by a dot. The color of the dot codes the simulated time at detection. The dashed line represents the border between the differently heated areas.

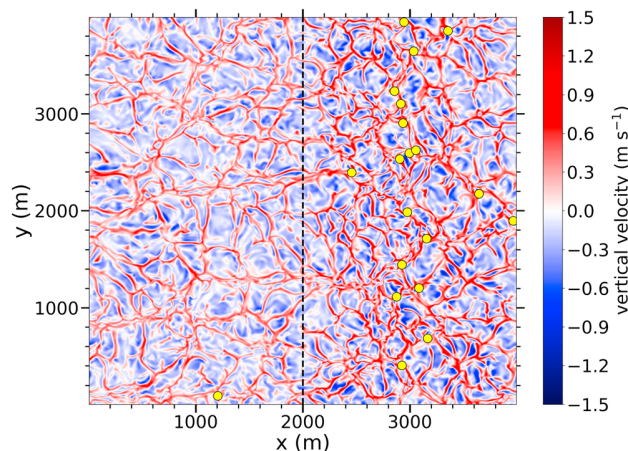


Figure 13. Horizontal cross sections of the instantaneous vertical velocity at 10-m height after 10,800-s simulated time derived from simulation HE. Detected vortex centers are depicted as yellow dots. The dashed line represents the border between the differently heated areas.

heat flux of $0.12 \text{ K}\cdot\text{m}\cdot\text{s}^{-1}$ and the right part ($2,000 \text{ m} \leq x < 4,000 \text{ m}$) with $0.36 \text{ K}\cdot\text{m}\cdot\text{s}^{-1}$, resulting in the same net surface heat flux of $0.24 \text{ K}\cdot\text{m}\cdot\text{s}^{-1}$ as applied in all previously presented simulations of this study.

Due to this differential heating, a secondary circulation develops (e.g., Avissar & Schmidt, 1998; Letzel & Raasch, 2003), in which air rises above the stronger heated region ($x = 3,000 \text{ m}$) and sinks above the less heated region ($x = 1,000 \text{ m}$, Figure 10). Due to mass continuity, this pattern is associated with a low-level convergence line above the stronger heated region, where dust devil centers seem to cumulate (Figure 11). Keep in mind that due to the staggered grid used in PALM, the horizontal velocity components are vertically shifted by half the grid spacing. Therefore, Figure 11 shows the horizontal cross section of the u component in 5 m and not in 10 m.

The spatial distribution of vortex tracks (Figure 12) indicates that dust devils are mostly generated over the stronger heated area close to the convergence line and are then advected toward it. Because the heating might not be sufficient for the development of dust devils, only a negligible amount is generated in the less heated region. Indeed, the upward vertical velocities associated with the cell edges and vertices (Figure 13) are lower in the less heated region than in the stronger heated region, making the less heated region less favorable for the development of dust devils. Moreover, the cells above the stronger heated region are more dense than above the less heated region, containing more vertices responsible for generating dust devils. This compression is a result of the secondary circulation, which low-level convergence compacts the cells above the stronger heated region, whereas the low-level divergence broadens the cells above the less heated area.

The number of detected vortex tracks with a lifetime $>120 \text{ s}$ decreases by about 50% for HE in comparison to HO, which is mainly due to geometric reasons (area of intense heating is halved, Table 5), and the secondary circulation: The subsidence of air together with the small magnitude of the heat flux over the less heated region prevents the development of dust devils, whereas dust devils are triggered along the convergence line and by the high heat flux above the stronger heated region more frequently. The stimulation of vertical vortices along the convergence line is mainly due to the fact that air parcels flowing toward each other tend to produce rotation in a horizontal plane and, consequently, vortices with a vertical axes.

Table 5

Dust Devil Characteristics Derived From Simulation HE

N	$\bar{\tau}$ (s)	$\overline{v_{t,\text{mean}}}$ (m/s)	$\overline{r_{\text{mean}}}$ (m)	$\overline{ p _{\text{max}}}$ (Pa)	$\overline{ \zeta _{\text{max}}}$ (s^{-1})	$\overline{\langle u_{\text{tan}} \rangle_{\text{max}}}$ (m/s)
463	300 ± 256	1.09 ± 0.53	21.19 ± 4.72	11.15 ± 7.23	0.485 ± 0.125	2.61 ± 0.75
	2,163	2.95	47.24	60.26	1.097	6.03

Note. The second row represents the maximum values with respect to all 463 dust devils fulfilling equation (2). HE = heterogeneous.

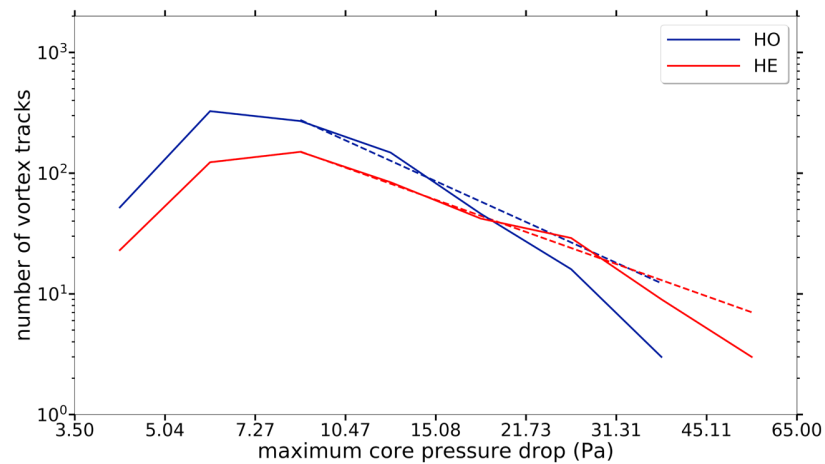


Figure 14. Number of vortex tracks as a function of each track's maximum core pressure drop for simulations HO (blue) and HE (red). The dashed lines indicate fitted power laws using nonlinear least squares analysis. HE = heterogeneous; HO = homogeneous.

The mean lifetime, translation speed, and radius values do not change significantly compared to HO (a little higher values for HE). However, the mean of the maximum core pressure drop increases from 9.01 Pa for HO to 11.15 Pa for HE with a confidence interval of [10.49 Pa, 11.81 Pa], indicating that more intense vortices are produced in simulation HE. This is additionally supported by a higher overall maximum of the pressure drop, increasing from 44.03 Pa (HO) to 60.26 Pa (HE). The more intense vortices during simulation HE are caused by the higher sensible surface heat flux in the stronger heated region, which directly produces stronger vortices as theoretical models of Renno and Ingersoll (1996) and Renno et al. (2000), and Renno et al. (1998) suggest. Additionally, the secondary circulation induces a low-level wind that is favorable for the production of more intense vortices due to additional shear similar to the simulations with an imposed geostrophic wind (see section 3.3). Consequently, the dust devil's vorticity and tangential velocity values increase.

The line plot shown in Figure 14 underlines again the production of more intense vortices in HE compared to HO. Although only half as many dust devils as in HO were recorded, the number of dust devils for the bins with high maximum core pressure drops increases significantly compared to HO. In total, the core pressure drop data can be approximated with slopes of -1.38 (HO, -2.13 if the bin with the second highest number is used as indicated in Figure 14) and -1.68 (HE).

To isolate the effect of the secondary circulation from the higher surface heat flux in one half of the modeling domain, a homogeneous simulation with a sensible surface heat flux of $0.36 \text{ K}\cdot\text{m}\cdot\text{s}^{-1}$ was conducted (HO_{hf}, results not shown). If the increased surface sensible heat flux was the only reason for the increased vortex strength, more stronger vortices than in simulation HE would occur because the surface heating of $0.36 \text{ K}\cdot\text{m}\cdot\text{s}^{-1}$ covers the whole model domain instead of the half as in simulation HE. However, though more and stronger vortices occur in HO_{hf} than in the homogeneous simulation with a net sensible surface heat flux of $0.24 \text{ K}\cdot\text{m}\cdot\text{s}^{-1}$ (HO), there is no significant difference concerning the mean maximum core pressure drop between the stronger heated homogeneous (HO_{hf}, $11.35 \text{ Pa} \pm 6.52 \text{ Pa}$, confidence interval of [11 Pa, 11.35 Pa]) and the heterogeneous simulation (HE, $11.15 \text{ Pa} \pm 7.23 \text{ Pa}$, confidence interval of [10.49 Pa, 11.81 Pa]). In fact, the overall maximum pressure drop in HE (60.26 Pa) is even higher than in simulation HO_{hf} (55.57 Pa). Thus, it can be concluded that the structure of the surface heating and the resulting secondary circulation has a significant impact on the formation of vortices by allowing the development of stronger dust devils.

Another variable probably affecting the generation of vortices is the width of the surface heterogeneity. To address this, additional simulations with a striped pattern and a width of 2 km (HE2), 8 km (HE8), and 16 km (HE16) have been conducted (results not shown). Simulation HE2 has the same horizontal domain like HO ($4 \text{ km} \times 4 \text{ km}$), while the simulations HE8 and HE16 have a horizontal domain of $8 \text{ km} \times 4 \text{ km}$ and $16 \text{ km} \times 4 \text{ km}$, respectively, to capture the larger strip widths. In simulation HE2 the vortices are weaker in comparison to the above-described simulation with a width of 4 km (HE), whereas stronger vortices appear for

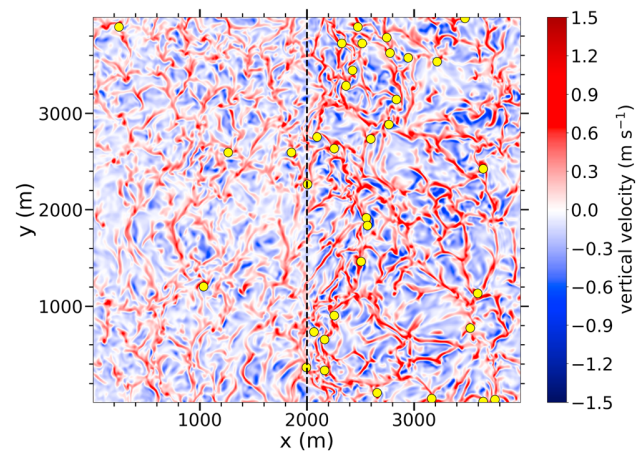


Figure 15. Horizontal cross sections of the instantaneous vertical velocity at 10-m height after 10,800-s simulated time derived from simulation HEv5. Detected vortex centers are depicted as yellow dots. The dashed line represents the border between the differently heated areas.

stripes of 8 km (HE8) and even stronger ones for stripes of 16 km (HE16), which is in agreement with previous studies showing that the secondary circulation intensifies with increasing width (Avisar & Schmidt, 1998; Letzel & Raasch, 2003; Shen & Leclerc, 1995).

3.5. The Effect of Background Wind on a Heterogeneous Simulation

By imposing an additional background wind on a heterogeneously heated simulation, it is expected to combine the effects of heterogeneity and wind, resulting in even stronger vortices. For this reason, we extended the setup of the heterogeneously heated simulation HE with a geostrophic wind of 5 m/s to test this hypothesis (simulation HEv5). In contrast to the homogeneous simulations, the direction of the background wind matters. A background wind perpendicular to the heterogeneity would weaken the secondary circulation (e.g., Avisar & Schmidt, 1998; Letzel & Raasch, 2003) and the effect on dust devils. Therefore, the background wind is imposed parallel to the heterogeneity (i.e., in positive y direction).

In simulation HEv5 a secondary circulation and a convective cell pattern similar to simulation HE develop, but with structures more and more aligned along the y axis (see Figure 15). In addition, less intense convective cells occur over the less heated patch. Due to the additionally considered background wind, the low-level convergence line shifts to the left during the simulation (not shown). This is a result of the Coriolis force, generating a negative u component at the surface that accelerates with time (see Figure 5). As

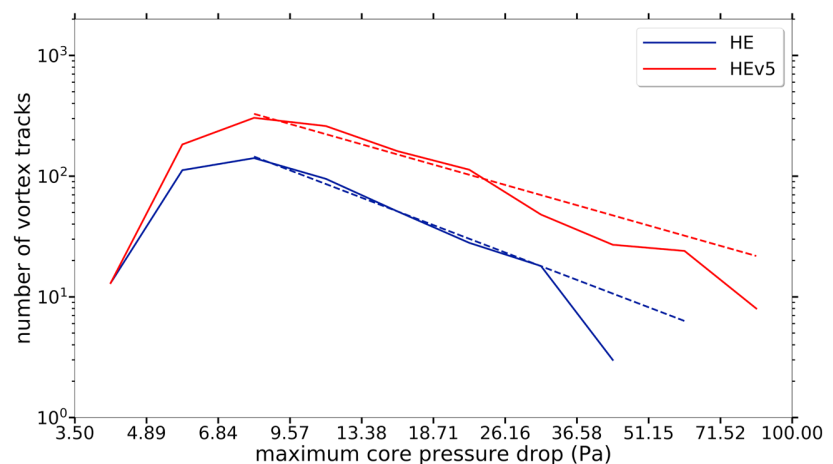


Figure 16. Number of vortex tracks as a function of each track's maximum core pressure drop for simulations HE (blue) and HEv5 (red). The dashed lines indicate fitted power laws using nonlinear least squares analysis. HE = heterogeneous.

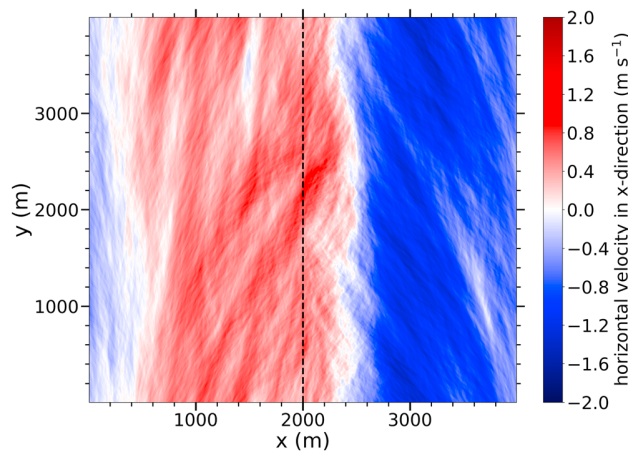


Figure 17. Horizontal cross section of the u component of the horizontal velocity (averaged over the previous 900 s) at 5-m height and at 10,800-s simulated time for simulation HEv5hr. The dashed line represents the border between the differently heated areas.

in the previous simulations, most vortices are located at the cell edges and vertices. Besides, the vortices are primarily generated above the stronger heated region and are advected toward the convergence line of the secondary circulation (as in simulation HE). In addition to the movement in x direction caused by the secondary circulation, the vortices also move with the imposed background wind in y direction.

Figure 16 shows the number of detected vortex tracks having a certain maximum core pressure drop for simulations HE and HEv5. The total number of vortices with a duration of at least 120 s is larger in simulation HEv5 (1141) than in simulation HE (463) due to the overall increase of tracks by the additional shear as a result of the background wind (see discussion in section 3.3). The occurrence of intense vortices also increases in simulation HEv5, which is indicated by the mean maximum core pressure drop, which increases from 11.15 Pa for simulation HE to 14.25 Pa for simulation HEv5, with a confidence interval of [13.58 Pa, 14.93 Pa] and with the strongest vortex in HEv5 having a core pressure drop of 95.44 Pa. Additionally, Figure 16 displays differential power law slopes of -1.56 for HE and -1.16 for HEv5. The changes in the other dust devil characteristics caused by a moderate background wind in a heterogeneous environment demonstrate a similar picture as those already discussed in section 3.3, where a geostrophic wind of 5 m/s was imposed on simulation HO.

3.6. Combined Effect of All Factors Enhancing Vortex Strength

As shown in the previous subsections, the physical parameters of background wind and surface heterogeneity and a high spatial resolution as a numerical parameter enhance the strength of simulated vortices. Now, we combine all parameters in a final simulation, that is, a heterogeneous surface with a striped pattern of 4-km width, a background wind of 5 m/s parallel to the pattern of heating, and a high spatial resolution of 2 m.

Figure 17 shows the location of the convergence line for simulation HEv5hr in a horizontal cross section of the u component at a height of 5 m after 10,800-s simulated time. As in simulation HEv5, the convergence line of the secondary circulation is shifted to the left during the simulation. At the end of the simulation, the convergence line is located close to the border of the differently heated areas.

The convective cell pattern at the first grid point above the surface is less pronounced in HEv5hr compared to HEv5 (see Figure 18). In HEv5hr, much more finer structures are resolved, which appear as streaks mostly orientated along y due to the imposed background wind. However, the displayed height is 2 m instead of 10 m, which makes a direct comparison to Figure 15 difficult. For example, small structures, which occur in particular just above the surface, are only represented in horizontal cross sections extracted at several meters height. Nevertheless, the usage of 2 m as the analysis height is much more meaningful since observations of parameters describing dust devils are mainly carried out at height levels less than 10 m (e.g., Metzger et al., 2011; Tratt et al., 2003). Further away from the surface (100 m), the cellular structure is also strongly modified by the background wind and the secondary circulation. Besides, vortices are again mainly located over the stronger heated area close to the current position of the convergence line, where strong updrafts

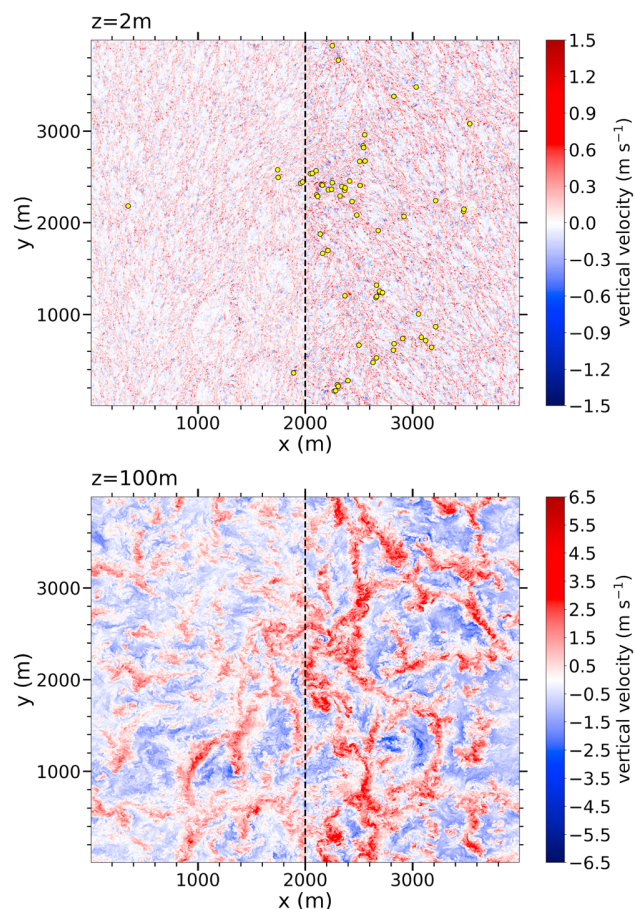


Figure 18. Horizontal cross sections of the instantaneous vertical velocity at 2-m (top) and 100-m (bottom) height after 10,800-s simulated time derived from simulation HEv5hr. Detected vortex centers are depicted as yellow dots.

occur and structures are merging. After the generation of the vortices, they are advected toward the low-level convergence line (not shown).

The distribution of the maximum core pressure drop is given in Figure 19 showing a quite gradual differential power law slope of -0.96 due to the lack of very strong and long-living vortices. Nevertheless, vortices are much stronger than in all previous simulations. Two vortices occur with a maximum core pressure drop of more than 200 Pa, with the strongest vortex having a value of 218.93 Pa, which is very close to the range of observed intensities (250 to 450 Pa, Kanak, 2005, 2006; Sinclair, 1973). Besides the increased vortex strength, the number of detected vortex tracks with a duration of at least 120 s decreases substantially (193), which supports the findings of Raasch and Franke (2011), where for the 2-m run in combination with a background wind of 5 m/s significantly less centers and well-developed tracks than in all other runs were detected. The strong decrease of dust devil-like structures was not really expected because of the 2.5 times higher number in simulation HEv5 compared to HE and more dust devil detections during the high-resolution run presented in section 3.2. Anyhow, the reason for the low number of detected vortex tracks with a duration of at least 120 s is, first, the reduced averaged lifetime of dust devil-like vortices for high-resolution runs as discussed in section 3.2. This counteracts the overall increase of vortices with decreasing grid spacing. Second, values of 120 s and more belong to the longest registered lifetimes (not shown). At such lifetimes, a further increase in background wind reduces the number of tracks (see Figure 8). Moreover, the secondary circulation can also be interpreted as an additional background wind, which reduces the number of vortices with a lifetime of at least 120 s even further.

Finally, Table 6 gives an overview of dust devil characteristics. For HEv5hr, the interaction of the high resolution, background wind, and secondary circulation result in shorter lifetimes than for HEv5 (as explained

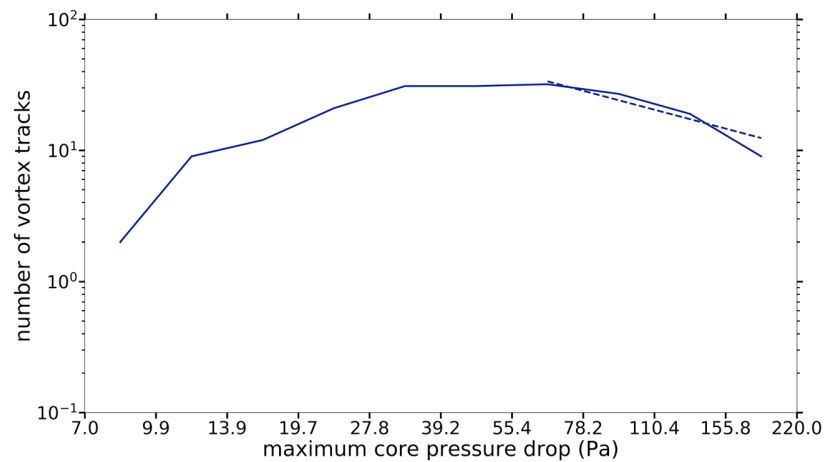


Figure 19. Number of vortex tracks as a function of each track's maximum core pressure drop for simulation HEv5hr. The dashed line indicates a fitted power law with a slope of -0.96 using nonlinear least squares analysis.

above). However, lifetimes around 200 s (several minutes) still agree well with observations (Balme & Greeley, 1998). The migration velocity resembles the ones of simulation HEv5 and HOu5, whereas the mean radius is much smaller due to the finer resolution. In line with the pressure, also mean vorticity and tangential velocity values increases a lot compared to HEv5. The confidence level of the mean maximum core pressure drop is [56.76 Pa, 69.27 Pa].

Run HEv5hr was repeated but with slightly different initial conditions with respect to the random perturbations, which were imposed on the horizontal velocity field in the beginning (see section 2.1). That way, the statistics of dust devils for HEv5hr could be improved. All in all, three vortices occur with a maximum core pressure drop of more than 250 Pa, with the strongest vortex having a value of 306.17 Pa, which is well in the range of observed intensities (250 to 450 Pa, Kanak, 2005, 2006; Sinclair, 1973). Note that these three vortices are the first simulated vortices as intense as observed dust devils.

4. Summary and Conclusion

The purpose of this study was to examine the effect of grid spacing, background wind, and surface heat flux heterogeneities on simulated dust devil-like vortices with the aim of simulating vortices as strong as observed in nature. Though previous studies could successfully reproduce the characteristic structure of dust devils, the core pressure drop of the simulated vortices was almost 1 order of magnitude too small (e.g., Cortese & Balachandar, 1993; Gheynani & Taylor, 2010; Ito et al., 2013; Kanak et al., 2000; Raasch & Franke, 2011).

As a first step, we analyzed the effect of the LES model resolution. Due to an increased resolution of the vortex microstructure, dust devil-like vortices are more numerous and the core pressure drop is more intense, which is in accordance with a previous study by Raasch and Franke (2011).

Another factor known to enhance vortex strength is an imposed background wind (e.g., Raasch & Franke, 2011; Sinclair, 1969). While Raasch and Franke (2011) found a background wind of 2.5 m/s to cause the largest increase in vortex strength, this study shows that the ideal wind speed concerning the averaged vortex strength seems to be higher (though the exact optimum wind speed was not determined). However, the

Table 6
Dust Devil Characteristics Derived From Simulation HEv5hr

N	$\bar{\tau}$ (s)	$\overline{v_{t, \text{mean}}}$ (m/s)	$\overline{r_{\text{mean}}}$ (m)	$\overline{ p _{\text{max}}}$ (Pa)	$\overline{ \zeta _{\text{max}}}$ (s^{-1})	$\overline{\langle u_{\text{tan}} \rangle_{\text{max}}}$ (m/s)
193	200 ± 93	3.86 ± 0.72	5.37 ± 1.66	63.02 ± 44.06	5.01 ± 1.81	5.66 ± 2.02
	729	5.63	17.40	218.93	9.78	11.28

Note. The second row represents the maximum values with respect to all 193 dust devils fulfilling equation (2).

number of detected dust devils lasting several minutes decreases drastically if a certain wind speed threshold is exceeded.

Heterogeneous surfaces, which are found in observations to increase vortex strength (Renno et al., 2004; Sinclair, 1969), were never before considered in numerical simulations of dust devils. We examined the effect of a 1-D striped heating pattern. Due to a developing secondary circulation (e.g., Avissar & Schmidt, 1998), the convective cells over the stronger heated area are more intense and compact, leading to an increase in vortex strength. Interestingly, the simulation shows that dust devils accumulate at the low-level convergence line above the stronger heated region and not at the border of surface heterogeneities as observations suggest (Renno et al., 2004; Sinclair, 1969). Since this study has only focused on heat flux heterogeneities and not on roughness heterogeneities, which might be the more significant heterogeneity in the above-mentioned observations, further investigations are necessary.

A final simulation combined all previously studied effects. The simulation featured a grid resolution of 2 m, a background wind of 5 m/s, and a surface heating heterogeneity. The combination of all features leads to a significant increase in dust devil intensity. It also leads to a maximum core pressure drop of 306 Pa, which agrees well with observed values ranging from 250 to 450 Pa. This simulation is the first to produce dust devil-like vortices with observed intensities.

However, this study should be seen as a first step toward the simulation of dust devils with observed intensity. Individual influences, especially that of heterogeneities introducing baroclinity and hence an additional source of vorticity, need to be investigated more carefully in follow-up studies. Due to the erratic occurrence of dust devils, future studies should also extend the model domain or simulation time, which have been limited in this study due to computational restrictions. In this way, the statistics on dust devils intensity can be improved, especially with respect to the strongest and therefore rarest dust devils. Also, an ensemble-based approach would improve the statistics even further. However, the general tendencies of grid spacing, background wind, and surface heat flux heterogeneities on the intensity could be shown clearly.

In the future, we want to investigate the statistics of dust devils with observed intensity in more detail. Especially, the three-dimensional structure, correlations between dust devil features, the initial generation process, and the mechanism of maintaining dust devils will be addressed by using a nesting technique, which has been recently implemented in PALM and which will allow for near-surface grid spacings of 1 m and below. Our future studies will also incorporate laboratory studies to represent atmospheric convection and hence dust devil-like structures. The barrel of Ilmenau, which is a large-scale experimental facility to investigate turbulent convection, will be an appropriate environment for these studies (e.g., du Puits et al., 2013). Such a controlled environment will allow the derivation of similar statistics as done in the simulations presented here (and which are almost impossible to derive in a real-world environment). By comparing dust devil-like structures in simulations and laboratory, we will be able to identify and to understand distinct differences and, if necessary, figure out appropriate ways to improve our simulations toward reality even further.

Acronyms

CBL	Convective boundary layer
LES	Large-eddy simulation
PALM	The Parallelized Large-Eddy Simulation Model

References

- Alekseenko, S. V., Kuibin, P. A., & Okulov, V. L. (2007). *Theory of concentrated vortices: An introduction*. Heidelberg, HD: Springer. <https://doi.org/10.1007/978-3-540-73376-8>
- Avissar, R., & Schmidt, T. (1998). An evaluation of the scale at which ground-surface heat flux patchiness affects the convective boundary layer using large-eddy simulations. *Journal of the Atmospheric Sciences*, *55*, 2666–2689. [https://doi.org/10.1175/1520-0469\(1998\)055<2666:AEOTSA>2.0.CO;2](https://doi.org/10.1175/1520-0469(1998)055<2666:AEOTSA>2.0.CO;2)
- Balme, M., & Greeley, R. (1998). Dust devils on Earth and Mars. *Reviews of Geophysics*, *44*, RG3003. <https://doi.org/10.1029/2005RG000188>
- Balme, M., Metzger, S., Towner, M., Ringrose, T., Greeley, R., & Iversen, J. (2003). Friction wind speeds in dust devils: A field study. *Geophysical Research Letters*, *30*(16), 1830. <https://doi.org/10.1029/2003GL017493>
- Bluestein, H. B., Weiss, C. C., & Pazmany, A. L. (2004). Doppler radar observations of dust devils in Texas. *Monthly Weather Review*, *44*, 209–224. [https://doi.org/10.1175/1520-0493\(2004\)132<0209:DRODD>2.0.CO;2](https://doi.org/10.1175/1520-0493(2004)132<0209:DRODD>2.0.CO;2)

Acknowledgments

This work was funded by the German Research Foundation (DFG) under Grant RA 617/31-1. All simulations were performed on the Cray XC40 and Atos system of the North-German Supercomputing Alliance (HLRN-3/4) located in Berlin and Göttingen. The LES model PALM is freely available (revision 3094, <http://palm.muk.uni-hannover.de/trac/browser/?rev=3094>). The output, which was used to generate figures and tables, is accessible via the <https://doi.org/10.25835/0095133> website. Also, the user-specific code for detecting dust devils, model steering files, and scripts for postprocessing the raw data is stored there.

- Cellier, P., Richard, G., & Robin, P. (1996). Partition of sensible heat fluxes into bare soil and the atmosphere. *Agricultural and Forest Meteorology*, *82*, 245–265. [https://doi.org/10.1016/0168-1923\(95\)02328-3](https://doi.org/10.1016/0168-1923(95)02328-3)
- Cortese, T., & Balachandar, S. (1993). Vortical nature of thermal plumes in turbulent convection. *Physics of Fluids*, *5*, 3226–3232. <https://doi.org/10.1063/1.858679>
- Deardorff, J. W. (1980). Stratocumulus-capped mixed layers derived from a three-dimensional model. *Boundary-Layer Meteorology*, *18*, 495–527. <https://doi.org/10.1007/BF00119502>
- du Puits, R., Resagk, C., & Theiss, A. (2013). Thermal boundary layers in turbulent Rayleigh-Bénard convection at aspect ratios between 1 and 9. *New Journal of Physics*, *15*, 013040. <https://doi.org/10.1088/1367-2630/15/1/013040>
- Durrant, D. R. (2010). *Numerical methods for fluid dynamics: With applications to geophysics*. New York, NY: Springer. <https://doi.org/10.1007/978-1-4419-6412-0>
- Gheymani, B. T., & Taylor, P. A. (2010). Large-eddy simulations of vertical vortex formation in the terrestrial and martian convective boundary layers. *Boundary-Layer Meteorology*, *137*, 223–235. <https://doi.org/10.1007/s11214-016-0284-x>
- Gu, Z., Qiu, J., Zhao, Y., & Li, Y. (2008). Simulation of terrestrial dust devil patterns. *Advances in Atmospheric Sciences*, *25*, 31–42. <https://doi.org/10.1007/s00376-008-0031-7>
- Hirsch, C. (2007). *Numerical computation of internal and external flows: The fundamentals of computational fluid dynamics*. Oxford, OXF: Butterworth Heinemann.
- Ito, J., Niino, H., & Nakanishi, M. (2013). Formation mechanism of dust devil-like vortices in idealized convective mixed layers. *Journal of the Atmospheric Sciences*, *70*, 1173–1186. <https://doi.org/10.1175/JAS-D-12-085.1>
- Jemmett-Smith, B. C., Marsham, J. H., Knippertz, P., & Gilkeson, C. A. (2015). Quantifying global dust devil occurrence from meteorological analyses. *Geophysical Research Letters*, *42*, 1275–1282. <https://doi.org/10.1002/2015GL063078>
- Kanak, K. M. (2005). Numerical simulation of dust devil-scale vortices. *Quarterly Journal of the Royal Meteorological Society*, *131*, 1271–1292. <https://doi.org/10.1256/qj.03.172>
- Kanak, K. M. (2006). On the numerical simulation of dust devil-like vortices in terrestrial and martian convective boundary layers. *Geophysical Research Letters*, *33*, L19S05. <https://doi.org/10.1029/2006GL026207>
- Kanak, K. M., Lilly, D. K., & Snow, J. T. (2000). The formation of vertical vortices in the convective boundary layer. *Quarterly Journal of the Royal Meteorological Society*, *126*, 2789–2810. <https://doi.org/10.1002/qj.49712656910>
- Koch, J., & Renno, N. O. (2005). The role of convective plumes and vortices on the global aerosol budget. *Geophysical Research Letters*, *32*, L18806. <https://doi.org/10.1029/2005GL023420>
- Letzel, M. O., & Raasch, S. (2003). Large eddy simulation of thermally induced oscillations in the convective boundary layer. *Journal of the Atmospheric Sciences*, *60*, 2328–2341. [https://doi.org/10.1175/1520-0469\(2003\)060<2328:LESOTI>2.0.CO;2](https://doi.org/10.1175/1520-0469(2003)060<2328:LESOTI>2.0.CO;2)
- Lorenz, R. D. (2014). Vortex encounter rates with fixed barometer stations: Comparison with visual dust devil counts and large-eddy simulations. *Journal of the Atmospheric Sciences*, *71*, 4461–4472. <https://doi.org/10.1175/JAS-D-14-0138.1>
- Lorenz, R. D. (2016). Heuristic estimation of dust devil vortex parameters and trajectories from single-station meteorological observations: Application to insight at mars. *Icarus*, *271*, 326–337. <https://doi.org/10.1016/j.icarus.2016.02.001>
- Lorenz, R. D., & Jackson, B. K. (2016). Dust devil populations and statistics. *Space Science Reviews*, *203*, 277–297. <https://doi.org/10.1007/s11214-016-0277-9>
- Maronga, B., Gryscha, M., Heinze, R., Hoffmann, F., Kanani-Sühring, F., Keck, M., et al. (2015). The Parallelized Large-Eddy Simulation Model (PALM) version 4.0 for atmospheric and oceanic flows: Model formulation, recent developments, and future perspectives. *Geoscientific Model Development*, *8*, 2515–2551. <https://doi.org/10.5194/gmd-8-2515-2015>
- Metzger, S. M., Balme, M. R., Towner, M. C., Bos, B. J., Ringrose, T. J., & Patel, M. R. (2011). In situ measurements of particle load and transport in dust devils. *Icarus*, *214*, 766–772. <https://doi.org/10.1016/j.icarus.2011.03.013>
- Moeng, C.-H., & Wyngaard, J. C. (1988). Spectral analysis of large-eddy simulations of the convective boundary layer. *Journal of the Atmospheric Sciences*, *45*, 3573–3587. [https://doi.org/10.1175/1520-0469\(1988\)045<3573:SAOLES>2.0.CO;2](https://doi.org/10.1175/1520-0469(1988)045<3573:SAOLES>2.0.CO;2)
- Nishizawa, S., Oda, M., Takahashi, Y. O., Sugiyama, K., Nakajima, K., Ishiwatari, M., et al. (2016). Martian dust devil statistics from high-resolution large-eddy simulations. *Geophysical Research Letters*, *43*, 4180–4188. <https://doi.org/10.1002/2016GL068896>
- Ohno, H., & Takemi, T. (2010). Mechanisms for intensification and maintenance of numerically simulated dust devils. *Atmospheric Science Letters*, *11*, 27–32. <https://doi.org/10.1002/asl.249>
- Parlow, E. (2003). The urban heat budget derived from satellite data. *Geographica Helvetica*, *58*, 99–111.
- Patrinos, A. A. N., & Kistler, A. L. (1977). A numerical study of the Chicago lake breeze. *Boundary-Layer Meteorology*, *12*, 93–123. <https://doi.org/10.1007/BF00116400>
- Piacsek, S. A., & Williams, G. P. (1970). Conservation properties of convection difference schemes. *Journal of Computational Physics*, *6*, 392–405. [https://doi.org/10.1016/0021-9991\(70\)90038-0](https://doi.org/10.1016/0021-9991(70)90038-0)
- Raasch, S., & Franke, T. (2011). Structure and formation of dust devil-like vortices in the atmospheric boundary layer: A high-resolution numerical study. *Journal of Geophysical Research*, *116*, D16120. <https://doi.org/10.1029/2011JD016010>
- Rafkin, S., Jemmett-Smith, B., Fenton, L., Lorenz, R., Takemi, T., Ito, J., & Tyler, D. (2016). Dust devil formation. *Space Science Reviews*, *203*, 183–207. <https://doi.org/10.1007/s11214-016-0307-7>
- Renno, N. O., Abreu, V. J., & Koch, J. (2004). Matador 2002: A pilot field experiment on convective plumes and dust devils. *Journal of Geophysical Research*, *109*, E07001. <https://doi.org/10.1029/2003JE002219>
- Renno, N. O., Burkett, M. L., & Larkin, M. P. (1998). A simple thermo-dynamical theory for dust devils. *Journal of the Atmospheric Sciences*, *55*, 3244–3252. [https://doi.org/10.1175/1520-0469\(1998\)055<3244:ASTTFD>2.0.CO;2](https://doi.org/10.1175/1520-0469(1998)055<3244:ASTTFD>2.0.CO;2)
- Renno, N. O., & Ingersoll, A. P. (1996). Natural convection as a heat engine: A theory for CAPE. *Journal of the Atmospheric Sciences*, *53*, 572–585. [https://doi.org/10.1175/1520-0469\(1996\)053<0572:NCAAHE>2.0.CO;2](https://doi.org/10.1175/1520-0469(1996)053<0572:NCAAHE>2.0.CO;2)
- Renno, N. O., Nash, A. A., Lunine, J., & Murphy, J. (2000). Martian and terrestrial dust devils: Test of a scaling theory using pathfinder data. *Journal of Geophysical Research*, *105*, 1859–1865. <https://doi.org/10.1029/1999JE001037>
- Sagaut, P. (2006). *Large eddy simulation for incompressible flows: An introduction*. Berlin, BE: Springer. <https://doi.org/10.1007/b137536>
- Saiki, E. M., Moeng, C.-H., & Sullivan, P. P. (2000). Large-eddy simulation of the stably stratified planetary boundary layer. *Boundary-Layer Meteorology*, *95*, 1–30. <https://doi.org/10.1023/A:1002428223156>
- Schmidt, H., & Schumann, U. (1989). Coherent structure of the convective boundary layer derived from large-eddy simulations. *Journal of Fluid Mechanics*, *200*, 511–562. <https://doi.org/10.1017/S0022112089000753>
- Shao, Y., Wyrwoll, K.-H., Chappell, A., Huang, J., Lin, Z., McTainsh, G. H., et al. (2011). Dust cycle: An emerging core theme in Earth system science. *Aeolian Research*, *2*, 181–204. <https://doi.org/10.1016/j.aeolia.2011.02.001>
- Shen, S., & Leclerc, M. Y. (1995). How large must surface inhomogeneities be before they influence the convective boundary layer structure? A case study. *Quarterly Journal of the Royal Meteorological Society*, *121*, 1209–1228. <https://doi.org/10.1002/qj.49712152603>



- Sinclair, P. C. (1969). General characteristics of dust devils. *Journal of Applied Meteorology and Climatology*, *8*, 32–45. [https://doi.org/10.1175/1520-0450\(1969\)008<0032:GCODD>2.0.CO;2](https://doi.org/10.1175/1520-0450(1969)008<0032:GCODD>2.0.CO;2)
- Sinclair, P. C. (1973). The lower structure of dust devils. *Journal of the Atmospheric Sciences*, *30*, 1599–1619. [https://doi.org/10.1175/1520-0469\(1973\)030<1599:TLSODD>2.0.CO;2](https://doi.org/10.1175/1520-0469(1973)030<1599:TLSODD>2.0.CO;2)
- Tratt, D. M., Hecht, M. H., Catling, D. C., Samulon, E. C., & Smith, P. H. (2003). In situ measurement of dust devil dynamics: Toward a strategy for Mars. *Journal of Geophysical Research*, *108*(E11), 5116. <https://doi.org/10.1029/2003JE002161>
- Wicker, L. J., & Skamarock, W. C. (2002). Time-splitting methods for elastic models using forward time schemes. *Monthly Weather Review*, *130*, 2088–2097. [https://doi.org/10.1175/1520-0493\(2002\)130<2088:TSMFEM>2.0.CO;2](https://doi.org/10.1175/1520-0493(2002)130<2088:TSMFEM>2.0.CO;2)
- Williamson, J. H. (1980). Low-storage Runge-Kutta schemes. *Journal of Computational Physics*, *35*, 48–56. [https://doi.org/10.1016/0021-9991\(80\)90033-9](https://doi.org/10.1016/0021-9991(80)90033-9)

Chapter 4

Evolution and Features of Dust Devil-Like Vortices in Turbulent Rayleigh-Bénard Convection - A Numerical Study Using Direct Numerical Simulation

4.1 Declaration of Contributions

The author contributions are given on the left at the first page of the research article.

4.2 Research Article

Giersch, S. and Raasch, S.: Evolution and Features of Dust Devil-Like Vortices in Turbulent Rayleigh-Bénard Convection — A Numerical Study Using Direct Numerical Simulation, *J. Geophys. Res. Atmos.*, **126**, e2020JD034 334, doi:10.1029/2020JD034334, 2021.

©2021. The Authors. CC BY 4.0 License.

Evolution and Features of Dust Devil-Like Vortices in Turbulent Rayleigh-Bénard Convection—A Numerical Study Using Direct Numerical Simulation

S. Giersch¹  and S. Raasch¹ 

¹Institute of Meteorology and Climatology, Leibniz University Hannover, Hannover, Germany

Key Points:

- First direct numerical simulations of dust devil-like structures for Rayleigh numbers up to 10^{11} are presented
- Dust devils are strongly affected by Rayleigh number and surface friction but less affected by the aspect ratio of the model domain
- The 3-D structure of simulated dust devils is very similar to the one in large-eddy simulations of the atmospheric boundary layer

Correspondence to:

S. Giersch,
giersch@muk.uni-hannover.de

Citation:

Giersch, S., & Raasch, S. (2021). Evolution and features of dust devil-like vortices in turbulent Rayleigh-Bénard convection—A numerical study using direct numerical simulation. *Journal of Geophysical Research: Atmospheres*, 126, e2020JD034334. <https://doi.org/10.1029/2020JD034334>

Received 30 NOV 2020

Accepted 8 MAR 2021

Author Contributions:

Conceptualization: S. Giersch, S. Raasch
Data curation: S. Giersch
Formal analysis: S. Giersch
Funding acquisition: S. Raasch
Investigation: S. Giersch
Methodology: S. Giersch, S. Raasch
Project Administration: S. Giersch, S. Raasch
Resources: S. Raasch
Software: S. Giersch, S. Raasch
Supervision: S. Raasch
Validation: S. Giersch
Visualization: S. Giersch
Writing – original draft: S. Giersch
Writing – review & editing: S. Giersch, S. Raasch

© 2021. The Authors.

This is an open access article under the terms of the [Creative Commons Attribution License](https://creativecommons.org/licenses/by/4.0/), which permits use, distribution and reproduction in any medium, provided the original work is properly cited.

Abstract Dust devils are convective vortices with a vertical axis of rotation that are made visible by entrained soil particles. These soil particles contribute to the atmospheric aerosol input, influencing the Earth radiation budget. Quantifying this contribution requires reliable information about the statistics of dust devils, their formation process, and how they are maintained. In the past, this information was mainly derived from field experiments and large-eddy simulations (LESs). Field experiments suffer from the erratic occurrence of dust devils and the limited area that can be monitored reliably. In LESs, dust devils cannot be resolved completely, especially close to the ground. Additionally, they are affected by numerical features of surface boundary conditions, as well as subgrid-scale models in an unknown way. To mitigate these limitations, we employ direct numerical simulations (DNSs) to improve our understanding of dust devils. We comprehensively investigate the statistics and structure of dust devils for Rayleigh numbers up to 10^{11} using DNS of Rayleigh-Bénard convection between two plates for the first time. We find that dust devil-like structures occur in DNS with Rayleigh numbers much lower than in the atmosphere ($\geq 10^7$). These results support previous DNS studies in which vortices with vertical axes were observed but not further investigated. The dust devil statistics strongly depend on the Rayleigh number and velocity boundary conditions, but depend little on the aspect ratio of the model domain. Simulated dust devils show very similar properties to convective vortices analyzed in LESs of the atmospheric boundary layer.

1. Introduction

1.1. Motivation

Dust devils, also known as whirlwinds or willy willies, are organized, convective vortices with a vertically aligned axis of rotation. They occur on Earth (e.g., Bluestein et al., 2004; Sinclair, 1969) and Mars (e.g., Ellehoj et al., 2010; Kahanpää et al., 2016), and are made visible by soil particles (e.g., dust) that are swirled up from the ground. This makes dust devils not only a dynamically and optically interesting phenomenon (e.g., Kurgansky et al., 2016), but also a possible hazard to light aircraft (e.g., R. D. Lorenz & Myers, 2005) or future Mars explorations (e.g., Balme & Greeley, 2006). In addition, they significantly increase the aerosol transport from the surface to the atmosphere on a regional (e.g., Gillette & Sinclair, 1990; Han et al., 2016; Ito et al., 2010; Renno et al., 2004) and global scale (e.g., Jemmett-Smith et al., 2015; Koch & Renno, 2005). Therefore, dust devils need to be considered in Earth's energy, carbon, and water cycle (Shao et al., 2011). However, quantitative estimates of the dust devils contribution to the overall amount of aerosols in the atmosphere are subject to great uncertainties (e.g., Han et al., 2016; Jemmett-Smith et al., 2015; Koch & Renno, 2005). To improve existing estimates, detailed statistical information on, i.e., the frequency of occurrence, strength, and dust fluxes of convective vortices is required. This demand has led to extensive research on dust devil-like structures through laboratory experiments (e.g., Greeley et al., 2003; Neakrase & Greeley, 2010), measurement campaigns (e.g., Murphy et al., 2016; Renno et al., 2004), and numerical investigations using large-eddy simulation (LES; e.g., Giersch et al., 2019; Kanak, 2005). Laboratory experiments have the disadvantage of being conducted in an artificial environment. This constraint limits the realism of the experiments. Alternatively, measurement campaigns are limited by the sporadic nature of dust devils that can be captured only in confined monitoring areas. Numerical simulations of dust devils have been performed over the past 20 years mainly due to a large increase in computing power (Spiga et al., 2016). However, numerical simulations via LES, from which the derivation of statistics would be straightforward,

are still unable to completely resolve the near-surface region, that is, the region most critical to the dust devil induced fluxes of heat and aerosols. Our study aims to extend the knowledge of dust devils by evading the previously mentioned disadvantages of experiments, measurements, and LES using direct numerical simulation (DNS) of Rayleigh-Bénard convection (RBC), an approach that has never been used before for a comprehensive study on dust devil-like structures.

So far, most numerical investigations of dust devils have been carried out employing LES, allowing simulations of convective vortices in the atmospheric boundary layer with a resolution down to a few meters (e.g., Giersch et al., 2019; Kanak, 2005; Ohno & Takemi, 2010; Raasch & Franke, 2011). However, LES requires the parameterization of unresolved sub-grid scale (SGS) processes. These are realized by SGS models that try to describe the influence of any turbulent process in the range of, or smaller than, the grid spacing on the resolved flow. The SGS models, as an inherent part of LES models, introduce errors, especially in those areas where small-scale mixing plays a crucial role (e.g., Sorbjan, 1996; Sullivan et al., 1994). The surface layer is a typical example of such an area (Spiga et al., 2016). Dust-devil like structures are located in the surface layer and might be influenced by the SGS model that is used. Although Kanak (2005) does not believe that the choice of the SGS closure scheme would make a difference between the existence or nonexistence of vertical vortices in LES simulations, an influence on dust devil quantities cannot be excluded. In addition to the parameterization of turbulent diffusion through the SGS model, the surface layer requires careful and realistic treatment of model surface stresses and surface heat fluxes. Typically, this is realized by using bulk parameterizations (e.g., Kanak, 2005; Ohno & Takemi, 2010) or Monin-Obukhov similarity theory, which implies the assumption of a constant flux layer between the surface and the first grid level (e.g., Giersch et al., 2019; Raasch & Franke, 2011). A quantification of the uncertainties of dust devil statistics caused by parameterizations is still missing. LES grid convergence studies down to grid spacing of less than 1 m would overcome this shortcoming, but a too high demand on computational resources has been prohibited such studies so far. In DNS, however, neither the parameterization of SGS processes nor the parameterization of surface stresses and heat fluxes are required. Therefore, no parameterization uncertainties must be considered. This study will compare DNS results of dust devil-like vortices with LES results, to illuminate potential effects of parameterizations used in LES on the dust devil structure.

Although DNS is an appropriate tool for studying dust devil-like vortices, only a few publications exist that show first steps toward a comprehensive investigation of their structure and statistics. Cortese and Balachandar (1993) recognized strong vertical vorticity in thermal plumes, resulting in spiraling hot updrafts and cold downdrafts. Fiedler and Kanak (2001) investigated intense columnar vortices in RBC. They discovered similarities between dust devils investigated with DNS and LES. However, both studies lack statistics and quantitative features of dust devils in DNS simulations. In addition, Cortese and Balachandar (1993) and Fiedler and Kanak (2001) only considered free-slip boundary conditions for Rayleigh numbers up to 10^7 . Therefore, their investigations did not allow for frictionally induced flow convergence toward the vortex center. Iijima and Tamura (2008) investigated the formation process and the physical mechanism of strong vertical vortices in convection with and without applying external forces. These forces caused artificial, anticlockwise rotation in the flow field and an upward flow component with the aim to strengthen the naturally developing vertical vortices in their simulations by vorticity concentration and vortex stretching. Still, also Iijima and Tamura (2008) did not provide any detailed statistical, structural, or quantitative features of vertical vortices that develop in natural convection. Consequently, our DNS study aims to allow a free, frictionally influenced development of vortices, by convection alone, for Rayleigh numbers up to 10^{11} to mimic the planetary boundary layer as much as possible.

Even if no-slip boundary conditions better represent a realistic environment under which dust devils develop, a simulation with free-slip conditions will also be carried out to analyze and quantify the effect of surface friction on dust devil statistics. The strong and nontrivial effects of surface friction on vertical vortices has been already investigated in other studies. For example, Gu et al. (2010) simulated dust devils with the help of initial tangential velocity and found that surface friction significantly affects the near-surface shape of dust devils. The laboratory-like simulations from Neakrase and Greeley (2010), focusing on the sediment transport of dust devils, showed that vortex size increases and tangential velocity decreases as surface roughness is increased. In addition, they found that a small increase in surface roughness enables reduced threshold velocities to lift fine particles from the surface. Also, LES studies of the atmospheric,

convective boundary layer show significant effects of near-surface, frictionally induced horizontal vorticity on dust devil development (e.g., Giersch et al., 2019; Kanak et al., 2000; Raasch & Franke, 2011). Ito and Niino (2013) claim that effects of surface friction are not essential for the formation of dust devil-like vortices and that absolute values of vertical vorticity and the overall convection pattern are similar between simulations with and without surface friction. Thus, the consequences of applying free-slip boundary conditions on dust devil statistics will be clarified in this study.

Flow properties and structures in RBC are strongly influenced by the Rayleigh number $Ra = \alpha g \Delta \theta H^3 / (\nu \kappa)$, as well as the aspect ratio $\Gamma = L/H$ (e.g., Bailon-Cuba et al., 2010; Pandey et al., 2018; Stevens et al., 2018). Here, α is the thermal expansion coefficient, g the gravitational acceleration, $\Delta \theta$ the potential temperature difference between the lower and upper plate, H the distance between the plates, ν the kinematic viscosity, κ the thermal diffusivity, and L the lateral extent of the model domain. Bailon-Cuba et al. (2010) found that large-scale patterns in time-averaged flow fields change from a one-roll to a two-roll flow pattern at around $\Gamma = 2.5$ for Rayleigh numbers 10^7 and 10^8 . However, they have also shown that the exact aspect ratio needed for getting a multi-roll system depends on the Rayleigh number and that there is a reorganization of flow from the roll shape to pentagonal or hexagonal structures with increasing Γ (up to 12) for a fixed Ra . This is true for a fixed Γ with increasing Ra (up to 10^8), as well. Consistent with these structural changes in flow patterns, flow statistics in RBC are strongly modified by the Rayleigh number and aspect ratio. Stevens et al. (2018) concluded from their investigations of thermal superstructures that integral quantities such as the Nusselt number converge for $\Gamma = 4$. Reaching a convergence of the peak location of the temperature variance and turbulent kinetic energy (TKE) spectra requires an astonishing aspect ratio of 64. The previously cited findings make it very likely that dust devil evolution depends on Rayleigh number and/or aspect ratio, because the existence of vertical vortices appears to be tied to specific flow patterns (Kanak, 2006). To study this, Ra and Γ will be varied between 10^6 and 10^{11} and 2 to 4, respectively.

This study will offer an overview of the effects of surface friction, Rayleigh number, and aspect ratio on dust devil statistics, providing the first comprehensive DNS investigation of dust devil-like structures. The study is organized as follows. The applied simulation setups and analysis methods are described in Section 2. The results are presented in Section 3. A summary and conclusions are given in Section 4. The appendix details validation results of the DNS mode of the numerical model used in this study. In addition, further information on resolution requirements and a grid resolution study are presented.

1.2. Dust Devil Formation and Maintenance

This subsection will briefly summarize the vortex formation and maintenance hypothesis established by Raasch and Franke (2011) because it will be frequently used in the following discussion. The budget equation for the vertical vorticity reads (see also Raasch & Franke 2011):

$$\frac{\partial \zeta}{\partial t} = -(\bar{v}_h \cdot \bar{\nabla}_h) \zeta - w \frac{\partial \zeta}{\partial z} - \underbrace{\zeta (\bar{\nabla}_h \cdot \bar{v}_h)}_{\zeta_{\text{div}}} - \underbrace{\left(\frac{\partial w}{\partial x} \frac{\partial v}{\partial z} + \frac{\partial w}{\partial y} \frac{\partial u}{\partial z} \right)}_{\zeta_{\text{twi}}} + \nu \nabla^2 \zeta, \quad (1)$$

where \bar{v}_h represents the horizontal velocity vector and $\bar{\nabla}_h$ is the nabla operator in the horizontal direction. The Coriolis and solenoidal terms have been neglected here. The Coriolis force is not considered in the simulated DNS setups at all and the solenoidal term, which describes the generation of vertical vorticity by baroclinic processes, does not exist under the Boussinesq-Approximation used in this study (see Section 2). Equation 1 indicates that vertical vorticity can be modified by the so-called twisting term, ζ_{twi} , which describes the transformation of horizontal vorticity into the vertical direction. It is the only term in the above equation that can generate vertical vorticity from a flow that did not previously rotate around the vertical axes. The remaining terms are only able to rearrange existing vertical vorticity by advection, increasing/decreasing it by convergence/divergence of the horizontal velocity field, ζ_{div} , or equalizing it by molecular diffusion. A detailed analysis of the budget equation by Raasch and Franke (2011) indicates that the rotation of a dust devil is maintained by a combination of convergence and twisting effects. The convergence

effect is caused by the strong updraft that is located above a dust devil. The updraft provokes near-surface flow convergence, which further concentrates vorticity in the vortex core. This process is represented in the vorticity budget equation by ζ_{div} . Additionally, horizontal vorticity created by the vertical shear near the surface is converted to vertical vorticity as soon as the flow enters the updraft region around the vortex core. This is described in Equation 1 by ζ_{twi} . Some values for the twisting, divergence and advection terms are stated in Section 3.5.

The budget equation for the vertical vorticity from above can be used to describe how the vortex maintains its vertical vorticity. But because the equation already assumes an initially rotating flow, it does not explain where and why vortices form at all (see also, Raasch & Franke, 2011; S. Rafkin et al., 2016). It is already known that dust devils occur mainly at the vertices of the hexagonal cells that develop in the convective boundary layer (e.g., Giersch et al., 2019; Kanak, 2005; Raasch & Franke, 2011). Raasch and Franke (2011) argue that the initial vertical vorticity at these vertices is created by chance in the following way: the flow converges at the cell vertices due to high vertical wind velocities occurring there. Normally, this happens in a nonuniform way with velocity components of different strength pointing toward the convergence lines, which are located around the vertex and are merging in its center. By chance, the flow might have a structure where the overall vertical vorticity of the flow around the vertex is nonzero (see Figure 15a in Raasch & Franke, 2011). This initial vorticity is then further concentrated by the general flow convergence and a vortex is created.

2. Methodology

In the following, a dust devil is defined as a convective vortex exceeding certain core pressure drop and vertical vorticity thresholds (see Section 2.2). Furthermore, (convective) vortex, dust devil, and dust devil-like vortex are used as synonyms.

All numerical simulations are carried out with the PALM model system (Maronga et al., 2020), which has been specifically designed for LES studies of the atmospheric boundary layer (e.g., El Guernaoui et al., 2019; Heinze et al., 2012; Maronga & Raasch, 2013). In this study, however, PALM will be used in DNS mode, in which every turbulent fluctuation is resolved. This is possible by using PALM's default system of equations as mentioned in Maronga et al. (2015) and assuming constant diffusivities equal to the molecular values of the fluid. The nonhydrostatic and nonfiltered incompressible system of equations in Boussinesq-approximated form are then:

$$\frac{\partial u_i}{\partial t} = -\frac{\partial u_i u_j}{\partial x_j} - \frac{1}{\rho_0} \frac{\partial p^*}{\partial x_i} + g \frac{\theta - \langle \theta \rangle}{\langle \theta \rangle} \delta_{i3} + \nu \frac{\partial^2 u_i}{\partial x_j^2}, \quad (2)$$

$$\frac{\partial u_j}{\partial x_j} = 0, \quad (3)$$

$$\frac{\partial \theta}{\partial t} = -\frac{\partial u_j \theta}{\partial x_j} + \kappa \frac{\partial^2 \theta}{\partial x_j^2}. \quad (4)$$

Equations 2–4 describe the conservation of momentum, mass, and thermal internal energy, respectively. Here, $i, j \in \{1, 2, 3\}$. u_i are the velocity components along x , y , and z . t is the time, and ρ is the density of dry air. p^* represents the perturbation pressure, $g = 9.81 \text{ m s}^{-2}$ is the gravitational acceleration, and δ is the Kronecker delta. Finally, $\langle \cdot \rangle$ indicates a horizontally averaged value at a fixed height and a subscript zero denotes a surface value. No Coriolis or large-scale pressure gradient forces are considered here. Neither of these forces affect the fluid in classical RBC.

Time integration of the above set of equations is realized by using a third-order Runge-Kutta scheme (Williamson, 1980). The advection terms are approximated by a fifth-order scheme from Wicker and

Skamarock (2002), which well conserves strong gradients that frequently occur in dust devils, covering only a couple of grid points (e.g., Giersch et al., 2019). To guarantee the incompressibility condition (3), a predictor-corrector method is used (e.g., Patrinos & Kistler, 1977), in which a Poisson equation for p^* is solved after every time step. As done in similar studies of dust devils with horizontally homogeneous setups, the absolute value of p^* is interpreted as the pressure drop within dust devils (e.g., Giersch et al., 2019; Kanak, 2005; Raasch & Franke, 2011). Here, PALM's DNS mode is used for the first time. Therefore, a validation of the DNS mode was carried out. A short summary of the validation is provided in Appendix A.

2.1. Numerical Setups

This subsection will give an overview of the simulations that have been conducted to study dust devil-like structures in RBC between two flat plates. The selected simulation parameters shall enable a comparison with laboratory experiments (e.g., du Puits et al., 2007). In all cases, air is considered at 1013.25 hPa with a domain-averaged temperature of $\theta_{\text{ref}} = 303.15$ K. With these pressure and temperature values, the constant fluid properties ν and α are set to $1.598 \times 10^{-5} \text{ m}^2 \text{ s}^{-1}$ and $3.32 \times 10^{-3} \text{ K}^{-1}$, respectively. α is only specified here to allow the recalculation of the Rayleigh number. For solving the model equations, the exact value of the thermal expansion coefficient is irrelevant. A Prandtl number $Pr = \nu/\kappa = 0.7$ is assumed.

At the impermeable plates, no-slip boundary conditions ($u = v = 0$) are applied in most of the cases. Only once, free-slip conditions ($\partial u/\partial z|_{\text{wall}} = \partial v/\partial z|_{\text{wall}} = 0$) are assumed to study the effects of friction on the vortices. Additionally, a Neumann condition for the perturbation pressure is set at the bottom and top boundary ($\partial p^*/\partial z|_{\text{wall}} = 0$). The forcing of convection is realized by applying a fixed temperature difference $\Delta\theta = \theta_1 - \theta_2$ of 40 K between the lower ($\theta_1 = 323.15$ K) and upper plate ($\theta_2 = 283.15$ K). These temperature values allow a direct comparison with experimental results, for example, derived from the Barrel of Ilmenau (e.g., du Puits et al., 2007, 2013). Such a comparison is already planned for the near future (see also Section 4). The temperature difference of 40 K might question the application of the Boussinesq-approximation. However, according to Bazdidi-Tehrani et al. (2018), Gray and Giorgini (1976), and Niemela and Sreenivasan (2003) the approximation is applicable here and uncertainties due to nonBoussinesq effects are limited to several percent. In the horizontal directions, cyclic boundary conditions are used.

The domain size is quadratic horizontally and characterized by the variable height ($0.066 \text{ m} \leq H \leq 3.036 \text{ m}$) or Rayleigh number ($10^6 \leq Ra \leq 10^{11}$) and the aspect ratio ($2 \leq \Gamma \leq 4$). Because dust devil-like structures have been found to be connected to the cellular pattern that develops within the convective, atmospheric boundary layer (e.g., Giersch et al., 2019; Kanak, 2006; Kanak et al., 2000; Raasch & Franke, 2011), a sufficiently large aspect ratio is required to allow for the development of these hexagonal cells. In LESs of the atmospheric boundary layer, a ratio of three between the horizontal model extent and the height of the mixed layer is sufficient (e.g., Kanak et al., 2000). However, DNS of RBC shows that stationary hexagonal cell structures would require aspect ratios of 12 or more (e.g., Bailon-Cuba et al., 2010; von Hardenberg et al., 2008), which is not feasible with the Rayleigh numbers under study and present-day computing power. As a compromise between domain size and computing costs, a ratio of three is selected for most of the simulations. Consequently, the hexagonal cells that appear are nonstationary. They grow in time before they finally approach the domain size (see Section 3). Nevertheless, an aspect ratio of three allows for the calculation of sufficient dust devil statistics. For Rayleigh numbers of up to 10^8 , DNSs with 1 mm grid spacing are carried out. In case of higher Rayleigh numbers, the grid spacing is uniformly set to 2 mm, as a compromise between resolution and computing costs. Two millimeter grid spacing is still fine enough to adequately simulate the bulk of the flow (see Appendix B for a grid resolution study). The simulated time is restricted to 100 s. This is another compromise between computational costs and providing sufficient statistics of dust devils, which heavily depend on domain size and simulated time.

At initialization, zero velocities are assumed everywhere and their mean values remain zero for all times. The initial condition for the potential temperature at every x, y position is defined as in Mellado (2012) through

$$\theta(z) = \begin{cases} \theta_{\text{ref}} + (\theta_1 - \theta_{\text{ref}}) \left[1 - \operatorname{erf} \left(\frac{\sqrt{\pi} z}{2\delta_t} \right) \right] & \text{for } \frac{z}{H} \leq 0.5, \\ \theta_{\text{ref}} + (\theta_2 - \theta_{\text{ref}}) \left[1 - \operatorname{erf} \left(\frac{\sqrt{\pi} (H - z)}{2\delta_t} \right) \right] & \text{for } \frac{z}{H} > 0.5, \end{cases} \quad (5)$$

where $\delta_t = 11\Delta z$ is the thickness of the initial temperature profile with Δz being the vertical grid spacing (see Figure 2 for initial potential temperature profile). In addition to the unstably stratified fluid, random perturbations are necessary to trigger the onset of convection. These perturbations are imposed on the horizontal velocity field at the beginning of the simulation.

Table 1 summarizes all conducted simulations together with the varied parameters: domain size, number of grid points, grid spacing, velocity boundary condition, Rayleigh number, and aspect ratio. Each simulation is accompanied by an identifier (ID), which will be used as a reference henceforth. Each ID consists of the Rayleigh number (“RA”) and the aspect ratio (“A”). The simulation with free-slip boundary conditions at the plates is marked with an asterisk.

2.2. Vortex Detection and Analysis

The vortex detection and analysis algorithm explained in Raasch and Franke (2011) and Giersch et al. (2019) is used for determining the averaged features of dust devil-like vortices. This subsection will mention the points of the algorithm that are relevant for the discussions in this study. Also changes and additions to Raasch and Franke (2011) and Giersch et al. (2019) will be noted.

The vortex center detection is realized during a run after each model time step by identifying local minima of the perturbation pressure drop and local maxima of the absolute value of the vertical vorticity, which corresponds to the vertical component of rotation of the velocity field

$$|\zeta| = \left| \frac{\partial v}{\partial x} - \frac{\partial u}{\partial y} \right|. \quad (6)$$

Here, the derivatives are approximated by difference quotients over one grid spacing. These difference quotients are subsequently interpolated onto the scalar grid point. PALM uses a staggered grid. Therefore, the horizontal velocity components are defined at the grid volume edges, whereas all scalars are defined at the center. Furthermore, the horizontal velocity components and scalars are vertically shifted by half the grid spacing compared to the vertical component and the first grid point above the surface is defined at $\Delta z/2$. The detection procedure is only executed at the first grid plane above the bottom surface, that is, at 0.5 mm for RA1006A3, RA1007A3, RA1008A3 and at 1 mm for all other simulations in Table 1. Due to the symmetry of the studied setups, vertical vortices also occur at the upper plate, which are neglected for technical reasons (The detection and analysis algorithm was originally designed for atmospheric vortices that are bounded at the lower surface). Even if they would be considered, it is not expected that they would improve the vortex statistics because structures at the bottom and top plate are strongly correlated.

In order to consider a local pressure minimum and vorticity maximum as a dust devil-like vortex, thresholds must be defined. Whenever the defined thresholds are exceeded, the information related to the vortex (e.g., the position) is recorded. As explained in Giersch et al. (2019), 5 times the standard deviation of vorticity and 3 times the standard deviation of perturbation pressure are defined as the thresholds. The standard deviation is calculated as a mean value derived from 8 instantaneous horizontal cross sections taken from the analysis height between 30 and 100 s simulated time (every 10 s). For each cross section, a single standard deviation is calculated. Subsequently, an arithmetic mean is determined and used to compute the thresholds. The first 30 s of the simulations are not taken into account for dust devil detection and analysis because of the model spin-up phase (see Section 3.1). Because standard deviations vary strongly with Rayleigh number, simulations with different Rayleigh number causes different detection thresholds. Table 2 displays the threshold values used for each simulation. For example, a dust devil-like vortex is identified only if $|p^*| > 40$ mPa and $|\zeta| > 13$ s⁻¹ for simulation RA1009A3. Note, each simulation in Table 1 is executed at least

Table 1
 Main Characteristics of the Conducted Simulations^a

Simulation ID	Domain size $L_x \times L_y \times L_z$ (m ³)	Number of grid points	Grid spacing (mm) ^b	Velocity boundary condition	Ra	Γ
RA1006A3	0.198 × 0.198 × 0.066	198 × 198 × 66	1 (1.69)	No-slip	10 ⁶	3
RA1007A3	0.420 × 0.420 × 0.140	420 × 420 × 140	1 (1.31)	No-slip	10 ⁷	3
RA1008A3	0.912 × 0.912 × 0.304	912 × 912 × 304	1 (1.05)	No-slip	10 ⁸	3
RA1009A3	1.968 × 1.968 × 0.656	984 × 984 × 328	2 (0.83)	No-slip	10 ⁹	3
RA1009A3*	1.968 × 1.968 × 0.656	984 × 984 × 328	2 (0.83)	Free-slip	10 ⁹	3
RA1010A2	2.816 × 2.816 × 1.408	1,408 × 1,408 × 704	2 (0.65)	No-slip	10 ¹⁰	2
RA1010A3	4.224 × 4.224 × 1.408	2,112 × 2,112 × 704	2 (0.65)	No-slip	10 ¹⁰	3
RA1010A4	5.632 × 5.632 × 1.408	2,816 × 2,816 × 704	2 (0.65)	No-slip	10 ¹⁰	4
RA1011A3	9.108 × 9.108 × 3.036	4,554 × 4,554 × 1,518	2 (0.52)	No-slip	10 ¹¹	3

DNS in the near-wall region (see Appendix B).

^aThe simulations conducted for the grid resolution study (see Appendix C) are not listed. ^bThe values in brackets show the actually required grid widths for guaranteeing a perfectly resolved DNS in the near-wall region (see Appendix B).

twice, once for determining the correct standard deviations and once for detecting dust devil-like vortices based on the correct thresholds. An exception is RA1011A3. Here, two simulations are computationally too expensive and the thresholds are estimated instead (see remark b in Table 2).

In a post processing step, dust devil centers are combined to vortex tracks with the following procedure:

1. A dust devil center at the current time step is compared to all detected centers within the next three consecutive model time steps
2. Two vortex centers are connected if after a maximum of three time steps the position of the second center is not more than two grid points away from the first one
3. An additional criterion for connecting centers that might belong to the same track is that the vorticities must have the same sense of rotation at all-time steps of the track
4. Because neighboring centers can belong to the same vortex, some of them are ignored before track analysis. As soon as a center is within the radius of another (sub)vortex at the current time step, the weaker center (rated by the vorticity) is disregarded

Point 4 requires the vortex radius to be known. As in Giersch et al. (2019) and Raasch and Franke (2011), the vortex radius is determined from the tangentially averaged pressure drop distribution around each center. It is defined as the distance at which the absolute pressure drop is reduced to 50% of the core pressure. For further details on dust devil track analysis, the reader is referred to Giersch et al. (2019).

The radius of a vortex might be underestimated due to technical restrictions. The horizontal domain decomposition implemented for parallelization implies that each processor core has principal access to only

Table 2
 Detection Thresholds and Lifetime Limits for the Simulations Mentioned in 1^{a,b}

	RA1006A3	RA1007A3	RA1008A3	RA1009A3	RA1010A3	RA1011A3 ^c
$ p^* $ (mPa)	10	16	23	40	70	100
$ \zeta $ (s ⁻¹)	3	4	4.5	13	18	25
	RA1009A3	RA1009A3*	RA1010A2	RA1010A3	RA1010A4	RA1011A3
$\tau_{N_{\max}}$	0.3	0.27	0.24	0.2	0.25	0.14

^aThe thresholds for RA1010A2 and RA1010A4 are the same as for RA1010A3 and the thresholds for RA1009A3* are the same as for RA1009A3. ^bRemarks on the lifetime limits are given at the end of this subsection. ^cThe listed thresholds are estimated values based on the simulations with lower Rayleigh numbers.

grid point data of a subdomain of the total domain. In order to calculate the radius for cases where the vortex center is situated near subdomain boundaries, data of directly adjacent subdomains are required, and are fetched from the respective neighboring cores before calculation. Due to technical restrictions (memory requirements and long data transfer times), data from nonadjacent subdomains are not considered. This means that vortices larger than the subdomain size might not be detected correctly. Increasing the subdomain size to be able to capture dust devils of any size is not a solution, because it would significantly increase the wallclock time of the simulations and would cause the core memory limit to be exceeded. As a compromise, subdomains with 24 grid points along x and y are used so that vortices that extend over more than this distance might not be correctly captured. This problem is referred to as the “radius restriction.”

Similar to previous dust devil studies (e.g., Giersch et al., 2019; Raasch & Franke, 2011), the statistical focus is on the dust devil maximum values regarding the absolute pressure drop $|p^*|_{\max}$ and vertical vorticity $|\zeta|_{\max}$ at the center, as well as the tangentially averaged horizontal $\{u_h\}_{\max}$, vertical $\{w\}_{\max}$, radial $\{u_{\text{rad}}\}_{\max}$, and tangential velocity $\{u_{\text{tan}}\}_{\max}$. The index “max” refers to the highest value during the lifetime of a specific vortex. $\{\cdot\}$ indicates the maximum of a tangentially averaged value around the dust devil center. The total number of detected dust devil-like vortices N , their lifetime τ , mean translation speed \bar{v}_t , and mean radius \bar{r} will also be discussed. The overbar $\bar{\cdot}$ represents a value averaged over the lifetime of a single vortex.

Only long-lived vortices are considered in the statistics for two reasons. First, dust devils with a short lifetime are of less interest because their contribution to the overall transport of heat and dust are negligible compared to the long-lived vortices; and second, short lifetimes often do not allow for a well-developed vertical vortex, resulting in strong deviations from the typical circular shape. Therefore, only dust devils with a lifetime of

$$\tau > \max\left(\frac{2\pi\bar{r}}{\{u_{\text{tan}}\}}, \tau_{N_{\max}}\right) \quad (7)$$

are analyzed. Here, $\overline{\{u_{\text{tan}}\}}$ is the mean tangential velocity. The first constraint of Equation 7 restricts the statistics to vortices that allow an air parcel flowing with $\overline{\{u_{\text{tan}}\}}$ to circulate the vortex once or more during its lifetime. This restriction is referred as the “velocity constraint.” $\tau_{N_{\max}}$ is defined as the lower limit of the bin having the highest number of detected vortex tracks in the lifetime frequency distribution. An example histogram of the lifetime frequency distribution from simulation RA1010A3 is displayed in Figure 1. By convention, the axes are logarithmically scaled with an interval or bin size ratio of about $\sqrt{2}$ on the x -axis (e.g., Giersch et al., 2019; R. D.; Lorenz & Jackson, 2016). The number of vortex tracks decreases with increasing lifetime and the lifetime distribution indicates a relatively strong positive skew, which is typical for dust devil statistics derived from observations and numerical simulations (e.g., Giersch et al., 2019; R.; Lorenz, 2011; R. D.; Lorenz & Jackson, 2016; Nishizawa et al., 2016). The bin counts are fit by a truncated power law, which starts at the mode bin and is determined by using nonlinear least squares analysis. $\tau_{N_{\max}}$ is equal to 0.2 s for run RA1010A3 and a differential slope (power law exponent) of -0.79 is calculated. The main purpose of the power law calculation is to enable quantitatively better comparisons with other dust devil studies.

The lifetime frequency distribution must be calculated for each simulation to filter out the short-lived vortices. The determined values for $\tau_{N_{\max}}$ are listed in Table 2. As discussed in Section 3.3 below, the simulation RA1006A3 contains no dust devil-like structures. In simulation RA1007A3 only one vortex fulfilling the velocity constraint in Equation 7 is detected. Furthermore, RA1008A3 contains only 11 vortices, which is too sparse to calculate meaningful statistics. Therefore, no $\tau_{N_{\max}}$ is set for these three simulations.

3. Results

The following section gives a general overview of the main characteristics of the simulations introduced in Section 2.1. This overview is mainly based on results derived from RA1010A3, the so-called control simulation. Afterward, the three-dimensional dust devil structure is analyzed and compared to LES results.

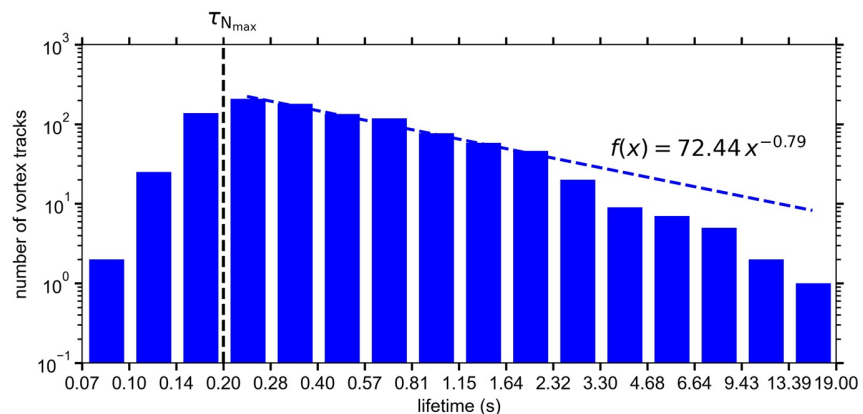


Figure 1. Number of vortex tracks fulfilling the velocity constraint of Equation 7 as a function of each track's lifetime for simulation RA1010A3. The labels on the x-axis demarcate the limits of each bin. The blue dashed line indicates a fitted power law with a slope of -0.79 using nonlinear least squares analysis. $\tau_{N_{\max}}$ is marked by a black dashed line.

Finally, the setup for RA1010A3 is systematically modified to test the effect of the Rayleigh number, aspect ratio and surface friction on the dust devil statistics.

3.1. Control Simulation RA1010A3

The general flow features in RA1010A3 can be partly generalized to all other simulations performed in this study. For example, Figure 2 shows the change of horizontally and temporally averaged profiles of the potential temperature $\langle \theta \rangle_t$ and total sensible heat flux in vertical direction $\langle w\theta \rangle_t$ with time. The index t illustrates temporal averaging. Changes are marginal after 30 s. Therefore, a well-mixed bulk of the flow is reached after an initial spin-up of 30 s simulated time due to strong convection. The near-wall region is characterized through sharp temperature gradients because turbulent heat transport, and therefore mixing, drastically reduces in the vicinity of the plates. However, the exact value for the spin-up time increases with Rayleigh number from less than 10 s in RA1006A3 to about 30 s in RA1011A3. This increase directly follows from the vertical extent of the model domain, which is larger for higher Rayleigh numbers. As a consequence, the flow needs more time to mix up and to reach a statistically stationary state. If not otherwise stated, time averaging, indicated as $\langle \cdot \rangle_t$, henceforth refers to the dust devil detection and analysis period of 70 s, following spin-up. In a stationary state, the heat flux profile should be constant with height because in the horizontal average the temporal change of temperature only depends on the divergence of the vertical heat flux along z . Figure 2 indicates that stationarity appears after 30 s. The global time-averaged Nusselt number, a measure of the ratio between the total heat transport and heat conduction, is 136, which is well in the range of results from similar setups (e.g., Scheel & Schumacher, 2014; Shi et al., 2012; Stevens et al., 2010; Zou et al., 2019). For reference purposes, the large-eddy turnover time (for calculations see Sakievich et al., 2016) and Deardorff's convective velocity scale are also computed. The values for the control simulation are ~ 20 s and 0.16 m s^{-1} , respectively. Both quantities decrease if the Rayleigh number is reduced.

Beside the height independent heat flux and the constant potential temperature values in the bulk of the flow with sharp gradients close to the plates (Figure 2), further typical flow features of RBC are reproduced (see also, De et al., 2017; Sakievich et al., 2016). An overview of the most relevant quantities is provided in Figure 3. Here, the horizontally and temporally averaged vertical profiles of variances of the horizontal velocity components and potential temperature have maximum values close to the bottom and top boundary with few changes in the bulk, whereas fluctuations of the vertical velocity component constantly increase away from the plates to a maximum in the middle part of the model domain. The averaged molecular contribution to the total sensible heat flux peaks at the plates and rapidly decreases to nearly zero in the bulk of the flow. For the turbulent heat flux, it is the opposite. The horizontal wind components have absolute values slightly above zero but with a more irregular structure. However, theoretically, zero values for the

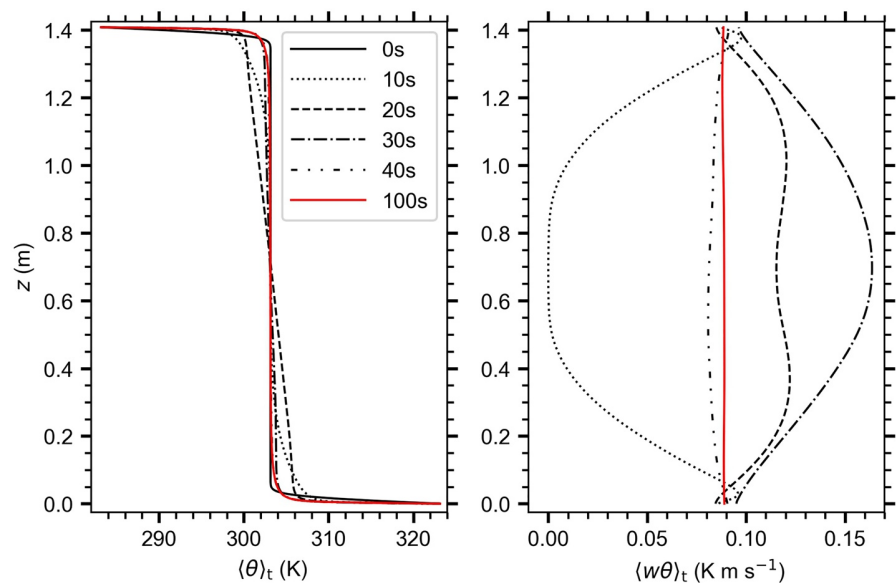


Figure 2. Horizontally and temporally averaged vertical profiles of the potential temperature (left) and total vertical sensible heat flux (right) for five different simulation times taken from RA1010A3. The black, broken curves show a 10 s average, whereas the red, solid lines indicate a 70 s (detection and analysis period for dust devils) average. The initial profile of the potential temperature is indicated by the solid black line. On the left, the line for 40 s simulated time is not apparent because it coincides with the 100 s (red) curve.

long-term averaged horizontal wind components should be assumed because no background wind is applied. This assumption is also valid because, on the one hand, the strength of the 70 s averaged horizontal flow components is only about 1% of the maximum fluctuations that occur in the flow ($\mathcal{O}(100\text{cm s}^{-1})$ in RA1010A3). On the other hand, the horizontal model extent of $2 \leq \Gamma \leq 4$ and averaging time of 70 s (roughly 67 times the free-fall time or 3 times the large-eddy turnover time in RA1010A3) are too small and short, respectively, to completely filter out the largest and most time-persistent structures that can exist in classical RBC (e.g., Pandey et al., 2018; Stevens et al., 2018). The magnitude of the horizontal wind derived from the averaged vertical profiles of u and v reaches its maxima slightly above/below the adjacent plate, with approximately constant positive values in between. However, because $\langle u \rangle_t$ and $\langle v \rangle_t$ can be approximated as zero, the horizontal wind defined as $\langle v_h \rangle_t = \sqrt{\langle u \rangle_t^2 + \langle v \rangle_t^2}$ is also negligible.

The boundary layer height $\delta_\theta = H/(2Nu_{\text{wall}})$ is defined as the distance at which the linear extrapolation of the temperature profile from the wall equals the domain averaged temperature of 303.15 K (e.g., Belmonte et al., 1994; Shishkina et al., 2010). Nu_{wall} describes the horizontally and temporarily averaged Nusselt number at the wall. It is defined as

$$Nu_{\text{wall}} = \frac{\left| \frac{\partial \langle \theta \rangle_t}{\partial z} \right|_{z=0}}{\Delta \theta H^{-1}}. \quad (8)$$

Figure 3 illustrates the well-known decrease of the scaled boundary layer height with the Rayleigh number (e.g., Hay & Papalexandris, 2019), which can be seen in the variance profiles of u , v , and θ by the shifted maximum in RA1010A3 compared to RA1007A3 (see zoomed profiles).

In horizontal cross sections of the vertical velocity, typical flow structures form pentagonal or hexagonal cells with narrow edges of high vertical velocity and broad centers with descending air. As discussed in Section 2 and 2.1, the occurrence of dust devils is likely directly connected to these structures. Figure 4 provides an overview of flow patterns changes in height and time. From top to bottom, three horizontal cross sections of the vertical velocity at different heights are displayed. The uppermost cross sections show the vertical velocity close to the lower thermal boundary layer height at 4 mm. The middle row of cross sections

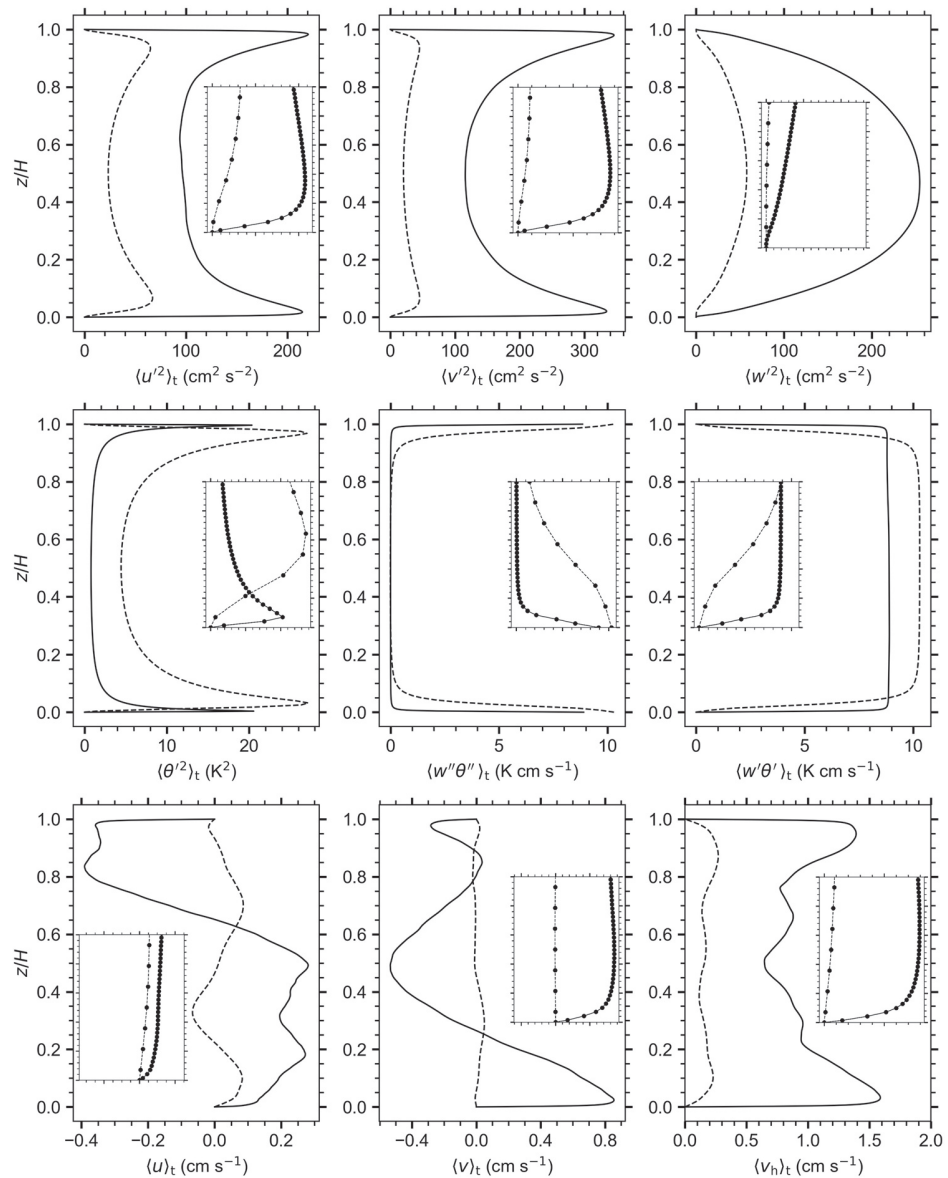


Figure 3. Horizontally and temporally averaged vertical profiles of variances (u^2 , v^2 , w^2 , θ^2), molecular and turbulent heat fluxes ($w''\theta''$, $w'\theta'$), and horizontal wind velocities for simulation RA1007A3 (dashed lines) and RA1010A3 (solid lines). The horizontal velocity is defined by $\langle v_h \rangle_t = \sqrt{\langle u \rangle_t^2 + \langle v \rangle_t^2}$. In each inset, profiles of the near-wall region of the lower plate are magnified up to $z/H = 0.05$.

in Figure 4 are from well above the lower boundary layer but still quite close to the heated plate. The lowermost cross sections in Figure 4 are taken from the mid-plane. Additionally, from left to right, two snapshots of the vertical velocity at the beginning and end of the dust devil detection period are shown. Within the boundary layer close to the surface, structures are very small. This is reminiscent of results from other DNS studies on RBC (e.g., Mellado, 2012; Shi et al., 2012; Stevens et al., 2018; van Reeuwijk et al., 2008). The near-surface structure develops from a uniform, honeycomb-like pattern during the spin-up phase (not shown) to a more irregular pattern, where the small hexagonal structures appear stretched and compressed by the diverging and converging of the flow. Also the large-scale pattern from above is visible at 4 mm, especially through long bands of clustered upward motion. These patterns are also the dominant structures at 100 mm. After 30 s, they clearly resemble the pentagonal or hexagonal cells often reported in LES of

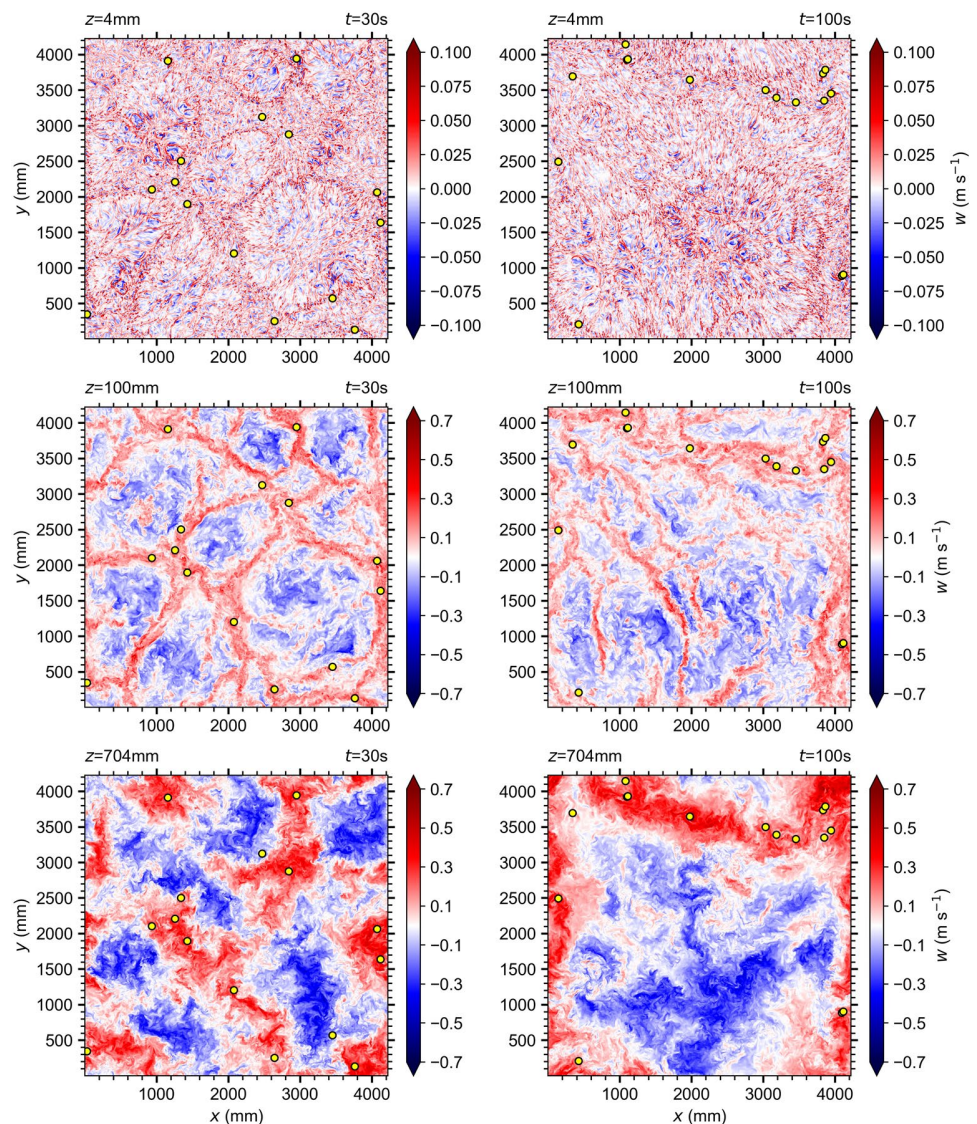


Figure 4. Horizontal cross sections of the instantaneous vertical velocity at 4 mm (top), 100 mm (middle), and 704 mm height (bottom) after 30 s (left) and 100 s (right) simulated time taken from simulation RA1010A3. Detected vortex centers at the first grid point above the surface are depicted as yellow dots. Note the different scale for $z = 4$ mm.

dust devils in the atmospheric boundary layer (e.g., Kanak, 2005; Raasch & Franke, 2011). DNS studies of RBC also show the occurrence of these forms in instantaneous flow fields (e.g., Bailon-Cuba et al., 2010). We call this state of the fluid the first flow regime. The hexagonal pattern at 100 mm disappears when its size matches the width of the computational domain. This happens in each simulation due to a broadening of the patterns. As a result, relatively long and narrow bands occur at later times (second flow regime), as exemplified in Figure 4 for 100 mm at the end of the simulation. Similarly, structures in the mid-plane grow to larger scales after 30 s simulated time. Starting from isolated plumes of ascending and descending air at 30 s, clustered regions with high- and low-vertical velocities develop. These regions are a consequence of merging plumes. That is why they appear much larger. The broadening process of structures until the horizontal domain size is reached is thoroughly discussed in Parodi et al. (2004), von Hardenberg et al. (2008), and Stevens et al. (2018). These publications suggest that an aspect ratio of 4 (our maximum) is still too low for capturing the finite horizontal saturation scale of the convection pattern. A minimum of 4π would be required to resolve this scale (von Hardenberg et al., 2008). However, it is critical to simulate high

Table 3
 Dust Devil Properties at Detection Height Derived From Simulation RA1010A3^a

N	T (s)	\bar{v}_1 (cm s ⁻¹)	\bar{r} (mm)	$ p^* _{\max}$ (mPa)	$ \zeta _{\max}$ (s ⁻¹)	$\{u_{\tan}\}_{\max}$ (cm s ⁻¹)	$\{u_{\text{rad}}\}_{\max}$ (cm s ⁻¹)	$\{w\}_{\max}$ (cm s ⁻¹)
865	0.82 ± 1.21	15.3 ± 6.74	6.47 ± 3.13	255 ± 235	310 ± 125	32.8 ± 13.3	18.1 ± 7.76	13.5 ± 3.19
434⊙/431⊙	18.8	44.3	26.3	1,708	928	101	52.6	32.2

^aThe first row shows the population mean and standard deviation. The overall maximum values are displayed in the second row. For N , the number of clockwise and counterclockwise vortices is given.

Rayleigh numbers, rather than high aspect ratios, to achieve a sufficient count of dust devil-like vortices (see Section 3.3 and 3.4). Realizing both is currently not feasible due to limited computational resources. Note, dust devil statistics are not affected by the ongoing increase in cell size because statistical information about vortices derived from two different periods (30 to 65 s and 65 to 100 s) do not change significantly (not shown). The most crucial requirement for acquiring stationary statistics is to reach a well-mixed state of the flow. This requirement is satisfied before 30 s in every simulation.

Figure 4 depicts the location of detected dust devil-like vortices by yellow dots. As long as a coherent cellular pattern is visible at the lower part of the model domain (first flow regime), vertical vortices appear at cell edges and especially vertices, as already detailed by LES studies (e.g., Giersch et al., 2019; Kanak, 2005; Raasch & Franke, 2011). Once the size of the cells has reached the horizontal domain size (second flow regime), which occurs between 50 and 60 s in RA1010A3, dust devils persist and continue developing. During second flow regime, dust devils appear to be connected to the widest bands of high vertical velocities, where near-surface convergence is relatively strong (see cross sections for 100 and 704 mm at 100 s). These findings support the LES results of Raasch and Franke (2011), who also investigated the distribution of dust devil-like vortices in a domain that did not allow for the development of cellular flow structures due to the limited horizontal size. In their LES study, dust devil centers were also located along convergent bands of high vertical velocity.

The reasons for the preferred occurrence at certain locations in the flow pattern are summarized well by Raasch and Franke (2011). Their explanations can be applied to both flow regimes. For the first one, this has already been done in Section 1.2. In the second flow regime, high vertical wind velocities occur at pronounced flow convergence zones indicated by long bands with upward motions. Along these bands, flow convergence is irregularly shaped, often having a significant wind component parallel to the band. By chance, the parallel wind component is opposite on both sides of the convergence line and an overall initial rotation is created. This might also explain the occurrence of dust devils along the cell edges in the first flow regime. A further explanation for the occurrence of vortices along the near-surface convergence lines is the so-called hairpin mechanism, which is highlighted in Renno et al. (2004) and Kanak (2005). Near-surface horizontal vorticity created by directional shear is lifted by the updraft along the convergence lines and a vortex loop forms. The apex of the loop thins and weakens as it rises. Finally, the vortex breaks into two vortices of opposite rotation. Normally, one of these vortices decays, leaving a single vertical vortex. However, this vortex is more unstable and infrequent than those created at the vertices of the cellular pattern (Raasch & Franke, 2011). In addition, the simulation results show that two vortices of opposite rotation are rarely created along the convergence zones of the convective cells. This makes the hairpin mechanism not very probable for the formation of vertical vortices studied here.

Bulk properties at detection height (first grid point above the plate) are presented in Table 3 for the control simulation RA1010A3. Parameters are described in Section 2.2. The first row describes an average over all N detected vortices. The second row shows the maximum values with respect to all 865 dust devils fulfilling Equation 7. For N , however, the number of clockwise and counterclockwise rotating vortices is displayed. Additionally, standard deviations from the sample mean are given.

As expected, there are nearly the same number of clockwise and counterclockwise rotating vortices because no force exists that prefers a direction of rotation. Atmospheric observations and LES simulations, where the Coriolis force is considered, suggest the same (e.g., Balme & Greeley, 2006; Kanak, 2006; Raasch & Franke, 2011). Most of the dust devil-like vortices have a lifetime of ~ 1 s. This is relatively short-lived

compared to, for example, the large-eddy turnover time (roughly 20 s for RA1010A3). Nevertheless, due to the strongly skewed probability distribution of dust devil parameters, there are single events within the simulation time of 100 s where persistent vertical vortices develop. The three longest lifetimes are 18.84, 11.66, and 9.85 s. In the convective boundary layer of the atmosphere, large-eddy turnover times of ~600–1,200 s occur (e.g., Rizza et al., 2013), while dust devils have a lifetime from seconds to minutes. This shows that atmospheric dust devils typically last for less than the large-eddy turnover time, which is supported by the dust devil-like structures studied here. The translation speed is in the range of the background turbulent velocities of the horizontal components close to the plates if the root of the u -variance is interpreted as a typical velocity fluctuation (see Figure 3). In addition, the horizontal size has maximum values of several tens of millimeters. However, due to the radius restriction explained in Section 2.2, the mean values of 6.47 and 26 mm in Table 3 slightly underestimate the real mean radii. This can be inferred by the fact that 3% of all instantaneously detected radii from the investigated vortex tracks reach 48 mm (24 grid points), which is the maximum distance that is considered along each horizontal direction from the dust devil core during detection (see Section 2.2). The vortex strength measured through the pressure drop at the center is a factor of 1/100 smaller than values observed in dust devils in the planetary boundary layer, whereas the vorticity is a factor of 100 higher (e.g., Balme & Greeley, 2006; Giersch et al., 2019). Because vorticity is calculated across one grid spacing (see Section 2.2), it highly depends on the chosen resolution. Wind velocities are one order of magnitude smaller than measured and simulated dust devil velocities in the planetary boundary layer. As in other studies, the largest velocity component is the tangential, followed by the radial, and finally the vertical (e.g., Balme & Greeley, 2006; Giersch et al., 2019; Raasch & Franke, 2011). Note, the largest absolute values of vortex properties like pressure drops, vorticities, or velocities, might occur above the detection height (see next section).

3.2. Averaged Three-Dimensional Vortex Structure—A Comparison With LES

After discussing the effects of the Rayleigh number, the aspect ratio, and the velocity boundary conditions on the dust devil statistics, this section will briefly compare the simulated three-dimensional dust devil structure with LES results. According to Fiedler and Kanak (2001), a high degree of similarity between intense columnar vortices in convective layers explored with DNS and LES is expected.

Figure 5 exhibits time-averaged horizontal cross sections of the near-surface pressure, vorticity, velocity, and temperature fields around the vortex with the longest lifetime in simulation RA1010A3. The time-averaged horizontal and vertical cross sections around a vortex core as well as the transects in Section 3.5 are derived with the same procedure as described in Raasch and Franke (2011). The basis of this procedure is the sampling of different variables on a $31 \times 31 \times 100$ points ($x/y/z$) moving grid with the vortex center in its middle and the lowest grid point at the bottom boundary of the model. The structure in Figure 5 appears very similar to that observed in dust devil-like vortices simulated with LES (e.g., Kanak, 2005; Ohno & Takemi, 2010; Raasch & Franke, 2011; Spiga et al., 2016). In general, the pressure, vorticity, and vertical velocity fields exhibit an axially symmetric behavior with distinct maximum absolute values at, or close to, the center—the vorticity especially so. The near-surface convergent flow around the dust devil is counterclockwise and has a strong radial inflow that advects air from the surrounding into the dust devil. Actually, three tongues of warmer air are advected from west, north, and southeast into the vortex center where the maximum temperature is reached. A temperature increase of 2–3 K is found, which is well in the range of common core temperature excursions in atmospheric dust devils (Murphy et al., 2016). The mean radius of the vortex, here defined as the distance where the mean absolute pressure drop is reduced to 50% of the mean core pressure drop, is between 3 and 4 mm.

In contrast to the LES of Raasch and Franke (2011), the maximum vertical velocity is directly at the center, rather than outside of it. This difference is attributed to the different physical analysis heights. In Raasch and Franke (2011), cross sections were analyzed at a physical height of 1 m (first grid point above the surface). This is well above the diffusive wall layer, which is completely parameterized in LES. Figure 5 shows cross sections at the first grid point above the surface, which corresponds to a physical height of 1 mm. This height is well within the diffusive wall layer. Accordingly, differences in the three-dimensional dust devil structure are expected. At higher altitudes, 10 mm for example, our DNS results indicate maximum vertical velocities adjacent to the center. Time-averaged vertical cross sections of the example vortex are displayed in

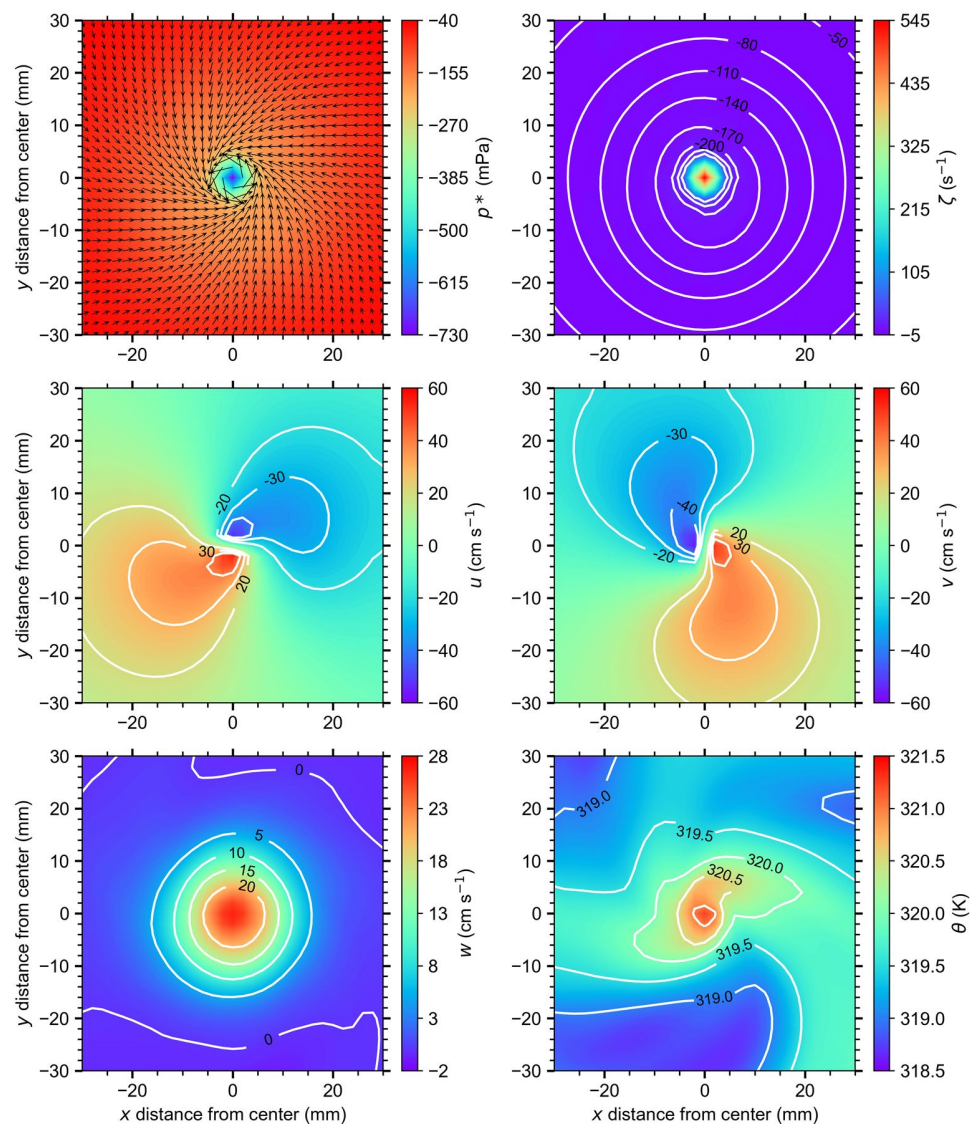


Figure 5. Time-averaged horizontal cross sections of the perturbation pressure, vorticity, velocities, and potential temperature at 1 mm height for the vortex with the longest lifetime derived from simulation RA1010A3. Additionally, vectors of horizontal velocity are shown in the pressure cross section and isolines of constant pressure are displayed in the vorticity field.

Figure 6. As in Raasch and Franke (2011), two isolated maxima to the left and right of the center occur. In zoomed vertical cross sections up to a height of 40 mm (not shown), the flow structure becomes very similar to the flow in atmospheric dust devils depicted schematically by Balme and Greeley (2006, Figure 8) or that of Rotunno (2013, Figure 9b). Although features like a stagnation point and a downward flow well above the plate are not observed in the averaged fields, it is expected that they are observable in the instantaneous data (the averaging is done during the simulation and the instantaneous data are not stored). This is supported by the significant reduction of positive vertical velocity in the central region above 20 mm height. However, Balme and Greeley (2006) also stated that the reversal in flow might not be present at all (upward flow throughout dust devil). Also Rotunno (2013) highlighted a single-celled below and doubled-celled above vortex form for certain swirl ratios similar to the vortices studied here. An estimation of the swirl ratio for the averaged vortex structure in Figure 6 yields 0.2–0.3.

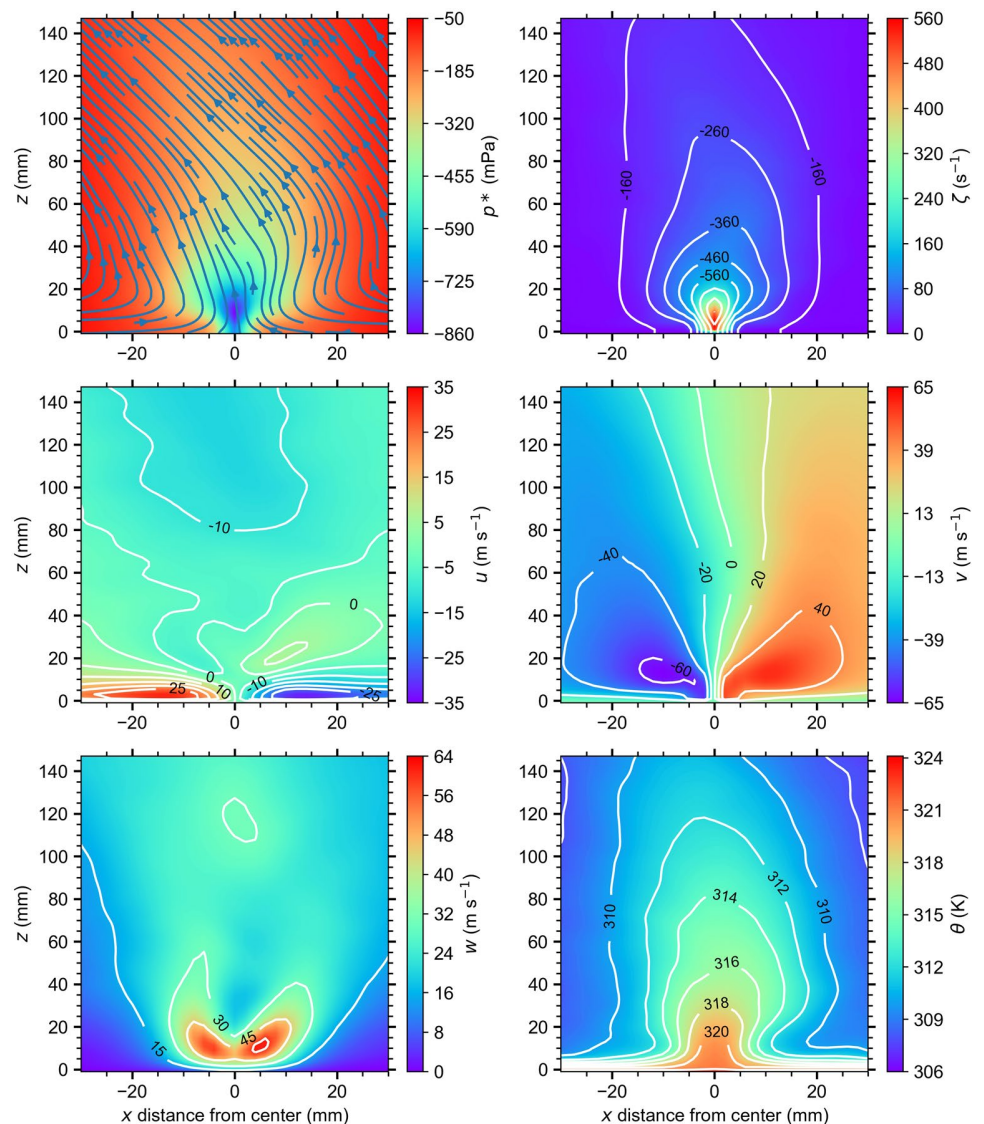


Figure 6. Time-averaged vertical cross sections of the perturbation pressure, vorticity, velocities, and potential temperature through the center for the vortex with the longest lifetime derived from simulation RA1010A3. Additionally, streamlines are shown in the pressure cross section and isolines of constant pressure are displayed in the vorticity field.

As in Raasch and Franke (2011), a time-persistent updraft at the vortex position that extends to the top of the mixed layer occurs. This is particularly evident in the streamlines of the pressure cross section and averaged vertical velocity displayed in Figure 6. However, the maximum upward motions occur within the lower region of the dust devil, whereas in Raasch and Franke (2011) vortices show the strongest time-averaged vertical velocities in their upper region. This inconsistency might be explained by the differences in the chosen setups. In the DNS of RBC, the domain is heated from below and cooled from above, resulting in both strong up- and down-drafts. In LES setups, where the convective layer is restricted by a temperature inversion, no cooling occurs. This lack of cooling could enable stronger and more persistent updrafts above the dust devil core, while in DNS of RBC updrafts could be partially suppressed by the cooling from the upper plate.

Regarding the general flow structure around the vortex, Figure 6 indicates that the inflow is restricted to the near-surface region (u -component). Conversely, the spiraling upward motion is visible up to 150 mm and

even above (v and w -component). This result is in agreement with the fluid dynamics discussion of atmospheric dust devils in Kurgansky et al. (2016), who also point out that the convergence of radial air flows is confined to the lowest part of the vortices.

Determining the height of a simulated dust devil is not trivial because of the potential vortex tilt and the absence of visible dust. For example, Gheynani and Taylor (2011), S. C. R. Rafkin et al. (2001), and Toigo et al. (2003) qualitatively estimated the height from the general flow pattern and vertical vorticity. Kanak et al. (2000) and Ohno and Takemi (2010) used information about the updraft region for their estimations. Raasch and Franke (2011) determined the vortex height based on the thresholds used for the detection of the vortex centers. However, Figure 6 indicates that the dust devil height depends on the quantity that is considered. If the same criterion as for the radius is used in vertical direction above the vortex center, a height of ~ 50 mm (and therefore a height to diameter ratio of roughly 7) is obtained for the regarded vortex. This ratio is well in the range of atmospheric dust devils (e.g., Morton, 1966). Nevertheless, the other variables (e.g., v -component velocity, potential temperature) are significantly modified up to roughly 150 mm and even above.

Overall, the results presented here suggest that the main properties of dust devil-like vortices in DNS are very similar to those observed in nature and LES simulations.

3.3. Effects of the Rayleigh Number

To investigate the effect of the Rayleigh number on the dust devil statistics, simulation RA1010A3 is repeated with $Ra = 10^6, 10^7, 10^8, 10^9$, and 10^{11} (see also Table 1). Although the Rayleigh number is varied over five orders of magnitude, time-averaged vertical profiles, as indicated in Figure 3 and discussed in the previous section, remain mostly unchanged. Only the scaled height of the boundary layer decreases if Ra increases. The most relevant differences in the investigated flow features that are related to dust devils occur in the developing convective pattern.

The increase of cell size mentioned in Section 3.1 is not relevant for dust devil analysis for Rayleigh numbers less than 10^9 because the size already reaches the horizontal domain limit when the detection period starts after 30 s (not shown). This is due to the fact that the domain height is reduced for lower Rayleigh number cases, which also results in a smaller horizontal model extent (aspect ratios remain constant at $\Gamma = 3$). Thus, the fluid is always in the second flow regime during the dust devil detection and analysis period of 70 s if $Ra < 10^9$.

Furthermore, the appearance of structures changes significantly at every height if the Rayleigh number is modified by one order of magnitude or more. This is exemplified in Figure 7, where instantaneous cross sections of the vertical velocity are compared between RA1010A3 and RA1007A3. Cross sections were selected from heights within the boundary layer (4 and 4 mm, respectively; top row), above the boundary layer (100 and 25 mm, respectively; middle row), and from the vertical center of the model domain (704 and 70 mm, respectively; bottom row). A hexagonal pattern cannot be observed in simulation RA1007A3. This is also the case for simulation RA1008A3 and RA1006A3 (not shown). In addition, structures in the right column of Figure 7 are artificially enlarged because the axes scales are 1/10 of the left column due to a smaller model domain. The cross sections on the right can be seen as a smoother version of a zoomed sub-area of the respective cross section on the left. Because scale separation increases with Reynolds, and therefore Rayleigh number (e.g., Grossmann & Lohse, 2002; Wyngaard, 2010), the difference between the largest scales ($\mathcal{O}(1000\text{mm})$) in the mid-plane and the smallest scales in the boundary layer ($\mathcal{O}(1\text{mm})$) is quite large for $Ra = 10^{10}$ and much smaller in case of RA1007A3 ($\mathcal{O}(100\text{mm})$ and $\mathcal{O}(1\text{mm})$). Furthermore, the magnitude of the vertical velocity fluctuations decreases significantly with decreasing Rayleigh number because turbulent mixing is replaced by heat conduction at low Rayleigh numbers.

No dust devil centers are detected for simulation RA1007A3 at 30 s simulated time, which already suggests that the number of detected vortices reduces drastically at lower Rayleigh numbers. For example, results from RA1010A6 yield no vortex tracks at all, whereas at least 154 vortex tracks (3152 centers) are found for a Rayleigh number of 10^7 . There is only a single vortex that fulfills our requirement on dust devil lifetime (Equation 7). In simulation RA1011A3, a total of 40,770 vortex tracks (2,358,967 centers) are detected.

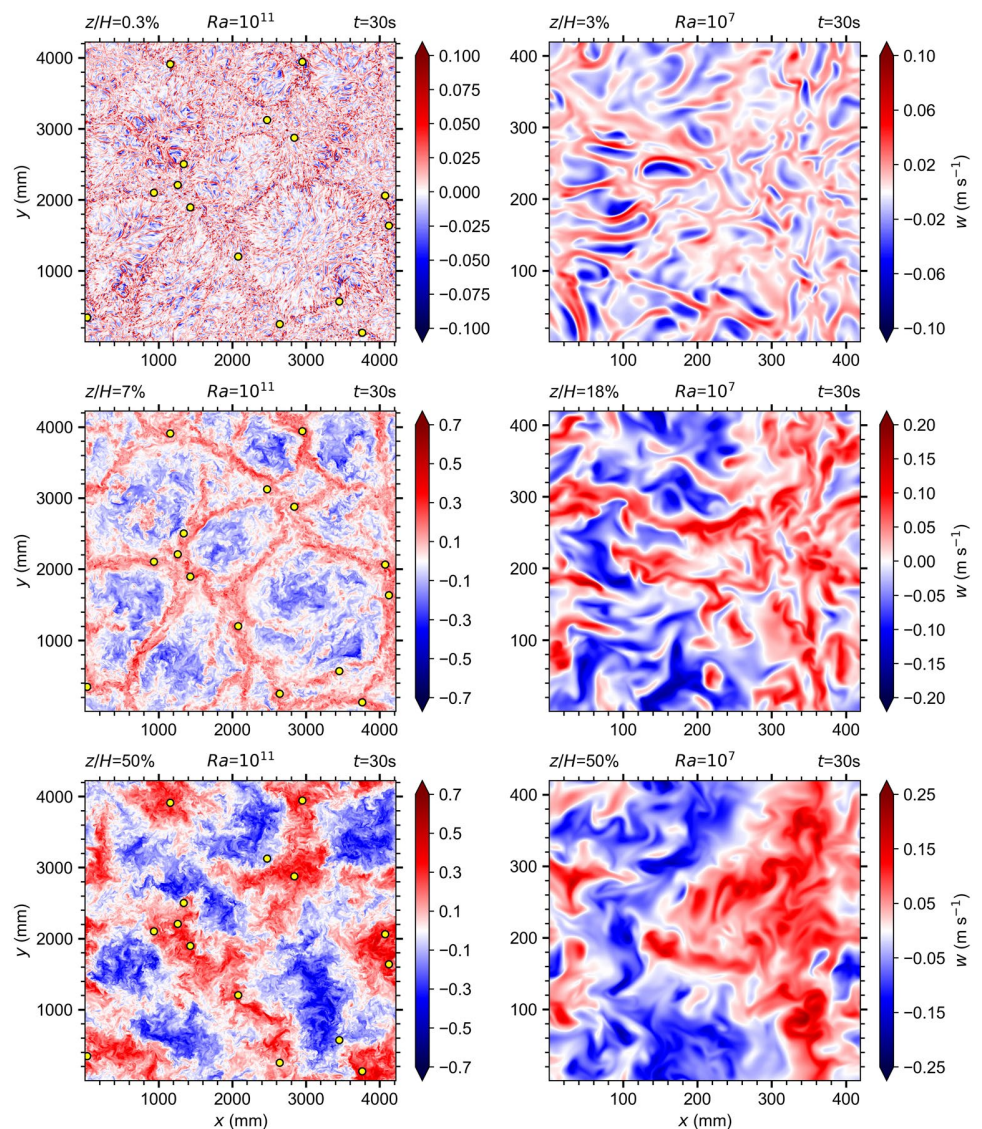


Figure 7. Horizontal cross sections of the instantaneous vertical velocity at three different heights after 30 s simulated time derived from RA1010A3 (left) and RA1007A3 (right). Detected vortex centers at the first grid point above the surface are depicted as yellow dots. Note the different scales. An explanation to the chosen heights is given in the text.

Therefore, a Rayleigh number of about 10^7 seems to be a minimum condition to identify dust devil-like vortices in numerical simulations of RBC. This Rayleigh number is consistent with the suggested value of 4×10^7 in Cortese and Balachandar (1993). For lower Rayleigh numbers, the scale separation and developing turbulence is not sufficient to create turbulent, time-persistent, coherent structures, such as dust devils. Hence, we are unable to derive meaningful dust devil statistics for $Ra \leq 10^8$. The number of detected vortices in RA1008A3 that fulfill Equation 7 is merely 11. For larger Rayleigh numbers, however, enough dust devil-like vortices are detected and analyzed to calculate bulk properties. The results are displayed in Figure 8, which shows the dependence of bulk vortex parameters on the Rayleigh number.

In total, 215, 865, and 3,834 dust devil-like vortices are recognized for RA1009A3, RA1010A3, and RA1011A3, respectively. The 95% confidence interval width in Figure 8 decreases with increasing Ra because the real population value is estimated from a much higher sample size. The increased formation of convective vortices for higher Rayleigh numbers is directly related to the more pronounced and stronger convective structures that develop as Ra becomes larger (see Figures 4 and 7). Furthermore, the higher the Rayleigh

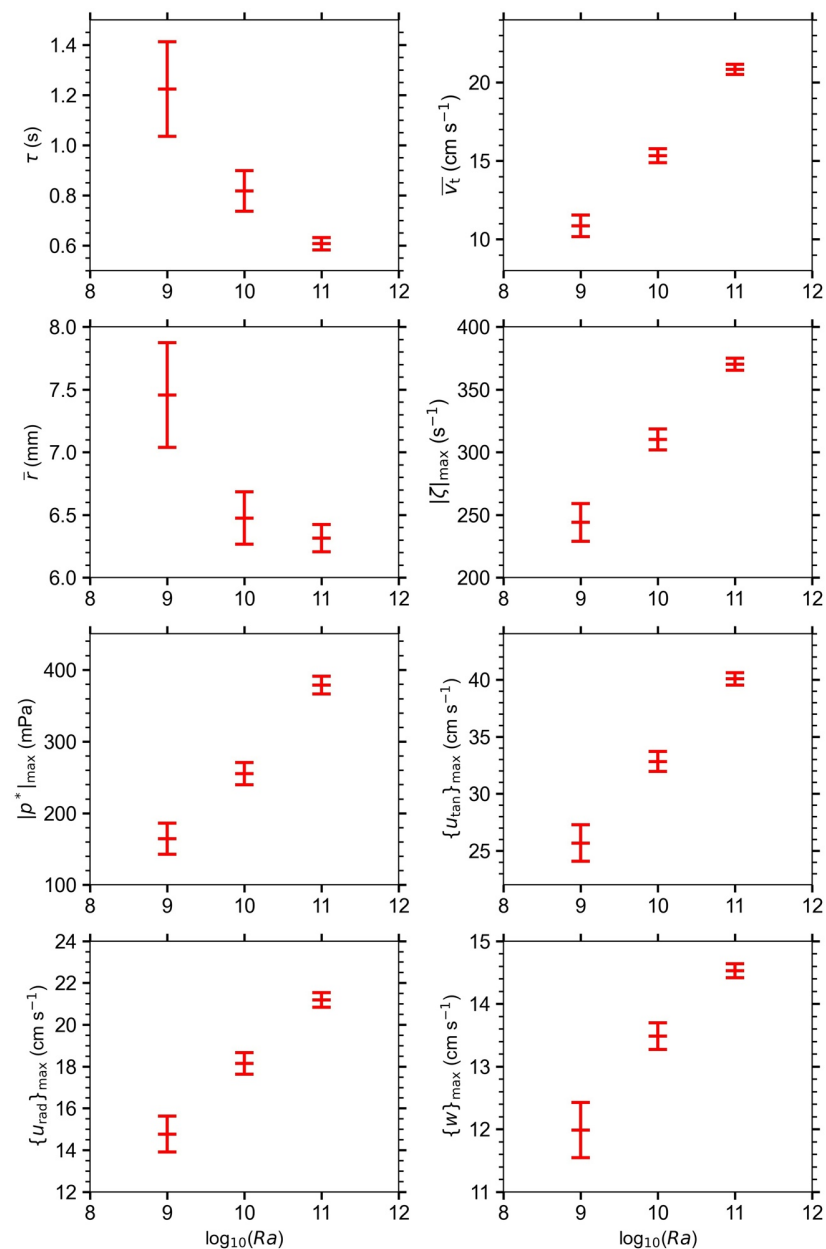


Figure 8. Dependence of dust devil characteristics on the Rayleigh number. Error bars (outer red lines) represent the 95% confidence intervals of the mean (middle red line). The mean is calculated over all N dust devils.

number, the higher the averaged dust devil strength, as indicated by increased maximum pressure drops, vorticities, and velocities. These increases are a consequence of stronger convective cells, which increase flow convergence and the twisting of horizontal vorticity, two mechanisms that are suggested to be mainly responsible for maintaining and strengthening the convective vortices (see Section 1.2). Stronger convection also causes higher background velocities and, by association, translation speeds as Rayleigh numbers increase. A parameter that decreases as Ra increases is the average lifetime. This is not the case because of a reduced number of long-lived dust devils, but rather due to an increased percentage of short-lived vortices in the entire sample. Hence, it seems that stronger turbulence especially favors the development of short-lived vortices and increases the probability of the initial development of coherent structures, like dust devils. Similar results were derived from LES by Giersch et al. (2019).

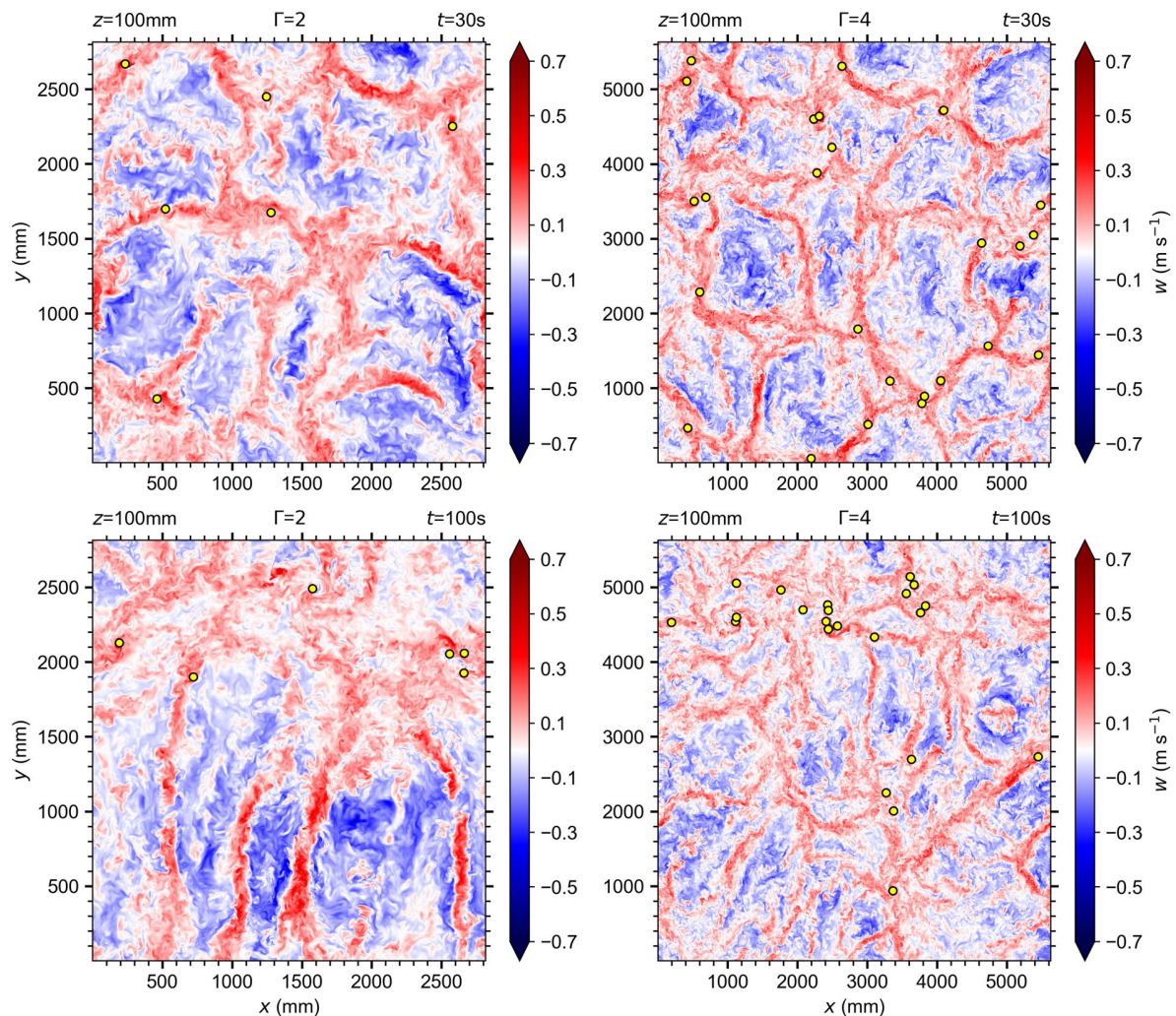


Figure 9. Horizontal cross sections of the instantaneous vertical velocity at 100 mm height after 30 s (top) and 100 s (bottom) simulated time taken from simulation RA1010A2 (left) and RA1010A4 (right). Detected vortex centers at the first grid point above the surface are depicted as yellow dots.

Ultimately, no statistically significant conclusions are drawn from the lifetime-averaged radii because the uncertainties are too high. First, the confidence intervals of the sample mean overlap between the two simulations RA1010A3 and RA1011A3. This overlap does not allow for a statistically significant conclusion. Second, the radius restriction explained in Section 2.2 increasingly influences the results for $Ra \geq 10^{10}$. The instantaneous radii of all detected vortex tracks in simulation RA1011A3 reach the numerical limitation of 48 mm in 8.43% of the cases, which is ~ 5.1 and 6.7% more than for RA1010A3 and RA1009A3, respectively. This alone suggests that the portion of large dust devil-like vortices increases with Ra . However, the lifetime-averaged radius of a single vortex must not be affected by this because radius fluctuations can increase in both directions, toward higher as well as lower values, not modifying the mean. Therefore, an increased rate of vortex tracks that become instantaneously larger than the restricted detection range is not sufficient to draw any conclusions for the mean radius, especially because Figure 8 indicates exactly the opposite. Here, the mean radius averaged over all dust devils that fulfill our requirement on dust devil lifetime (Equation 7) decreases, at least from RA1009A3 to RA1010A3.

No linear correlation exists between vortex radius and core pressure drop, nor between the vortex radius and its duration. This absence of correlation is true in all performed simulations with both Rayleigh numbers larger than 10^8 and no-slip conditions. This is in agreement with the LES of Giersch et al. (2019). The Pear-

son correlation coefficients are ~ 0.2 or lower. For the core pressure drop and the duration, dust devil data show a moderate linear correlation with Pearson coefficients between 0.4 and 0.7. As expected from vortex theory, the strongest correlation is between the vorticity and the pressure drop, where coefficients of more than 0.9 are calculated.

In summary, for strong vertical vortices to frequently appear in the flow, Rayleigh numbers of at least 10^9 are necessary if an aspect ratio of 3 is used. This combination between a sufficiently large aspect ratio and Rayleigh number requires substantial computational resources that are presently available but have been largely prohibitive in the past (e.g., for RA1010A3, 105,000 core hours are necessary). The huge amount of computing power is one of the reasons why no comprehensive DNS study of dust devil-like vortices exists so far.

3.4. Effects of the Aspect Ratio

Previous studies (e.g., Giersch et al., 2019; Kanak, 2006; Raasch & Franke, 2011) and the results presented in Section 3.3 suggest that dust devil-like vortices are connected to specific patterns that develop in buoyancy-driven flows. Because these patterns depend on the chosen aspect ratio (e.g., Bailon-Cuba et al., 2010; Stevens et al., 2018; van der Poel et al., 2012), this section will clarify if the dust devil statistics also depend on the horizontal width of the model domain. Two additional simulations with an aspect ratio of 2 and 4 (RA1010A2 and RA1010A4) are performed and compared with the control simulation RA1010A3 for this purpose. Figure 9 displays how structures change with aspect ratio. For higher ratios, more cells exist at the beginning of the dust devil detection period. Consequently, more dust devil-like structures occur at the vertices and branches of these cells. The size of the cellular pattern increases and vanishes by $t = 100$ s in RA1010A2 because the horizontal scale of the largest structures exceeds the model domain size. For higher aspect ratios, this happens later than for lower ones. In case of $\Gamma = 4$, cellular structures are still apparent at $t = 100$ s, though they are much more distorted compared to $t = 30$ s. After the cells have grown to sizes comparable to the domain extent, vertical vortices occur within regions of clustered high vertical velocities. Similar to the vertices of the cellular pattern, these clusters are associated with points where several band-like structures merge and dust devils are recorded, which again supports the dust devil formation hypothesis of Raasch and Franke (2011) (see Section 1.2). The merging is especially apparent in the case with $\Gamma = 4$. Here, more of these points can be identified compared to RA1010A2, which results in a higher number of detected vortices in RA1010A4. However, the case with $\Gamma = 4$ is also unable to appropriately capture the time-persistent, large-scale cellular pattern after the initial growth period of the cells (several tens of seconds).

Consistent with previous studies (e.g., Bailon-Cuba et al., 2010; van der Poel et al., 2012), a transition from a single circulation to a multiple circulation system occurs if the aspect ratio increases. Figure 10 shows vertical cross sections of the instantaneous vertical velocity taken from the center of the model domain. In RA1010A2, there is only one large-scale circulation with an updraft at the center, whereas RA1010A4 has a two-circulation form. Even three-circulation forms occur at points during simulation RA1010A4. They also exist in the time-averaged flow field (not shown). Their diameters are comparable to the domain height and they develop a wide variety of structures depending on their y -positions. As indicated in Figure 9, the location of dust devils is connected to strong updrafts. In principle, this is supported by Figure 10, where a single dust devil center is detected by chance at the position of the output slice. The dust devil is clearly embedded in upward motions.

Regarding the dust devil statistics, no significant changes or trends are identified if the aspect ratio is varied between 2 and 4 except for the number of detected vortices, their mean translation speeds, and their maximum values of all other variables. In simulation RA1010A2, 353 vortices that fulfill our lifetime criterion (Equation 7) are detected. In RA1010A4, 1239 dust devil-like structures are found. Maximum values in RA1010A4 tend to be larger because the larger sample size increases the occurrence of extreme values. Additionally, larger aspect ratios increase the mean translation speeds from a population-averaged value of 14.21 cm s^{-1} (RA1010A2) to 16.12 cm s^{-1} (RA1010A4). The averaged translation speed in the control simulation (RA1010A3) is 15.33 cm s^{-1} (see Section 3.1). Interestingly, the instantaneous and time-averaged background velocities remain nearly constant between simulations with different aspect ratios (not shown). Therefore, higher translation speeds cannot be explained by an increase in background winds. It might be

that the translation speed is quite sensitive against the population size and that the real value is underestimated in case of low Γ .

After discussing the effects of the main control parameters in RBC, namely the Rayleigh number and the aspect ratio, on the dust devil statistics, the next section gives an insight on how the surface friction influences dust devil-like vortices.

3.5. Effects of Surface Friction

The importance of surface friction for the development of vertical vortices, such as tornadoes or dust devils, is addressed often in literature (e.g., Davies-Jones, 2015; Gu et al., 2010; Ito & Niino, 2013; Raasch & Franke, 2011; Roberts et al., 2016; Roberts & Xue, 2017). An overview of this topic is given in Kurgansky et al. (2016). In our simulations, the choice of velocity boundary conditions greatly influences the results. This section aims to highlight the effects of surface friction on dust devil-like vortices in DNS of RBC. For this purpose, simulation RA1009A3*, where free-slip boundary conditions are used, is performed and compared to RA1009A3.

Consistent with Ito and Niino (2013) and Mellado (2012), the overall convective pattern in RA1009A3* is similar to RA1009A3 except that stronger and more pronounced convergence lines at the cell borders arise close to the plates (not shown). Another difference is that the large-scale pattern well above the boundary layer is more dominant close to the plates if no surface friction is considered. Thus, structures inside the boundary layer and well above seem to be more strongly correlated. However, friction is not essential to generate dust devil-like vortices in the flow (see also Ito and Niino (2013)). In fact, simulation RA1009A3* produces 6,790 vortices—6,575 more than produced in RA1009A3 (215). This increased production suggests that the initial conditions for the development of vertical vortices are more favorable if surface friction is disabled. Because the initial formation process is not yet fully understood (e.g., Ito & Niino, 2013; Raasch & Franke, 2011; Renno et al., 2004), a rigorous explanation for this result is not given here. It is possible that the overall initial vorticity is larger due to the stronger opposing and staggered flows toward the convergence lines at the borders and vertices of the convective cells near the ground (see also Section 1.2 and 3.1). In addition, the increased flow convergence alone, and consequently the vorticity concentration, provides more favorable conditions for vortex generation in simulation RA1009A3*. Mellado (2012) made similar observations of enhanced vorticity at the nodal points of the cellular network when free-slip, instead of no-slip, conditions are used.

The mean translation speeds and tangential, and consequently horizontal, velocities increase without surface friction, as well (see Table 4). The population-averaged value of \bar{v}_t is 25 cm s^{-1} in RA1009A3* and 11 cm s^{-1} in RA1009A3. The translation speeds are higher due to the larger background velocities that occur in RA1009A3* because no frictional force exists that slows down the flow near the plates. The missing surface friction also explains the increase of tangential (and horizontal) velocities associated with dust devils in the case of free-slip conditions. Figure 11 illustrates this relationship. It shows horizontal transects at 1 mm height through the centers of two time-averaged, counter-rotating vortices that have the longest lifetime in their respective simulations RA1009A3 (vortex *A*) and RA1009A3* (vortex *B*). From the transects, it is clear that higher absolute tangential values are reached with free-slip conditions. This is additionally supported by Table 4. The value averaged over the vortex lifetime and subsequently over all detected dust devils ($\{u_{\text{tan}}\}$) yields an increase of $\sim 30\%$: from 17 cm s^{-1} in RA1009A3 to 22 cm s^{-1} in RA1009A3*. The laboratory study from Dessens (1972) also found a substantial increase of tangential velocities without surface friction.

Sinclair (1973) showed that the radial distribution of the tangential velocity of atmospheric dust devils can be approximated through a Rankine vortex described by

$$u_{\text{tan}}(r) = \begin{cases} \omega r & \text{for } r \leq R_0, \\ \frac{\omega R_0^2}{r} & \text{for } r > R_0. \end{cases} \quad (9)$$

Table 4
 Dust Devil Properties at Detection Height Derived From Simulation RA1009A3 and RA1009A3*^a

N	τ (s)	\bar{v}_t (cm s ⁻¹)	\bar{r} (mm)	$ p^* _{\max}$ (mPa)	$ \zeta _{\max}$ (s ⁻¹)	$\overline{\{u_{\tan}\}}$ (cm s ⁻¹)	$\overline{\{u_{\text{rad}}\}}$ (cm s ⁻¹)	$\overline{\{w\}}$ (cm s ⁻¹)
215	1.22 ± 1.4	10.9 ± 5.08	7.46 ± 3.1	164 ± 161	244 ± 112	17.2 ± 4.71	11.1 ± 3.63	8.36 ± 1.6
98C/117C	8.57	29.1	19.7	1158	753	42.5	25.6	13.2
6790	0.73 ± 0.49	24.8 ± 10.1	6.12 ± 2.28	107 ± 59.4	164 ± 46.2	21.8 ± 4.97	9.92 ± 2.77	1.88 ± 0.46
3422C/3368C	5.26	59.6	28.5	519	391	45.5	23.7	5.13

^aThe first row shows the population mean and standard deviation. The overall maximum values are displayed in the second row. For N , the number of clockwise and counterclockwise vortices is given. The upper part shows the data for RA1009A3 and the lower part RA1009A3*. Here, lifetime-averaged velocities are displayed because they reveal a more obvious trend than the maximum values.

here, $\omega = \zeta/2$ is the constant angular velocity. r describes the distance from the center and R_0 the location where u_{tan} becomes maximum. In Figure 11, Rankine profiles are displayed for vortex A and B under the assumption that ζ is equal to the central value (225 s⁻¹ and -176 s⁻¹) and that R_0 can be described by the mean distance from the center where $\{u_{\text{tan}}\}$ occurs (3.52 and 5.43 mm). In addition, a perfectly symmetric dust devil is assumed. It is evident, that vortex A and B can be approximated by the Rankine vortex model similar to atmospheric dust devils (Sinclair, 1973). However, the model tends to overestimate the tangential velocities, especially in the vicinity of R_0 . This is also observed for atmospheric dust devils (Sinclair, 1973). The overestimation has several reasons. The Rankine vortex model does not take into account the friction force and, consequently, neglects the radial inflow. In addition, the model assumes a constant vorticity within the core region. For vortex A and B, the vorticity is approximated by the mean value in the center. There, ζ reaches its maximum. Also R_0 contains uncertainties. In the Rankine model, R_0 is the position where u_{tan} becomes maximum and where the total pressure deficit reaches 50% of its central value. For vortex A and B, however, these positions are not the same and it has to be decided which value is taken for Equation 9. Therefore, there might be a combination of ζ and R_0 that fits the tangential velocities shown in Figure 11 even better. The above mentioned values for ζ and R_0 enable together with the Rankine model an estimation of the core pressure drop using $\rho\omega^2 R_0^2$. With $\rho = 1 \text{ kg m}^{-3}$ a value of 156 mPa for vortex A and 229 mPa for vortex B is calculated. This corresponds well to the actually simulated range of p^* close to the vortices' core (100–200 mPa). The similarity of the detected vortices to the Rankine vortex model confirms again that they are similar to atmospheric dust devils (see also Section 3.2).

Table 4 indicates that the absolute radial and vertical velocities of the vortices close to the vortex core tend to be smaller if no surface friction is considered. The decrease in the mean radial ($\overline{\{u_{\text{rad}}\}}$) and vertical ($\overline{\{w\}}$) component is about 10% and 80%, respectively. These findings are additionally supported by Figure 11. The time-averaged vertical velocity is nearly zero for the vortex extracted from simulation RA1009A3* (vortex B). Instead, vortex A shows much higher vertical velocities of $\sim 10 \text{ cm s}^{-1}$, especially near the center. The transects of the radial velocity show a completely different behavior, however. Vortex A displays the expected constant and symmetric inflow along the center (positive u_{rad}), while vortex B shows an inflow at the left and an outflow at the right side of the vortex core indicated by a change of sign. Figure 12, where time-averaged horizontal cross sections of the perturbation pressure together with vectors of the horizontal flow field are shown, clarifies this behavior. The horizontal flow along the transect at $y = 0 \text{ mm}$ is continuously directed in the positive x -direction for vortex B. Therefore, u_{rad} , defined as positive if there is an inflow into the vortex core, must change its sign in Figure 11.

From a fluid dynamics perspective, the dependency of the dust devil radial and vertical velocity component on the velocity boundary conditions is explained as follows. The wind around the vortices results from a balance of the pressure gradient, centrifugal, and frictional force, whereas the friction is responsible for creating the radial inflow into the vortex (see also Kurgansky et al., 2016). The result is a pronounced, rotating inflow into the vortex center and a single, well-defined vortex is created, as illustrated in Figure 12 (left). Due to the incompressibility of the flow, the air must move upwards and high vertical velocities occur in the central region. However, if no friction at the plates is considered, no radial inflow develops and the vortex is described by the cyclostrophic balance, which explains the reduced radial and vertical velocities in RA1009A3*.

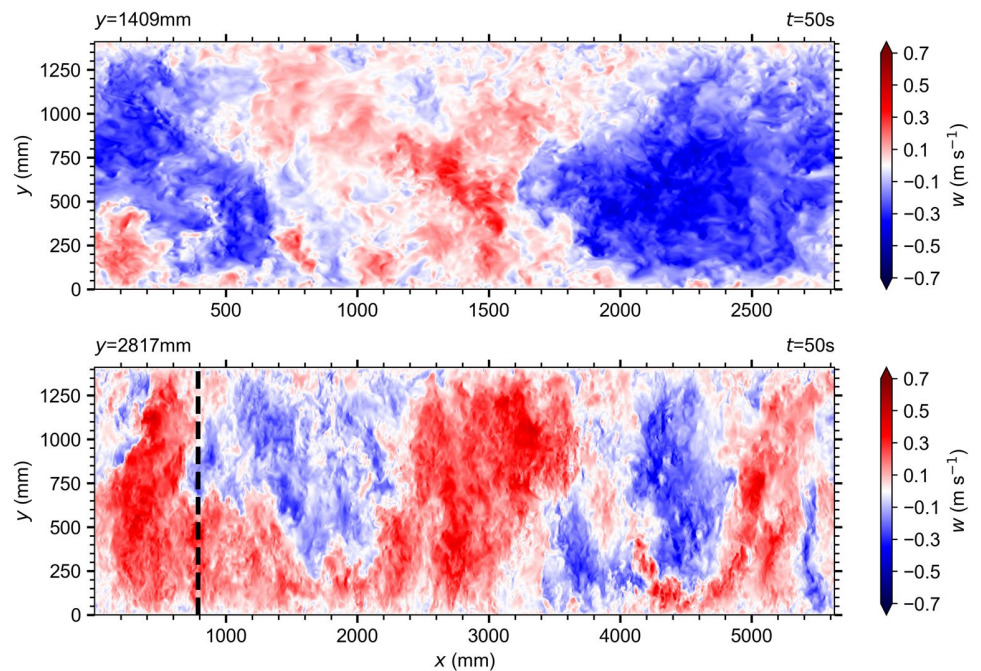


Figure 10. Vertical cross sections of the instantaneous vertical velocity at the center after 50 s simulated time taken from simulation RA1010A2 (top) and RA1010A4 (bottom). The black line indicates the position of a dust devil center defined at the first grid point above the bottom surface.

Furthermore, the size of vortices increases under no-slip conditions (see Figure 12). It is obvious that the vortex A influences the entire horizontal flow, whereas the vortex B is more concentrated. The size increase is additionally supported by the lifetime-averaged radius (\bar{r}), which has a population mean of 7.46 mm in the case of no-slip conditions and 6.12 mm if free-slip conditions are used. These results are consistent with results from Wilkins et al. (1975), who also found larger vortices formed in the friction layer.

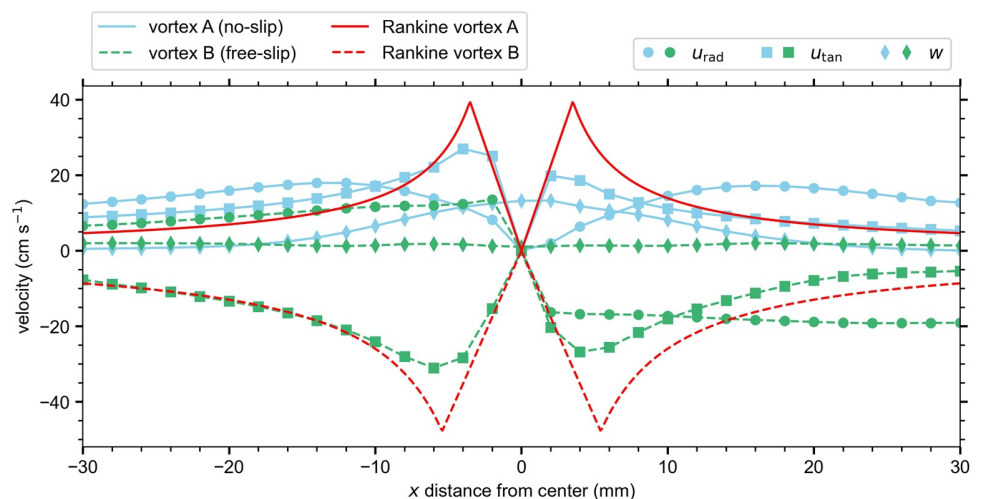


Figure 11. Horizontal transects at 1 mm height through the centers of the time-averaged vortices with the longest lifetimes. Blue solid lines describe the velocities for the vortex in RA1009A3 (vortex A), whereas green dashed lines indicate the velocities for the vortex in RA1009A3* (vortex B). Circles indicate radial (u_{rad}), squares indicate tangential (u_{tan}), and diamonds indicate vertical velocity (w). The radial velocity is defined as positive toward the center and the tangential velocity is defined as positive in the counterclockwise (cyclonic) direction. Red lines illustrate profiles according to the Rankine vortex model.

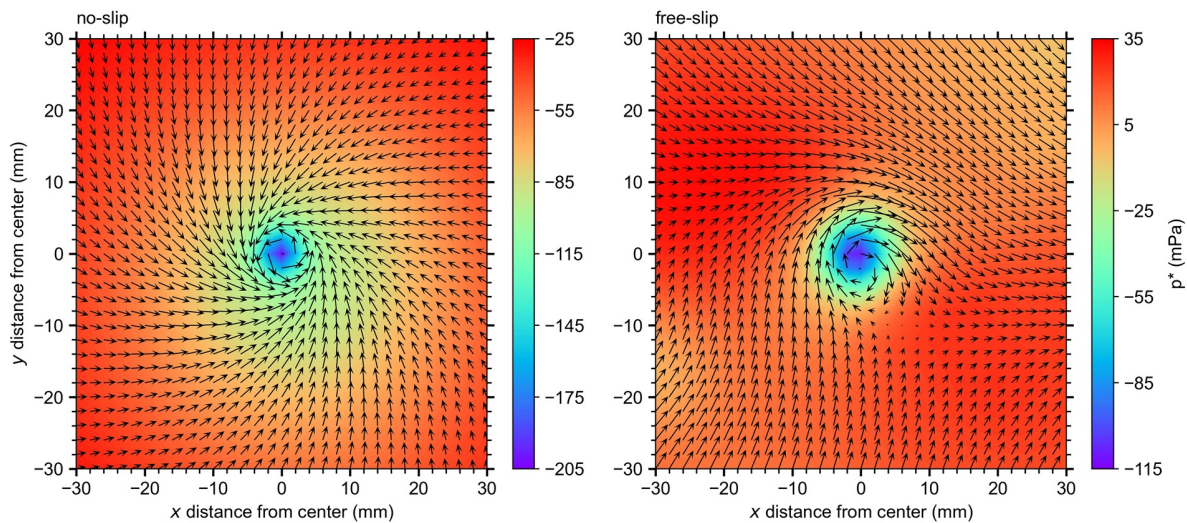


Figure 12. Time-averaged horizontal cross sections of the perturbation pressure at 1 mm height for the vortex with the highest lifetime derived from simulation RA1009A3 (left, vortex A) and RA1009A3* (right, vortex B). Note the different scales. Additionally, vectors of horizontal velocity are shown.

The pressure drop associated with vortex formation is larger with surface friction, an effect that has already been reported by Zhao et al. (2004). Figure 12 highlights this finding for the single vortices A and B. Vortex A has a mean core pressure drop of -202 mPa, whereas vortex B has a value of -110 mPa. In addition, the maximum pressure drop during the vortex lifetime averaged over all detected dust devils ($\overline{|p^*|_{\max}}$) increases by more than 50% from 107 mPa in RA101009* to 164 mPa in RA101009. Vorticity increases significantly if surface friction is considered because the vorticity correlate with the magnitude of the central pressure low.

The more intense vortices are explained by the budget equation for the vertical vorticity given in Section 1.2. As already discussed, the near-surface flow convergence in the vortex core is reduced under free-slip conditions due to the lower or even missing radial inflow (less vorticity concentration). Therefore, ζ_{div} contributes less to the generation and maintenance of vorticity. An analysis of the horizontally averaged ζ_{div} around the vortex core (11×11 grid points) at the second grid point above the surface yields absolute values between 200 and $2,500 \text{ s}^{-2}$ during the lifetime of vortex A. Vortex B show values between 0 and 400 s^{-2} . Also, the horizontally averaged ζ_{twis} is much smaller for vortex B (0 – 100 s^{-2}) than for vortex A (100 – $1,400 \text{ s}^{-2}$) because there is less shear without friction. Both effects significantly decrease the vertical vorticity of the vortices and, consequently, the pressure drop in the center of vortex B. The remaining budget terms in Equation 1 causes an overall reduction of absolute vertical vorticity in both vortex centers. Low values of $|\zeta|$ are horizontally advected toward the core, high values are vertically advected upward away from the center, and molecular diffusion balances extreme values. The vertical advection in vortex B is much weaker (0 – 50 s^{-2}) compared to the horizontal (0 – 500 s^{-2}) due to low vertical velocities in the core. In vortex A, however, both advection terms are of similar size (100 – $1,000 \text{ s}^{-2}$).

A consequence of the reduced vertical vorticity increase through convergence and twisting is the reduced averaged lifetime under free-slip conditions. A vortex that develops under no-slip conditions has a mean lifetime of 1.22 s, which is about 70% higher than the averaged lifetime under free-slip conditions (0.73 s). Therefore, surface friction is important for maintaining vortices once they are created. The longest vortex lifetime in RA101009 is 8.57 s and is 5.26 s in RA101009*.

4. Summary and Conclusion

This study extensively investigated dust devil-like vortices using DNS of RBC for the first time. The special focus was on the effects of the Rayleigh number, aspect ratio, and surface friction on dust devil statistics. Previous studies mostly used LES to investigate vertical vortices in convective flows (e.g., Giersch et al., 2019;

Kanak, 2006; Raasch & Franke, 2011) or they analyzed dust devils as a side-note in their studies (e.g., Mellaudo, 2012). Especially, DNS results of dust devils in flows with Rayleigh numbers larger than 10^7 are lacking in the literature (see Cortese & Balachandar, 1993; Fiedler & Kanak, 2001; Iijima & Tamura, 2008).

After introducing the numerical methods and setups that were used, it was shown that dust devil-like vortices were frequently identified in a simulation, where a Rayleigh number of 10^{10} , an aspect ratio of 3, and no-slip boundary conditions were applied. The vertical vortices mainly occurred at the cell vertices and edges of the convective cells, similar to LES results (e.g., Giersch et al., 2019; Kanak, 2005). However, due to an increase in structure size up to the horizontal domain size, the cellular pattern disappeared over time. Dust devil-like structures preferentially occurred in regions, where strong near-surface convergence lines were clustered. This is in agreement with Raasch and Franke (2011), who also investigated dust devils in a domain that was too small to allow for an undisturbed development of the cellular pattern. However, their statistics were not influenced by the broadening effect.

DNS results were compared to existing LES data with focus on the three-dimensional structure of dust devil-like vortices. Dust devils simulated with DNS and LES displayed similar results. Only differences in the distribution of the vertical velocity around the vortex center arose, which were attributed to the discrepancies of the underlying setups that were used to investigate dust devils with DNS and LES. The similarity of results suggests that there is no need to explicitly resolve the small-scale turbulence near the ground and that the surface layer parameterizations in LES do not have a dramatic effect on the simulated dust devil-like structures. The results from LES are reliable if a sufficiently small grid spacing is used. This is especially true for larger dust devils. However, the exact value of a sufficiently small grid spacing for acquiring converged, quantitative dust devil information is still unknown in LES. This grid spacing will be determined in a follow-up study in which nesting techniques enable LES with 1 m grid spacing and even lower.

One of the main control parameters in RBC that significantly influences flow properties and structures is the Rayleigh number (e.g., Stevens et al., 2018). Our results suggested that a minimum Rayleigh number of 10^7 was necessary for the development of dust devil-like vortices, which is much less than the Rayleigh number in the atmosphere ($\sim 10^{18}$). Higher values increased the number of detected vortices significantly, from one single vortex in the simulation with $Ra = 10^7$ to 3,834 vortices in the run with $Ra = 10^{11}$ (70 s detection time). In addition, the higher the Rayleigh number, the higher the translation speeds and dust devil intensities, which were accompanied by an increase in pressure drop, vertical vorticity, and velocity. However, the averaged lifetime of dust devils decreased if the Rayleigh number increased. Nevertheless, long-lasting vertical vortices of around 10 s still developed.

Another parameter known to significantly modify flow properties in RBC is the aspect ratio (e.g., Bailon-Cuba et al., 2010). Due to limited computing power, only aspect ratios between 2 and 4 were addressed in this study. Our results, as well as the results from previous studies (e.g., Stevens et al., 2018; von Hardenberg et al., 2008), showed that even an aspect ratio of four was far from able to resolve large-scale convective patterns in RBC. Dust devil statistics were established for each aspect ratio. Interestingly, no statistically significant effect of the aspect ratio on most of the vortex properties was identified, although large-scale flow circulations were captured more realistically within larger model domains. Only the number, averaged translation speed, and probability for very strong dust devils increased. These findings, except the relation between aspect ratio and translation speed, were directly attributed to the larger horizontal domain for higher aspect ratios.

Velocity boundary conditions are still being researched in connection with convective vortices due to the potentially high influence of friction on the vortex properties (e.g., Gu et al., 2010; Raasch & Franke, 2011). Our DNS results confirmed the significant influence of surface friction. With free-slip conditions, the number of detected vortices increased by a factor of 30. Mean translation speeds and tangential velocities were higher by a factor of 2.3 and 1.3, respectively. However, because there was no surface friction, dust devil-like vortices were in approximately cyclostrophic balance, with reduced radial, and consequently, vertical velocities. Furthermore, lifetimes, radii, and intensities were much smaller under free-slip boundary conditions. Therefore, friction is essential for strengthening and maintaining dust devil-like vortices.

This study was a first step toward the simulation of dust devils with DNS. Additional influencing factors, such as the background wind or surface heterogeneities, were not regarded. It is expected that conclusions

would be similar to LES studies (e.g., Giersch et al., 2019; Kanak, 2005; Raasch & Franke, 2011) or field campaigns (e.g., Renno et al., 2004; Ryan, 1972; Sinclair, 1969). Furthermore, it is possible that the restricting domain size in this study had an effect on the dust devil statistics. For this reason, simulations with very high aspect ratios that allow for an undisturbed development of large-scale structures in RBC should be performed. High aspect ratios, together with extended simulation time, would further improve the dust devil statistics, as well. Nevertheless, the general effects of the Rayleigh number, aspect ratio, and surface friction on dust devils were shown clearly.

In follow-up studies, we will compare our DNS results to laboratory-like experiments that were performed on the same scale (Loesch & du Puits, 2020). The Barrel of Ilmenau, which is a large-scale experimental facility to investigate turbulent convection, and hence dust devil-like structures, is an appropriate environment for creating the experimental data (e.g., du Puits et al., 2013). The comparison will allow us to identify possible differences and reveal the weaknesses and strengths of each method used to analyze convective vortices. However, because our numerical results produced maximum horizontal vortex sizes on the order of several tens of millimeters, it will require some technical effort to detect dust devil-like vortices of such small scale in the laboratory.

Appendix A: Validation of PALM's DNS Mode

For the validation of the DNS mode, the setup NsD of Mellado (2012), who investigated free (unbounded) convection over a heated, rigid, and impermeable plate with the numerical model Tlab (<https://github.com/turbulencia/tlab>), is repeated with PALM. The setup requires constant buoyancy and no-slip boundary conditions for the velocities at the bottom. At the top, free-slip boundary conditions with Neuman conditions for scalars are used. To save computational costs, the simulation with $1,024 \times 1,024 \times 768$ grid points introduced in the appendix of Mellado (2012) is simulated. He demonstrated that this number of grid points is already sufficient to capture the physics of the setup realistically. However, the results, which are used here for comparison to the PALM data, are taken from the high-resolution NsD case published in the main part of Mellado (2012). The NsD setup from the appendix is defined through the so-called reference Rayleigh number

$$Ra_0 = \frac{b_0 L_0^3}{\nu \kappa} = 9 \times 10^8, \quad (\text{A1})$$

where ν is equal to κ ($Pr = 1$) and is set to $1.76 \times 10^{-5} \text{ m}^2 \text{ s}^{-1}$. For the constant buoyancy at the surface b_0 , a value of 0.40875 m s^{-2} is assumed. Setting the horizontal model extent L_0 to 0.88 m yields $Ra_0 = 9 \times 10^8$ as defined in Equation A1. The above mentioned number of grid points results in a resolution of 0.86 mm and a model height of 0.66 m. As in Mellado (2012), the simulations are stopped when the boundary layer thickness is equal to about $0.3L_0$ to avoid finite-size effects on the results. During initialization of the model, zero velocities and a strong unstably stratified layer close to the bottom plate with neutral stratification above are assumed. The initial potential temperature profile is constructed using the error function similar to Equation 5 but without assuming symmetry. The only real difference in the NsD setup compared to Mellado (2012) is the way how horizontal perturbations are initiated to trigger off convection at the beginning of the model run. Mellado (2012) applied initial broadband perturbations to the buoyancy field, whereas in the PALM setup uniformly distributed random perturbations are imposed on the horizontal velocities.

For evaluating the validation run NsD, the temporal evolution of the scaled gradient thickness δ_g^+ is considered. If not otherwise stated, symbols, variables, and scaling are the same as in the original publication of Mellado (2012). δ_g^+ contains all mean surface properties in one quantity and can be seen as a measure of the diffusive wall layer thickness (Mellado, 2012). In addition to δ_g^+ , the vertical profiles of the scaled molecular and turbulent contribution to the overall heat flux at the end of the simulation are discussed. All quantities are displayed in Figure A1. The δ_g^+ curves are very similar. In both cases, a maximum right after the start of the simulation occurs, combined with a rapid decrease afterward, and followed by a slight increase until the end of the simulation. The only difference is the initial transition to a near-steady behavior, marked by the initial overshooting of δ_g^+ and the subsequent decline, which takes more time in the PALM simulation.

This might be attributed to the different ways in which perturbations are imposed on the flow at the beginning of the runs. Mellado (2012) imposed initial perturbations on the buoyancy field by using a random field characterized by a zero mean value and a Gaussian power spectral density centered at some given spatial frequency. Thus, more energy could be explicitly distributed into the smaller scales, where dissipation is maximum. This procedure allows a more rapid development into a steady-state compared to imposing random perturbations on the velocity field by using uniformly distributed random numbers, as it is done by default in the PALM simulation.

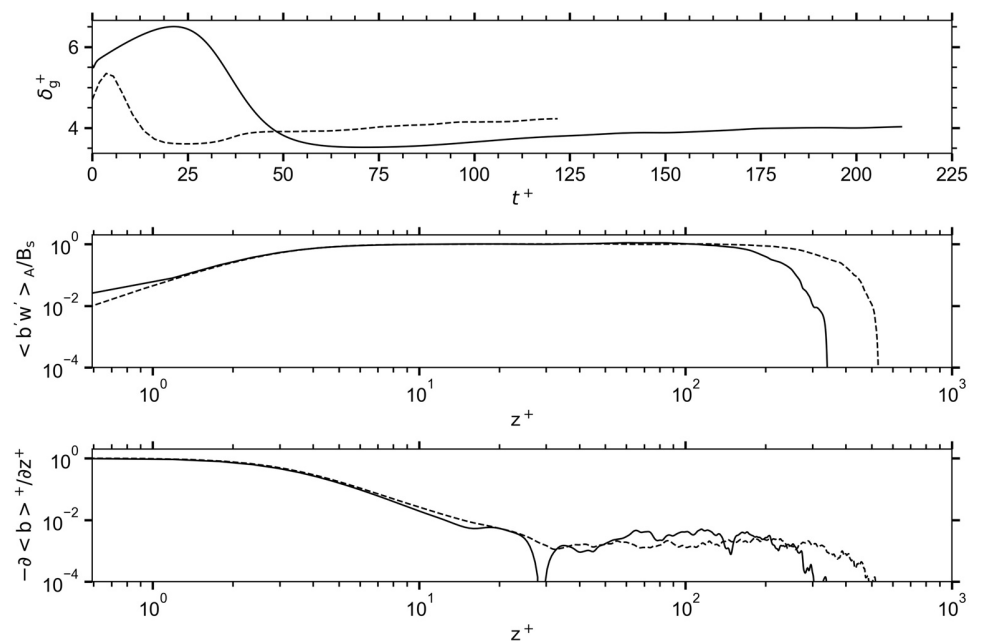


Figure A1. Comparison of simulation results from the original NsD case published in Mellado (2012) (dashed lines) with results from a similar setup simulated with the model PALM (solid lines). The following quantities are displayed (from top to bottom): the temporal evolution of the gradient thickness scaled with the diffusion length as well as the vertical profiles of the horizontally averaged turbulent and molecular contribution to the total buoyancy flux scaled with the buoyancy flux at the surface at the end of the simulation. The time is measured with respect to the time scale of the diffusion process and the height is specified in relation to the diffusion length. For more information to symbols, variables, or scaling see Mellado (2012).

The vertical profiles of the turbulent and molecular sensible heat flux also show similar shapes for both runs. The turbulent heat flux profiles overlap except close to the bottom surface and at the boundary layer top. A difference at the bottom is, in fact, only visible at the first grid point of the PALM domain. This difference is due to the higher resolution and the less dissipative advection scheme used in Mellado (2012). Both enable a better representation of the physical situation in the near-wall region. The deviations in the turbulent heat flux for 200 wall units and more are related to the different heights of the boundary layers at the end of the simulations. In both cases, the simulations are stopped when the boundary layer height is roughly $0.3 L_0$. For the original high-resolution NsD case, L_0 is larger because a reference Rayleigh number of 3.6×10^9 instead of 9×10^8 was chosen (see also Equation A1). As a consequence, the boundary layer thickness at the end is higher. The different boundary layer thicknesses are also the explanation for the deviations that are visible in the profiles of the molecular heat flux for 300 wall units and more. The remaining lower part of the profiles can be approximately regarded as identical.

The final value for the gradient thickness is 4.22 in the original simulation, whereas PALM simulates a value of 4.03. This difference can be again explained by the different boundary layer thicknesses already men-

tioned above. They indicate that the turbulent flow in the original simulation is in a later state compared to the flow in the PALM simulation. Because there is a slight increase in δ_g^+ with time, it is expected that the gradient thickness of the PALM simulation would match even better if both boundary layer heights would have been the same at the end of the simulation. This is also true for the convection length scale and convective Rayleigh number defined in Mellado (2012), which show smaller values in the PALM simulation due to the shallower boundary layer.

Appendix B: Resolution Requirements

The most important requirement to perform accurate DNS is to resolve the finest length scales of the fluid. For flows with Prandtl numbers of $\mathcal{O}(1)$, the Kolmogorov length scale $\eta_K = (\nu^3 / \epsilon)^{1/4}$ (Kolmogorov, 1941) and the Obukhov-Corrsin scale $\eta_\theta = (\kappa^3 / \epsilon)^{1/4} = \eta_K Pr^{-3/4}$ (Corrsin, 1951; Obukhov, 1949) must be adequately resolved (e.g., Shishkina et al., 2010). ϵ indicates the local, instantaneous energy dissipation rate per unit mass (e.g., Hamlington et al., 2012; Pope, 2000; Shishkina et al., 2010)

$$\epsilon = \frac{\nu}{2} \left(\frac{\partial u'_i}{\partial x_j} + \frac{\partial u'_j}{\partial x_i} \right)^2, \quad (\text{B1})$$

with u'_i the fluctuation of the velocity component u_i with respect to the horizontal mean of the velocity field. Note, the Obukhov-Corrsin scale is sometimes called the Batchelor scale (e.g., Hay & Papalexandris, 2019; Stevens et al., 2010), which is, strictly speaking, wrong. The Batchelor scale is defined as $\eta_B = (\nu \kappa^2 / \epsilon)^{1/4} = \eta_K Pr^{-1/2}$ and can be considered as the most restrictive length scale for $Pr \gg 1$ (Shishkina et al., 2010). Additionally, an accurate DNS must be able to resolve the steep velocity and temperature gradients close to the wall (Grötzbach, 1983).

The most common criterion that enables an *a priori* calculation of the allowed maximum grid width $h_{\max} = \max(\Delta x, \Delta y, \Delta z)$ in the bulk of the flow is

$$h_{\max} \leq \pi \eta_K = \pi \left(\frac{\nu^3}{\epsilon} \right)^{1/4}, \quad (\text{B2})$$

$$\pi \eta_K \approx \pi H \left(\frac{Pr^2}{RaNu} \right)^{1/4}, \quad (\text{B3})$$

$$h_{\max} \leq \pi \eta_\theta = \pi \left(\frac{\kappa^3}{\epsilon} \right)^{1/4}, \quad (\text{B4})$$

$$\pi \eta_\theta \approx \pi H \left(\frac{1}{RaPrNu} \right)^{1/4}. \quad (\text{B5})$$

Here, Nu is the global Nusselt number, which is calculated based on the temporarily and spatially averaged turbulent heat flux (e.g., Bailon-Cuba et al., 2010; Scheel et al., 2013)

$$Nu = 1 + \frac{H}{\kappa \Delta \theta} \langle w\theta \rangle_{V,t}, \quad (\text{B6})$$

where $\langle \cdot \rangle_{V,t}$ denotes a time and volume average over the whole model domain. The above criterion for the grid width was originally proposed by Grötzbach (1983). However, he uses the less restrictive definition of a mean grid width $(\Delta x \Delta y \Delta z)^{1/3}$, whereas Stevens et al. (2010) suggests to take the largest grid width in any spatial direction (h_{\max}). When $Pr < 1$, which is true for the flows under study, equation (B2) is more restrictive and determines the maximum allowed grid spacing. To enable a calculation of h_{\max} , the Nusselt number has to be known in advance. For estimating the Nusselt number, a formula derived by Scheel and Schumacher (2016) is used, which relates the Nusselt and the Rayleigh number for $Pr = 0.7$ as follows:

$$Nu = 0.15 Ra^{0.29}. \quad (\text{B7})$$

This formula allows an estimation of Nu for a given Rayleigh number and the result is used in Equation (B3) to calculate the maximum allowed grid width in the bulk of the flow before running the simulations. Regarding the setups in Table 1, Equation B3 is always fulfilled because the calculated h_{\max} is larger than 3 mm for each simulation.

Additionally, the grid resolution must be evaluated *a posteriori* similar to Bailon-Cuba et al. (2010) by using Equation B2 together with the temporarily and horizontally averaged dissipation rate $\langle \epsilon(z) \rangle_t$:

$$\frac{h_{\max}}{\eta_K(z)} = h_{\max} \left(\frac{\nu^3}{\langle \epsilon(z) \rangle_t} \right)^{-1/4} \leq \pi. \quad (\text{B8})$$

Figure B1 shows the above ratio over the normalized domain height for all different Rayleigh numbers and velocity boundary conditions used in this study. As expected, the profiles for no-slip boundaries peak close to the plates and are nearly constant in between, whereas the profile for the free-slip boundaries is approximately constant over the whole cell. The resolution criterion (B8) is also fulfilled for RA1010A2 and RA1010A4, which show a similar profile to simulation RA1010A3.

The criterion of Grötzbach (1983) is based on simulations with Rayleigh numbers up to 3.81×10^5 ($Pr = 0.7$) and assumes that the TKE dissipation is flat (i.e., height constant) and equals the production of TKE through buoyancy. This is especially not true in the near-wall region (Figure B1, see also Scheel & Schumacher, 2016). Thus, a different *a priori* resolution criterion must be applied to ensure that the velocity and thermal boundary layers are well-resolved. Shishkina et al. (2010) developed such a criterion based on the laminar Prandtl-Blasius boundary layer equations. It reads for $3 \times 10^{-4} \leq Pr \leq 1$:

$$h_{\max} \leq 2^{-3/2} a^{-1} Nu^{-3/2} H Pr^{0.5355 - 0.033 \log(Pr)}. \quad (\text{B9})$$

Here, a is an empirical value of 0.482. The Nusselt number can be again estimated in advance of the simulation using Equation B7. The resulting grid spacings that would guarantee a perfectly resolved DNS (according to Equation B9) are listed in Table 1. It is obvious that the cases for $Ra \geq 10^9$ insufficiently resolve the

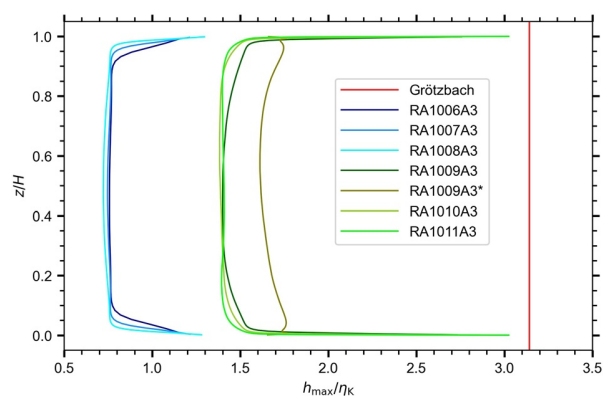


Figure B1. Ratio of the applied maximum grid width h_{\max} and the Kolmogorov scale η_K for all conducted simulation with aspect ratio 3. Blue lines show the ratios for simulations with 1 mm grid spacing whereas green lines represent the ratios for simulations with 2 mm resolution. The red line indicates the limit π of the resolution criterion (B8).

boundary layers at the plates. To clarify the effect of this insufficient resolution on the dust devil statistics, a grid resolution study is performed. Results and conclusions of that study are discussed in Appendix C. Regardless of the insufficiently resolved boundary layers, the resolution criterion of Grötzbach (1983), which has been often used as the standard for evaluating the grid spacing (e.g., Bailon-Cuba et al., 2010; Shishkina & Wagner, 2007, 2008; Stevens et al., 2010), is fulfilled in all cases.

Appendix C: Grid Resolution Study

To estimate the effect of insufficiently resolved boundary layers near the plates on the dust devil statistics, three additional simulations with a Rayleigh number of 10^9 , no-slip boundary conditions, an aspect ratio of $\Gamma = 3$ and grid spacings of 8, 4, and 1 mm have been conducted. Here, a grid spacing of 1 mm is regarded as a sufficient resolution according to Equation B9. In addition to these three single simulations, an ensemble of 10 members has been created for the case with 2 mm grid spacing, which is the resolution used for the main simulations introduced in Section 2.1 having a Rayleigh number larger than 10^8 . With this ensemble, confidence intervals of the ensemble mean and standard deviation can be calculated with the aim to check the statistical significance of differences and similarities caused by differently resolved simulations. The focus in this section is on $Ra = 10^9$ because lower Rayleigh numbers do not show a sufficiently large number of dust devils for statistical analysis (see Section 3.3) and larger Rayleigh numbers would exceed the computational resources. The limited computing power is also the reason why an ensemble is only created for the simulation with 2 mm grid resolution. For example, the single model run with 1 mm grid spacing, $1,920 \times 1,920 \times 640$ grid points, a simulation time of 100 s, and about 80,000 time steps consumes about 41 h CPU time on 4096 PEs of an Atos/Bull system equipped with Intel Xeon Platinum 9242 processors.

For a meaningful comparison of dust devil characteristics between differently resolved simulations, the vortex detection and analysis described in Section 2.2 has to be unified from a physical point of view. Once the dust devil centers are connected to tracks, the time period and distance, in which/where the algorithm tries to find the next dust devil center of the same track, must be the same. For all simulations, the time period is equal to three temporarily averaged model time steps of the 8 mm run (43.55 ms). Simultaneously, the maximum allowed distance to the next dust devil center of the same track must be less than or equal to 16 mm (two times the grid spacing of the 8 mm run). The physical detection height is (roughly) 4 mm in all cases, which corresponds to the first, second, third, or fifth grid point above the surface for a grid spacing of 8, 4, 2, and 1 mm, respectively.

To evaluate the convergence behavior of the dust devil statistics with decreasing grid spacing, a significance interval for the simulation with 2 mm resolution is determined as follows. At first, the 95% confidence interval of the ensemble mean μ is calculated. For example, the confidence interval for the ensemble mean of the total number of detected dust devils is [93.13, 105.87] with a central value of 99.5 (see Figure C1). Second, the 95% confidence interval of the standard deviation σ is calculated, which is [6.13, 16.27] for N . Subsequently, the upper limit of the significance interval is determined by adding the upper limit of the confidence interval of the mean (i.e., 105.87) to 2 times the upper limit of the confidence interval of the standard deviation (i.e., 32.54). For N , this results in a value of 138.41. The lower limit of the significance interval is calculated in the same way using the lower limit from [93.13, 105.87], which yields a value of 60.59. In these calculations, 2 standard deviations are considered because they cover roughly 95% of a normally distributed data set assumed here. Finally, the statistics for the simulations with 8, 4, and 1 mm grid widths are compared to the significance intervals taken from the ensemble members. If a value lies within the significance interval, the difference is considered to be statistically insignificant. In other words, it is very likely that if a value does not lie within the significance interval, the respective simulation is not part of the same ensemble and differences are statistically significant.

Figure C1 shows the averaged bulk characteristics and significance intervals of all relevant quantities for the differently resolved simulations. Here, a lifetime of 1.07 s and more is considered as long-lived because this value indicates the maximum of the lifetime frequency distribution for the 8 mm run (see also Section 2.2). N and τ are considered as almost converged for every resolution because all values are within the respective significance interval. However, for \bar{v}_1 and \bar{v} , a grid spacing of at least 4 mm and for $|p^*|_{\max}$, $\{u_{\text{tan}}\}_{\max}$, $\{u_{\text{rad}}\}_{\max}$, and $\{u_h\}_{\max}$, a grid spacing of at least 2 mm is necessary to adequately capture the statistics.

$|\zeta|_{\max}$ and $\{w\}_{\max}$ are not converged at all because the values for the run with 1 mm resolution (408.75 s^{-1} , 45.68 cm s^{-1}) are still far away from the upper significance interval limits (341.28 s^{-1} , 35.73 cm s^{-1}). The large deviation in the vorticity arises from the way it is calculated. In the discretized form of Equation 6, smaller grid spacings automatically create larger values because similar velocity gradients are evaluated across smaller distances. Therefore, the vorticity become larger and larger with decreasing grid width, as also the theoretical model of a line vortex suggests. To make the quantitative vorticity values in differently resolved simulations comparable, Equation 6 should have been evaluated based on the same distance, that is 8 mm. Because this did not happen by mistake, no convergence in the vorticity occurs. The vorticity eval-

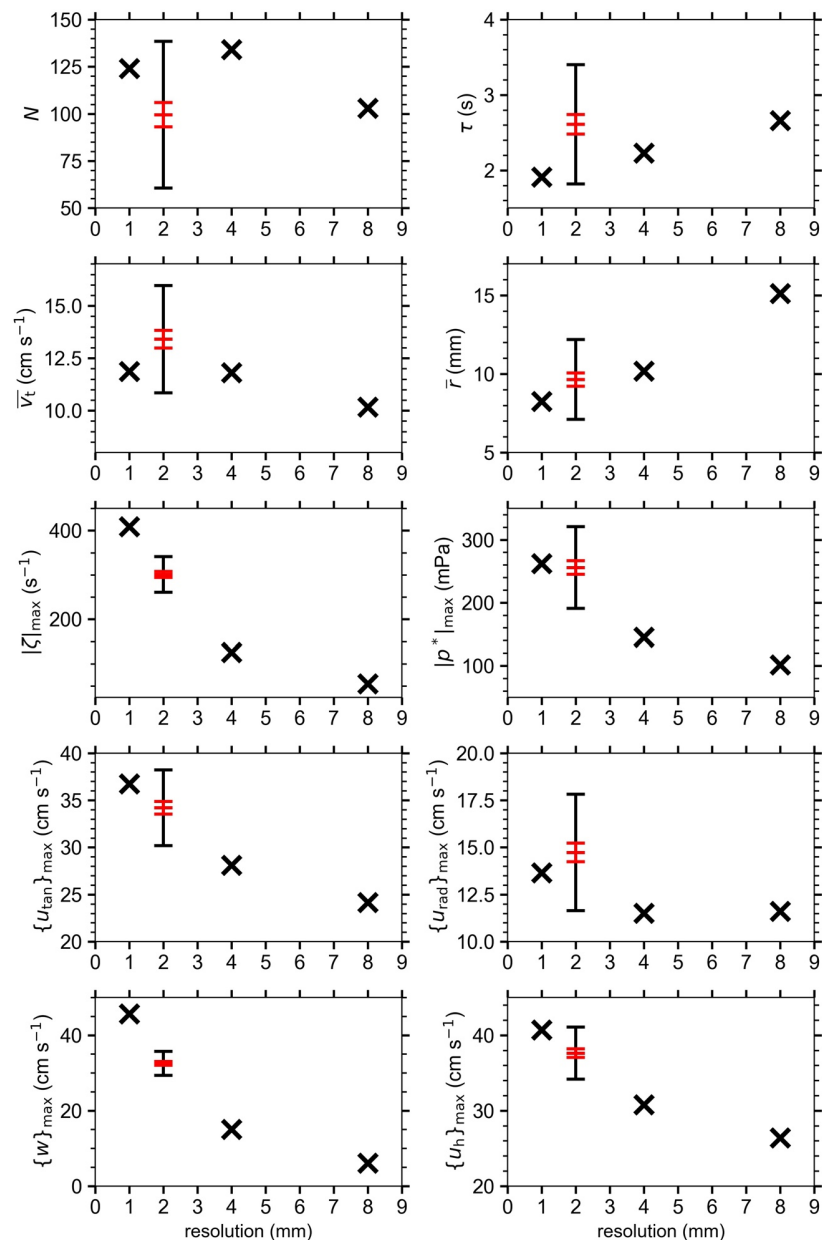


Figure C1. Dust devil characteristics for a Rayleigh number of 10^9 and an aspect ratio of 3 using a grid resolution of 8 mm, 4 mm, 2 mm, and 1 mm. Only long-lived vortices with a lifetime of more than 1.07 s are considered. Crosses mark the averaged values over all N dust devils. For a grid spacing of 2 mm, the 95% confidence interval of the ensemble mean with its central value (red lines) and the statistical significance interval (black lines, for explanation see text) are shown.

uated along the same distance is expected to be converged for a resolution of 2 mm because the pressure drop is already converged and vertical rotation and pressure reduction in the center are strongly connected to each other in dust devil-like vortices, as it is proposed by the theoretical model of a Rankine vortex. The reason for the large deviation in $\overline{\{w\}_{\max}}$ between all differently resolved simulations is explained through the highly localized maximum values of w that occur in the dust devil center. Our results show two pronounced regions of maximum vertical velocity (see Figure 6). These regions have extent of 10–15 mm. This spatial extent of localized vertical velocity maxima is small compared to the regions associated with tangential and radial velocity maxima. Capturing smaller regions with strong velocity fluctuations requires higher resolution. Therefore, a grid spacing of 2 mm is not fine enough to resolve the pronounced maximum values of w in the dust devils, but it is sufficient for the maximum values of tangential and radial velocity.

Limited computational resources do not allow a grid resolution study for higher Rayleigh numbers (i.e., 10^{10} and 10^{11}). With the above mentioned results for $Ra = 10^9$ and guaranteeing that the resolution criterion of Grötzbach (1983) is always fulfilled, it is assumed that a grid spacing of 2 mm is also sufficient for Rayleigh numbers up to 10^{11} , although the gap to fulfill criterion (B9) (~ 0.5 mm grid width for $Ra = 10^{10}$ and $Ra = 10^{11}$) is even larger compared to 1 mm for $Ra = 10^9$.

To sum up, a 2 mm grid spacing, which fulfills the resolution criterion after Grötzbach (1983), is fine enough to adequately capture most of the dust devil properties. However, quantitative comparisons of $\overline{\{w\}_{\max}}$ and $|\zeta|_{\max}$ between simulations with different Ra , Γ , or velocity boundary conditions are avoided in this study to account for the findings mentioned in this section. But also quantitative information about the other quantities should be treated carefully because the grid resolution study has been only performed for $Ra = 10^9$. In addition, the estimates of the statistics from the main simulations (see Table 1) are based on just one ensemble member. Furthermore, single statistical values, like averaged velocities or pressure drops, are highly influenced by the detection/analysis height (see Section 2.2). A qualitative comparison of all regarded quantities is possible though without constraints.

Data Availability Statement

All simulations were performed on the Cray XC40 and Atos system of the North-German Supercomputing Alliance (HLRN-3/4) located in Berlin and Göttingen. The LES model PALM is freely available (revision 4221, <http://palm.muk.uni-hannover.de/trac/browser/?rev=4221>). For the validation of PALM's DNS mode, revision 3867 was used. The PALM output used to generate figures and tables is accessible via <https://doi.org/10.25835/0071502>. Also, the user-specific code for detecting dust devils, model steering files, and scripts for post-processing the raw data are stored there.

References

- Bailon-Cuba, J., Emran, M. S., & Schumacher, J. (2010). Aspect ratio dependence of heat transfer and large-scale flow in turbulent convection. *Journal of Fluid Mechanics*, 655(1), 152–173. <https://doi.org/10.1017/S0022112010000820>
- Balme, M., & Greeley, R. (2006). Dust devils on earth and mars. *Reviews of Geophysics*, 44(3), RG3003. <https://doi.org/10.1029/2005RG000188>
- Bazdidi-Tehrani, F., Moghaddam, S., & Aghaamini, M. (2018). On the validity of Boussinesq approximation in variable property turbulent mixed convection channel flows. *Heat Transfer Engineering*, 39(5), 473–491. <https://doi.org/10.1080/01457632.2017.1312902>
- Belmonte, A., Tilgner, A., & Libchaber, A. (1994). Temperature and velocity boundary layers in turbulent convection. *Physical Review E—Statistical Physics, Plasmas, Fluids, and Related Interdisciplinary Topics*, 50(1), 269–279. <https://doi.org/10.1103/PhysRevE.50.269>
- Bluestein, H. B., Weiss, C. C., & Pazmany, A. L. (2004). Doppler radar observations of dust devils in Texas. *Monthly Weather Review*, 132(1), 209–224. [https://doi.org/10.1175/1520-0493\(2004\)132<0209:droidd>2.0.co;2](https://doi.org/10.1175/1520-0493(2004)132<0209:droidd>2.0.co;2)
- Corrsin, S. (1951). On the spectrum of isotropic temperature fluctuations in an isotropic turbulence. *Journal of Applied Physics*, 22(4), 469–473. <https://doi.org/10.1063/1.1699986>
- Cortese, T., & Balachandar, S. (1993). Vortical nature of thermal plumes in turbulent convection. *Physics of Fluids A: Fluid Dynamics*, 5(12), 3226–3232. <https://doi.org/10.1063/1.858679>
- Davies-Jones, R. (2015). A review of supercell and tornado dynamics. *Atmospheric Research*, 158–159(1), 274–291. <https://doi.org/10.1016/j.atmosres.2014.04.007>
- De, A. K., Eswaran, V., & Mishra, P. K. (2017). Scalings of heat transport and energy spectra of turbulent Rayleigh-Bénard convection in a large-aspect-ratio box. *International Journal of Heat and Fluid Flow*, 67(1), 111–124. <https://doi.org/10.1016/j.ijheatfluidflow.2017.08.002>
- Dessens, J. (1972). Influence of ground roughness on tornadoes: A laboratory simulation. *Journal of Applied Meteorology*, 11(1), 72–75. [https://doi.org/10.1175/1520-0450\(1972\)011<0072:iogrot>2.0.co;2](https://doi.org/10.1175/1520-0450(1972)011<0072:iogrot>2.0.co;2)
- du Puits, R., Resagk, C., & Thess, A. (2013). Thermal boundary layers in turbulent Rayleigh-Bénard convection at aspect ratios between 1 and 9. *New Journal of Physics*, 15, 013040. <https://doi.org/10.1088/1367-2630/15/1/013040>

Acknowledgments

This work was funded by the German Research Foundation (DFG) under Grant RA 617/31-1. Open access funding enabled and organized by Projekt DEAL.

- du Puits, R., Resagk, C., Tilgner, A., Busse, F. H., & Thess, A. (2007). Structure of thermal boundary layers in turbulent Rayleigh-Bénard convection. *Journal of Fluid Mechanics*, 572(1), 231–254. <https://doi.org/10.1017/S0022112006003569>
- El Guernaoui, O., Reuder, J., Esau, I., Wolf, T., & Maronga, B. (2019). Scaling the decay of turbulence kinetic energy in the free-convective boundary layer. *Boundary-Layer Meteorology*, 173(1), 79–97. <https://doi.org/10.1007/s10546-019-00458-z>
- Ellehoj, M. D., Gunnlaugsson, H. P., Taylor, P. A., Kahanpää, H., Bean, K. M., Cantor, B. A., et al. (2010). Convective vortices and dust devils at the phoenix mars mission landing site. *Journal of Geophysical Research*, 115(E4), E00E16. <https://doi.org/10.1029/2009JE003413>
- Gheynani, B., & Kanak, K. M. (2001). Rayleigh-Bénard convection as a tool for studying dust devils. *Atmospheric Science Letters*, 2(1), 104–113. <https://doi.org/10.1006/asle.2001.0043>
- Gheynani, B. T., & Taylor, P. A. (2011). Large Eddy Simulation of typical dust devil-like vortices in highly convective Martian boundary layers at the Phoenix lander site. *Planetary and Space Science*, 59(1), 43–50. <https://doi.org/10.1016/j.pss.2010.10.011>
- Giersch, S., Brast, M., Hoffmann, F., & Raasch, S. (2019). Toward large-eddy simulations of dust devils of observed intensity: Effects of grid spacing, background wind, and surface heterogeneities. *Journal of Geophysical Research - D: Atmospheres*, 124(14), 7697–7718. <https://doi.org/10.1029/2019JD030513>
- Gillette, D. A., & Sinclair, P. C. (1990). Estimation of suspension of alkaline material by dust devils in the United States. *Atmospheric Environment Part A. General Topics*, 24(5), 1135–1142. [https://doi.org/10.1016/0960-1686\(90\)90078-2](https://doi.org/10.1016/0960-1686(90)90078-2)
- Gray, D. D., & Giorgini, A. (1976). The validity of the Boussinesq approximation for liquids and gases. *International Journal of Heat and Mass Transfer*, 19(5), 545–551. [https://doi.org/10.1016/0017-9310\(76\)90168-X](https://doi.org/10.1016/0017-9310(76)90168-X)
- Greeley, R., Balme, M. R., Iversen, J. D., Metzger, S., Mickelson, R., Phoreman, J., & White, B. (2003). Martian dust devils: Laboratory simulations of particle threshold. *Journal of Geophysical Research*, 108(E5), 5041. <https://doi.org/10.1029/2002JE001987>
- Grossmann, S., & Lohse, D. (2002). Prandtl and Rayleigh number dependence of the Reynolds number in turbulent thermal convection. *Physical Review E - Statistical Physics, Plasmas, Fluids, and Related Interdisciplinary Topics*, 66(1), 016305. <https://doi.org/10.1103/PhysRevE.66.016305>
- Grötzbach, G. (1983). Spatial resolution requirements for direct numerical simulation of the Rayleigh-Bénard convection. *Journal of Computational Physics*, 49(2), 241–264. [https://doi.org/10.1016/0021-9991\(83\)90125-0](https://doi.org/10.1016/0021-9991(83)90125-0)
- Gu, Z., Wei, W., & Zhao, Y. (2010). An overview of surface conditions in numerical simulations of dust devils and the consequent near-surface air flow fields. *Aerosol Air Quality Research*, 10(3), 272–281. <https://doi.org/10.4209/aaqr.2009.12.0077>
- Hamlington, P. E., Krasnov, D., Boeck, T., & Schumacher, J. (2012). Local dissipation scales and energy dissipation-rate moments in channel flow. *Journal of Fluid Mechanics*, 701(1), 419–429. <https://doi.org/10.1017/jfm.2012.170>
- Han, Y., Wang, K., Liu, F., Zhao, T., Yin, Y., Duan, J., & Luan, Z. (2016). The contribution of dust devils and dusty plumes to the aerosol budget in western China. *Atmospheric Environment*, 126, 21–27. <https://doi.org/10.1016/j.atmosenv.2015.11.025>
- Hay, W. A., & Papalexandris, M. V. (2019). Numerical simulations of turbulent thermal convection with a free-slip upper boundary. *Proceedings of the Royal Society A*, 475(2232), 20190601. <https://doi.org/10.1098/rspa.2019.0601>
- Heinze, R., Raasch, S., & Etling, D. (2012). The structure of Kármán vortex streets in the atmospheric boundary layer derived from large eddy simulation. *Metz*, 21(3), 221–237. <https://doi.org/10.1127/0941-2948/2012/0313>
- Iijima, R., & Tamura, T. (2008). *DNS on growth of a vertical vortex in convection due to external forces*. In Paper presented at 24th Conference on Severe Local Storms. Savannah: American Meteorological Society.
- Ito, J., & Niino, H. (2013). Formation mechanism of dust devil-like vortices in idealized convective mixed layers. *Journal of the Atmospheric Sciences*, 70(4), 1173–1186. <https://doi.org/10.1175/JAS-D-12-085.1>
- Ito, J., Niino, H., & Nakanishi, M. (2010). Large Eddy simulation on dust suspension in a convective mixed layer. *Solanus*, 6(1), 133–136. <https://doi.org/10.2151/sola.2010-034>
- Jemmett-Smith, B. C., Marsham, J. H., Knippertz, P., & Gilkeson, C. A. (2015). Quantifying global dust devil occurrence from meteorological analyses. *Geophysical Research Letters*, 42(4), 1275–1282. <https://doi.org/10.1002/2015GL063078>
- Kahanpää, H., Newman, C., Moores, J., Zorzano, M.-P., Martín-Torres, J., Navarro, S., et al. (2016). Convective vortices and dust devils at the MSL landing site: Annual variability. *Journal of Geophysical Research: Planets*, 121(8), 1514–1549. <https://doi.org/10.1002/2016JE005027>
- Kanak, K. M. (2005). Numerical simulation of dust devil-scale vortices. *Quarterly Journal of the Royal Meteorological Society*, 131(607), 1271–1292. <https://doi.org/10.1256/qj.03.172>
- Kanak, K. M. (2006). On the numerical simulation of dust devil-like vortices in terrestrial and Martian convective boundary layers. *Geophysical Research Letters*, 33(19), L19S05. <https://doi.org/10.1029/2006GL026207>
- Kanak, K. M., Lilly, D. K., & Snow, J. T. (2000). The formation of vertical vortices in the convective boundary layer. *Quarterly Journal of the Royal Meteorological Society*, 126(569), 2789–2810. <https://doi.org/10.1002/qj.49712656910>
- Koch, J., & Renno, N. O. (2005). The role of convective plumes and vortices on the global aerosol budget. *Geophysical Research Letters*, 32(18), L18806. <https://doi.org/10.1029/2005GL023420>
- Kolmogorov, A. N. (1941). The local structure of turbulence in incompressible viscous fluid for very large Reynolds numbers. *Doklady Akademii Nauk SSSR*, 30(1), 301–305.
- Kurgansky, M. V., Lorenz, R. D., Renno, N. O., Takemi, T., Gu, Z., & Wei, W. (2016). Dust devil steady-state structure from a fluid dynamics perspective. *Space Science Reviews*, 203(1–4), 209–244. <https://doi.org/10.1007/s11214-016-0281-0>
- Loesch, A., & du Puits, R. (2020). *Investigation of dust devil-like vortices in a large-scale laboratory experiment using particle tracking velocimetry*. In Paper presented at EGU General Assembly 2020 (Online). European Geosciences Union.
- Lorenz, R. (2011). On the statistical distribution of dust devil diameters. *Icarus*, 215(1), 381–390. <https://doi.org/10.1016/j.icarus.2011.06.005>
- Lorenz, R. D., & Jackson, B. K. (2016). Dust devil populations and statistics. *Space Science Reviews*, 203(1), 277–297. <https://doi.org/10.1007/s11214-016-0277-9>
- Lorenz, R. D., & Myers, M. J. (2005). Dust devil hazard to aviation: a review of united states air accident reports. *Journal of Meteorology*, 30(298), 178–184.
- Maronga, B., Banzhaf, S., Burmeister, C., Esch, T., Forkel, R., Fröhlich, D., et al. (2020). Overview of the PALM model system 6.0. *Geoscientific Model Development*, 13(3), 1335–1372. <https://doi.org/10.5194/gmd-13-1335-2020>
- Maronga, B., Gryschka, M., Heinze, R., Hoffmann, F., Kanani-Sühring, F., Keck, M., et al. (2015). The parallelized large-eddy simulation model (PALM) version 4.0 for atmospheric and oceanic flows: Model formulation, recent developments, and future perspectives. *Geoscientific Model Development*, 8(8), 2515–2551. <https://doi.org/10.5194/gmd-8-2515-2015>
- Maronga, B., & Raasch, S. (2013). Large-eddy simulations of surface heterogeneity effects on the convective boundary layer during the LITFASS-2003 experiment. *Boundary-Layer Meteorology*, 146(1), 17–44. <https://doi.org/10.1007/s10546-012-9748-z>
- Mellado, J. P. (2012). Direct numerical simulation of free convection over a heated plate. *Journal of Fluid Mechanics*, 712(1), 418–450. <https://doi.org/10.1017/jfm.2012.428>

- Morton, B. R. (1966). Geophysical vortices. *Progress in Aerospace Sciences*, 7(1), 145–194. [https://doi.org/10.1016/0376-0421\(66\)90008-X](https://doi.org/10.1016/0376-0421(66)90008-X)
- Murphy, J., Steakley, K., Balme, M., Deprez, G., Esposito, F., Kahanpää, H., et al. (2016). Field measurements of terrestrial and Martian dust devils. *Space Science Reviews*, 203(1), 39–87. <https://doi.org/10.1007/s11214-016-0283-y>
- Neakrase, L. D. V., & Greeley, R. (2010). Dust devils in the laboratory: Effect of surface roughness on vortex dynamics. *Journal of Geophysical Research*, 115(E5), E05003. <https://doi.org/10.1029/2009JE003465>
- Niemela, J. J., & Sreenivasan, K. R. (2003). Confined turbulent convection. *Journal of Fluid Mechanics*, 481(1), 355–384. <https://doi.org/10.1017/S0022112003004087>
- Nishizawa, S., Odaka, M., Takahashi, Y. O., Sugiyama, K.-i., Nakajima, K., Ishiwatari, M., et al. (2016). Martian dust devil statistics from high-resolution large-eddy simulations. *Geophysical Research Letters*, 43(9), 4180–4188. <https://doi.org/10.1002/2016GL068896>
- Obukhov, A. M. (1949). Structure of the temperature field in turbulent streams. *Izvestija Akademii Nauk SSSR Seriya Geograficheskaya I Geofizicheskaya*, 13(1), 58–69.
- Ohno, H., & Takemi, T. (2010). Mechanisms for intensification and maintenance of numerically simulated dust devils. *Atmospheric Science Letters*, 11(1). <https://doi.org/10.1002/asl.249>
- Pandey, A., Scheel, J. D., & Schumacher, J. (2018). Turbulent superstructures in Rayleigh-Bénard convection. *Nature Communications*, 9(1), 2118. <https://doi.org/10.1038/s41467-018-04478-0>
- Parodi, A., von Hardenberg, J., Passoni, G., Provenzale, A., & Spiegel, E. A. (2004). Clustering of plumes in turbulent convection. *Physical Review Letters*, 92(19), 194503. <https://doi.org/10.1103/PhysRevLett.92.194503>
- Patrinos, A. A. N., & Kistler, A. L. (1977). A numerical study of the Chicago lake breeze. *Boundary-Layer Meteorology*, 12(1), 93–123. <https://doi.org/10.1007/BF00116400>
- Pope, S. B. (2000). *Turbulent flows*. Cambridge: Cambridge University Press. <https://doi.org/10.1017/CBO9780511840531>
- Raasch, S., & Franke, T. (2011). Structure and formation of dust devil-like vortices in the atmospheric boundary layer: A high-resolution numerical study. *Journal of Geophysical Research*, 116(D16), D16120. <https://doi.org/10.1029/2011JD016010>
- Rafkin, S., Haberle, R. M., & Michaels, T. I. (2001). The Mars regional atmospheric modeling system: Model description and selected simulations. *Icarus*, 151(2), 228–256. <https://doi.org/10.1006/icar.2001.6605>
- Rafkin, S., Jemmett-Smith, B., Fenton, L., Lorenz, R., Takemi, T., Ito, J., & Tyler, D. (2016). Dust devil formation. *Space Science Reviews*, 203(1), 183–207. <https://doi.org/10.1007/s11214-016-0307-7>
- Renno, N. O., Abreu, V. J., & Koch, J. (2004). Matador 2002: A pilot field experiment on convective plumes and dust devils. *Journal of Geophysical Research*, 109(E7), E07001. <https://doi.org/10.1029/2003JE002219>
- Rizza, U., Miglietta, M. M., Degrazia, G. A., Acevedo, O. C., & Marques Filho, E. P. (2013). Sunset decay of the convective turbulence with large-eddy simulation under realistic conditions. *Physica A: Statistical Mechanics and Its Applications*, 392(19), 4481–4490. <https://doi.org/10.1016/j.physa.2013.05.009>
- Roberts, B., & Xue, M. (2017). The role of surface drag in mesocyclone intensification leading to tornadogenesis within an idealized supercell simulation. *Journal of the Atmospheric Sciences*, 74(9), 3055–3077. <https://doi.org/10.1175/JAS-D-16-0364.1>
- Roberts, B., Xue, M., Schenkman, A. D., & Dawson, D. T. (2016). The role of surface drag in tornadogenesis within an idealized supercell simulation. *Journal of the Atmospheric Sciences*, 73(9), 3371–3395. <https://doi.org/10.1175/JAS-D-15-0332.1>
- Rotunno, R. (2013). The fluid dynamics of tornadoes. *Annual Review of Fluid Mechanics*, 45(1), 59–84. <https://doi.org/10.1146/annurev-fluid-011212-140639>
- Ryan, J. A. (1972). Relation of dust devil frequency and diameter to atmospheric temperature. *Journal of Geophysical Research*, 77(36), 7133–7137. <https://doi.org/10.1029/JC077i036p07133>
- Sakievich, P. J., Peet, Y. T., & Adrian, R. J. (2016). Large-scale thermal motions of turbulent Rayleigh-Bénard convection in a wide aspect-ratio cylindrical domain. *International Journal of Heat and Fluid Flow*, 61(1), 183–196. <https://doi.org/10.1016/j.ijheatfluidflow.2016.04.011>
- Scheel, J. D., Emran, M. S., & Schumacher, J. (2013). Resolving the fine-scale structure in turbulent Rayleigh-Bénard convection. *New Journal of Physics*, 15(11), 113063. <https://doi.org/10.1088/1367-2630/15/11/113063>
- Scheel, J. D., & Schumacher, J. (2014). Local boundary layer scales in turbulent Rayleigh-Bénard convection. *Journal of Fluid Mechanics*, 758(1), 344–373. <https://doi.org/10.1017/jfm.2014.536>
- Scheel, J. D., & Schumacher, J. (2016). Global and local statistics in turbulent convection at low Prandtl numbers. *Journal of Fluid Mechanics*, 802(1), 147–173. <https://doi.org/10.1017/jfm.2016.457>
- Shao, Y., Wyrwoll, K.-H., Chappell, A., Huang, J., Lin, Z., McTainsh, G. H., et al. (2011). Dust cycle: An emerging core theme in earth system science. *Aeolian Research*, 2(4), 181–204. <https://doi.org/10.1016/j.aeolia.2011.02.001>
- Shi, N., Emran, M. S., & Schumacher, J. (2012). Boundary layer structure in turbulent Rayleigh-Bénard convection. *Journal of Fluid Mechanics*, 706(1), 5–33. <https://doi.org/10.1017/jfm.2012.207>
- Shishkina, O., Stevens, R. J. A. M., Grossmann, S., & Lohse, D. (2010). Boundary layer structure in turbulent thermal convection and its consequences for the required numerical resolution. *New Journal of Physics*, 12(7), 075022. <https://doi.org/10.1088/1367-2630/12/7/075022>
- Shishkina, O., & Wagner, C. (2007). Local heat fluxes in turbulent Rayleigh-Bénard convection. *Physics of Fluids*, 19(8), 085107. <https://doi.org/10.1063/1.2756583>
- Shishkina, O., & Wagner, C. (2008). Analysis of sheet-like thermal plumes in turbulent Rayleigh-Bénard convection. *Journal of Fluid Mechanics*, 599(1), 383–404. <https://doi.org/10.1017/S002211200800013X>
- Sinclair, P. C. (1969). General characteristics of dust devils. *Journal of Applied Meteorology*, 8(1), 32–45. [https://doi.org/10.1175/1520-0450\(1969\)008<0032:GCODD>2.0.CO;2](https://doi.org/10.1175/1520-0450(1969)008<0032:GCODD>2.0.CO;2)
- Sinclair, P. C. (1973). The lower structure of dust devils. *Journal of the Atmospheric Sciences*, 30(8), 1599–1619. [https://doi.org/10.1175/1520-0469\(1973\)030<1599:TLSODD>2.0.CO;2](https://doi.org/10.1175/1520-0469(1973)030<1599:TLSODD>2.0.CO;2)
- Sorbjan, Z. (1996). Joint effects of subgrid-scale diffusion and truncation errors in large-eddy simulations of the convective boundary layer. *Boundary-Layer Meteorology*, 79(1), 181–189. <https://doi.org/10.1007/BF00120080>
- Spiga, A., Barth, E., Gu, Z., Hoffmann, F., Ito, J., Jemmett-Smith, B., et al. (2016). Large-eddy simulations of dust devils and convective vortices. *Space Science Reviews*, 203(1), 245–275. <https://doi.org/10.1007/s11214-016-0284-x>
- Stevens, R. J. A. M., Blass, A., Zhu, X., Verzicco, R., & Lohse, D. (2018). Turbulent thermal superstructures in Rayleigh-Bénard convection. *Physical Review Fluids*, 3(4), 041501. <https://doi.org/10.1103/PhysRevFluids.3.041501>
- Stevens, R. J. A. M., Verzicco, R., & Lohse, D. (2010). Radial boundary layer structure and Nusselt number in Rayleigh-Bénard convection. *Journal of Fluid Mechanics*, 643(1), 495–507. <https://doi.org/10.1017/S0022112009992461>
- Sullivan, P. P., McWilliams, J. C., & Moeng, C.-H. (1994). A subgrid-scale model for large-eddy simulation of planetary boundary-layer flows. *Boundary-Layer Meteorology*, 71(3), 247–276. <https://doi.org/10.1007/BF00713741>

- Toigo, A. D., Richardson, M. I., Ewald, S. P., & Gierasch, P. J. (2003). Numerical simulation of Martian dust devils. *Journal of Geophysical Research*, 108(E6), 5047. <https://doi.org/10.1029/2002JE002002>
- van der Poel, E. P., Stevens, R. J. A. M., Sugiyama, K., & Lohse, D. (2012). Flow states in two-dimensional Rayleigh-Bénard convection as a function of aspect-ratio and Rayleigh number. *Physics of Fluids*, 24(8), 085104. <https://doi.org/10.1063/1.4744988>
- van Reeuwijk, M., Jonker, H. J. J., & Hanjalić, K. (2008). Wind and boundary layers in Rayleigh-Bénard convection. I. Analysis and modeling. *Physical Review E - Statistical Physics, Plasmas, Fluids, and Related Interdisciplinary Topics*, 77(3), 036311. <https://doi.org/10.1103/PhysRevE.77.036311>
- von Hardenberg, J., Parodi, A., Passoni, G., Provenzale, A., & Spiegel, E. A. (2008). Large-scale patterns in Rayleigh-Bénard convection. *Physics Letters A*, 372(13), 2223–2229. <https://doi.org/10.1016/j.physleta.2007.10.099>
- Wicker, L. J., & Skamarock, W. C. (2002). Time-splitting methods for elastic models using forward time schemes. *Monthly Weather Review*, 130(8), 2088–2097. [https://doi.org/10.1175/1520-0493\(2002\)130%E82088:TSMFEM%E92.0.CO;2](https://doi.org/10.1175/1520-0493(2002)130%E82088:TSMFEM%E92.0.CO;2)
- Wilkins, E. M., Sasaki, Y., & Johnson, H. L. (1975). Surface friction effects on thermal convection in a rotating fluid: A laboratory simulation. *Monthly Weather Review*, 103(4), 305–317. [https://doi.org/10.1175/1520-0493\(1975\)103\(0305:SFOTC\)2.0.CO;2](https://doi.org/10.1175/1520-0493(1975)103(0305:SFOTC)2.0.CO;2)
- Williamson, J. H. (1980). Low-storage runge-kutta schemes. *Journal of Computational Physics*, 35(1), 48–56. [https://doi.org/10.1016/0021-9991\(80\)90033-9](https://doi.org/10.1016/0021-9991(80)90033-9)
- Wyngaard, J. C. (2010). *Turbulence in the atmosphere*. Cambridge: Cambridge University Press. <https://doi.org/10.1017/CBO9780511840524>
- Zhao, Y. Z., Gu, Z. L., Yu, Y. Z., Ge, Y., Li, Y., & Feng, X. (2004). Mechanism and large eddy simulation of dust devils. *Atmosphere-Ocean*, 42(1), 61–84. <https://doi.org/10.3137/ao.420105>
- Zou, H.-Y., Zhou, W.-F., Chen, X., Bao, Y., Chen, J., She, Z.-S., & She, Z.-S. (2019). Boundary layer structure in turbulent Rayleigh-Bénard convection in a slim box. *Acta Mechanica Sinica*, 35(4), 713–728. <https://doi.org/10.1007/s10409-019-00874-x>

Chapter 5

How Do Dust Devil-Like Vortices Depend On Model Resolution? A Grid Convergence Study Using Large-Eddy Simulation

5.1 Declaration of Contributions

The author contributions are given after the summary and conclusions section of the research article.

5.2 Research Article

Giersch, S. and Raasch, S.: How Do Dust Devil-Like Vortices Depend On Model Resolution? A Grid Convergence Study Using Large-Eddy Simulation, *Bound.-Layer Meteorol.*, **187**, 703–742, doi:10.1007/s10546-023-00792-3, 2023.

©2023. The Authors. CC BY 4.0 License.



How Do Dust Devil-Like Vortices Depend on Model Resolution? A Grid Convergence Study Using Large-Eddy Simulation

Sebastian Giersch¹ · Siegfried Raasch¹

Received: 6 October 2022 / Accepted: 14 February 2023 / Published online: 6 March 2023
© The Author(s) 2023

Abstract

Dust devils are organized convective vortices with pressure drops of hundreds of pascals that spirally lift surface material into the air. This material modifies the radiation budget by contributing to the atmospheric aerosol concentration. Quantification of this contribution requires good knowledge of the dust devil statistics and dynamics. The latter can also help to understand vortex genesis, evolution and decay, in general. Dust devil-like vortices are numerically investigated mainly by large-eddy simulation (LES). A critical parameter in these simulations is the grid spacing, which has a great influence on the dust devil statistics. So far, it is unknown which grid size is sufficient to capture dust devils accurately. We investigate the convergence of simulated convective vertical vortices that resemble dust devils by using the LES model PALM. We use the nesting capabilities of PALM to explore grid spacings from 10 to 0.625 m. Grid spacings of 1 m or less have never been used for the analysis of dust devil-like vortices that develop in a horizontal domain of more than 10 km². Our results demonstrate that a minimum resolution of 1.25 m is necessary to achieve a convergence for sample-averaged quantities like the core pressure drop. This grid spacing or smaller should be used for future quantifications of dust devil sediment fluxes. However, sample maxima of the investigated dust devil population and peak velocity values of the general flow show no convergence. If a qualitative description of the dust devil flow pattern is sufficient, we recommend a grid spacing of 2.5 m or smaller.

Keywords Convective boundary layer · Dust devils · Grid convergence · Large-eddy simulation · PALM model system

1 Introduction

Dust devils are columnar convective vortices with a vertical axis of rotation. On Earth, they typically extend to 1–10 m horizontally and 10–100 m vertically and last for several minutes

Sebastian Giersch
giersch@meteo.uni-hannover.de

¹ Institut für Meteorologie und Klimatologie, Leibniz Universität Hannover, Herrenhäuser Str. 2, 30419 Hannover, Germany

(Balme and Greeley 2006). Dust devils mainly occur in arid regions like deserts (Lorenz et al. 2016) and swirl up loose material from the ground, which makes them visible. The basic meteorological conditions for dust devil development are clear skies with strong insolation that favors a large super-adiabatic lapse rate near the surface and background winds below certain critical values ($\sim 5 \text{ m s}^{-1}$) (Ives 1947; Williams 1948; Horton et al. 2016; Giersch et al. 2019). These conditions cause a convective boundary layer characterized by a near-surface cellular pattern with a size on the order of the boundary layer height ($\sim 1 \text{ km}$). This pattern shows small cell boundaries where the horizontal flow converges and the air rises. Simultaneously, the cell centers contain broad regions of descending air (e.g., Khanna and Brasseur 1998). Dust devil-like vortices preferentially appear at the cell branches and vertices (Kanak 2006; Raasch and Franke 2011).

Typical characteristics of dust devils include high vertical vorticity as well as positive temperature and negative pressure deviations (Sinclair 1964; Mullen and Maxworthy 1977). Their mean flow features a radial inflow near the surface, with highest wind speeds just outside the dust devil core, and a spiraling upward motion with positive peak vertical velocities located near the border of the visible dust column similar to the maximum tangential velocities (Sinclair 1973; Balme and Greeley 2006). However, the short-term flow structure is often more complicated and is influenced by, for example, secondary vortices (Sinclair 1973; Zhao et al. 2004) or central downdraughts (Kaimal and Businger 1970; Sinclair 1973).

In addition to the impressive appearance and dynamical behavior described above, dust devils carry particles into the atmosphere that may effect cloud microphysics (DeMott et al. 2003) and the radiation budget (Myhre and Stordal 2001). The contribution of dust devil sediment flux to the terrestrial dust budget is still under debate (Koch and Rennó 2005; Neakrase and Greeley 2010; Jemmett-Smith et al. 2015; Klose and Shao 2016). Also, dust devils modify the vertical momentum and heat fluxes significantly (as shown by field measurements from Kaimal and Businger (1970)). All this motivates the ongoing research on dust devils.

Since the late 1990s, direct numerical simulations (DNS, e.g., Cortese and Balachandar 1998; Giersch and Raasch 2021) and large-eddy simulations (LES) (e.g., Kanak 2005; Ohno and Takemi 2010a; Raasch and Franke 2011; Spiga et al. 2016; Giersch et al. 2019) have been increasingly used to study convective vertical vortices. One crucial parameter in numerical set-ups is the grid spacing, which often affects the simulated flow dynamics and the statistics of dust devils. However, meaningful numerical results must not depend on the model resolution. A prerequisite for an adequate simulation of dust devils is the sufficient resolution of the mean flow and its low-order moments. For daytime convective planetary boundary layers (PBLs) in which dust devils can form, Sullivan and Patton (2011) proposed a resolution of $z_i/\Delta_f > 60$ so that the majority of the low-order moments (means, variances, and fluxes) become grid independent in the boundary layer interior ($0.1 < z/z_i < 0.9$). z_i and Δ_f describe the boundary layer height and LES filter width, respectively. In our LES simulations, Δ_f can be interpreted as the spatially uniform grid spacing Δ . For $z_i/\Delta_f > 230$ ($\Delta \approx 5 \text{ m}$), Sullivan and Patton (2011) demonstrated a coupling between large-scale thermal plumes and dust devil-like vortices. The dust devil cores tended to develop in the branches or spokes of the surface updrafts. Wurps et al. (2020) concluded that for convective simulations ($z_i \sim 1000 \text{ m}$) a resolution of 20 m is adequate to accurately capture the profiles of the mean flow variables, the resolved turbulence kinetic energy (TKE), the resolved turbulent shear stresses, and the energy spectra. From Bopape et al. (2020), it can be inferred that a minimum grid width on the order of 25 m is sufficient to provide an accurate simulation of the convective boundary layer. However, the aforementioned studies focused on the grid-resolution requirements for low-order moments or flow structures with scales much larger than those of dust devils.

Numerical simulations by Ito et al. (2010) (20 and 50 m grid spacing) and Zhao et al. (2004) (50 m grid spacing vertically and 100 m horizontally) indicated that relatively coarse-resolution LES are capable of resolving basic dust devil characteristics qualitatively but Ito et al. (2010) admitted that higher resolutions would affect the intensity and structures of the vortices. To simulate smaller dust devils, they suggested a grid spacing of a few meters. Resolutions of several tens of meters only capture very large dust devils, which are quite rare in nature (Kurgansky 2006). Even the largest vortices may not be accurately captured but only the large-scale thermal updraughts associated with them (Sinclair 1969). According to Kanak et al. (2000), horizontal wind speeds of the dust devil-like vortices are expected to strengthen and their circulation diameters are expected to decrease with increasing horizontal resolution. Kanak (2005) performed high-resolution LES with 2 m grid spacing that enabled the detection of smaller vortices. Despite the high resolution, vortex characteristics did not match the observations, especially the lower vortex vertical wind speed and the absolute pressure drop at the center. Raasch and Franke (2011) and Giersch et al. (2019) partly focused on the effects of grid resolution on simulated dust devils. Raasch and Franke (2011) concluded that vortices were stronger and appeared more frequently in high-resolution runs, whereas vortex diameter and height were the same. Therefore, a 2 m grid spacing should be sufficient to simulate the typical spatial structure of vortices. However, they only compared two different resolutions (1 and 2 m) and used model domains that were far too small to capture the large-scale cellular patterns to which the dust devils are tied. By comparing a 10 m to a 2 m simulation, Giersch et al. (2019) obtained a similar result as Raasch and Franke (2011). Dust devil-like vortices were more numerous and intense with finer model resolution. Giersch et al. (2019) also showed that the mean radius and lifetime of a whole dust devil sample decreased with higher resolutions and stated that a further reduction of the grid spacing (below 2 m) might result in even higher core pressure drops. Klose and Shao (2016) concluded that their number density, defined by the number of dust devils per square kilometer and per hour was smaller than in other studies due to the lower horizontal resolution they used (10 m). This was explained by an underestimation of the number of small dust devils. Interestingly, Ito et al. (2013) found no significant change in the dust devil strength (measured by vertical vorticity) between model runs with 50 and 5 m grid size. Both resolutions suggested a typical value of $\sim 10^{-1} \text{ s}^{-1}$. Zhao et al. (2004) and Gu et al. (2008) simulated dust devils at ultra-fine resolution (down to 0.1 m). These studies modeled single, idealized dust devils in a cylindrical domain by applying appropriate boundary and initial conditions to force vortex development. While the results helped to understand basic vortex physics, it is unclear how applicable they are to atmospheric dust devils in more realistic environments.

For individual dust devils, some of the aforementioned studies showed that higher resolutions reveal more flow details. For example, Zhao et al. (2004) examined the flow structure of dust devil-like vortices at different grid spacings. Their vortex at 100 m resolution was characterized by local maxima in vertical vorticity, vertical velocity and temperature. However, their high-resolution vortex at 0.1 m suggested that these maxima do not necessarily occur at the same location, which is consistent with the simulations of Raasch and Franke (2011). The high-resolution vortex of Zhao et al. (2004) also revealed dynamic flow features like downdraughts at the core or several intense secondary vortices. Both phenomena were not observed in their coarse-resolution vortex. As admitted by Kanak et al. (2000), structures at the dust devil scale can not be resolved by a grid size of several tens of meters. Instead, the larger-scale circulations in which dust devils are embedded are captured. Our investigations of selected vortices will show how smaller grid spacings modify the appearance of dust devils and reveal many more flow details. However, a detailed investigation of the flow dynamics is

Table 1 Summary of simulation parameters of several dust devil studies

Study	Grid spacing Δ (m)	Domain size $L_x \times L_y \times L_z$ (m ³)	Number of grid points
Ohno and Takemi (2010a)	3	999 × 999 × 1500	333 × 333 × 185
Ohno and Takemi (2010b)	10	2000 × 2000 × 1500	200 × 200 × 70
Raasch and Franke (2011)	2	4096 × 4096 × 1704	2049 × 2049 × 449
Ito et al. (2013)	5	1800 × 1800 × 1600	362 × 362 × 320
Klose and Shao (2016)	10	2000 × 2000 × 1500	200 × 200 × 90
Giersch et al. (2019)	2	4000 × 4000 × 1782	2000 × 2000 × 640

not part of this study. Instead, we focus on the minimum grid spacing at which various dust devil features reach statistical convergence.

By determining the resolution where convergence occurs, future studies can improve estimations of particle concentrations and fluxes within dust devils. Numerical simulations require emission schemes that connect the turbulent wind to the particle release and transport (e.g. Klose and Shao 2013). Therefore, a prerequisite for these schemes to work appropriately is a well-resolved flow within and around dust devils. Currently available concentration and emission data vary a lot and are subject to great uncertainties. For example, Rennó et al. (2004) found through field experiments a typical dust content and vertical dust flux of 0.1 g m^{-3} and $0.1\text{--}1 \text{ g m}^{-2} \text{ s}^{-1}$, respectively. Neakrase and Greeley (2010) estimated the sediment flux of dust devils by means of laboratory investigations to be between 10^{-3} and $10^3 \text{ g m}^{-2} \text{ s}^{-1}$. Estimates from LES studies indicate dust concentrations of $10^{-5}\text{--}10^{-4} \text{ g m}^{-3}$ (Ito et al. 2010) and $10^{-4}\text{--}10^{-3} \text{ g m}^{-3}$ (Klose and Shao 2016). In these studies, grid spacings of 20 and 10 m were applied, which is too high for an adequate quantification of the particle load, especially within smaller dust devils with a horizontal size of a few meters. Both Ito et al. (2010) and Klose and Shao (2016) mentioned this insufficient resolution with respect to smaller vortices.

Table 1 provides a summary of simulation parameters that have been used to study terrestrial dust devil-like vortices by LES while being able to capture the large-scale cellular pattern (about $1 \text{ km} \times 1 \text{ km}$ horizontal domain size or more) and while using a grid spacing of 10 m or below. L_i describes the spatial extents along the x -, y -, and z -axis. All grids were stretched vertically except the one of Ito et al. (2013). For all we know, a grid spacing of 2 m is the highest resolution that has ever been used so far to investigate terrestrial dust devils in the convective PBL. Higher resolutions at large domains or larger domains at high resolutions were computationally too intensive. We overcome this problem by using a nesting technique (Hellsten et al. 2021) that enables simulations of a $4 \text{ km} \times 4 \text{ km}$ large horizontal model domain with grid spacings down to 0.625 m.

The above considerations indicate that there is a strong need to know which model resolution is necessary to adequately resolve terrestrial dust devils with LES and to capture their characteristics qualitatively and quantitatively correctly. Considering this, the paper structure results as follows. Section 2 gives an overview of the dust devil detection and analysis algorithm, the analyzed quantities characterizing a dust devil, the PALM model system, which is used in this study to perform the LES simulations, and the numerical set-ups. The results are introduced and discussed in Sect. 3 with a focus on the convergence behavior of general flow features, the dust devil statistics, and their three-dimensional structure. In Sect. 4, a summary and conclusions are given.

2 Methodology

This section introduces the numerical and analysis methods that are used in our study. First, the PALM model system with its nesting technique is presented, followed by an introduction to the numerical set-ups that are performed. We will only concentrate on those features of PALM (formerly an abbreviation for Parallelized Large-eddy Simulation Model but now an independent name) which are actually used. Second, it is clarified how a dust devil center is detected during the numerical simulation and how centers are combined to form a dust devil with a certain lifetime. To conclude this section, specific dust devil quantities are introduced, which are statistically analyzed and provide the basis for the grid convergence study. Note, (convective) vortex, dust devil, and dust devil-like vortex are used as synonyms in the following and do not distinguish between a dust-laden vortex and an invisible one. Neither dust lifting nor dust transport processes are included in our simulations and, consequently, no potential effects of the particles on the turbulent flow (e.g., Richter and Sullivan 2013) are considered.

2.1 The PALM Model System and its Nesting Technique

The numerical simulations are carried out with the PALM model system (revision 4732, Raasch and Schröter 2001; Maronga et al. 2015, 2020), which is an open source model code written in Fortran designed for atmospheric and oceanic boundary-layer flows. It is publicly available at <http://palm.muk.uni-hannover.de/trac/browser/?rev=4732> and designed for massively parallel computer architectures with distributed memory, utilizing the message passing interface (e.g., Gropp et al. 1999). In its default state, PALM calculates the flow solution based on the non-hydrostatic, filtered, Navier–Stokes equations in a Boussinesq-approximated form by solving the conservation equations for momentum, mass, and internal energy on a staggered Cartesian Arakawa-C grid (Arakawa and Lamb 1977). On such a grid, scalars like the potential temperature θ are defined in the grid box center, whereas the velocity components u , v , and w are shifted by half of the grid spacing in x -, y -, and z -direction, respectively. Hence, the velocities are defined in the middle of the side walls of the grid box. The filtering of the smallest eddies is done implicitly based on a spatial scale separation approach after Schumann (1975). The spatial discretization of the model domain is realized through finite differences with an equidistant horizontal and a variable vertical grid width. A third-order Runge–Kutta scheme (Williamson 1980) is used for the integration in time. Advection is discretized by a fifth-order scheme of Wicker and Skamarock (2002). The parameterization of the SGS turbulence uses a 1.5-order closure after Deardorff (1980) but in the revised formulation of Moeng and Wyngaard (1988) and Saiki et al. (2000). PALM's data output is based on the [UC]² data standard (Scherer et al. 2020) and is performed with the open, self-describing netCDF format.

One main assumption of the Boussinesq-approximated system of equations is the incompressibility of the flow. To reach this, a Poisson equation for the so-called perturbation pressure p^* is solved by applying a predictor-corrector method (Patrinos and Kistler 1977) together with a fast Fourier transform after every Runge–Kutta sub-time step. The total dynamic pressure perturbation $\pi^* = p^* + 2/3 \rho e$ is interpreted as the dust devil pressure drop with respect to the surroundings, similar to other LES studies of dust devils (e.g., Kanak et al. 2000; Raasch and Franke 2011; Giersch et al. 2019). The second term includes the air density ρ and the SGS TKE e . It describes the isotropic part of the SGS tensor that arises from the filtering of the model equations.

In order to allow for a high resolution of small-scale turbulent processes near the surface and to simulate a sufficiently large model domain to capture the large-scale cellular flow pattern in the convective PBL, PALM's self-nesting capabilities are used (Hellsten et al. 2021). In our study, we apply the pure vertical (one-dimensional) nesting, where the high-resolution nested and coarse-resolution domains (also called child and parent domains) have identical horizontal model extents and where the children only obtain their boundary conditions from the parent at the top boundary instead of all boundary surfaces. Identical horizontal model extents are mandatory to capture the large-scale cellular pattern in all domains and enough high-resolved dust devil-like structures for statistical analysis. Regions above the dust devils can be simulated with the coarser parent resolutions to spare computational costs. The domain with the coarsest resolution is called the root domain.

2.2 Numerical Set-ups

To study the effects of model resolution on the dust devil statistics, we performed differently resolved and mostly nested simulations while maintaining the horizontal model extent. In the following, an overview about the simulation initialization is given (see also Fig. 1). To force convection, a homogeneous heating is prescribed at the surface with a temporally and spatially constant vertical sensible heat flux $w\theta_0$ of 0.24 K m s^{-1} (approximately 285 W m^{-2}). The subscript 0 indicates a surface value. The vertical potential temperature profile at the beginning features a constant value of 300 K up to a height of 1000 m . Above, a capping inversion with a gradient of 0.02 K m^{-1} is prescribed. For heights of 1300 m and more, a sponge layer (Rayleigh damping) is applied for all prognostic variables to reduce spurious reflections of vertically propagating waves from the model top. Wind velocities are initially set to zero everywhere because no background wind is considered. To accelerate the development of convection, random perturbations with a maximum amplitude of 0.25 m s^{-1} are imposed on the horizontal velocity field during the beginning of the simulation until a prescribed domain-averaged perturbation energy (or resolved-scale TKE) limit of $0.01 \text{ m}^2 \text{ s}^{-2}$ is exceeded. Besides, large-scale subsidence with a magnitude of up to 0.023 m s^{-1} guarantees a constant boundary layer height during the simulation. Otherwise, the dust devil statistics might change in time because of the dependency between the boundary layer height and dust devils (e.g., Hess and Spillane 1990; Fenton and Lorenz 2015). With these initial conditions, a quasi-stationary state of the convective PBL is simulated that mimics the reality during the afternoon of a sunny day.

The bottom and top boundary are regarded as impermeable ($w = 0 \text{ m s}^{-1}$) with no-slip (Dirichlet) conditions ($u = v = 0 \text{ m s}^{-1}$) at the ground and free-slip (Neumann) conditions ($\partial u/\partial z = \partial v/\partial z = 0 \text{ s}^{-1}$) at the top. For the perturbation pressure and the SGS TKE, a Neumann condition ($\partial p^*/\partial z = 0 \text{ Pa m}^{-1}$, $\partial e/\partial z = 0 \text{ m s}^{-2}$) is applied at the bottom surface. At the top surface, a fixed value of $p^* = 0 \text{ Pa}$ is set, except for child domains, where a Neumann condition ($\partial p^*/\partial z = 0 \text{ Pa m}^{-1}$) is used. The potential temperature at the model top is derived locally by linear interpolation during each time step, utilizing the initial gradient at that height (horizontally homogeneous and constant during the run) and the temperature one grid point below, which is calculated through the prognostic model equation for the thermal internal energy. A further Neumann condition is set for e ($\partial e/\partial z = 0 \text{ m s}^{-2}$) at the top boundary. The nested domains obtain their top boundary conditions for the prognostic variables (θ , u , v , w) from their respective parent solution through a zero-order interpolation as described in Hellsten et al. (2021). In addition, a constant flux layer is assumed between the surface and the first computational grid point above. In this layer, unknown fluxes are calculated using

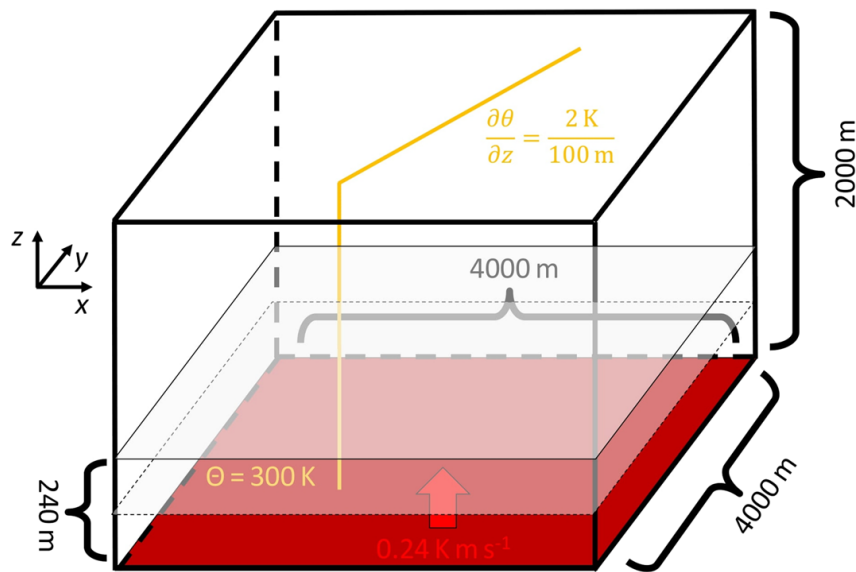


Fig. 1 Simulation domain with the initial potential temperature profile (orange line) and surface heat flux (red arrow). The spatial extents are only approximated. The exact values are listed in Table 2. If nesting is applied, two transparent planes visualize the model top of the first (solid lines) and, if present, second nested domain (dashed lines)

Monin-Obukhov similarity theory (MOST), which requires to specify a roughness length of the surface. We choose a value of 0.1 m (typical for rural areas). In the horizontal directions, cyclic boundary conditions are applied. Finally, the Coriolis force, although probably not that important for dust devils (e.g., Balme and Greeley 2006), is considered by setting the earth's angular velocity to $7.29 \times 10^{-5} \text{ rad s}^{-1}$ and the latitude to 52° .

The computational domain has a horizontal extent of $4 \text{ km} \times 4 \text{ km}$ in order to resolve the large-scale polygonal convective cells. This is necessary because vertical vortices in the convective PBL are strongly tied to these cells (see Sect. 1). By the application of the vertical grid stretching above 1.2 km height, a vertical extent of the model domain of approximately 2 km is reached, which is well above the inversion layer. The child domains are about 240 m high, except for the simulation with the highest resolution (0.625 m), where a two-stage nesting (three domains) is used. Here, the second child domain has a height of 120 m. The selected heights are a compromise between computational costs and the demand to resolve the whole vertical thickness of a dust devil with fine resolution. The grid spacings in the root domains are 10 or 5 m along each spatial direction (except where the vertical grid stretching is applied) to capture the general flow statistics of the convective PBL well enough (see Sect. 1) and to limit the grid spacing ratio between parent and child domain to a maximum value of 5. This limitation is applied due to observations made by Hellsten et al. (2021) who state that the child solutions are almost independent of the chosen grid spacing ratio and that they all match to the non-nested case with the child resolution everywhere. Besides, our own test simulations show no significant difference between the dust devil statistics derived from an ensemble of 10 nested simulations with grid spacing ratio 5 (parent: 10 m, child: 2 m grid spacing) and the non-nested case, where a fine resolution of 2 m is used everywhere. In the nested set-ups of the convergence study, the child grid spacing is uniform in each direction and gradually reduced from 5 to 0.625 m (5, 2.5, 2, 1.25, 1, and 0.625 m), which results in 7 simulations each with a total simulated time of 4 h. An overview of all performed simulations is given in Table 2, stating the simulation name, the grid spacing, the domain size, and the number of grid points. The name is used as a reference in this study and is

Table 2 Main numerical features of conducted simulations

Simulation name	Grid spacing Δ (m)	Domain size $L_x \times L_y \times L_z$ (m ³)	Number of grid points
R10	10	4000 × 4000 × 2019	400 × 400 × 146
R10N5	10	4000 × 4000 × 2019	400 × 400 × 146
	5	4000 × 4000 × 245	800 × 800 × 50
R10N2.5	10	4000 × 4000 × 2019	400 × 400 × 146
	2.5	4000 × 4000 × 242.5	1600 × 1600 × 98
R10N2	10	4000 × 4000 × 2019	400 × 400 × 146
	2	4000 × 4000 × 242	2000 × 2000 × 122
R5N1.25	5	4000 × 4000 × 2248	800 × 800 × 277
	1.25	4000 × 4000 × 241.25	3200 × 3200 × 194
R5N1	5	4000 × 4000 × 2248	800 × 800 × 277
	1	4000 × 4000 × 241	4000 × 4000 × 242
R10N2.5N0.625	10	4000 × 4000 × 2019	400 × 400 × 146
	2.5	4000 × 4000 × 242.5	1600 × 1600 × 98
	0.625	4000 × 4000 × 120.625	6400 × 6400 × 194

selected as follows: The first part indicates the root domain's grid spacing (e.g., R10). The second part, if any, describes the nested domain's grid spacing (e.g., N5) and simultaneously clarifies that a single-stage nesting (one child) is applied. If a two-stage nesting is used, a third part illustrates the resolution of the second nest and the first nest acts also as a parent domain. In the same row of the simulation name, the root domain characteristics are given. The first and second line below show the characteristics of the first and second child domain, respectively. Due to the grid stretching, the vertical extent of the root domains is rounded. Note that the dust devil data of a simulation are only taken from the nested domain with the finest resolution.

2.3 Detection of Vortex Centers and the Generation of Vortex Tracks

In the following, we will comprehensively clarify how a vortex center is identified and how various centers compose a vortex track, which we interpret as a dust devil-like vortex with a certain lifetime. The different tracks form the basis for our statistical analysis of dust devil-like vortices (see Sect. 2.4). Our experiences show that the dust devil statistics can strongly depend on details of the detection and analysis algorithm, especially if a quantitative analysis is performed. In principle, the algorithm is based on the vortex detection and analysis approach from Raasch and Franke (2011) and Giersch et al. (2019), which we abbreviate with VDA11 (Vortex Detection and Analysis approach 2011) in the following. However, their approach has some drawbacks, which would heavily affect the comparison of results from runs with different resolution. For example, their vortices were detected on a horizontal plane taken from the first computational grid level above the surface at $\Delta/2$. If the grid spacing changes, the physical detection height also changes, which will result in different statistics. Such a procedure would complicate or even prevent a quantitative comparison between differently resolved simulations. Therefore, a requirement for the algorithm in this study is a constant detection/analysis height, which we fix to 10 m or the next higher level, where a scalar grid

point is located (e.g., 12.5 m height in the 5 m simulation). We select this height level to exclude potential effects of the SGS model on the statistics at least for high-resolution runs (only the first grid points above the surface are significantly affected by the SGS model (e.g., Schmidt and Schumann 1989; Gadde et al. 2021) and to enable comparisons with field measurements. Besides, dust devils are ground-level vortices and their vertical extent is often limited to several tens of meters (Balme and Greeley 2006), which is why the detection height is chosen close to the ground.

Vortex centers are identified during the simulation after each model time step and after the model spin-up time of 45 min (see Sect. 3) by local minima of the dynamic perturbation pressure and local maxima of the absolute value of the vertical vorticity once certain thresholds are exceeded (see below). The vertical vorticity (hereafter only “vorticity”) is defined as the vertical component of the rotation of the velocity field:

$$|\zeta| = \left| \frac{\partial v}{\partial x} - \frac{\partial u}{\partial y} \right|. \quad (1)$$

The local minima/maxima refer to the lowest/highest value within a resolution-independent square of size $20 \times 20 \text{ m}^2$ instead of just considering the eight neighbouring grid points as in VDA11. This square size reproduces typical sizes of large dust devils (e.g., Kurgansky 2006) and simultaneously guarantees comparability between all performed simulations of different resolution. For example, an area of $20 \times 20 \text{ m}^2$ is the smallest possible square that can be defined for a local minima/maxima in R10.

The exact position of the center is exclusively defined by the location of the pressure minimum and not by the location of the absolute vorticity maximum, which is a further difference to VDA11. This definition is more consistent with the calculation of the vortex radius that is determined from the tangentially (in circular direction) averaged pressure drop distribution around each center. The radial distance at which the absolute pressure drop is 50% of that at the center is interpreted as the (core) radius (see also Kanak 2005; Raasch and Franke 2011; Giersch et al. 2019; Giersch and Raasch 2021). This procedure agrees well with analytical and empirical models of dust devils, where the radius also often describes the location of the maximum tangential velocity (Lorenz 2014). The numerically calculated core radius can be used as an estimate for the visible dust column radius of real vortices.

Simultaneously to the pressure minimum, an absolute vorticity maximum must be located within a square of size $20 \times 20 \text{ m}^2$ around a center. In this way, the positions of the maximum rotation and the pressure minimum can be slightly shifted, which can especially happen for high resolutions (see discussion about Fig. 3). The size of the square should not be too large. Otherwise, rotations in the flow field that do not belong to the same vortex structure might be assigned to it by mistake.

The vortex center is only considered for the generation of vortex tracks if certain pressure and vorticity thresholds are exceeded. Different values have been proposed in former studies that mainly depend on the model resolution or the detection height (Ohno and Takemi 2010a; Raasch and Franke 2011; Klose and Shao 2016; Nishizawa et al. 2016). These studies have in common that certain pressure and vorticity deviations from the horizontal mean are chosen for the thresholds. In our simulations, 3 times the standard deviation of the dynamic perturbation pressure and 5 times the standard deviation of the vorticity are chosen. The standard deviation is calculated as the arithmetic mean of the standard deviations from 4 instantaneous horizontal cross-sections at analysis height after 1, 2, 3, and 4 h simulated time. It must be taken into account that all simulations from Table 2 (except R10N2.5N0.625) are executed at least twice, once for calculating the correct thresholds and once for identifying the dust devil-like vortices. Two simulations of R10N2.5N0.625 with 4 h simulated time are too expensive

for us in terms of time and available computational resources (one simulation needs about 20 days wall-clock time on 6688 cores of an Atos/Bull system equipped with Intel Xeon Platinum 9242 processors) and thresholds are based on the first cross-section after the model spin-up time of 45 min. For the vorticity, the values 0.1, 0.24, 0.51, 0.63, 0.92, 1.08, and 1.56 s^{-1} are used, which indicates a continuous increase in local vorticity fluctuations with decreasing grid spacing, similar to other studies (Nishizawa et al. 2016; Giersch et al. 2019). The thresholds for π^* show no clear trend and a grid-independent value of 3.5 Pa is taken. Note, the threshold values are derived empirically to capture most of the vortex lifetime, to eliminate the background noise of non-coherent turbulence, and to limit the data for the post processing, which especially includes the formation of vortex tracks (see next paragraph).

To form dust devil tracks, the detected centers are sequentially processed after the simulation in a grid-independent way. The processing steps are first described technically. Details for each step and the main differences to VDA11 are explained further below.

1. Centers of vortices with a radius $r \geq 100\text{ m}$ are neglected.
2. For finer resolutions than 10 m (all nested simulations), only the strongest center (rated by π^*) is considered if two or more centers are closer than 20 m to each other at the same time.
3. Two centers at different times are combined to the same vortex track if the displacement speed from the location of the center detected first to the center detected at later times (second center) is $\leq \sqrt{2} \times 10\text{ m}$ (corresponds to the distance of one R10 grid spacing in each horizontal direction) per 1.4 s (this time is defined by the mean time step of R10). If no second center is found after 4.2 s (three mean time steps in R10), a new dust devil track is initiated.
4. For simulations with $\Delta < 10$ (all nested runs), centers of the same vortex can move up to 20 m in just one time step (see detailed explanation below), which would exceed the allowed maximum displacement speed by criterion 3. Therefore, two centers from a nested simulation that are detected at different time steps will be connected regardless of the third criterion if they have a distance to each other of 20 m or less even for very short time periods between the detections.
5. A further condition for connecting two vortex centers to a track is that their difference in π^* must be less than 10% of the value of the first center.
6. Finally, the area-averaged (over $20 \times 20\text{ m}^2$ around the center's location) local vorticities must have the same sign to connect two vortex centers.

The first action, which was not part of VDA11, guarantees that only well-developed dust devil-like centers are connected. An investigation of the events with radii above 100 m has shown that such centers are weakly pronounced with values close to the detection thresholds so that they often vanish again quite quickly.

The second step avoids counting a single dust devil with several sub-vortices (see e.g., Bluestein et al. 2004) twice or even more and it takes care of the merging of centers, which is an important process for vortex intensification (Ohno and Takemi 2010a). Additionally, the comparability between differently resolved simulations is increased. Due to the definition of a center as a local extremum within a square of $20 \times 20\text{ m}^2$, the 10 m run can not resolve situations where two or more centers are closer than 20 m (see Fig. 2, which shows the smallest possible distance between two centers A and B that might occur in R10). However, all nested simulations can principally resolve distances below 20 m as it is shown in Fig. 2 for R10N5 (center A and C). With the second criterion, we prohibit this technical discrepancy. The old algorithm VDA11 disregards all weaker vortex centers as soon as a center is within the radius of another (sub)vortex at the same time step. Taking the radius instead of a fixed value of

20 m is critical. Our results will show that the radius is strongly affected by the resolution. As a consequence, the detection and analysis method would indirectly depend on the grid, which we want to avoid as much as possible.

The third step allows the dust devil to occasionally have absolute vorticity or pressure drop values less than the thresholds. For example, consecutive centers of a dust devil track in R10 might have a temporal distance of three mean R10 time steps (3×1.4 s) if thresholds were not exceeded after the first and second time step and, thus, no suitable center was stored at these times. For the nested runs, the physical scales regarding time and space are maintained, i.e., the maximum allowed covered distance in 1.4 s is always $\sqrt{2} \times 10$ m, which corresponds to a displacement speed of about 10 m s^{-1} , and a period of 4.2 s is always scanned for a potentially subsequent center independent of the actual number of time steps that are needed to cover this time frame. For the highest resolution (R10N2.5N0.625), it follows that consecutive centers of a dust devil track are allowed to have temporal distances of more than 100 time steps (the mean time step in R10N2.5N0.625 is 0.038 s). In VDA11, two vortex centers were only connected if the position of the second center is not more than two grid points away from the first one after a maximum of three time steps. This procedure links the detection of dust devils to the model resolution. Therefore, we reject it.

Criterion 3 is completed by step 4 to allow a center displacement speed of much more than 10 m s^{-1} , which might be physically unrealistic but can happen technically anyway. Imagine a situation in the child of simulation R10N5 (mean time step of 0.75 s) where two centers of the same dust devil-like vortex with similar strength are closer than 20 m to each other (see Fig. 2 center A and C, distance is approximately 18 m). It might happen that at one time step center A is preferred and C is sorted out (based on criterion 2) but at the subsequent time step center C is preferred because it becomes stronger than A, which is then rejected. For this situation, the vortex center's displacement speed is 24 m s^{-1} ($18 \text{ m}/0.75 \text{ s}$) and, thus, it exceeds the maximum allowed value of 10 m s^{-1} according to point 3. Therefore, a new track would be generated by mistake instead of connecting center A (remaining center after first time step) with center C (remaining center after second time step). We enable this connection by step 4.

Finally, point 5 and 6 describe additional criteria that intend to avoid counting two centers from different dust devils to the same track and to prohibit unrealistically high short-term fluctuations of the dust devil features during its lifetime. The area-averaged local vorticity is taken instead of the local vorticity as used in VDA11 because the area average is more robust with respect to the overall rotation direction of the dust devil-like vortex, especially for finer resolutions. To illustrate this, Fig. 3 shows two snapshots of the local vorticity in and around a cyclonic (a) and anticyclonic vortex (b) resolved with 10 and 1 m grid spacing, respectively. For 1 m, the structure is quite diverse and although the overall rotation is in clockwise direction some locations show a pronounced positive vorticity (anticlockwise spin), even in the central region. Therefore, it can happen that the value of the local vorticity attributed to a vortex center can change its sign within just two consecutive time steps. This would initiate a new dust devil track and centers would not be combined if local vorticity values are taken. However, the area averages of the local vorticities around the two vortex centers possess a clear positive and negative value (0.4 s^{-1} and -0.58 s^{-1}).

The high positive vorticities in the clockwise rotating vortex can be better understood by transforming the vorticity into natural coordinates:

$$\zeta = -\frac{\partial V}{\partial n} + \frac{V}{R}, \quad (2)$$

with V the horizontal wind speed, n the normal direction to the velocity vector, and R the curvature radius ($R > 0$ for \odot and $R < 0$ for \ominus). Accordingly, the first term describes the

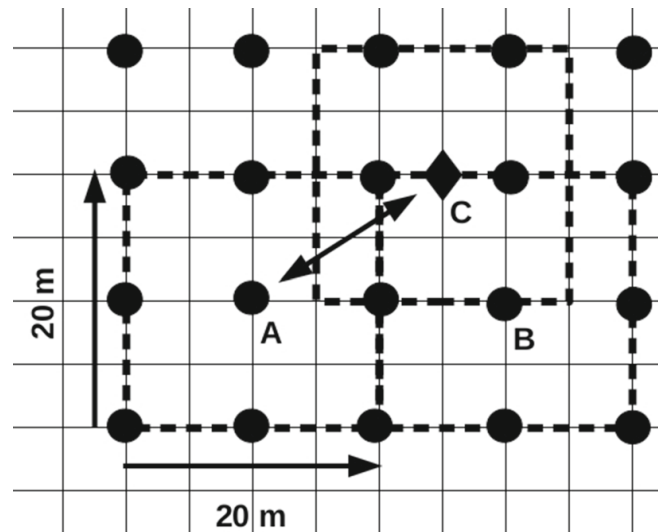


Fig. 2 Horizontal grid structure for the child domain of R10N5 (thin solid lines) overlapped by grid points from simulation R10 (dots). The markers A, B, and C show locations of different vortex centers, representing a local pressure minimum with respect to an area of $20 \times 20 \text{ m}^2$ (dashed squares). Center C is located at a grid point that only exist in the child of simulation R10N5, which is why it is visualized by a diamond. The line with two arrows highlights the distance of about 18 m between center A and C. Note, point A is used in the text as a reference location for a center that occurs in R10 as well as in the child of R10N5

rate of change of V normal to the direction of the flow (shear vorticity) and the second term describes the turning of the wind along a streamline (curvature vorticity). By analyzing high-density streamlines and vector fields (see Fig. 3c, d), it turns out that the high positive vorticity values in the vortex center are a combination of both the shear and curvature vorticity. At these locations (e.g., at around $x = -11 \text{ m}$, $y = 4 \text{ m}$, see white rectangle), the flow shows a cyclonic curvature (Fig. 3c) and also partly a decelerating flow along the normal direction (Fig. 3d), resulting in an overall positive vorticity.

2.4 Statistical Vortex Analysis

The resulting vortex tracks from the formation algorithm above create a subset of an unknown dust devil population for which statistics shall be derived. We call this subset a dust devil sample. Each simulation creates such a sample but with a different resolution the underlying dust devil population changes. For example, high-resolution runs produce very short-lived vortices of a few seconds, while coarse-resolution runs do not capture them at all because of their higher time steps. This complicates a comparison between the statistics of differently resolved simulations. Therefore, it is mandatory to restrict the statistical analysis only to those vortices with a lifetime above a certain threshold. In this way, the dust devil population can be compared much better among the differently resolved simulations because all dust devil lifetimes that might occur in the population can principally be captured with every resolution. Additionally, we assume that very short-lived vertical vortices of several tens of seconds do not appear in nature as well-developed dust devils because of the small time frame for reaching a significant strength that initiates strong dust lifting. Therefore, they are usually not considered in any dust devil statistics which is based on observations. To increase the comparability with data from field studies and between simulations with different grid spacings, we restrict our dust devil population to those vortices with a lifetime τ of at least 120 s.

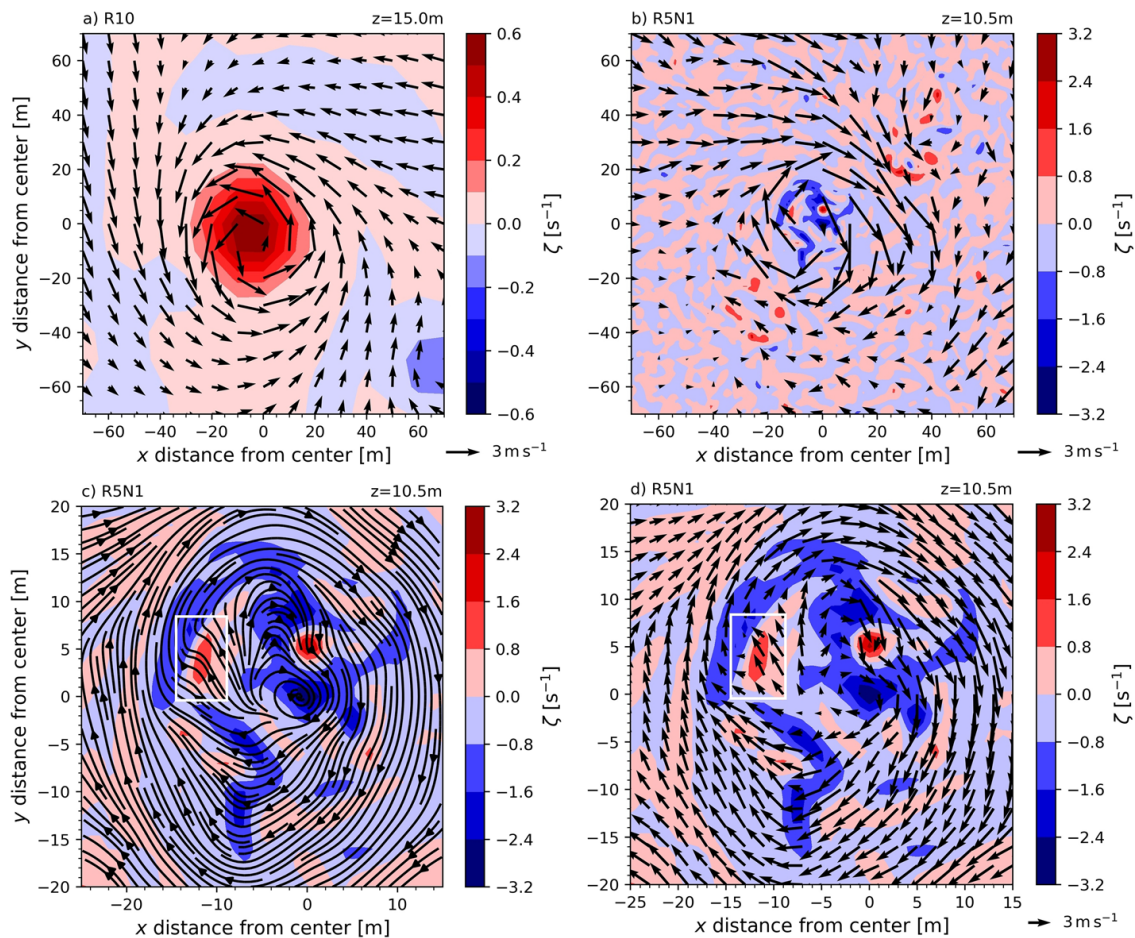


Fig. 3 Snapshots of horizontal cross-sections of the local vorticity at detection height for two dust devils that occur in R10 (a) and R5N1 (b). The c, d a zoomed version of b. The different color scales consider the different vortex strengths. Arrows in a, b, d horizontal wind vectors, whereas in c streamlines are used to visualize the horizontal flow. In b, only every tenth arrow is shown, in d every second one. The meaning of the white rectangle in c, d is explained in the text

The horizontal size of the vortices within the regarded population must also be constrained to allow for a good comparability between the differently resolved simulations. If the grid spacing is reduced, more and more smaller vortices occur (e.g., Giersch et al. 2019). For example, R10 allows a minimum radius of 10m, while in R5N1 also vortices with radii of several meters can be simulated. Therefore, we limit the spatial vortex scale at the lower bound, i.e., the vortex must have a certain size and all other vortices smaller than this size are not considered. If the lower bound is selected high enough, a detection of vortices with spatial scales close to this bound would become possible for each applied grid spacing. In addition, limiting the statistics to larger vortices enables a proper resolution of their dynamics, which typically requires a minimum of 5–10 grid points along the dust devil's axes. In our study, the most obvious selection for the lower bound would be a minimum radius of 10m because such a vortex could principally occur in each simulation, even though poorly resolved in the coarse-resolution runs. However, the minimum vortex radius must not be too large either. Otherwise, each sample contains only a few dust devil-like vortices from which a statistically profound derivation of vortex characteristics is impossible. Observational data suggest that a core radius of 10m and more is already too large to get a sufficient number of dust devils during a simulated time of 4h (Houser et al. 2003; Balme and Greeley 2006; Kurgansky 2006). They usually show radii of around 5m. That is why we exclude all vortices with a lifetime-averaged

radius lower than this value from our statistical investigation as a compromise between the above requirements for comparability and statistical analysis.

As explained above, our regarded dust devil population only considers vortex tracks with lifetimes of at least 120 s and lifetime-averaged radii of ≥ 5 m. We mainly calculate double-averaged quantities at the detection height of 10 m to describe this population statistically. The first average is executed over the vortex lifetime. Subsequently, an average over the sample is performed. In this way, each model run creates one value for one specific quantity. Instantaneous events of single dust devils or extreme values of a sample might be rare events and do not necessarily represent typical characteristics of a population. Taking only these events would make it difficult to compare results among the differently resolved simulations. That is why we focus our statistical analysis to mean values (if not otherwise specified).

The application of the sample average necessitates the first quantity that is analyzed: the sample size, which is expressed by the number of dust devil-like vortices N or the number density n in $\text{km}^{-2} \text{h}^{-1}$ or $\text{km}^{-2} \text{d}^{-1}$. In addition, the statistical focus is on the sample-averaged quantities $\overline{\pi^*}$, τ , \bar{r} , the tangential, radial, and vertical velocity $\overline{u_{\text{tan}}}$, $\overline{u_{\text{rad}}}$, and $\overline{w_{\text{d}}}$ ("d" for dust devil), respectively, the area-averaged vorticity $\overline{\zeta_{\text{av}}}$ and, finally, $\overline{\theta}$. Here, the overbar indicates a time-averaged value over the whole vortex lifetime. The quantities π^* , ζ_{av} and θ are defined in the vortex center. Instead, u_{tan} , u_{rad} , and w_{d} represent the maximum of the tangentially averaged velocity distribution of the respective cylindrical component around the vortex center. Note that the radial and tangential components are calculated during the simulation through the transformation of the total Cartesian velocity components u and v to polar coordinates. Thus, radial and tangential velocities also contain the translational speed of the dust devil.

Based on the quantities above, the minimum lifetime of a vortex, which shall be considered in the statistics, is further restricted. An air parcel, which moves with the velocity $\overline{u_{\text{tan}}}$, must be able to circulate the vortex with a circumference of $2\pi\bar{r}$ at least once during its lifetime. This is a further reasonable condition to focus the dust devil analysis only to well-developed vortices.

3 Results and Discussion

This section starts with an overview of general flow characteristics, which describe the physics of the simulated PBL in more detail. A focus is on the grid convergence of flow quantities that are typically used within studies of the PBL, like vertical profiles of the potential temperature or the friction velocity. In Sect. 3.2, dust devil statistics for variable grid spacings are analyzed with respect to their convergence. In addition, a quantitative comparison to observational data is performed. Finally, features of the three-dimensional structure of selected dust devil-like vortices are addressed without the claim to give a comprehensive description and explanation of the dust devil flow dynamics. A focus is again on how these features change with grid spacing.

3.1 General Flow Features

The general development of the flow in all root domains is very similar and can be evaluated through results from R10. A quasi-stationary state, where the turbulence statistics do not change substantially, is reached after 45 min as, for example, indicated by time series of the domain-averaged total kinetic energy $E = 0.5 \times (u^2 + v^2 + w^2)$ of the flow (see Fig. 5a).

Here, the domain average refers to all heights up to the top of the (first) child domain (240 m) in every simulation to enable better comparability between the different model domains. The subsequent analysis only includes periods after the spin-up time of 45 min.

Figure 4 shows horizontally and temporally averaged vertical profiles of the potential temperature (a), the total vertical turbulent heat flux (b), composed of the resolved-scale and subgrid-scale turbulent heat flux, and variances of v (c) and w (d). The horizontal average is marked by angular brackets, the overbar describes a temporal average over a period of 15 min before the respective output time, and the prime denotes a resolved-scale turbulent fluctuation, which is interpreted as the deviation of an instantaneous resolved-scale quantity from its horizontal domain average. The profiles reveal the typical characteristics of a convective PBL (see also Schmidt and Schumann 1989; Moeng and Sullivan 1993; Park and Baik 2014). The potential temperature indicates constant values in the so-called mixed layer and strong vertical gradients near the surface and in the entrainment zone at around 1 km, where the heat flux becomes negative (downward flux). The negative slope of $\overline{\langle w\theta \rangle}$ indicates negative divergences, causing a mean temperature increase in the PBL with time. In upper layers (≈ 1000 – 1100 m), overshooting thermals mix warmer air from the inversion layer downwards. This, together with the large-scale subsidence (see Sect. 2.2), results in a warming of the PBL and the free atmosphere during the simulation. Variances of the horizontal velocity components (only $\overline{\langle v'^2 \rangle}$ is shown because $\overline{\langle u'^2 \rangle}$ looks very similar) show stronger turbulence near the surface and in the entrainment zone generated by wind shear and buoyancy forces. Vertical velocity fluctuations reach a maximum at the lower third of the boundary layer height, which is constant over time (≈ 1 km). In our study, the boundary layer height is defined as the point where the minimum of the total sensible heat flux profile is reached. Profiles in b, c, and d still show fluctuations around the actual mean state because the temporal average refers to a period of only 15 min (\sim one to two times the large-eddy turnover time defined by the ratio of the boundary layer height z_i and the convective velocity scale w_* , which is also referred to as the Deardorff velocity scale). Normally, several large-eddy turnover times are necessary to better capture the mean state. However, the shape remains similar.

The grid convergence of the general flow state is first investigated by time series of E , the horizontal average of the friction velocity $\langle u_* \rangle$ calculated by means of MOST (Maronga et al. 2020), and the maximum of the vertical velocity w_{\max} of the whole domain (see Fig. 5). The domain-averaged total kinetic energy represents the whole (resolved) flow, including a mean and turbulent contribution. However, because no mean wind is applied, E and the domain-averaged resolved-scale TKE of the flow are the same. All simulations show similar values for E that oscillate around a mean state of approximately $1.7 \text{ m}^2 \text{ s}^{-2}$. Therefore, this quantity can be regarded as converged for every resolution.

The friction velocity, characterizing the turbulent momentum exchange near the surface, shows a grid spacing independent behaviour. This indicates that a resolution of 10 m is already fine enough to resolve the mean turbulent transport in the surface layer. According to Lyons et al. (2008), the ratio of the convective velocity scale and the friction velocity must amount to larger than 5 for dust devil formation. Our simulations indicate a grid-independent value of 2 m s^{-1} (not shown) for the convective velocity scale and, thus, a ratio w_*/u_* of approximately 10.

In contrast to the friction velocity, the total maximum values of the velocity components, which occur somewhere in the respective domain and which represent extraordinary flow events, do not converge (the time evolution of u_{\max} and v_{\max} look very similar to w_{\max}). The magnitude constantly increases with a decrease in the grid spacing, resulting in peak velocities of about 20 m s^{-1} for each component in simulation R10N2.5N0.625. This corresponds to

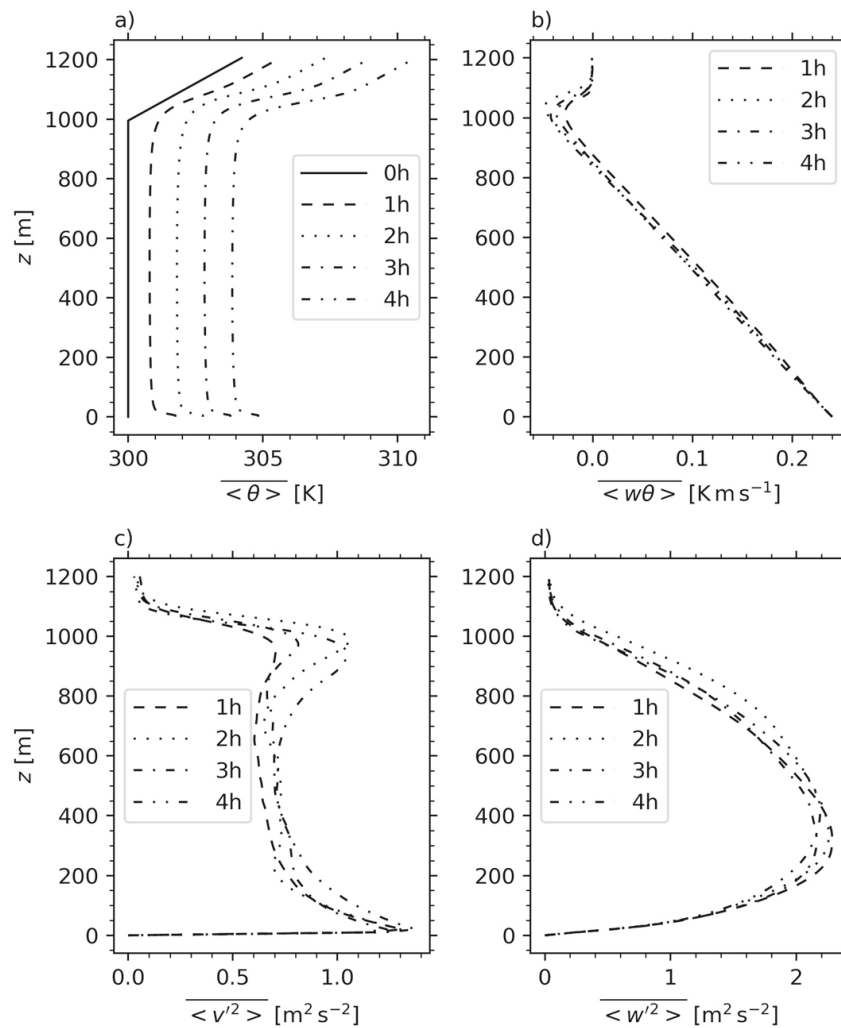


Fig. 4 Horizontally and temporally averaged (over 15 min) vertical profiles of the potential temperature (a), total vertical sensible heat flux (b), and the variances of the v - (c) and w -component (d) for four different times taken from R10. The initial profile of the potential temperature is indicated by the solid line

about 10 times the convective velocity scale. In R5N1, maximum vertical velocities always occur near the center of a dust devil-like vortex after 1, 2, 3, and 4 h simulated time. The average height of the location of w_{\max} after the spin-up time is 30 m. In most cases, maxima occur below 20 m. Only in sporadic cases, the strongest updrafts in the child are simulated at heights between 100 and 240 m. Thus, we presume that maximum velocities are mostly caused by dust devils or the strong larger scale updrafts connected to them. Because w_{\max} values of up to 25 m s^{-1} have already been reported for dust devils (Balme and Greeley 2006), we assume that our u_{\max} , v_{\max} , and w_{\max} are still realistic and we speculate that a grid spacing of 0.625 m is just before the limit of what is required to show a convergence of maximum velocities. To clarify this point, a further simulation with even finer resolution would be required, which is currently beyond our available computational resources. However, the time series are a first indicator that extreme values in the dust devil statistics are not well suitable at this stage for evaluating a grid convergence (see Sect. 3.2).

In Fig. 6a, vertical profiles of the potential temperature show a constant increase of the surface temperature and the near-surface temperature gradients with a decrease in the grid spacing (the surface value is set to the value at the first computational grid level above but does not enter the prognostic model equations). With higher resolution, the thin super-adiabatic

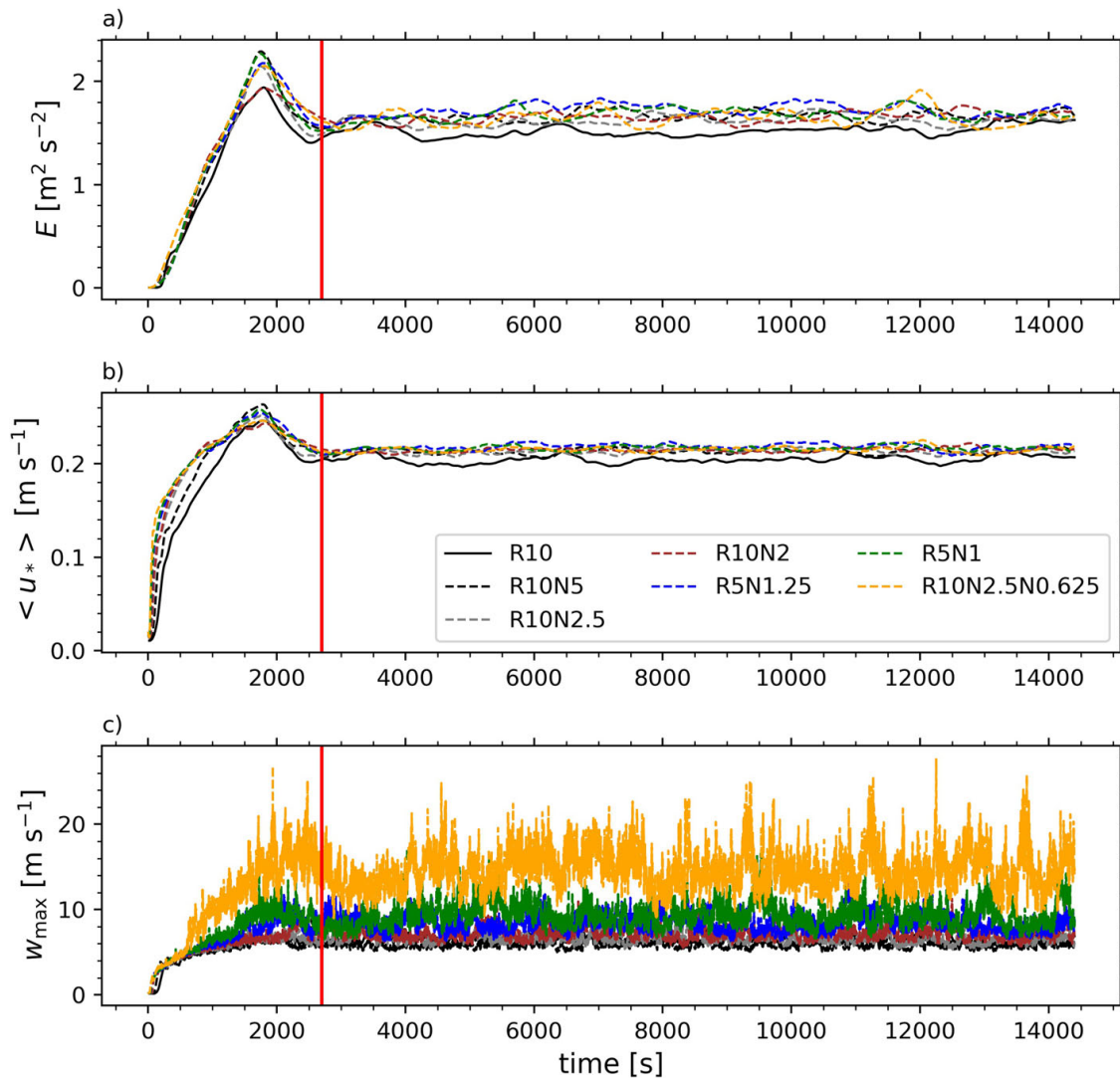


Fig. 5 Time series of the domain-averaged total kinetic energy E , the horizontal average of the friction velocity u_* , and the maximum vertical velocity of the whole domain for R10 (solid line) and all simulated child domains (dashed lines). The vertical red line marks the spin-up time for reaching a quasi-stationary state

layer close to the ground, showing strong vertical temperature gradients, is much better resolved. According to the theoretical work by Horton et al. (2016), a critical value of 1–10 K m^{-1} is needed in the first few meters above the hot surface for the onset of dust devils. This has also been shown by observations (e.g., Oke et al. 2007; Ansmann et al. 2009). Such high gradients are only simulated in the simulations with child grid spacings of 1 and 0.625 m. As a consequence of increasing surface temperatures, stronger plumes are probably be generated, resulting in higher vertical velocities. This fits to the result that w_{max} constantly increases with decreasing grid spacing (see previous paragraph). For heights of 20 m and above, all profiles of the potential temperature overlap, indicating a converged situation. This is also true for the potential temperature variance displayed in Fig. 6b. Very close to the surface, however, more intense temperature fluctuations are simulated if the grid spacing is reduced, which is directly related to stronger gradients in the mean profile. With such gradients, even small displacements of air parcels cause high temperature fluctuations.

As Fig. 6c shows, the mean variance of the u -component $\langle u'^2 \rangle$ ($\langle v'^2 \rangle$ (almost the same) increases if the resolution changes from 10 to 5 m. A further reduction causes a

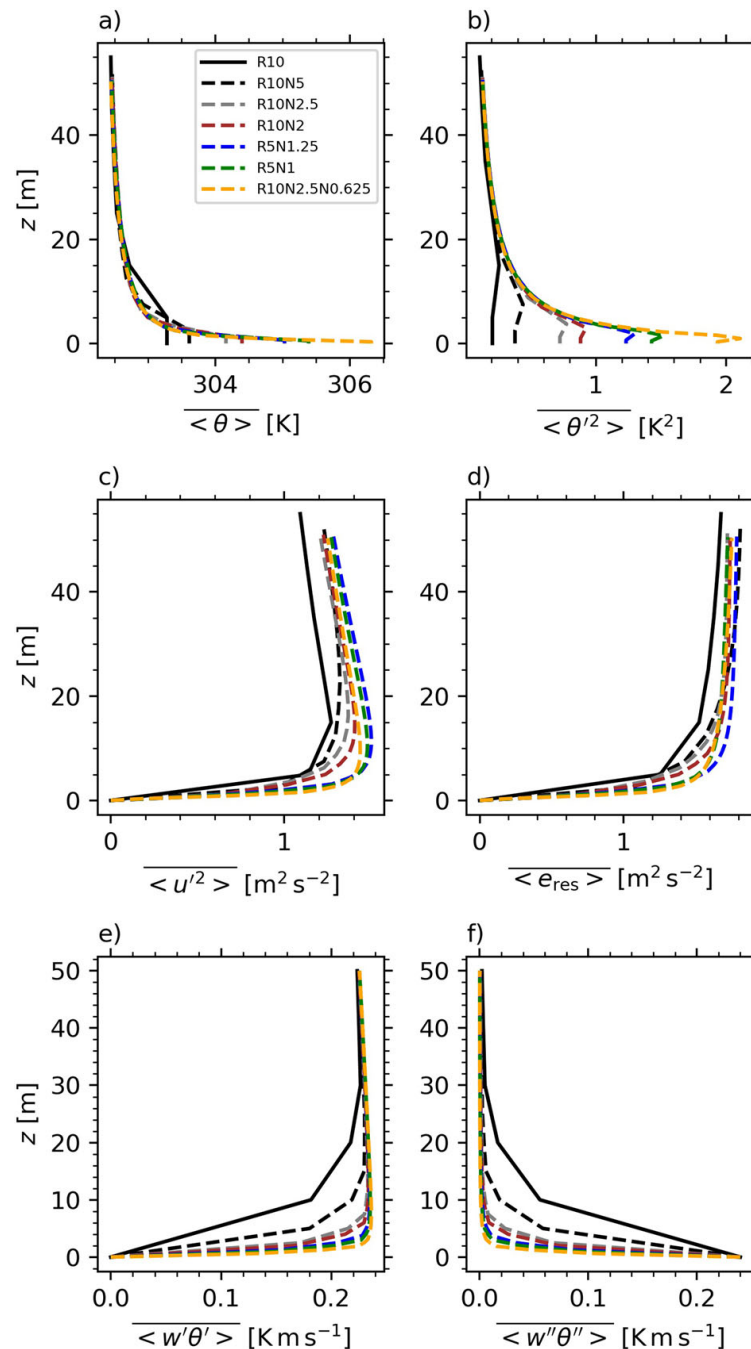


Fig. 6 Horizontally and temporally averaged (over 15 min) vertical profiles of the potential temperature (a), the variances of the potential temperature (b) and the u -component (c), the resolved-scale TKE (d), and the resolved-scale (e) and SGS turbulent vertical heat flux (f) for R10 and all child domains up to a height of 100 m (or the next higher grid level). The averaging period is 3 h and 15 min (from 45 to 240 min)

significant increase below heights of 20 m only until a resolution of 1.25 m is reached. For 1.25, 1, and 0.625 m grid spacing, profiles almost overlap, even very close to the surface. This is confirmed by the resolved-scale TKE $e_{res} = 0.5 \times (u'^2 + v'^2 + w'^2)$ (see Fig. 6d), which includes all variances in one quantity. For resolutions of 5 m and below, maximum differences among the profiles amount to several per cent only if heights above 20 m are regarded. At lower heights, only the profiles of R5N1.25, R5N1, and R10N2.5N0.625 match well.

Finally, the resolved-scale and SGS vertical turbulent heat flux is displayed in Fig. 6e, f (a double prime denotes SGS quantities). In each simulation, the first two vertical grid levels above the surface are significantly affected by non-resolved processes. At 20 m and above, however, SGS fluxes can be neglected for all resolutions because they contribute to the total flux only marginally (less than 10%). From a height of 30 m, all profiles start to overlap and are converged. As discussed in Sect. 2.3, the detection height of dust devil-like vortices is set to 10 m or the next higher grid level. The heat flux profiles show that the turbulence is already well-resolved at that height for most of the simulations except R10. Therefore, uncertainties that might be introduced by the surface parameterization are mostly negligible in the subsequent dust devil statistics. The total vertical turbulent heat flux profiles overlap for all resolutions (not shown).

Dust devils are connected to the large-scale cellular pattern of the convective PBL (see e.g., Kanak 2006; Raasch and Franke 2011). Figure 7 reveals this pattern by horizontal cross-sections of the instantaneous vertical velocity at 100 m height and it shows how structures depend on model resolution. With a resolution of 10 m, the large-scale polygonal structures are well-resolved. However, more flow details become apparent for R10N5 (Fig. 7b). A further reduction in grid spacing does not change the overall flow pattern, although smaller and smaller turbulent scales are captured but the displayed figure size in Fig. 7 does not allow to see them. The number of detected vortex centers at 4 h simulated time amounts to 33, 58, 178, 256, 254, and 261 for R10, R10N5, R10N2.5, R10N2, R5N1.25, and R5N1, respectively. Consequently, simulations with grid spacings of 2 m and below create a similar amount of centers. A more detailed discussion about the number of detected vortex centers and, thereby, dust devil-like vortices follows in Sect. 3.2.

All in all, our results support the findings from past studies about resolutions requirements for LES of the convective PBL (see Sect. 1). These studies mainly recommend a grid spacing on the order of 10 m. However, if the research focus is more on the surface layer, processes that originate from there, or details of the flow structures, 10 m is still too coarse. This is probably also true for dust devils, that are quite small-scale flow phenomena. Especially the above number of detected vortex centers and the resolution dependent variation of the near-surface temperature profile suggest a strong influence of the grid spacing on dust devils. We will investigate this in the next Sects. 3.2 and 3.3 in more detail.

3.2 Dust Devil Statistics

In the subsequent paragraphs, dust devil statistics at detection height are quantitatively analyzed for samples of a dust devil population, which only contains vortices with a lifetime-averaged radius of 5 m or more and with a lifetime of at least 120 s. This limited population and the quantities that are analyzed have already been motivated and explained in Sect. 2.4. The statistics are usually based on one simulation with a certain grid spacing. However, to estimate statistical uncertainties, ensembles with 10 members have been created for grid spacings of 5 (R10N5) and 2.5 m (R10N2.5) by applying different random perturbations at the beginning of the respective simulation (see also Sect. 2.2). From these members, 95% confidence intervals have been derived for the mean and the standard deviation of the corresponding ensemble. Such an interval covers the true value with a probability of 95%. We take the same statistical significance interval as defined by (Appendix C Giersch and Raasch 2021) to assess if a value might be part of the same ensemble or not, i.e., as soon as a value lies outside the significance interval, differences are rated as statistically significant. A calculation of the confidence intervals for higher resolutions was not possible because the required

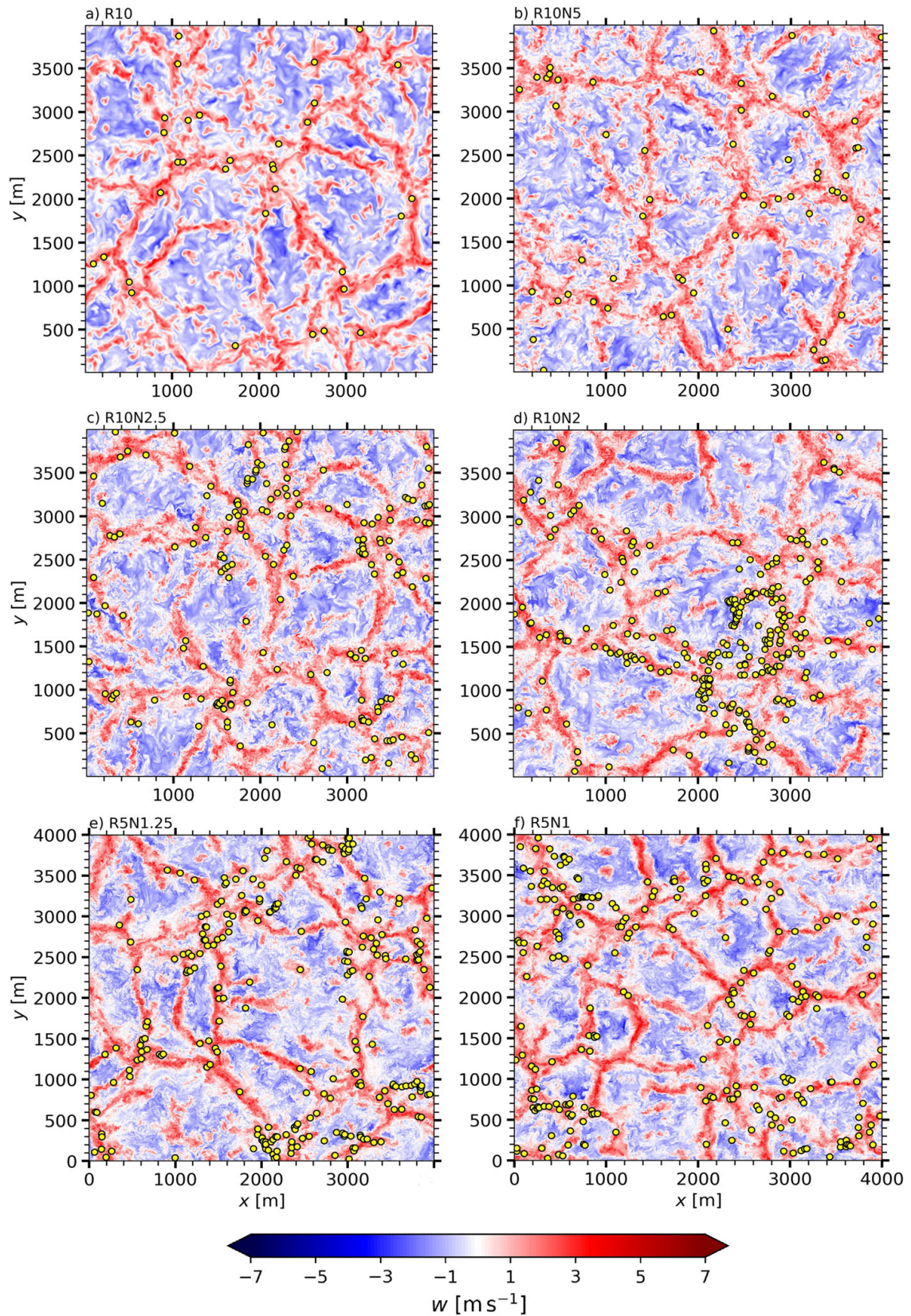


Fig. 7 Horizontal cross-sections of the instantaneous vertical velocity at 100 m after 4 h simulated time taken from the simulations R10, R10N5, R10N2.5, R10N2, R5N1.25, and R5N1. Vortex centers at detection height are depicted as yellow dots

ensemble runs were beyond our current computational resources. The statistical uncertainty ranges of R10N5 and R10N2.5 are very similar for most of the analyzed quantities (see Fig. 8), which is why we assume that they are also applicable to the other resolutions. Note, the exact detection height varies with the grid spacing due to the arrangement of the numerical grid. In case of 10 m grid spacing, dust devil centers are actually detected at 15 m and for 1 m resolution at a height of 10.5 m. This creates a systematic uncertainty to higher or lower values. However, with decreasing grid spacing the analyzed grid level approaches the physical height of 10 m and the systematic bias is reduced.

The dust devil characteristics and their dependencies on the grid width are shown in Fig. 8. The number of detected dust devil-like vortices (Fig. 8a) varies between 700 and 2400, which corresponds to number densities of $13 \text{ km}^{-2} \text{ h}^{-1}$ and $46 \text{ km}^{-2} \text{ h}^{-1}$, respectively (the dust devil detection time during the simulation is 3 h and 15 min). Therefore, the order of magnitude for n is assumed to be $10 \text{ km}^{-2} \text{ h}^{-1}$. The deviations between coarser resolutions (10–2.5 m) are mainly provoked by the definition of the regarded dust devil population. The smallest vortices with radii between 5 and 10 m, which occur more frequently than larger vortices, can hardly exist in R10, R10N5, and R10N2.5, if at all. The finer the resolution the more of these vortices are resolved, which can be seen in Fig. 9, where the radius data is grouped into bins with an equal size ratio of about $\sqrt{2}$. The maximum number moves towards smaller radii and increases. For R10, R10N5, and R10N2.5, it is located at the bins [15;21.63), [7.21;10.4), and [5;7.21), respectively. A further reduction in grid spacing (2.5–0.625 m) causes no further increase of N because dust devil-like vortices with radii smaller than 5 m are neglected in our population. Instead, the total number decreases. For grid spacings of 2 m or lower, Fig. 9 and observational data by Oncley et al. (2016) suggest that the maximum of the number distribution of \bar{r} is not captured anymore by a population, which neglects vortices smaller than 5 m. The maximum moves out of the considered radius range if the grid spacing reduces. According to the significance intervals from simulation R10N5 and R10N2.5, we assume a converged value of about $N=1000$, corresponding to $19 \text{ km}^{-2} \text{ h}^{-1}$ or $77 \text{ km}^{-2} \text{ d}^{-1}$ if a typical sunny day allows for 4 h of strong dust devil activity (see also Lorenz 2014). Optical detections during field experiments state frequencies between 0.1 and $800 \text{ km}^{-2} \text{ d}^{-1}$, depending on the survey area (Balme and Greeley 2006; Lorenz 2009; Lorenz and Jackson 2016). Lorenz (2009) proposes the formula $n \sim 50/A$, indicating that the number density in $\text{km}^{-2} \text{ d}^{-1}$ is inversely proportional to the survey area A in km^2 . An application of this formula to our study results in $n \approx 3 \text{ km}^{-2} \text{ d}^{-1}$, which is less than the simulated values. However, according to Lorenz (2014), approximately 100 dust devil counts per square kilometer and day is the most likely formation rate of visible dust devils under favorable meteorological conditions. The simulated value of $77 \text{ km}^{-2} \text{ d}^{-1}$ is quite close to this rate. It must be noted that not all of the simulated vortices would be visible in nature because pressure and vorticity detection thresholds in the numerical simulations correspond to intensities much lower than the values that would be needed for dust lifting. If we additionally assume a threshold core pressure drop of 30 Pa for the occurrence of dust lifting (Lorenz 2014), only 200–300 vortices occur in simulation R5N1.25, R5N1, and R10N2.5N0.625 that reach such a high value at least once during their lifetimes. This is approximately equal to a frequency of 20 instead of $77 \text{ km}^{-2} \text{ d}^{-1}$, illustrating how an apparently easy statistical quantity like the number density can fluctuate strongly depending on the details of the investigation approach.

A typical lifetime for the investigated dust devil population varies between 240 and 310 s (Fig. 8b). Maximum values fluctuate between 1500 and 2600 s. However, a convergence can not be identified. The changes from R5N1 to R10N2.5N0.625 are still statistically significant if error bars with comparable sizes to R10N5 or R10N2.5 are applied to the data of R5N1 and R10N2.5N0.625. Additionally, the results indicate that there is no benefit from performing

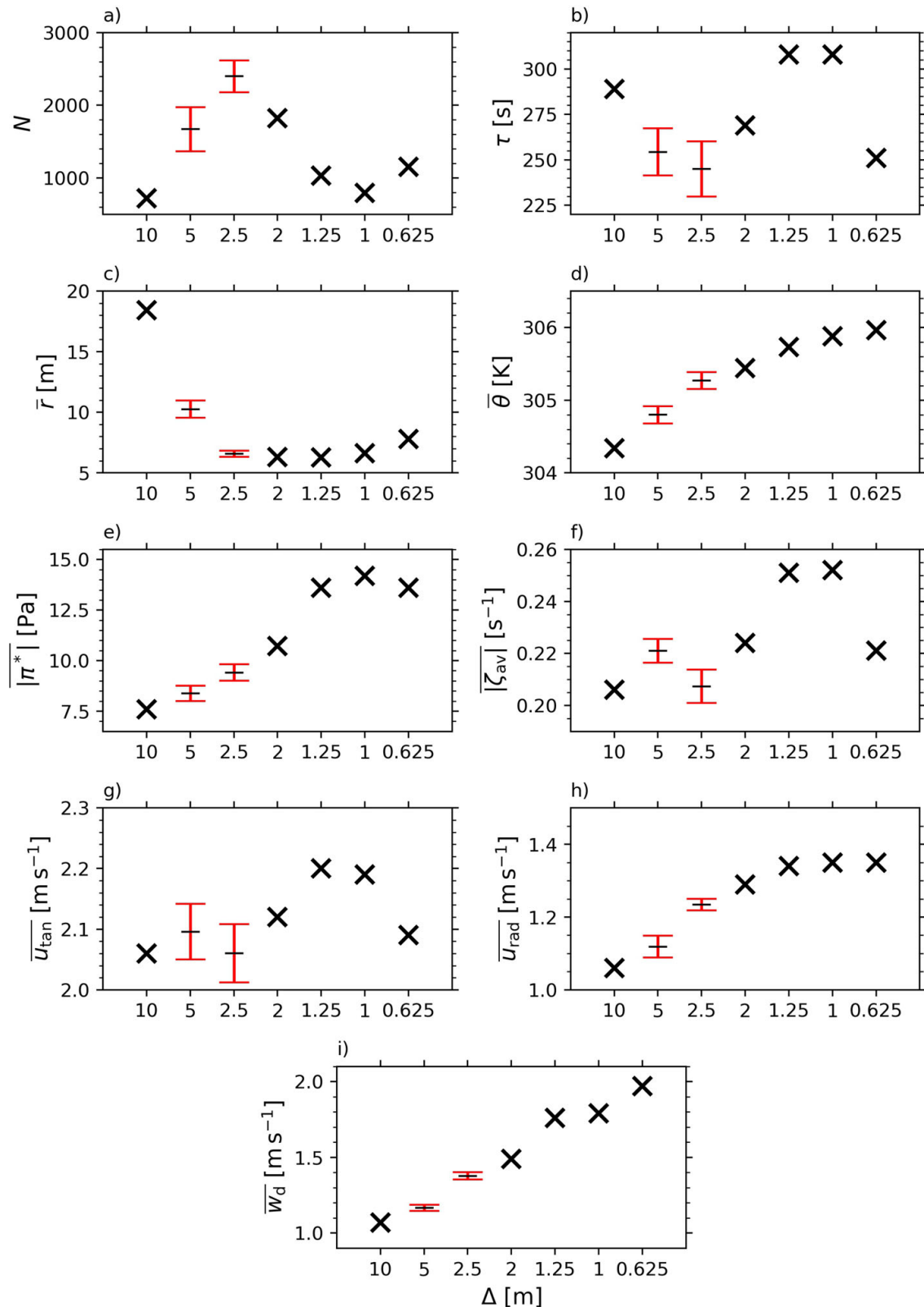


Fig. 8 Dependence of dust devil characteristics on the grid spacing. The black markers represent the sample size (a) and the mean values of the analyzed dust devil quantities calculated over all N dust devils (b–i). Crosses highlight values that are derived from a single model run. Black dashes indicate the centers of the 95% CIs that are determined from 10 ensemble members of the respective simulation. Red error bars show the statistical significance interval (see text)

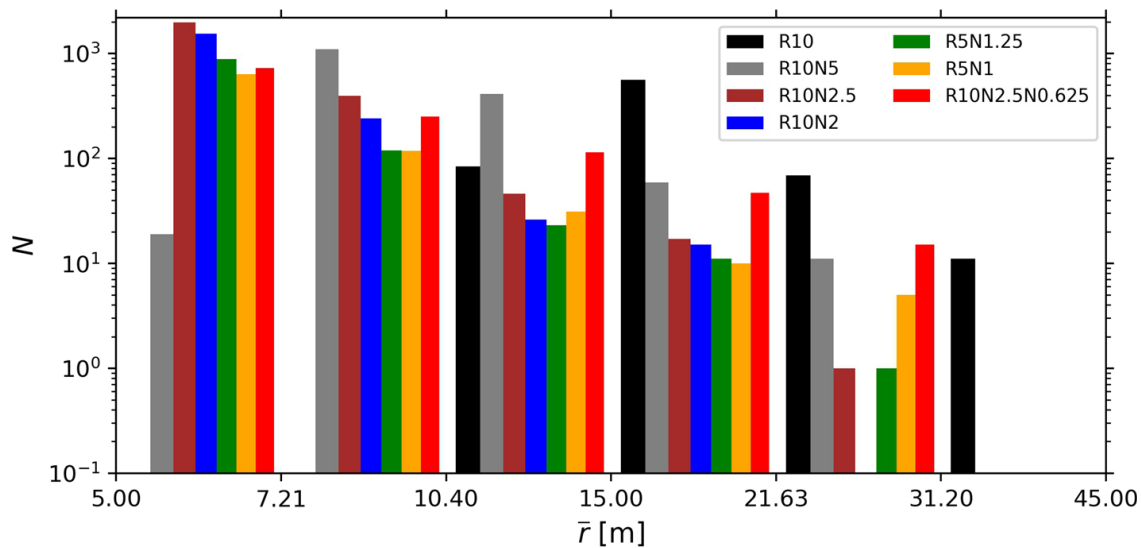


Fig. 9 Number of dust devil-like vortices as a function of the lifetime-averaged radius for all investigated model resolutions. The axes are logarithmically scaled with a bin size ratio of about $\sqrt{2}$ as suggested by Lorenz and Jackson (2016). The displayed values on the x -axis mark the lower and upper bound of a bin interval, e.g., [5,7.21) for the first one

high-resolution and costly simulations if the mean lifetime shall be estimated. No clear trend in a certain direction is visible. Observational data show that most dust devils last for only a few minutes (Lorenz 2013). In rare cases, a duration of several tens of minutes and even several hours is possible (Balme and Greeley 2006). Consequently, the simulated lifetimes match the observed range for each simulation. The absence of dust devil-like vortices with a duration of several hours might be attributed to the rareness of such events in combination with the idealized setups (e.g., lack of large-scale vorticity or limited simulation time). Note, lifetimes derived from field studies mostly refer to the time where the vortex is visible. Because our detection thresholds are rather low, simulated vortices would probably not be visible in nature during the whole lifetime. Therefore, our values might have a bias towards larger lifetimes compared to observations.

Figure 8c displays the mean radius of each sample and Fig. 9 indicates how many vortices belong to a certain size class. It is apparent that coarse resolutions strongly overestimate the horizontal dust devil size. A smaller grid spacing enables the resolution of smaller vortices, which is why the mean radius reduces with a decrease in the grid spacing. Because the defined population is limited to vortices with radii of 5 m and more, the radius reduction slows down for smaller grid widths and a converged value between 6 and 8 m arises at resolutions of 2.5 m and below. Kurgansky (2006) indicates a highly skewed size distribution with characteristic radii between 0.85 and 4.15 m, depending on the investigated field study. Balme and Greeley (2006) provide dust devil radius frequency distributions derived from six different data sets. A mean radius of 3.5 m was derived from the observations with a distribution skewed towards the smaller sizes (positive skewness). Thus, our simulated and converged vortex size of 6–8 m is larger compared to the findings in nature. This is probably because we cut off too much of the real dust devil population at the smaller sizes if we restrict our analysis only to those vortices that have at least a 5 m radius. An analysis of the population where each radius and lifetime is allowed reveals a constant but diminishing decline to a mean radius of approximately 3.2 m in simulation R10N2.5N0.625 (not shown), which fits much better to the observed range. As indicated by Fig. 9, the largest vortices in our simulations reach lifetime-averaged radii between 20 and 40 m.

The mean potential temperature at detection height (Fig. 8d) tends to increase with a reduction in grid width, especially for coarser resolutions of the investigated range. The development hypothesizes a converged value slightly above 306 K. This corresponds to a mean horizontal temperature difference between the dust devil core and the surroundings of about 3.5 K if the profile data from Fig. 6a are taken as a reference for the ambient conditions. The mean vertical temperature gradient (difference between the mean surface value and the mean value at analysis height) constantly increases with finer resolution and amounts to 0.13 K m^{-1} for $\Delta = 0.625 \text{ m}$. According to Balme and Greeley (2006), measured horizontal temperature excursions of less than 10 K are common. The total possible range is quite large and stated as 1–20 K. Sinclair (1973) did some measurements at 31 ft (similar to our analysis height) that indicate typical excursions of 2–4 K. Data derived from thermal image velocimetry show a temperature difference of up to 3 K for a single dust devil (Inagaki and Kanda 2022). However, measurement studies often refer to the maximum recorded temperature excursion during the dust devil's lifetime instead of lifetime-averaged values. If we consult our maximum values and average them over the sample size, they are 1–2 K higher than the sample mean of the lifetime-averaged temperatures. In R10N2.5N0.625, one dust devil even shows an instantaneous temperature of nearly 311 K, corresponding to a deviation of more than 8 K. All this suggests that our simulated values fit quite well to reality, at least for resolutions below 2 m. Coarser grids underestimate the temperature jump within dust devils significantly because the super-adiabatic layer close to the ground from which the heat is sucked into the dust devils core is poorly resolved (see also Fig. 6a).

Figure 8e demonstrates the development of the mean absolute pressure drop in the dust devil's core with the grid spacing. In accordance with Giersch et al. (2019), the strength increases with decreasing grid spacing. From a resolution of 1.25 m, the changes are insignificant and a converged value of approximately 14 Pa is reached. A fair comparison to measurements is only possible with the peak pressure drop of a dust devil-like vortex because this is the quantity that matches the most to what is reported in field studies. For finer resolutions (1.25, 1, and 0.625 m), single dust devils show maximum pressure drops between 200 and 300 Pa. Sample averages of the maximum values vary between 25 and 35 Pa. The coarser resolutions (5 and 10 m) only simulate maximum values below 120 Pa (sample averages between 10 and 20 Pa). Unlike the lifetime-averaged pressure drops, maximum values constantly increase and show no convergence similar to what has been shown in Fig. 5 for the peak vertical velocity of the model domain. In reality, intense and visible dust devils show pressure excursions of several 100 Pa (Balme and Greeley 2006), which is similar to the results from the high-resolution runs. Pressure measurements recorded by Lorenz and Lanagan (2014) disclose peak pressure dips of convective vortices that may or may not be dust-laden in a range of 20–150 Pa, which suggests smaller intensities compared to Balme and Greeley (2006). This might be due to the fact that Lorenz and Lanagan (2014) derived the pressure drops from fixed stations that were not necessarily inside the dust devil core and from dust devils that were not necessarily dust-laden. All in all, the simulated values for resolutions below 2 m agree well with the reality. Otherwise, pressure drops tend to be underestimated. Our numerical simulations would probably produce even stronger vortices if heterogeneities and background winds are considered (Giersch et al. 2019).

Another measure beside the pressure drop that is used to evaluate the vortex strength is the vertical vorticity. Figure 8f visualizes the mean absolute value of the area-averaged vorticity around the center (for the definition see Sect. 2.3) and how it depends on the resolution. Similar to the lifetime, no definite trend is observable and values fluctuate around 0.23 s^{-1} , which we define as our best vorticity estimate of the regarded population. The sample mean of the maximum area-averaged vorticity during a dust devil's lifetime varies between 0.3

and 0.4 s^{-1} , depending on the resolution. Single vortices with a very strong rotation even reach instantaneous area-averaged vorticities of approximately 1 s^{-1} . Higher resolutions tend to produce higher peak values. References to measured vorticities within terrestrial dust devils do rarely exist. Doppler radar measurements by Bluestein et al. (2004) show local core vorticities that range from $0.5\text{--}1 \text{ s}^{-1}$, similar to observations by Oncley et al. (2016). Temporally and tangentially averaged data for one single dust devil show a peak vertical vorticity of 1.8 s^{-1} in the core region, which reduces nearly linearly to approximately 0 s^{-1} at the core radius of about 12 m (Inagaki and Kanda 2022). All these values indicate typical vorticities of $\sim 1 \text{ s}^{-1}$ within the dust devil core. If the vorticity is additionally averaged in a horizontal plane of $20 \times 20 \text{ m}^2$ around that core, similar results as our estimate of 0.23 s^{-1} are expected. However, for getting this estimate, high-resolution runs are not mandatory.

The tangential velocity in Fig. 8g shows a similar pattern compared to $|\overline{\zeta_{\text{av}}}|$. This indicates that the horizontally averaged vorticity around a dust devil-like vortex strongly correlates with the maximum tangential velocity, occurring at a certain distance apart from the center. The pressure drop do not show this correlation, which could be expected from the cyclostrophic balance. It might be that the pressure drop in the center has less effects on the maximum tangential velocity but rather on the overall rotation, which could be better described by integral quantities like the circulation or the horizontally averaged tangential velocity. However, these results are contrary to observations made by (Fig. 9f Oncley et al. 2016), which showed a fairly well cyclostrophic balance for the maximum tangential velocity but a bad one for the averaged tangential velocity. This mismatch to our results might be caused by the different methodologies used to define a vortex. For example, Oncley et al. (2016) fitted the circular vortex structure by eye, whereas we use the pressure distribution to determine the vortex scale (see again Sect. 2.3). Consequently, completely different horizontal vortex surfaces could be determined for the same vortex, which significantly influences the calculation of maximum and averaged tangential velocities. Similar to Oncley et al. (2016), we additionally argue that the radial velocity causes a significant deviation from the cyclostrophic balance and, thus, disturb a potential correlation between $\overline{u_{\text{tan}}}$ and $|\overline{\pi^*}|$. Fluctuations of $\overline{u_{\text{tan}}}$ appear in a range of $2.05\text{--}2.20 \text{ m s}^{-1}$ with no distinct development to higher or lower values. Therefore, very fine resolutions are not beneficial for this measure. Instead, instantaneous peak values of 13 m s^{-1} are simulated in R10N2.5N0.625, whereas simulation R10 reveals much smaller peak tangential velocities ($\approx 5 \text{ m s}^{-1}$). This is also true for the sample averages of the maximum tangential velocity during a vortex lifetime that range from 2.5 to 3.5 m s^{-1} , depending on the resolution. Lower grid spacings simulate higher maximum velocities. Based on several measurement studies, Balme and Greeley (2006) stated that the peak tangential component of the wind speed usually reaches $5\text{--}10 \text{ m s}^{-1}$. In extreme cases, up to 20 m s^{-1} are possible. Likewise, observations from a fixed array of 31 turbulence sensors demonstrate a maximum value of tangential velocity of 8.9 m s^{-1} (Oncley et al. 2016). Stull (1988) specifies that tangential velocities are on the order of 10 m s^{-1} . Novel measurements with high spatial and temporal resolution show a tangential velocity component of up to 4.2 m s^{-1} for a single dust devil (Inagaki and Kanda 2022). Because this value represents an averaged velocity along the circular direction and over 40 s it appears to be smaller than the other measurements mentioned before. In summary, our numerical simulations with a grid spacing of $\sim 1 \text{ m}$ resemble the tangential velocity more realistic compared to, for example, the 10 m run.

The radial velocity converges to 1.35 m s^{-1} (see Fig. 8h) if grid spacings below 2 m are applied. A magnitude of about 1.35 m s^{-1} fits very well to the temporally and tangentially averaged measurements from Inagaki and Kanda (2022), which show radial velocities between 1 and 2 m s^{-1} along the radial direction of a single dust devil-like vortex. A typical maximum radial velocity that is simulated during a dust devil's lifetime and for resolutions

below 2 m is 2 m s^{-1} , while higher values are reached for higher resolutions. In extreme events and only for resolutions below 2 m, peak radial velocities up to 4 m s^{-1} are simulated at certain times. Based on measurements, Sinclair (1973) derived typical maximum radial velocities of $\sim 5 \text{ m s}^{-1}$, similar to Kaimal and Businger (1970) whose time series suggest maximum radial velocities between 3 and 6 m s^{-1} , depending on the measured height. Note, the surface roughness as the main reason for the radial velocity and the deviation from the cyclostrophic balance is assumed as 0.1 m in our simulations. A different roughness would produce different values that might fit better or worse to observations.

The vertical velocity component shows the smallest significance intervals of all investigated quantities with respect to the changes that occur due to a modification in the grid spacing. Over the entire resolution range, the lifetime-averaged vertical velocities almost double (from 1 to 2 m s^{-1}) with higher values at small grid spacings, whereas the relative statistical uncertainty expressed by the significance interval is just a few per cent. No convergence is reached for the vertical component. This might be related to the potential temperature, which also constantly increases for higher resolutions (see discussion above). The buoyancy and, thus, the strength of updraughts is determined by horizontal temperature differences. The profile data in Fig. 6 indicate a grid-independent reference temperature at 10 m height. If the core region of a dust devil-like vortex becomes warmer for higher resolutions at the same height, horizontal temperature differences increase on average and, consequently, updraughts become stronger. The maximum vertical velocities during the vortex lifetime show sample averages of about $4\text{--}5 \text{ m s}^{-1}$ for 1.25, 1 and 0.625 m grid spacing with peak values of 20 m s^{-1} . A constant increase with decreasing grid spacing is also evident for the sample-averaged maximum values. The coarsest resolution run R10 reveals a value of only 1.5 m s^{-1} . Comparisons with field studies suggest that fine resolutions below 2 m are necessary to capture the vertical component realistically. Using a mobile instrumented tower, Sinclair (1973) measures maximum vertical motions of $\sim 10 \text{ m s}^{-1}$ in all investigated dust devils and at all regarded height levels (7 (2), 17 (5), and 31 ft (9 m)). In-situ wind speed measurements by Kaimal and Businger (1970) also show roughly height independent magnitudes of the w -component. Peak values of 3 to 4 m s^{-1} are reported, similar to measurement data acquired by Fitzjarrald (1973) and Tratt et al. (2003). According to Balme and Greeley (2006), typical vertical wind speeds are less than 10 m s^{-1} .

In addition to a comparison with measurements, dust devil data can also be compared to theoretical models like the thermodynamical scaling theory of Rennó et al. (1998). In this theory, the pressure drop and the maximum tangential wind speed across a dust devil can be approximated by:

$$\Delta p \approx \frac{\gamma \eta c_p p_\infty \Delta T}{RT_\infty}, \quad (3)$$

and:

$$v_m \approx \sqrt{\gamma \eta c_p \Delta T}. \quad (4)$$

The variable γ describes the fraction of the total dissipation of mechanical energy consumed by friction at the surface with typical values between 0.5 and 1 Rennó et al. (1998), η is the thermal efficiency of a heat engine, $c_p = 1005 \text{ J kg}^{-1} \text{ K}^{-1}$ is the specific heat capacity at constant pressure, $R = 287 \text{ J kg}^{-1} \text{ K}^{-1}$ is the gas constant of dry air, p_∞ is the surface pressure (101,325 Pa in our simulations), T_∞ is the absolute temperature of the ambient air outside the dust devil determined by the profiles of Fig. 6a, and ΔT is the effective temperature perturbation. According to Souza et al. (2000) and Kurgansky et al. (2016), η

Table 3 Comparison between the dust devil scaling theory proposed by Rennó et al. (1998) and the simulated dust devil statistics

Simulation	T_∞ (K)	T_m (K)	Δp (Pa)	$ \pi^* _m$ (Pa)	v_m (m s ⁻¹)	u_{\tan_m} (m s ⁻¹)
R10	304.14	307.72	67–134	37	7.60 to – 10.75	5.03
R10N5	303.94	308.64	88–176	71	8.71 to – 12.32	7.08
R10N2.5	303.91	309.74	109–219	101	9.70 to – 13.72	8.20
R10N2	303.91	309.98	114–228	98	9.90 to – 14.00	7.45
R5N1.25	303.94	310.73	127–255	192	10.47 to – 14.80	9.41
R5N1	303.94	311.11	134–269	220	10.76 to – 15.21	10.89
R10N2.5N0.625	303.92	312.08	153–306	276	11.48 to – 16.23	12.97

can be calculated via:

$$\eta \approx \frac{gz_i}{c_p T_\infty}, \quad (5)$$

where $g = 9.81 \text{ m}^2 \text{ s}^{-1}$ is the gravitational acceleration. We use the simplified formulas suggested by Kurgansky et al. (2016). Because this model describes the order of magnitude of the maximum values, we apply it to the peak values of our simulated dust devil statistics at 10 m height. Therefore, $\Delta T = T_m - T_\infty$, with T_m the peak absolute core temperature of every simulated dust devil sample. Similarly, $|\pi^*|_m$ and u_{\tan_m} describe the simulated pressure drop and tangential velocity maxima for each sample. Table 3 shows the results. Only for resolutions of approximately 1 m or lower, the simulated peak values ($|\pi^*|_m$, u_{\tan_m}) match the range of the theoretical values (Δp , v_m). Otherwise, our simulations underestimate the magnitude, which is in agreement with the comparison to observational studies performed before.

The above discussion demonstrates that vortex properties can vary significantly if the grid spacing is changed and that the concrete resolution dependence differs between the regarded quantities. So far, no general answer can be given to the question at what resolution the overall statistics are converged. However, resolutions below 2 m show a convergence for most of the analyzed mean quantities and results fit very well to observations and measurements of real dust devils. Comparisons of the strongest dust devil events with observations and the thermodynamical theory of Rennó et al. (1998) suggest that a resolution of 0.625 m is short before the minimum grid spacing that is required to reach a convergence even of the peak values. This section also indicates that a quantitative comparison between numerical simulations and field experiments must be carefully performed. Different analysis heights might be relevant and lifetime-averaged values must not be mixed with maximum values. Additionally, huge differences of several orders of magnitude partly exist among various measurement data, which makes a comparison to numerical results quite challenging. Also, sometimes only visible, dust-laden vortices are considered in the statistics. In other cases, a pronounced pressure drop is enough to define a dust devil-like vortex. Therefore, it is mandatory to clearly define the characteristics of the regarded dust devil population. Changes in the considered population can cause significant changes in the results. Finally, different boundary conditions (e.g., roughness length, terrain type or slope) and meteorological conditions (e.g., background wind, boundary layer height, heating rate) complicate a comparison between numerical simulations and measurements. Nevertheless, it can be summarized that with grid spacings of less than 2 m dust devils with radii of more than 5 m are detected with sufficient accuracy. In the following, the three-dimensional flow structure is investigated regarding

grid spacing changes to review the above resolution suggestion of less than 2 m. However, a detailed and sophisticated flow analysis is not intended.

3.3 Three-Dimensional Structure

The study of the grid convergence of the three-dimensional vortex structure is realized by the analysis of instantaneous as well as time-averaged horizontal and vertical cross-sections of selected vortices. Only data from the most durable dust devil-like vortices are considered. These dust devils can be regarded as representative for well-developed and pronounced vertical vortices, occurring in the regarded population. The most persistent vortices in R10, R10N5, R10N2.5, R10N2, R5N1.25, R5N1, and R10N2.5N0.625 are tracked for 1829, 1590, 2549, 2207, 2203, 1838, and 1628 s, respectively. The sampling of the vortices' variables (p^* , θ , ζ , u , v , and w) uses the same algorithm as presented in Raasch and Franke (2011). It is based on a three-dimensional grid defined in the vortices' centers that moves together with them during their whole lifetime. Instantaneous (at every time step) as well as time-averaged data is stored after the simulation. The averaging procedure is performed during the model run. For each simulation, it is guaranteed that the output volume has at least an extent of $140 \times 140 \times 100 \text{ m}^3$ (see cross-section size in Figs. 12 and 13). This is a compromise between available storage space, memory, and to ensure that the dust devil's main sphere of influence is recorded. Note that two identical simulations are required for the three-dimensional analysis. Based on the first run, the dust devil to be examined is identified as well as its track. The second run uses the center coordinates from the first run to perform the sampling. A rerun of R10N2.5N0.625 was not possible due to the high computational demand associated with it. Therefore, only results for grid spacings between 10 and 1 m are discussed.

3.3.1 Instantaneous Data

This section provides an overview of instantaneous and short-term vortex features that are not visible in time-averaged fields. The main focus is on how these features change with the resolution. Our data reveal a frequent interaction of approaching vortices, independent of the grid spacing. The interaction can result in an intensification, dilution, or maintenance of the original vortex. Figure 10 shows an example of how a dust devil-like vortex is maintained and intensified by absorbing another vortex with the same sense of rotation (positive vorticity). Between about 6833 and 6866 s simulated time (Fig. 10a, b), the main vortex in the middle shows perturbation pressures between -37 and -44 Pa, whereas the second and weaker vortex on the right has minimum pressures in the range of -20 to -30 Pa. After the merging, only one strong vortex remains with a maximum pressure drop of more than 50 Pa (Fig. 10d). In Sect. 3.2, the clustered occurrence of dust devils along convergence lines and near vertices of the cellular flow pattern has already suggested a strong interaction between different vortex centers during their lifetimes (see Fig. 7). The results are in agreement with Ohno and Takemi (2010a), who pointed out that most of the strong dust devils are first intensified through the merger of multiple vortices and subsequently maintained and more enhanced by additionally incorporating small-scale vortices. Doppler radar observations by Bluestein et al. (2004) also support a frequent interaction between different dust devil-like vortices.

The decrease of the grid spacing discloses more and more instantaneous fine-scale flow features. Some of them are displayed in Fig. 11. Panel a and b show horizontal snapshots of the vertical velocity and the horizontal wind at detection height for the analyzed vortices taken from simulation R10 and R10N2, respectively. Beside the overestimation of the vortex size in

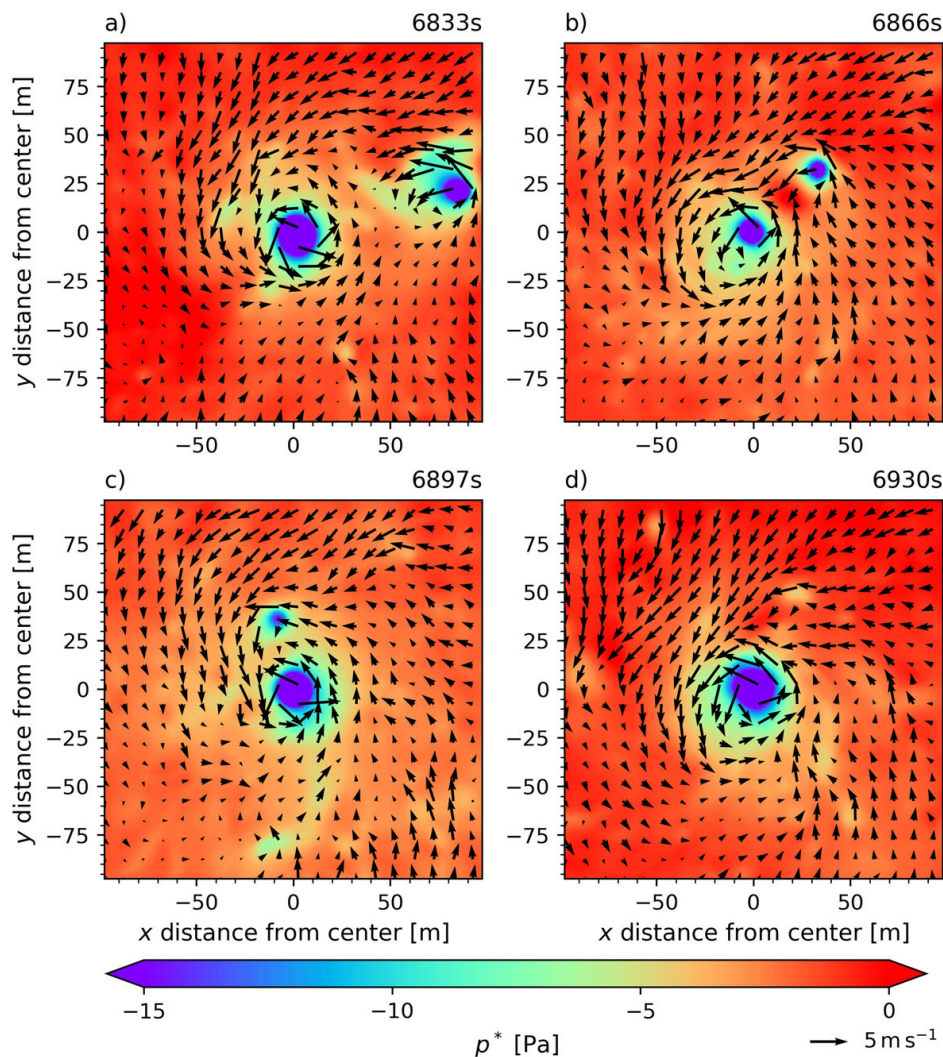


Fig. 10 Horizontal snapshots of the perturbation pressure of the most durable vortex that occurs in simulation R10N2.5 at detection height ($z = 11.25$ m) after approximately 6833, 6866, 6897, and 6930 s simulated time. Arrows indicate horizontal wind vectors. Every fourth vector is shown

R10 (see also Sects. 3.2 and 3.3.2), downdraughts are apparent in both core regions surrounded by pronounced positive vertical velocities. Such downdraughts appear to be an inherent feature for all investigated fully developed dust devils, which agrees well with measurements (Balme and Greeley 2006). However, vortices in R10 rarely show these central downdraughts, whereas vortices resolved with finer resolutions reveal a descending motion in or close to the center for most of the time. In the time-averaged dust devil data, upward motions are dominant nearly everywhere (see Sect. 3.3.2). This is not contradicting to the instantaneous data because the location of the region of descending air changes during the vortex lifetime. Thus, positive and negative vertical velocities alternate in the center (defined by the pressure minimum), still resulting in a positive time-averaged value. Horizontal gradients of w are much more distinct for the smaller grid spacings. The vortex in R10N2 partially shows an increase in the vertical velocity from -5 to 6 m s^{-1} over a distance of just 10 m. Observations related to dust devils have already shown the existence of pronounced downdraughts within the core (Kaimal and Businger 1970; Sinclair 1973). The two-cell vortex concept with descending air close the axis of rotation and upward motions aside (e.g., Mullen and Maxworthy 1977) fits also very well to our numerical simulations.

Figure 11c indicates an extended low pressure region southwest to the dust devil center ($x=[-30;0]$, $y=[-40;-20]$), which is another distinct flow feature that arises in our simulations independent of the resolution. We refer to this region as a tail-like structure in the following. The most striking pattern, however, is visible in the vertical velocity. Strong descending air is separated from strong upward motions in the same region where the tail in the pressure data is visible. The updraughts are always located closer to the center than the downdraughts. As far as we know, this dust devil characteristic has not been reported so far, probably because of missing high-resolution three-dimensional data. Nevertheless, a comprehensive analysis is not intended here and goes far beyond the scope of this study.

Finally, Fig. 11d indicates that dust devils can momentarily have several sub-centers that appear, for example, through neighbouring local pressure minima. This supports previous findings of secondary vortices within or around a main dust devil (Bluestein et al. 2004; Zhao et al. 2004; Lorenz et al. 2016; Oncley et al. 2016). Especially Zhao et al. (2004) highlight this issue in their dust-devil-scale simulation with a resolution down to 0.1 m. Pressure contours showed up to eight sub-centers that occur along the annular zone around the center where the strongest radial shear in both the tangential and the axial velocity components exist. In the most persistent vortex from R5N1.25, up to three distinct pressure drops appear next to each other. The number of secondary vortices scales with the resolution. A maximum of two sub-centers is visible in the dust devil data of simulation R10N2.5. For a grid width of 1 m, up to 4 sary vortices are observable. However, they seem to be quite unstable and last not more than several tens of seconds, which is why they can not be seen in the time-averaged fields.

The above discussion shows again that the model resolution is one of the most relevant parameters with respect to LES of dust devils. A definite recommendation which grid spacing must at least be used to capture the instantaneous vortex characteristics realistically is difficult to derive because appropriate field data that contain instantaneous, three-dimensional vortex information with high spatial and temporal resolution rarely exist or are limited to a few dust devil properties only (e.g., Bluestein et al. 2004; Oncley et al. 2016; Inagaki and Kanda 2022). Also the exact research question of follow-up studies will determine the resolution requirements. Our simulations with grid spacings of 10 and 5 m are missing some dust devil features like sub-vortices and they overestimate the sphere of influence significantly. This is why we suggest a minimum resolution below 5 m to qualitatively capture the instantaneous dust devil behaviour realistically.

3.3.2 Time-Averaged Data

A temporal average of quantities within the volume around the vortices' centers reveal typical dust devil features that have already been reported in other field or LES studies (for a comprehensive overview see Reiss et al. 2017). As indicated by horizontal cross-sections in Fig. 12, the surrounding region of a dust devil is characterized by negative pressure excursions with maximum values of the normalized perturbation pressure p^*/p_{\min}^* close to the center. The variable p_{\min}^* describes the minimum pressure drop that occurs in the whole region of $140 \times 140 \text{ m}^2$. Arrows of the horizontal wind vector show that the horizontal convergent flow rotates the strongest just outside the central region. Directly around the center, a flow with a weak radial component pointing away from the core is partly visible. This was already noticed by Sinclair (1973), who stated that there might be a radial outflow within the dust column. Also, Balme and Greeley (2006) illustrate this issue in their Fig. 8. The potential temperature, the vertical vorticity and velocity show distinct maximum values in or close to the center with a pattern similar to the one in Fig. 12. The local vertical vorticity is even

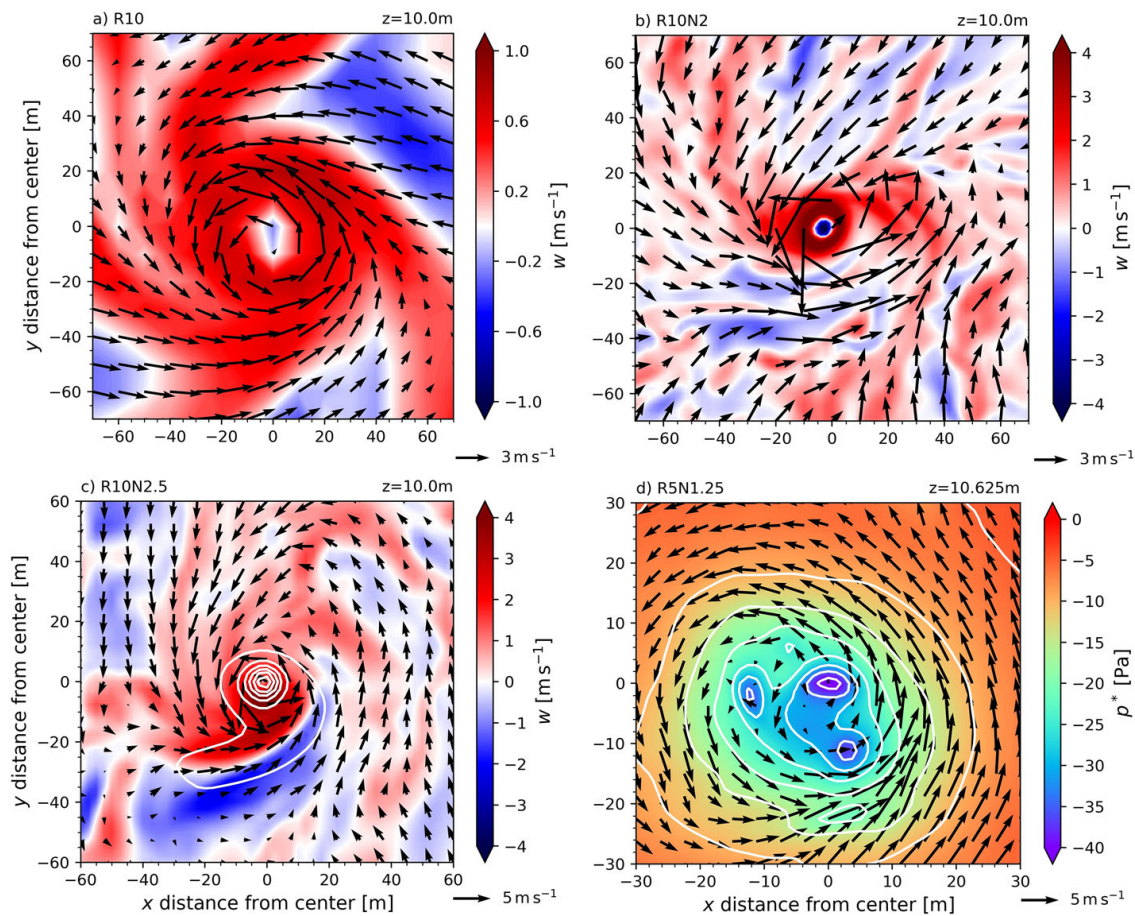


Fig. 11 **a–c** Display horizontal snapshots of the vertical velocity for the most durable vortices in simulation R10, R10N2, and R10N2.5. **d** Perturbation pressure for the most persistent vortex in simulation R5N1.25. Isolines with 8 Pa distance (**c**) and 5 Pa distance (**d**) highlight the distribution of the perturbation pressure. Arrows indicate horizontal wind vectors. Every fifth vector is plotted in (**b**). In the (**c**, **d**), every third vector is shown. Note the different color scales, reference arrows, and spatial ranges that are plotted for improving readability

more concentrated in the vortex core than the pressure drop and starts to randomly fluctuate around zero if a distance of more than 20–30 m to the center is reached (not shown). The mean vertical velocity maxima are mostly located several grid points adjacent to the vortex core similar to (Fig. 8 Raasch and Franke (2011)). Independent of the regarded quantity, all cross-sections demonstrate that coarser grid resolutions overestimate the horizontal vortex size and, thereby, the vortex sphere of influence significantly. Grid resolutions of 2.5 m or smaller (Fig. 12c–f) do not alter this sphere anymore, which is in agreement with the more quantitative analysis in Sect. 3.2 (see Fig. 8c).

Temporally averaged vertical cross-sections of the normalized temperature difference $(\theta - \theta_{\min}) / (\theta_{\max} - \theta_{\min})$ in Fig. 13 indicate the highest temperatures at ground level in the vortex core. The quantities θ_{\max} and θ_{\min} depict the maximum and minimum temperature occurring in the analyzed region of $140 \times 100 \text{ m}^2$. $\Delta\theta$ is defined as $\theta_{\max} - \theta_{\min}$. Temperature gradients tend to increase with lower grid spacings, which is a consequence of the better resolution of the super-adiabatic layer close to the surface. Throughout the whole displayed vertical range, warmer temperatures are apparent above the central region compared to temperatures outside the vortex core at the same height level. This is caused by the predominant vertical flow, which lifts the super-adiabatic surface layer of warm air. In agreement with the results

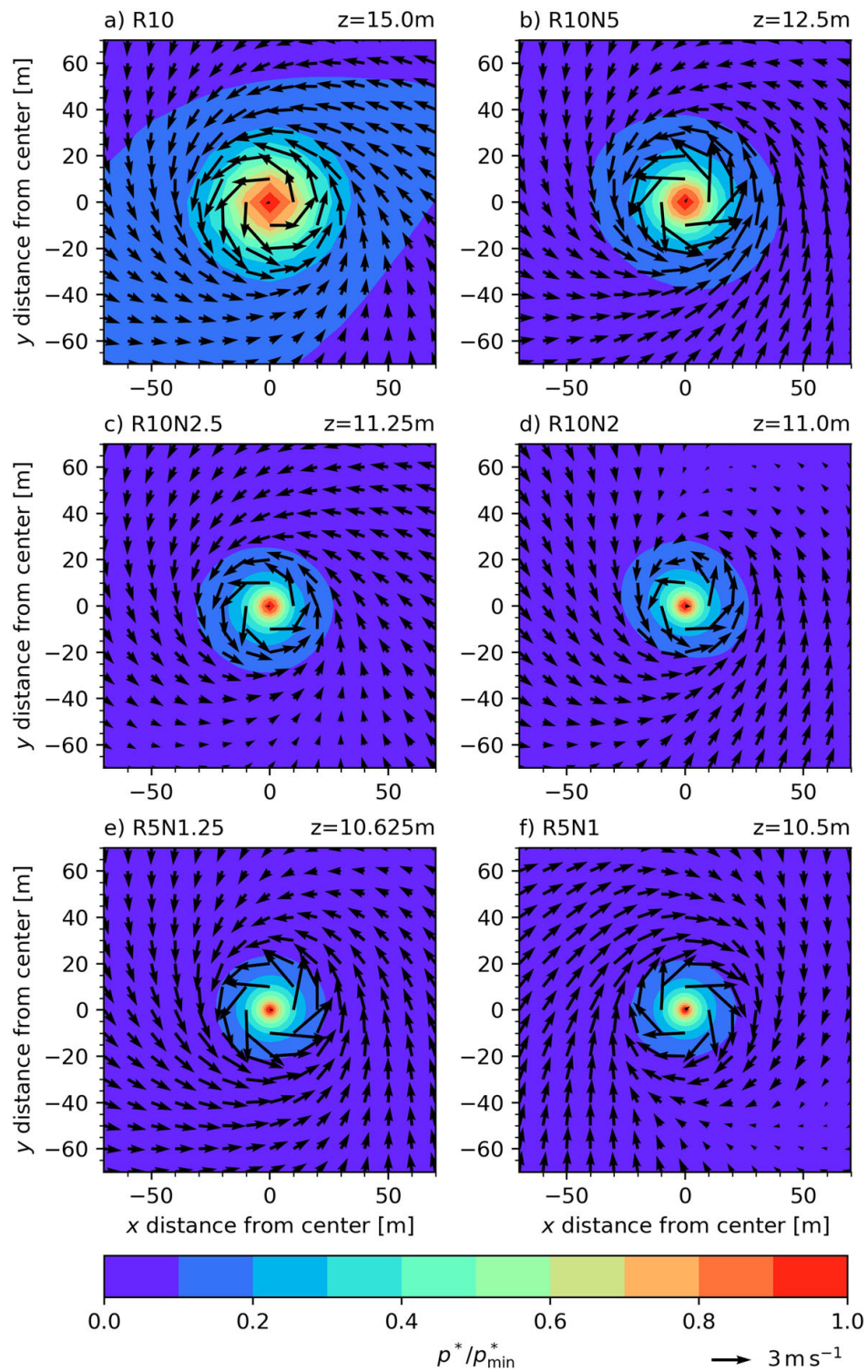


Fig. 12 Time-averaged horizontal cross-sections of the normalized perturbation pressure at detection height derived from different dust devil-like vortices that occur in R10, R10N5, R10N2.5, R10N2, R5N1.25, R5N1, and R10N2.5N0.625. Arrows indicate horizontal wind vectors. Their distance to each other is always 10m

from Sect. 3.1, the vertical extent of this layer outside the dust devil core is simulated to be very small for resolutions of around 2 m and below, but expands to several 10 m in height after being sucked into the vortex. A downward flow, which has often been reported (Kaimal and Businger 1970; Sinclair 1973; Balme and Greeley 2006), does not occur in the mean fields. However, reduced positive vertical velocities are visible in the vortex core compared to the values next to the center (not shown), which is in agreement with Raasch and Franke (2011). This is caused by instantaneous central downdraughts (see Sect. 3.3.1). Additionally, strong radial inflow is limited to the lower vortex regions. Air parcels that move near the surface heat up due to the prescribed positive surface heat flux and reach their highest temperatures when they approach the updraft region. Again, the size of the vortices is overestimated for resolutions larger than 2.5 m, which is also supported by vertical cross-sections of $\zeta/|\zeta|_{max}$ and p^*/p^*_{min} (not shown).

Isolines of the perturbation pressure in Fig. 13 reveal a minimum of the pressure at about 10 m height but only for grid spacings of 2 m and less. Such a pronounced and lifted minimum does not occur for coarser resolutions. Because DNS simulations of dust devils in Rayleigh-Bénard convection have also shown this feature (Giersch and Raasch 2021), we interpret it as an inherent characteristic of dust devil-like vortices. According to our knowledge, neither LES studies nor case studies of real dust devils have shown a lifted pressure minimum yet, probably because of a poor resolution or poorly available three-dimensional measurement data. A simple assumption of a steady circular vortex in cyclostrophic balance can explain this finding. Due to surface friction, maximum rotational velocities occur above the surface and not directly adjacent to it, which results in maximum radial pressure gradients at the same height level and, thus, stronger pressure drops. This situation is first captured for a resolution of 2 m. Also the mathematical model of whirlwinds by Pandey and Maurya (2017) includes a negative pressure gradient along z , which is especially important for the whirlwind to grow vertically.

To conclude, the mean three-dimensional structure of single dust devils reaches a nearly converged state at resolutions of approximately 2 m. For grid spacings above 2 m, especially the high spatial gradients and the vortex size are not captured appropriately. The overall convergent and spiraling upward flow is realistically simulated for each selected resolution, at least from a purely qualitative perspective.

4 Summary and Conclusions

In this study, we numerically investigated atmospheric dust devil-like vortices and their statistical properties. We focused on the resolution dependent convergence of various dust devil parameters. Simulations were performed with the large-eddy simulation (LES) model PALM. By using the nesting feature of PALM, we explored grid spacings between 10 and 0.625 m within a domain of approximately $4 \times 4 \times 2 \text{ km}^{-3}$. This domain and resolution captured the large-scale cellular pattern of the convective planetary boundary layer (PBL), in which dust devils naturally form.

As a first step, we developed a revised and resolution-independent version of the dust devil detection and analysis algorithm of Raasch and Franke (2011) and Giersch et al. (2019). It improved the comparability of dust devil statistics and properties between simulations of different resolutions and facilitated a direct comparison with field measurements and observations. We showed how careful this algorithm must be designed to adequately capture the natural spatial and temporal vortex scales and highlighted the challenges to create compa-

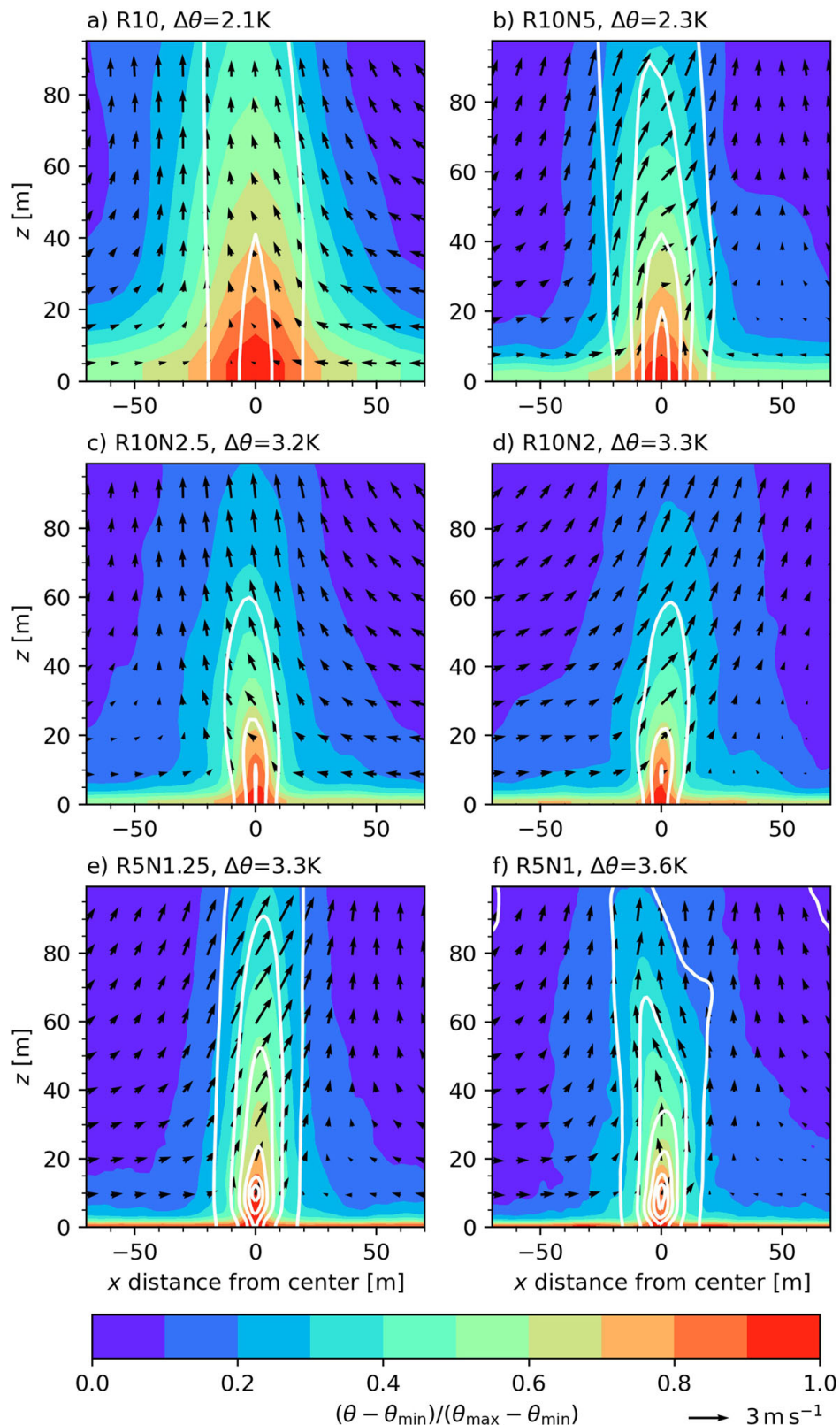


Fig. 13 Time-averaged vertical cross-sections of the normalized temperature difference through the center ($y = 0$) derived from different dust devil-like vortices that occur in R10, R10N5, R10N2.5, R10N2, R5N1.25, R5N1, and R10N2.5N0.625. Arrows indicate vertical wind vectors derived from u and w . Their distance to each other is always 10 m. Isolines with a distance of 8 Pa show the perturbation pressure

rable results between model runs with different resolutions. Also, the analyzed dust devil population for which the derived statistics are valid, must be clearly defined. Such a definition should include the detection algorithm itself, the current knowledge about real dust devils and changes in the dust devil physics that follow from a change in model resolution.

Convergence of the general flow in the convective PBL agrees well with previous studies (e.g., Sullivan and Patton 2011; Bopape et al. 2020; Wurps et al. 2020). For the boundary layer interior, grid spacings on the order of 10 m were sufficient to capture the mean flow and low-order moment statistics of the convective boundary layer appropriately. However, properties of the near surface layer, where dust devils mainly occur, still vary with resolution. Additionally, previous studies never analyzed convergence of peak values, like maximum wind velocities. Although not thoroughly investigated, our results indicated that extrema do not converge. Cursory analysis showed that most of the maxima are located within dust devils at heights below 30 m. Maxima at these heights are likely related to buoyancy caused by the super-adiabatic layer that is drawn into the cores of dust devils. Due to the non-convergence of the peak values, we concentrated our statistical analysis to mean dust devil properties. These mean properties were averaged over both the whole vortex lifetime and sample at a height of 10 m. We chose this height to avoid surface interference.

We defined the dust devil population to be investigated as all vortices with lifetimes of at least 120 s and lifetime-averaged radii of at least 5 m. The properties of this population were consistent with the results of field studies if resolutions of 1.25, 1, and 0.625 m were chosen. Therefore, we generally recommend a grid spacing below 2 m if quantitative results are desired from numerical simulations. However, the quantitative comparison between different measurement campaigns and model results remains challenging (e.g., because of poor three-dimensional measurement data or different analysis heights).

With a grid spacing of 1.25 or below, our results showed a converged dust devil occurrence rate of $19 \text{ km}^{-2} \text{ h}^{-1}$ or $77 \text{ km}^{-2} \text{ d}^{-1}$. Typical lifetimes were 4–5 min. The mean converged radius was between 6 and 8 m. Typical temperature excursions were 3–4 K with maxima of approximately 8 K. The mean strength of vortices, rated by the pressure drop at convergence, was approximately 14 Pa. Maximum instantaneous pressure drops of several hundreds of pascals existed in some vortices. The vertical vorticity averaged over a horizontal plane of $20 \times 20 \text{ m}^2$ around the dust devil center typically ranged between 0.1 and 1 s^{-1} . Finally, converged mean tangential and radial velocities were 2.1 m s^{-1} and 1.35 m s^{-1} , respectively, while maxima were 13 and 4 m s^{-1} , respectively. The vertical velocity never converged, even for the mean values. They constantly increased as grid spacing decreased from 1 to 2 m s^{-1} . At the finest resolution of 0.625 m, peak vertical velocities of nearly 20 m s^{-1} were simulated. A comparison with observations suggested that convergence is expected at resolutions of just less than 0.5 m, which might be affordable within the next years.

Finally, the analysis of the instantaneous and time-averaged three-dimensional flow structure indicates realistic results for grid spacings of 2.5 m or smaller. With such a resolution, all vortex features are qualitatively captured. This especially includes central downdrafts, sub-vortices and the near-ground convergent flow that becomes a dominant spiraling upward motion near the center. Also, the vertically-thin, super-adiabatic layer with high vertical temperature gradients in the dust devil surroundings, which is drawn into and stretched within the core, is captured appropriately. In instantaneous pressure fields, we frequently observe tail-like structures that separate strong updraughts from downdraughts. These structures have not been reported in the current literature.

Follow-up grid convergence studies should focus especially on convergence of extrema. Namely, do extrema converge at resolutions of just less than 0.5 m? These very high-resolution studies could then investigate the small-scale structures of dust devils in more detail. The

results presented here are useful for deriving better and more convincing quantitative estimates of dust devil phenomena (e.g., the amount of dust that is typically released by dust devil-like vortices). It is now clear that results derived from simulations at 10 m grid spacing or larger are not meaningful because pressure drops and wind velocities, which are directly related to turbulent dust emission, are too weakly simulated. In ongoing work, we are currently estimating the sediment fluxes and particle concentrations within dust devils. Generally speaking, this study can be taken as the basis for the resolution requirements that are needed to capture coherent vortex structures like dust devils in future LES studies.

Acknowledgements We are grateful to the HLRN supercomputer staff and to the provision of HLRN-IV-System on which the numerical simulations were performed. We also want to thank the staff from the Leibniz University IT Services (LUIS), especially Reiko Kaps for his support with the research repository.

Author Contributions SG and SR were involved in the conceptualization of the manuscript and the development of the applied methodology and software. The validation of model results was also done by both authors. SG wrote the main manuscript text, did the formal analysis and investigation of the research data, and prepared all the figures. He took care of the availability of numerical resources and the data management. SR acts as a supervisor and project coordinator. He also cared for the funding acquisition and was involved in reviewing and editing the manuscript.

Funding Open Access funding enabled and organized by Projekt DEAL. The work by Sebastian Giersch was funded by the German Research Foundation (DFG) under Grant RA 617/31-1 and supported by the North-German Supercomputing Alliance (HLRN). Siegfried Raasch supported the work as part of his employment at the Leibniz University Hannover.

Availability of data and materials The raw model output, user-specific code, model steering files and post-processing scripts can be accessed under the CC BY 3.0 licence via <https://doi.org/10.25835/x81j6gj2>. The PALM model system (<http://palm.muk.uni-hannover.de/trac/browser/?rev=4732>) is free software and can be redistributed and/or modified under the terms of the GNU General Public License (v3).

Declarations

Conflict of interest The authors declare that they have no known competing financial interests or personal relationships that could have appeared to influence the work reported in this paper.

Ethical Approval This declaration is not applicable.

Open Access This article is licensed under a Creative Commons Attribution 4.0 International License, which permits use, sharing, adaptation, distribution and reproduction in any medium or format, as long as you give appropriate credit to the original author(s) and the source, provide a link to the Creative Commons licence, and indicate if changes were made. The images or other third party material in this article are included in the article's Creative Commons licence, unless indicated otherwise in a credit line to the material. If material is not included in the article's Creative Commons licence and your intended use is not permitted by statutory regulation or exceeds the permitted use, you will need to obtain permission directly from the copyright holder. To view a copy of this licence, visit <http://creativecommons.org/licenses/by/4.0/>.

References

- Ansmann A, Tesche M, Knippertz P, Bierwirth E, Althausen D, Müller D, Schulz O (2009) Vertical profiling of convective dust plumes in southern morocco during SAMUM. *Tellus B Chem Phys Meteorol* 61(1):340–353. <https://doi.org/10.1111/j.1600-0889.2008.00384.x>
- Arakawa A, Lamb VR (1977) Computational design of the basic dynamical processes of the UCLA general circulation model. In: Chang J (ed) *Methods Comput Phys Adv Res Appl*, vol 17. Academic Press, New York, pp 173–265
- Balme M, Greeley R (2006) Dust devils on earth and mars. *Rev Geophys* 44(3):1–22. <https://doi.org/10.1029/2005RG000188>

- Bluestein HB, Weiss CC, Pazmany AL (2004) Doppler radar observations of dust devils in Texas. *Mon Weather Rev* 132(1):209–224. [https://doi.org/10.1175/1520-0493\(2004\)132<0209:DROODD>2.0.CO;2](https://doi.org/10.1175/1520-0493(2004)132<0209:DROODD>2.0.CO;2)
- Bopape MJM, Plant RS, Coceal O (2020) Resolution dependence of turbulent structures in convective boundary layer simulations. *Atmosphere* 11(9):1–28. <https://doi.org/10.3390/atmos11090986>
- Cortese T, Balachandar S (1998) Vortical nature of thermal plumes in turbulent convection. *Phys Fluids* 5(12):3226–3232. <https://doi.org/10.1063/1.858679>
- Deardorff JW (1980) Stratocumulus-capped mixed layers derived from a three-dimensional model. *Boundary-Layer Meteorol* 18(4):495–527. <https://doi.org/10.1007/BF00119502>
- DeMott PJ, Sassen K, Poellot MR, Baumgardner D, Rogers DC, Brooks SD, Prenni AJ, Kreidenweis SM (2003) African dust aerosols as atmospheric ice nuclei. *Geophys Res Lett* 30(14):1–4. <https://doi.org/10.1029/2003GL017410>
- Fenton LK, Lorenz R (2015) Dust devil height and spacing with relation to the Martian planetary boundary layer thickness. *Icarus* 260:246–262. <https://doi.org/10.1016/j.icarus.2015.07.028>
- Fitzjarrald DE (1973) A field investigation of dust devils. *J Appl Meteorol* 12(5):808–813. [https://doi.org/10.1175/1520-0450\(1973\)012<0808:AFIODD>2.0.CO;2](https://doi.org/10.1175/1520-0450(1973)012<0808:AFIODD>2.0.CO;2)
- Gadde SN, Stieren A, Stevens RJAM (2021) Large-eddy simulations of stratified atmospheric boundary layers: comparison of different subgrid models. *Boundary-Layer Meteorol* 178(3):363–382. <https://doi.org/10.1007/s10546-020-00570-5>
- Giersch S, Raasch S (2021) Evolution and features of dust devil-like vortices in turbulent Rayleigh–Bénard convection—a numerical study using direct numerical simulation. *J Geophys Res Atmos* 126(7):1–36. <https://doi.org/10.1029/2020JD034334>
- Giersch S, Brast M, Hoffmann F, Raasch S (2019) Toward large-eddy simulations of dust devils of observed intensity: effects of grid spacing, background wind, and surface heterogeneities. *J Geophys Res Atmos* 124(14):7697–7718. <https://doi.org/10.1029/2019JD030513>
- Gropp W, Lusk E, Skjellum A (1999) Using MPI: portable parallel programming with the message passing interface, 2nd edn. MIT Press, Cambridge
- Gu Z, Qiu J, Zhao Y, Li Y (2008) Simulation of terrestrial dust devil patterns. *Adv Atmos Sci* 25(1):31–42. <https://doi.org/10.1007/s00376-008-0031-7>
- Hellsten A, Ketelsen K, Sühling M, Auvinen M, Maronga B, Knigge C, Barmpas F, Tsegas G, Moussiopoulos N, Raasch S (2021) A nested multi-scale system implemented in the large-eddy simulation model palm model system 6.0. *Geosci Model Dev* 14(6):3185–3214. <https://doi.org/10.5194/gmd-14-3185-2021>
- Hess GD, Spillane KT (1990) Characteristics of dust devils in Australia. *J Appl Meteorol Clim* 29(6):498–507. [https://doi.org/10.1175/1520-0450\(1990\)029<0498:CODDIA>2.0.CO;2](https://doi.org/10.1175/1520-0450(1990)029<0498:CODDIA>2.0.CO;2)
- Horton W, Miura H, Onishchenko O, Couedel L, Arnas C, Escarguel A, Benkadda S, Fedun V (2016) Dust devil dynamics. *J Geophys Res Atmos* 121(12):7197–7214. <https://doi.org/10.1002/2016JD024832>
- Houser JG, Farrell WM, Metzger SM (2003) Ulf and elf magnetic activity from a terrestrial dust devil. *Geophys Res Lett* 30(1):1–27. <https://doi.org/10.1029/2001GL014144>
- Inagaki A, Kanda M (2022) Use of thermal image velocimetry to measure a dust-devil-like vortex within a sports ground in a residential area. *Boundary-Layer Meteorol* 183(1):125–141. <https://doi.org/10.1007/s10546-021-00674-6>
- Ito J, Niino H, Nakanishi M (2010) Large eddy simulation on dust suspension in a convective mixed layer. *SOLA* 6:133–136. <https://doi.org/10.2151/sola.2010-034>
- Ito J, Tanaka R, Niino H, Nakanishi M (2010) Large eddy simulation of dust devils in a diurnally-evolving convective mixed layer. *J Meteorol Soc Jpn* 88(1):63–77. <https://doi.org/10.2151/jmsj.2010-105>
- Ito J, Niino H, Nakanishi M (2013) Formation mechanism of dust devil-like vortices in idealized convective mixed layers. *J Atmos Sci* 70(4):1173–1186. <https://doi.org/10.1175/JAS-D-12-085.1>
- Ives RL (1947) Behavior of dust devils. *Bull Am Meteorol Soc* 28(4):168–174. <https://doi.org/10.1175/1520-0477-28.4.168>
- Jemmett-Smith BC, Marsham JH, Knippertz P, Gilkeson CA (2015) Quantifying global dust devil occurrence from meteorological analyses. *Geophys Res Lett* 42(4):1275–1282. <https://doi.org/10.1002/2015GL063078>
- Kaimal JC, Businger JA (1970) Case studies of a convective plume and a dust devil. *J Appl Meteorol Clim* 9(4):612–620. [https://doi.org/10.1175/1520-0450\(1970\)009<0612:CSOACP>2.0.CO;2](https://doi.org/10.1175/1520-0450(1970)009<0612:CSOACP>2.0.CO;2)
- Kanak KM (2005) Numerical simulation of dust devil-scale vortices. *QJR Meteorol Soc* 131(607):1271–1292. <https://doi.org/10.1256/qj.03.172>
- Kanak KM (2006) On the numerical simulation of dust devil-like vortices in terrestrial and Martian convective boundary layers. *Geophys Res Lett* 33(19):1–4. <https://doi.org/10.1029/2006GL026207>
- Kanak KM, Lilly DK, Snow JT (2000) The formation of vertical vortices in the convective boundary layer. *QJR Meteorol Soc* 126(569):2789–2810. <https://doi.org/10.1002/qj.49712656910>

- Khanna S, Brasseur JG (1998) Three-dimensional buoyancy- and shear-induced local structure of the atmospheric boundary layer. *J Atmos Sci* 55(5):710–743. [https://doi.org/10.1175/1520-0469\(1998\)055<0710:TDBASI>2.0.CO;2](https://doi.org/10.1175/1520-0469(1998)055<0710:TDBASI>2.0.CO;2)
- Klose M, Shao Y (2013) Large-eddy simulation of turbulent dust emission. *Aeolian Res* 8:49–58. <https://doi.org/10.1016/j.aeolia.2012.10.010>
- Klose M, Shao Y (2016) A numerical study on dust devils with implications to global dust budget estimates. *Aeolian Res* 22:47–58. <https://doi.org/10.1016/j.aeolia.2016.05.003>
- Koch J, Rennó NO (2005) The role of convective plumes and vortices on the global aerosol budget. *Geophys Res Lett* 32(18):1–5. <https://doi.org/10.1029/2005GL023420>
- Kurgansky MV (2006) Size distribution of dust devils in the atmosphere. *Izv Atmos Ocean Phys* 42(3):319–325. <https://doi.org/10.1134/S0001433806030054>
- Kurgansky MV, Lorenz RD, Rennó NO, Takemi T, Gu Z, Wei W (2016) Dust devil steady-state structure from a fluid dynamics perspective. *Space Sci Rev* 203(1–4):209–244. <https://doi.org/10.1007/s11214-016-0281-0>
- Lorenz RD (2009) Power law of dust devil diameters on mars and earth. *Icarus* 203(2):683–684. <https://doi.org/10.1016/j.icarus.2009.06.029>
- Lorenz RD (2013) The longevity and aspect ratio of dust devils: effects on detection efficiencies and comparison of landed and orbital imaging at mars. *Icarus* 226(1):964–970. <https://doi.org/10.1016/j.icarus.2013.06.031>
- Lorenz RD (2014) Vortex encounter rates with fixed barometer stations: comparison with visual dust devil counts and large-eddy simulations. *J Atmos Sci* 71(12):4461–4472. <https://doi.org/10.1175/JAS-D-14-0138.1>
- Lorenz RD, Jackson BK (2016) Dust devil populations and statistics. *Space Sci Rev* 203(1):277–297. <https://doi.org/10.1007/s11214-016-0277-9>
- Lorenz RD, Lanagan PD (2014) A barometric survey of dust-devil vortices on a desert playa. *Boundary-Layer Meteorol* 153(3):555–568. <https://doi.org/10.1007/s10546-014-9954-y>
- Lorenz RD, Balme MR, Gu Z, Kahanpää H, Klose M, Kurgansky MV, Patel MR, Reiss D, Rossi AP, Spiga A, Takemi T, Wei W (2016) History and applications of dust devil studies. *Space Sci Rev* 203(1–4):5–37. <https://doi.org/10.1007/s11214-016-0239-2>
- Lyons TJ, Nair US, Foster IJ (2008) Clearing enhances dust devil formation. *J Arid Environ* 72(10):1918–1928. <https://doi.org/10.1016/j.jaridenv.2008.05.009>
- Maronga B, Gryscha M, Heinze R, Hoffmann F, Kanani-Sühring F, Keck M, Ketelsen K, Letzel MO, Sühring M, Raasch S (2015) The Parallelized Large-Eddy Simulation Model (PALM) version 4.0 for atmospheric and oceanic flows: model formulation, recent developments, and future perspectives. *Geosci Model Dev* 8(8):2515–2551. <https://doi.org/10.5194/gmd-8-2515-2015>
- Maronga B, Banzhaf S, Burmeister C, Esch T, Forkel R, Fröhlich D, Fuka V, Gehrke KF, Geletic J, Giersch S, Gronemeier T, Groß G, Heldens W, Hellsten A, Hoffmann F, Inagaki A, Kadasch E, Kanani-Sühring F, Ketelsen K, Khan BA, Knigge C, Knoop H, Krc P, Kurppa M, Maamari H, Matzarakis A, Mauder M, Pallasch M, Pavlik D, Pfafferoth J, Resler J, Rissmann S, Russo E, Salim M, Schrempf M, Schwenkel J, Seckmeyer G, Schubert S, Sühring M, von Tils R, Vollmer L, Ward S, Witha B, Wurps H, Zeidler J, Raasch S (2020) Overview of the palm model system 6.0. *Geosci Model Dev* 13(3):1335–1372. <https://doi.org/10.5194/gmd-13-1335-2020>
- Maronga B, Knigge C, Raasch S (2020) An improved surface boundary condition for large-eddy simulations based on Monin–Obukhov similarity theory: Evaluation and consequences for grid convergence in neutral and stable conditions. *Boundary-Layer Meteorol* 174(2):297–325. <https://doi.org/10.1007/s10546-019-00485-w>
- Moeng CH, Sullivan PP (1993) A comparison of shear- and buoyancy-driven planetary boundary layer flows. *J Atmos Sci* 51(7):999–1022. [https://doi.org/10.1175/1520-0469\(1994\)051<0999:ACOSAB>2.0.CO;2](https://doi.org/10.1175/1520-0469(1994)051<0999:ACOSAB>2.0.CO;2)
- Moeng CH, Wyngaard JC (1988) Spectral analysis of large-eddy simulations of the convective boundary layer. *J Atmos Sci* 45(23):3573–3587. [https://doi.org/10.1175/1520-0469\(1988\)045<3573:SAOLES>2.0.CO;2](https://doi.org/10.1175/1520-0469(1988)045<3573:SAOLES>2.0.CO;2)
- Mullen JB, Maxworthy T (1977) A laboratory model of dust devil vortices. *Dyn Atmos Oceans* 1(3):181–214. [https://doi.org/10.1016/0377-0265\(77\)90006-9](https://doi.org/10.1016/0377-0265(77)90006-9)
- Myhre G, Stordal F (2001) Global sensitivity experiments of the radiative forcing due to mineral aerosols. *J Geophys Res Atmos* 106(D16):18,193–18,204. <https://doi.org/10.1029/2000JD900536>
- Neakrase DL, Greeley R (2010) Dust devil sediment flux on earth and mars: laboratory simulations. *Icarus* 206(1):306–318. <https://doi.org/10.1016/j.icarus.2009.08.028>
- Nishizawa S, Odaka M, Takahashi YO, Sugiyama K, Nakajima K, Ishiwatari M, Takehiro S, Yashiro H, Sato Y, Tomita H, Hayashi YY (2016) Martian dust devil statistics from high-resolution large-eddy simulations. *Geophys Res Lett* 43(9):4180–4188. <https://doi.org/10.1002/2016GL068896>

- Ohno H, Takemi T (2010) Mechanisms for intensification and maintenance of numerically simulated dust devils. *Atmos Sci Lett* 11(1):27–32
- Ohno H, Takemi T (2010) Numerical study for the effects of mean wind on the intensity and evolution of dust devils. *SOLA* 6A:5–8. <https://doi.org/10.2151/sola.6A-002>
- Oke AMC, Tapper NJ, Dunkerley D (2007) Willy-Willies in the Australian landscape: the role of key meteorological variables and surface conditions in defining frequency and spatial characteristics. *J Arid Environ* 71(2):201–215. <https://doi.org/10.1016/j.jaridenv.2007.03.008>
- Oncley SP, Hartogensis O, Tong C (2016) Whirlwinds and hairpins in the atmospheric surface layer. *J Atmos Sci* 73(12):4927–4943. <https://doi.org/10.1175/JAS-D-15-0368.1>
- Pandey SK, Maurya JP (2017) Exploration of characteristics governing dynamics of whirlwinds: application to dust devils. *Z Naturforsch* 72(8):763–778. <https://doi.org/10.1515/zna-2017-0163>
- Park SB, Baik JJ (2014) Large-eddy simulations of convective boundary layers over flat and urbanlike surfaces. *J Atmos Sci* 71(5):1880–1892. <https://doi.org/10.1175/JAS-D-13-0191.1>
- Patrinos AAN, Kistler AL (1977) A numerical study of the Chicago lake breeze. *Boundary-Layer Meteorol* 12(1):93–123. <https://doi.org/10.1007/BF00116400>
- Raasch S, Franke T (2011) Structure and formation of dust devil-like vortices in the atmospheric boundary layer: a high-resolution numerical study. *J Geophys Res Atmos* 116(D16):1–16. <https://doi.org/10.1029/2011JD016010>
- Raasch S, Schröter M (2001) Palm—a large-eddy simulation model performing on massively parallel computers. *Meteorol Z* 10(5):363–372. <https://doi.org/10.1127/0941-2948/2001/0010-0363>
- Reiss D, Lorenz R, Balme M, Neakrase L, Rossi AP, Spiga A, Zarnecki J (2017) *Dust devils*, 1st edn. Springer, Dordrecht
- Rennó NO, Burkett ML, Larkin MP (1998) A simple thermodynamical theory for dust devils. *J Atmos Sci* 55(21):3244–3252. [https://doi.org/10.1175/1520-0469\(1998\)055<3244:ASTTFD>2.0.CO;2](https://doi.org/10.1175/1520-0469(1998)055<3244:ASTTFD>2.0.CO;2)
- Rennó NO, Abreu VJ, Koch J, Smith PH, Hartogensis OK, Bruin HARD, Burose D, Delory GT, Farrell WM, Watts CJ, Garatuza J, Parker M, Carswell A (2004) Matador 2002: a pilot field experiment on convective plumes and dust devils. *J Geophys Res* 109(E7):1–10. <https://doi.org/10.1029/2003JE002219>
- Richter D, Sullivan P (2013) Momentum transfer in a turbulent, particle-laden Couette flow. *Phys Fluids* 25(5):1–20. <https://doi.org/10.1063/1.4804391>
- Saiki EM, Moeng CH, Sullivan PP (2000) Large-eddy simulation of the stably stratified planetary boundary layer. *Boundary-Layer Meteorol* 95(1):1–30. <https://doi.org/10.1023/A:1002428223156>
- Scherer D, Fehrenbach U, Grassmann T, Holtmann A, Meier F, Scherber K, Pavlik D, Höhne T, Kanani-Sühring F, Maronga B, Ament F, Banzhaf S, Langer I, Halbig G, Kohler M, Queck R, Stratbücker S, Winkler M, Wegener R, Zeeman M (2020) [uc]² data standard “urban climate under change.” Federal Ministry of Education and Research. Tech Rep 1(4):1
- Schmidt H, Schumann U (1989) Coherent structure of the convective boundary layer derived from large-eddy simulations. *J Fluid Mech* 200:511–562. <https://doi.org/10.1017/S0022112089000753>
- Schumann U (1975) Subgrid scale model for finite difference simulations of turbulent flows in plane channels and annuli. *J Comput Phys* 18(4):376–404. [https://doi.org/10.1016/0021-9991\(75\)90093-5](https://doi.org/10.1016/0021-9991(75)90093-5)
- Sinclair PC (1964) Some preliminary dust devil measurements. *Mon Weather Rev* 92(8):363–367. [https://doi.org/10.1175/1520-0493\(1964\)092<0363:SPDDM>2.3.CO;2](https://doi.org/10.1175/1520-0493(1964)092<0363:SPDDM>2.3.CO;2)
- Sinclair PC (1969) General characteristics of dust devils. *J Appl Meteorol Clim* 8(1):32–45. [https://doi.org/10.1175/1520-0450\(1969\)008<0032:GCODD>2.0.CO;2](https://doi.org/10.1175/1520-0450(1969)008<0032:GCODD>2.0.CO;2)
- Sinclair PC (1973) The lower structure of dust devils. *J Atmos Sci* 30(8):1599–1619. [https://doi.org/10.1175/1520-0469\(1973\)030<1599:TLSODD>2.0.CO;2](https://doi.org/10.1175/1520-0469(1973)030<1599:TLSODD>2.0.CO;2)
- Souza EP, Rennó NO, Dias MAFS (2000) Convective circulations induced by surface heterogeneities. *J Atmos Sci* 57(17):2915–2922. [https://doi.org/10.1175/1520-0469\(2000\)057<2915:CCIBSH>2.0.CO;2](https://doi.org/10.1175/1520-0469(2000)057<2915:CCIBSH>2.0.CO;2)
- Spiga A, Barth E, Gu Z, Hoffmann F, Ito J, Jemmett-Smith B, Klose M, Nishizawa S, Raasch S, Rafkin S, Takemi T, Tyler D, Wei W (2016) Large-eddy simulations of dust devils and convective vortices. *Space Sci Rev* 203(1–4):245–275. <https://doi.org/10.1007/s11214-016-0284-x>
- Stull RB (1988) *An introduction to boundary layer meteorology*, 1st edn. Kluwer Academic Publishers, Cambridge. <https://doi.org/10.1007/978-94-009-3027-8>
- Sullivan PP, Patton EG (2011) The effect of mesh resolution on convective boundary layer statistics and structures generated by large-eddy simulation. *J Atmos Sci* 68(10):2395–2415. <https://doi.org/10.1175/JAS-D-10-05010.1>
- Tratt DM, Hecht MH, Catling DC, Samulon EC, Smith PH (2003) In situ measurement of dust devil dynamics: toward a strategy for mars. *J Geophys Res* 108(E11):1–7. <https://doi.org/10.1029/2003JE002161>
- Wicker LJ, Skamarock WC (2002) Time-splitting methods for elastic models using forward time schemes. *Mon Weather Rev* 130(8):2088–2097. [https://doi.org/10.1175/1520-0493\(2002\)130<2088:TSMFEM>2.0.CO;2](https://doi.org/10.1175/1520-0493(2002)130<2088:TSMFEM>2.0.CO;2)

- Williams NR (1948) Development of dust whirls and similar small-scale vortices. *Bull Am Meteorol Soc* 29(3):106–117. <https://doi.org/10.1175/1520-0477-29.3.106>
- Williamson JH (1980) Low-storage Runge–Kutta schemes. *J Comput Phys* 35(1):48–56. [https://doi.org/10.1016/0021-9991\(80\)90033-9](https://doi.org/10.1016/0021-9991(80)90033-9)
- Wurps H, Steinfeld G, Heinz S (2020) Grid-resolution requirements for large-eddy simulations of the atmospheric boundary layer. *Boundary-Layer Meteorol* 175(2):179–201. <https://doi.org/10.1007/s10546-020-00504-1>
- Zhao YZ, Gu ZL, Yu YZ, Ge Y, Li Y, Feng X (2004) Mechanism and large eddy simulation of dust devils. *Atmos-Ocean* 42(1):61–84. <https://doi.org/10.3137/ao.420105>

Publisher's Note Springer Nature remains neutral with regard to jurisdictional claims in published maps and institutional affiliations.

Chapter 6

Saltation-Induced Dust Emission of Dust Devils in the Convective Boundary Layer - An LES Study on the Meter Scale

6.1 Declaration of Contributions

The author contributions are given on the left at the first page of the research article.

6.2 Research Article

Klamt, J., Giersch, S., and Raasch, S.: Saltation-Induced Dust Emission of Dust Devils in the Convective Boundary Layer - An LES Study on the Meter Scale, *J. Geophys. Res. Atmos.*, **129**, e2023JD040 058, doi:10.1029/2023JD040058, 2024.

©2024. The Authors. CC BY 4.0 License.¹

¹The dissertation submitted on September 27, 2023, to the faculty of mathematics and physics of the Leibniz University Hannover contained a manuscript of the research article that was submitted on the same date to the Journal of Geophysical Research: Atmospheres. This manuscript has been replaced here by the finally accepted and officially published article from March 28, 2024. Changes compared to the manuscript are only minor due to requirements and editorial processing of the journal.



RESEARCH ARTICLE

10.1029/2023JD040058

Saltation-Induced Dust Emission of Dust Devils in the Convective Boundary Layer—An LES Study on the Meter Scale

J. Klamt^{1,2} , S. Giersch¹ , and S. Raasch¹

¹Institute of Meteorology and Climatology, Leibniz University Hannover, Hannover, Germany, ²Deutsches Zentrum für Luft- und Raumfahrt, Institut für Physik der Atmosphäre, Oberpfaffenhofen, Germany

Key Points:

- Dust devils cause peak dust emission fluxes of $46.7 \text{ mg m}^{-2} \text{ s}^{-1}$, which is 1–2 orders of magnitude larger than previous numerical estimates
- Dust devils contribute an average of 5% to the total dust emission of the simulated domain, with instantaneous contributions of up to 15%
- Saltation-induced dust emission is arranged in large-scale patterns that are related to the polygonal convection cells of the boundary layer

Correspondence to:

J. Klamt,
janis.klamt@dlr.de

Citation:

Klamt, J., Giersch, S., & Raasch, S. (2024). Saltation-induced dust emission of dust devils in the convective boundary layer—An LES study on the meter scale. *Journal of Geophysical Research: Atmospheres*, 129, e2023JD040058. <https://doi.org/10.1029/2023JD040058>

Received 27 SEP 2023
Accepted 11 MAR 2024

Author Contributions:

Conceptualization: J. Klamt, S. Giersch, S. Raasch
Data curation: J. Klamt, S. Giersch
Formal analysis: J. Klamt
Investigation: J. Klamt, S. Giersch
Methodology: J. Klamt, S. Giersch, S. Raasch
Project administration: S. Giersch, S. Raasch
Resources: S. Giersch, S. Raasch
Software: J. Klamt, S. Giersch, S. Raasch
Supervision: S. Giersch, S. Raasch
Validation: J. Klamt, S. Giersch
Visualization: J. Klamt
Writing – original draft: J. Klamt, S. Giersch
Writing – review & editing: S. Giersch, S. Raasch

Abstract Dust devils are vertically oriented, columnar vortices that form within the atmospheric convective boundary layer (CBL) of dry regions. They are able to lift a sufficient amount of soil particles including dust to become visible and are considered as a potentially important dust source for the atmosphere. Mineral dust, a key component of atmospheric aerosols, influences the climate by affecting the radiation budget and cloud formation. Current estimates of the contribution of dust devils to the global, regional, and local dust release vary considerably from less than 1% to more than 50%. To address this uncertainty, we perform the highest resolved large-eddy simulation (LES) study on dust emission in the CBL to date, using the PALM model system and the saltation-based Air Force Weather Agency (AFWA) dust emission scheme. Our results show that under desert-like conditions, dust devils are responsible for an average of 5% of regional dust emissions, with temporary maxima of up to 15%. This contrasts with previous measurement-based (>35%) and LES-based estimates (~0.1%). Local emissions of dust devils (up to $10 \text{ mg m}^{-2} \text{ s}^{-1}$) are 1–3 orders of magnitude higher than the emission in the surroundings. This makes dust devils important for air quality and visibility. Additionally, our study reveals previously unknown large-scale convective dust emission patterns. These patterns are tied to the CBL's cellular flow structure and are the main cause of dust release. Contrary to other studies, our findings clarify the important role of saltation-induced dust emission.

Plain Language Summary Dust devils, vertically oriented convective vortices frequently observed in arid and semi-arid regions, are potential contributors to the atmospheric dust. This airborne dust has significant implications for climate, as it can alter the radiation budget and influence cloud formation. The exact proportion of atmospheric dust originating from dust devils is currently under debate, with widely varying estimates. To address this uncertainty, we used an advanced turbulence-resolving large-eddy simulation model, the PALM model system, combined with the saltation-based Air Force Weather Agency's dust emission scheme. Our results showed that under desert-like conditions, dust devils account for an average of 5% of regional dust emissions. Peaks can reach up to 15%. Notably, these figures challenge both previous measurement and simulation-based assessments. Additionally, our study found that dust devils produce local dust emission fluxes up to 1–3 orders of magnitude higher than ambient values. This suggests a notable effect on air quality and visibility. Moreover, we identified large-scale patterns of dust emission linked to the flow structure of the convective boundary layer. These patterns emerge as the primary contributors to the regional dust release. Our study underscored the importance of understanding saltation-induced dust emission and the role of dust devils in the atmosphere.

1. Introduction

Dust devils are atmospheric vortices with a vertical axis of rotation that frequently occur under convective conditions when the surface is heated by insulation, causing strong superadiabatic temperature gradients near the ground. During the last 80 years, dust devils have been studied extensively with field measurements (e.g., Ives, 1947; Lorenz & Lanagan, 2014; Sinclair, 1964), laboratory experiments (e.g., Kaestner et al., 2023; Mullen & Maxworthy, 1977; Neakrase & Greeley, 2010) and, especially since the 21st century, with numerical simulations, utilizing large-eddy simulation (LES) and direct numerical simulation (e.g., Giersch & Raasch, 2021; Kanak et al., 2000; Raasch & Franke, 2011). All these studies showed a wide range of values for the characteristics of dust devils, covering several orders of magnitude (Balme & Greeley, 2006; Murphy et al., 2016; Spiga et al., 2016). For

© 2024. The Authors.
This is an open access article under the terms of the [Creative Commons Attribution License](https://creativecommons.org/licenses/by/4.0/), which permits use, distribution and reproduction in any medium, provided the original work is properly cited.

example, dust devils have spatial extents of 1 m to more than 100 m horizontally, range from a few meters to more than 1,000 m vertically, and show lifetimes from a few seconds to hours. They cause pressure drops of up to several hundred pascal and maximum horizontal wind speeds of 25 m s^{-1} , which is why they are able to lift a sufficient amount of soil particles including dust to become visible. The lifted particles are often transported to altitudes far away from the ground by the swirling upward motion of up to 15 m s^{-1} . The dust fluxes provoked by dust devils and the corresponding contribution to the total atmospheric dust amount are frequently discussed (Klose et al., 2016). Especially larger dust devils might contribute significantly because they potentially lift a large amount of dust-sized particles into the boundary layer. These particles can be further transported into the free atmosphere, where they remain for several days or weeks, affecting the Earth's climate system (Knippertz & Stuut, 2014).

Atmospheric dust, as a major contributor to the atmospheric aerosol content, interacts with the climate system. The aerosols modify the radiation budget through scattering and absorbing shortwave radiation as well as absorbing and re-emitting longwave radiation (Miller et al., 2014). Additionally, they modify micro-physical processes of cloud formation by acting as ice nuclei and, thereby, influencing the cloud's feedback on the climate (Nenes et al., 2014). Moreover, dust contains a variety of organic and inorganic substances, which might serve as nutrients for the local ecology after deposition (Barcan et al., 2023), but which can also cause environmental and health issues (Morman & Plumlee, 2014). Despite this important role of atmospheric dust, its lifting mechanisms are inadequately assessed and estimates of the total global dust emission show large uncertainties, for example, Huneus et al. (2011) proposed a range of $0.5\text{--}4 \times 10^9 \text{ t yr}^{-1}$. These uncertainties can be partly explained by the contributions of small-scale phenomena such as dust devils, which are insufficiently quantified. Previous studies on the global and regional contribution by dust devils to the total dust emission did not show consistent results. Estimations based on data from the European Center for Medium-Range Weather Forecasts (ECMWF), theoretical considerations, and observational data like in-situ measurements of dust fluxes suggest a global contribution between 3.4% (Jemmett-Smith et al., 2015) and 35% (Koch & Renno, 2005). However, both studies presented large uncertainties of roughly 15%–50% (Koch & Renno, 2005) and 1%–30% (Jemmett-Smith et al., 2015) in their estimated global contributions, even though they did not take into account the variability in the estimates of the total global dust emissions, which would further increase the contribution uncertainty. Regional estimates based on the numerical Weather Research and Forecast (WRF) model, thermodynamic theory, and measurements vary between 38% for North Africa (Pan et al., 2021) and up to 53% for Western China (Han et al., 2016). Numerical simulations with the WRF Chemistry (WRF-Chem) model coupled with a new parameterization scheme for dust devils revealed a contribution in East Asia between 17.4% and 43.4% (Tang et al., 2018). Employing LES instead of large-scale weather prediction models, Klose and Shao (2016) estimated a regional contribution for Australia in the range of 0.03%–0.19%.

The primary challenge in estimating the contribution of dust devils to the overall dust release is the quantification of typical dust fluxes. For dust devils, laboratory investigations, in-situ measurements and numerical simulations have not been able to adequately quantify dust fluxes of similar magnitude so far (Klose et al., 2016). While laboratory studies usually require the artificial genesis of convective vortices in a vortex chamber (e.g., Mullen & Maxworthy, 1977), measurements of dust devils suffer from the limited area that can be reliably monitored (e.g., Lorenz, 2014), and numerical simulations are mainly constrained by limited computing power (e.g., Giersch & Raasch, 2023). In addition, field studies are restricted to arid or semi-arid regions and are further complicated by the sporadic genesis of dust devils. Nevertheless, spatially fixed and portable measurement techniques were able to quantify at least basic dust devil characteristics like wind speeds and pressure drops (Balme & Greeley, 2006; Murphy et al., 2016). However, measurements of dust fluxes by dust devils are particularly difficult. Dust fluxes are determined by the product of the mass (or particle) concentration and the vertical velocity. Therefore, two quantities instead of one must be measured simultaneously (Klose et al., 2016). There have been multiple attempts to quantify dust fluxes in the field, for example, the aircraft measurements of Gillette and Sinclair (1990), LIDAR measurements of Renno et al. (2004), or measurements derived from instrumented vehicles (e.g., Mason et al., 2014). One of the most extensive field campaign to date was conducted by Metzger et al. (2011), who estimated PM10 particle fluxes in 33 dust devils to be in the range of 4×10^{-1} to $1.1 \times 10^2 \text{ mg m}^{-2} \text{ s}^{-1}$. The studies of Koch and Renno (2005) and Jemmett-Smith et al. (2015) on the global contribution of dust devils and the studies of Han et al. (2016), Tang et al. (2018), and Pan et al. (2021) on the regional contribution assumed a dust flux per dust devil of $7 \times 10^2 \text{ mg m}^{-2} \text{ s}^{-1}$, a value that can be associated with the total suspended particle flux rather than the flux of dust-sized (PM10) particles (Metzger et al., 2011). This particle type dependency of the fluxes already clarifies that “typical” emission fluxes, on which the estimated contributions are based, must be carefully determined.

Assessing the statistics of dust entrainment by dust devils via measurements is challenging and very costly because dust devils of different intensities and sizes must be measured under a variety of atmospheric conditions and soil types. Nevertheless, such statistics are crucial for calculating typical fluxes and, thus, evaluating the global and regional contribution. Following Spiga et al. (2016), the numerical simulation with LES is a very promising approach to complement measurements of dust devils because it allows access to all properties of the simulated vortices such as wind speeds, temperature, and pressure as well as to local environmental conditions. Also, Neakrase et al. (2016) considers LES to be a viable option for assessing dust fluxes in dust devils.

Previous LES studies on convective vortices in the terrestrial convective boundary layer (CBL) were mostly able to reproduce the characteristic vortex structure and flow features of dust devils, similar to field measurements. However, the simulated intensities expressed through the pressure drop in the core were often too low (Ito et al., 2013; Kanak et al., 2000; Raasch & Franke, 2011). After the simulation of the first dust devils with intensities as observed (Giersch et al., 2019), Giersch and Raasch (2023) carried out a comprehensive grid sensitivity study on dust devil characteristics in LES, utilizing multiple resolutions down to a grid spacing of $\Delta = 0.625$ m. The authors confirmed the assumption of Ito et al. (2010) that the intensity of vortices in simulations is strongly affected by the grid spacing and found that an adequate quantitative investigation on dust devils requires a resolution of at least $\Delta = 1$ m. Apart from the required spatial resolution, a large horizontal model domain (~ 10 km²) is also essential to simulate dust devils of observed intensities because the occurrence of these vortices is connected to the large-scale convection pattern, which appears as polygonal cells in the vertical wind component (e.g., Giersch et al., 2019; Kanak, 2005; Kanak et al., 2000; Schmidt & Schumann, 1989). This cellular pattern is characterized by broad downward motions in the cell center and narrow upwind areas at the cell edges, also known as cell branches. It is reminiscent of a honeycomb-like pattern, or open cellular convection during cold air outbreaks. Due to flow continuity, the near-surface flow diverges beneath the downdrafts and converges beneath the updrafts. The strongest updrafts are usually found at the vertices, where several convergence lines merge. The strongest horizontal wind speeds are usually observed in regions of high horizontal gradients of the vertical velocity, that is, where up- and downdrafts alternate over short distances. In terms of the convective cells, this occurs at the transition from the broad downwind region to the narrow upwind region. Dust devils are exclusively located along the branches and vertices of the cellular pattern.

The numerical resolution requirements established by Giersch and Raasch (2023) have far-reaching consequences for studying dust fluxes with LES. As mentioned above, the grid spacing decisively influences the core pressure drops of simulated dust devils and, consequently, the horizontal and vertical wind speeds. Higher values are simulated for higher resolutions. We will show in Appendix B that also the friction velocities and dust fluxes are significantly larger for higher resolutions. Instead, the core radii of simulated dust devils decrease with better resolution (Giersch & Raasch, 2023). Therefore, dust devils cover smaller areas of higher friction velocities and higher dust fluxes at lower grid spacings, which stresses that LES-based dust fluxes are significantly affected by the resolution. The results of Giersch and Raasch (2023) suggest that studies with grid spacings much larger than 1 m lead to a significant underestimation of the dust flux. Therefore, we will focus on simulation results with a resolution of 1 m. This will be the highest-resolved LES on dust fluxes in the CBL to date. Previous investigations on dust fluxes by dust devils used grid spacings of $\Delta = 20$ m (Ito et al., 2010) and $\Delta = 10$ m (Klose & Shao, 2016). This is probably too coarse for a quantitative analysis and it is not surprising that the simulated fluxes and concentrations in these studies ($\sim 10^{-3}$ – 10^0 mg m⁻² s⁻¹ and $\sim 10^{-3}$ – 10^0 mg m⁻³) are rather at the lower end of the measured values by Metzger et al. (2011) ($\sim 10^0$ – 10^2 mg m⁻² s⁻¹ and ~ 10 – 10^2 mg m⁻³).

Beside the grid spacing, we expect the choice of the dust emission scheme to strongly influence the dust flux by dust devils in LES studies. Dust emission schemes calculate the dust emission flux based on bulk properties of the atmosphere and the underlying surface. This typically includes the surface drag given by the friction velocity u_* and soil properties like the particle size distribution or erodibility (see e.g., LeGrand et al., 2019; Neakrase et al., 2016). There are three different physical mechanisms of dust emission, namely direct aerodynamic entrainment, saltation bombardment, and aggregate disintegration (Shao, 2008). Emission schemes can be based on one or more of these mechanisms. Direct aerodynamic entrainment is the direct lifting of dust particles due to a strong aerodynamic drag. The most important form of direct aerodynamic entrainment is called convective turbulent dust emission (CTDE). It describes a mechanism that generates strong, localized and intermittent surface shear stresses which cause dust emission in the absence of saltation (Klose, 2014; Li et al., 2014). Schemes based on direct entrainment usually use the empirical parameterization of Loosmore and Hunt (2000) or the physics-based parameterization of Klose et al. (2014), which accounts for the stochastic behavior of inter-

particle cohesive forces and the statistical distribution of momentum fluxes. However, saltation bombardment and aggregate disintegration are the most effective dust emission mechanisms on Earth (e.g., Shao et al., 1993; Tingting et al., 2018). Both require saltation as an intermediate process before the lifting of dust-sized particles can occur (Neakrase et al., 2016).

Saltation describes the streamwise, hopping-motion of coarser particles or particle aggregates. As the hopping particles hit the ground, dust-sized particles are lifted and a vertical dust flux is generated (Shao, 2008). Saltation depends on several soil and surface properties like the soil moisture, the particles' density and diameter, and the distribution of vegetation and roughness elements (Bergametti et al., 2007; Shao & Lu, 2000). It is first initiated by sand-sized particles with a diameter of 80 μm as soon as the threshold friction velocity u_{*t} of approximately 0.2 m s^{-1} is exceeded (Marticorena & Bergametti, 1995; White, 1979), which is usually the case in the event of dust storms (Klose et al., 2016). However, even during such strong wind erosion events, the threshold is exceeded only occasionally (Stout & Zobeck, 1997). Thus, saltation is considered as an intermittent rather than a continuous process (Shao, 2008). Intermittent saltation is also observed in the CBL when turbulent motions of air exceed the saltation threshold (Shao, 2008). The frequency of such intermittent saltation is still unclear and its statistical behavior is not well understood until today (Liu et al., 2018). Klose et al. (2016) considered it as controversial whether or not the drag in dust devils is sufficient to initiate saltation. For example, the study of Klose and Shao (2016) stated that the saltation threshold is often not reached in dust devils. We will disprove this statement in the following.

While saltation bombardment, once initiated, is a dominant dust emission process for nearly all soil types, the contribution of aggregate disintegration to the total dust emission depends more on the specific type and its properties like the amount of aggregates in the surface layer and the binding strengths of the soil aggregates (Bergametti et al., 2007). Following Shao (2008), the importance of aggregate disintegration is probably similar to that of saltation bombardment. However, the vertical dust flux due to aggregate disintegration is often not parameterized independently of saltation bombardment due to its complexity. Instead, it is assumed that it scales with the horizontal saltation flux. It can be considered in the so-called sandblasting efficiency that links the horizontal saltation flux with the vertical dust flux (Marticorena & Bergametti, 1995). State-of-the-art saltation-based dust emission schemes are the mineral dust entrainment and deposition model (L. Zhang et al., 2001) and the Air Force Weather Agency (AFWA) dust emission scheme for the Goddard Chemistry Aerosol Radiation and Transport (GOCART) model, which is part of the WRF-Chem model (Jones et al., 2011, 2012; LeGrand et al., 2019). A more complex scheme which captures both saltation bombardment and aggregate disintegration is provided by Shao et al. (2011). However, all of these schemes have mainly been used for large-scale modeling and not for local investigations (Wang et al., 2012; Y. Zhang et al., 2018; Tian et al., 2021).

Both the observed near-surface sand skirts (Murphy et al., 2016) and the high concentration of sand-sized particles (Raack et al., 2018) in dust devils indicate that these vortices provoke saltation. As the saltation-induced vertical dust flux is assumed to be one order of magnitude larger than direct aerodynamic entrainment (Shao et al., 1993), Neakrase et al. (2016) suggest to use a saltation-based parameterization to estimate the dust entrainment in dust devils. However, all previous LES studies on dust fluxes caused by dust devils utilized emission schemes based on direct aerodynamic entrainment (Ito et al., 2010; Klose & Shao, 2016). To the best knowledge of the authors, local investigations of saltation-based dust emission in the CBL have never been performed with high-resolution LES. Therefore, we make use of the AFWA dust emission scheme and perform the first high-resolution LES of saltation bombardment in the CBL. The AFWA scheme recently showed good performance in simulating and forecasting dust storms (Yuan et al., 2019) and is rather simple (LeGrand et al., 2019).

The paper's structure is as follows: Section 2 gives an overview of the methodology including the PALM model system, the implemented dust scheme, the simulated setup, the detection and tracking of dust devils, and how the calculation of the contribution of the dust devils to the total dust emission is realized. The results are introduced and discussed in Section 3 with a focus on the spatial distribution of dust emission due to saltation bombardment and the contribution by dust devils to the total dust emission. A summary and conclusion completes our study.

2. Methodology

In the following, the PALM model system is used for the numerical simulations (Maronga, Banzhaf, et al., 2020). By default, it does not contain a physics-based parameterization of the local particle release and transport.

Therefore, the model must be coupled with such a scheme. We will focus on dust-sized particles. The coupling enables the simulation and investigation of dust fluxes, patterns of dust emission and the contribution of dust devil-like vortices to this emission. We start this section with a brief introduction to PALM, followed by an overview of the newly implemented dust physics. The simulated setup and the detection and tracking of convective vortices are described afterward. Finally, it is shown how the contribution of dust devil-like vortices to the total dust emission is determined. Note, as in other studies (e.g., Giersch et al., 2019; Kanak, 2005; Raasch & Franke, 2011), the term dust devil, dust devil-like vortex, and (convective) vortex are used as synonyms. A differentiation between visible and non-visible vortices is not made.

2.1. The PALM Model System

All numerical simulations are carried out with the PALM model system in LES mode (revision 4732). PALM is a Fortran-based code, which has been developed for studying a variety of atmospheric and oceanic flows (Maronga, Banzhaf, et al., 2020; Maronga et al., 2015; Raasch & Schröter, 2001). By default, PALM solves the non-hydrostatic, spatially filtered, incompressible Navier-Stokes equations in Boussinesq-approximated form, assuming a constant air density ρ_a . Prognostic equations for up to seven variables are solved on a staggered Cartesian Arakawa-C grid: the velocity components u , v , w , the potential temperature θ , the subgrid-scale turbulence kinetic energy e , the water vapor mixing ratio q_v and the passive scalar s . Dry conditions are assumed in this study ($q_v = 0$), and the dust mass concentration is implemented via the passive scalar s . To guarantee incompressibility of the flow, a Poisson equation for the so-called perturbation pressure p^* is solved by applying a predictor-corrector method after Patinos and Kistler (1977). As in other LES studies of dust devils (e.g., Giersch & Raasch, 2023; Kanak, 2005; Kanak et al., 2000; Raasch & Franke, 2011), we determine the dust devil pressure drop with respect to the surroundings from the total dynamic pressure perturbation $\pi^* = p^* + 2/3\rho_a e$.

For the resolved-scale advection, PALM employs the fifth-order scheme of Wicker and Skamarock (2002) together with a third-order Runge-Kutta-time-stepping scheme (Williamson, 1980). For the subgrid-scale transport, PALM follows the gradient approach, which assumes that the transport is proportional to the local gradients of the mean resolved quantities, and utilizes a 1.5th-order closure after Deardorff (1980) in the formulation by Moeng and Wyngaard (1988) and Saiki et al. (2000).

As outlined in Section 1, the friction velocity is an important quantity for dust emission. In PALM, the friction velocity is computed at each horizontal grid point through the local application of Monin-Obukhov similarity theory (MOST, Monin & Obukhov, 1954). A constant flux layer between the surface ($z = 0$ m) and the first computational grid level ($z = 0.5\Delta z$) is assumed, with z being the height above ground and Δz the vertical grid spacing. The calculation of u_* at every grid point in the surface layer requires the knowledge of the local resolved horizontal velocity components. Thus, the near-surface horizontal wind speeds of dust devils control the magnitude of the friction velocities. For more details about PALM, the reader is referred to Maronga, Banzhaf, et al. (2020).

2.2. Implemented Dust Physics

The dust physics in PALM shall consider five processes: dust emission from the surface, passive advection with the resolved-scale turbulent wind, subgrid-scale turbulent transport, gravitational settling, and dry deposition. The individual parameterizations and calculations, which are implemented in addition to PALM's standard treatment of a passive scalar, are presented in the following paragraphs.

The dust emission parameterization follows the AFWA dust scheme (LeGrand et al., 2019), which calculates the vertical dust emission flux F_e caused by saltation bombardment (Kawamura, 1951; Marticorena & Bergametti, 1995). At first, the total vertically-integrated streamwise (horizontal) saltation flux G in $\text{kg m}^{-1} \text{s}^{-1}$ is calculated by

$$G = \sum_p [H(D_p) dS_{\text{rel}}(D_p)], \quad (1)$$

where $H(D_p)$ denotes the partial vertically-integrated streamwise saltation flux of the saltation size bin p with the effective particle diameter D_p and $dS_{\text{rel}}(D_p)$ describes a bin-specific weighting factor. The bin-specific weighting factor is calculated from the mass distribution of particles in the surface soil $dM(D_p) = s_{\text{ssc}}(p) \times s_{\text{frac}}(D_p)$, where

Table 1

Configuration of Saltation Size Bins and Associated Attributes for the Air Force Weather Agency Scheme

Saltation size bin (p)	1	2	3	4	5	6	7	8	9	10
Effective diameter (D_p ; μm)	1.42	8	20	32	44	70	130	200	620	1,500
Soil separate class (ssc)	Clay	Silt	Silt	Silt	Silt	Sand	Sand	Sand	Sand	Sand
Particle density (ρ_p ; kg m^{-3})	2,500	2,650	2,650	2,650	2,650	2,650	2,650	2,650	2,650	2,650
Mass fraction (s_{frac})	1	0.25	0.25	0.25	0.25	0.0205	0.0410	0.0359	0.3897	0.5128
Mass contribution ^a (dM)	0.03	0.0125	0.0125	0.0125	0.0125	0.0189	0.0377	0.0330	0.3585	0.4718

^aAssuming the soil category 1 ("sand") of the STATSGO-FAO database (Pérez et al., 2011).

s_{sc} is the mass fraction of the soil separate class (ssc: sand, silt, clay) the bin p is assigned to and $s_{\text{frac}}(D_p)$ is the bin-specific mass fraction in the corresponding soil separate class. For more details, the reader is referred to LeGrand et al. (2019). We assume a homogeneous surface with mass fractions based on the soil type sand of the STATSGO-FAO database with $s_{\text{sand}} = 0.92$, $s_{\text{silt}} = 0.05$, $s_{\text{clay}} = 0.03$ (Pérez et al., 2011). For the saltation size bin configuration defining $s_{\text{frac}}(D_p)$, we follow the recommendation by LeGrand et al. (2019). All values are summarized in Table 1. Each bin-specific vertically-integrated streamwise flux $H(D_p)$ is calculated according to Kawamura (1951):

$$H(D_p) = \begin{cases} C_{\text{mb}} \frac{\rho_a}{g} u_*^3 \left(1 + \frac{u_{*i}}{u_*}\right) \left(1 - \frac{u_{*i}^2}{u_*^2}\right) & \text{for } u_* > u_{*i}, \\ 0 & \text{for } u_* \leq u_{*i}, \end{cases} \quad (2)$$

where g is the gravitational acceleration and C_{mb} is an empirical constant. Here, we use $C_{\text{mb}} = 1$ as suggested by Marticorena et al. (1997) and Darnenova et al. (2009) instead of the original value of 2.61 according to White (1979) and Marticorena and Bergametti (1995). The threshold friction velocity, as a function of the particle diameter D_p , is calculated via the semi-empirical equation of Marticorena and Bergametti (1995):

$$u_{*i}(D_p) = 0.129 \frac{\left(\frac{\rho_p g D_p}{\rho_a}\right)^{0.5} \left(1 + \frac{c}{\rho_p g D_p^{1.5}}\right)^{0.5}}{\left[1.928(aD_p^x + b)^{0.092} - 1\right]^{0.5}}, \quad (3)$$

with the empirical parameters $a = 1.75 \times 10^6 \text{ m}^{-x}$, $b = 0.38$, $c = 6 \times 10^{-5} \text{ kg m}^{0.5} \text{ s}^{-2}$ and $x = 1.56$.

In a second step, the vertical bulk emission flux of emitted dust-sized particles F_e in $\text{kg m}^{-2} \text{ s}^{-1}$ is determined by the product of G and the sandblasting efficiency α in m^{-1} through

$$F_e = \alpha \times G. \quad (4)$$

The sandblasting efficiency (LeGrand et al., 2019; Marticorena & Bergametti, 1995) is calculated via

$$\alpha = 100 \times 10^{0.134(\%_{\text{clay}} - 6)}, \quad (5)$$

where the factor 100 results from the conversion of cm^{-1} , as used in the formulation of LeGrand et al. (2019), to m^{-1} . The variable $\%_{\text{clay}} = 3$ is the mass fraction of clay in percentage. In this study, F_e represents the flux of dust particles that are assumed to be uniform and spherical with a diameter of $10 \mu\text{m}$ and a density of $2,650 \text{ kg m}^{-3}$.

Note, most of the in situ measurements evaluate the dust emission via the product of the dust mass concentration c and vertical velocity w . To enable a comparison between measurements and simulations, we also determine this dust flux, which we call the vertical dust transport F_t from now on. It is calculated via

$$F_t = cw - F_g = c(w - v_g) \quad (6)$$

with F_g and v_g being the gravitational settling flux and the gravitational settling velocity, respectively. The latter can be calculated by using Stokes' law (see also Farrell & Sherman, 2015; L. Zhang et al., 2001). Field observations usually do not use a standardized altitude to evaluate dust fluxes. Measurement heights vary from less than a meter (Metzger et al., 2011; Raack et al., 2018) to several 100 m (Gillette & Sinclair, 1990; Renno et al., 2004). In this study, we choose a height of 10 m for the assessment of the vertical dust transport F_t . This height level corresponds to the vortex detection height explained in Section 2.4.

Dry deposition is implemented for the land use category “desert” based on a scheme proposed by L. Zhang et al. (2001). It estimates the dry deposition flux in a bulk-transfer formulation via

$$F_d = -v_d \times c_1, \quad (7)$$

where

$$v_d = v_g + \frac{1}{R_a + R_s + (R_a R_s v_g)} \quad (8)$$

is the dry deposition velocity (here in the formulation by Zeng et al., 2020), c_1 denotes the bulk mass concentration of dust at the first computational grid layer, and R_a and R_s describe the aerodynamic resistances above the canopy and the surface, respectively. For more information, the reader is referred to L. Zhang et al. (2001).

As previously mentioned, the dust mass concentration field is equal to the passive scalar s in PALM. Dust emission and deposition are combined to the net surface flux $F_n = F_e + F_d$, which represents the surface scalar flux in the model. F_n modifies the concentrations at the first computational grid level above the surface as an additional source or sink term, depending on its sign. Gravitational settling is implemented for all heights above the surface layer and alters the local concentration as soon as a divergence of F_g occurs.

2.3. The Simulation Setup

The main simulation of this study follows the setup R5N1 of Giersch and Raasch (2023). All boundary conditions, the initialization, and the numerical schemes are the same. In the following, only the most relevant settings and the discrepancies to the original setup are explained. For more details, the reader is referred to Giersch and Raasch (2023). R5N1 features a temporally and spatially constant vertical sensible heat flux of 0.24 K m s^{-1} at the surface to force convection. The roughness length, which needs to be prescribed for the application of MOST at the lower boundary, is set to 0.1 m. During model initialization, vertical wind and potential temperature profiles are prescribed. The velocities are set to zero because no background wind is considered and free convection is simulated. The initial potential temperature is constant (300 K) up to a height of 1,000 m and increases with 0.02 K m^{-1} until the top of the domain. During the beginning of the simulation, random perturbations are imposed on the horizontal wind to accelerate the development of convection and to reach a quasi-stationary state of the CBL more quickly. In addition, PALM's nesting technique (Hellsten et al., 2021) is applied in vertical direction, that is, two domains with the same horizontal but different vertical extensions are simultaneously simulated, utilizing different resolutions. The inner domain, also called child domain, spans $4,000 \times 4,000 \times 240 \text{ m}^3$. The outer (parent) domain has a vertical extent of 2,248 m. The spatial resolutions are 5 and 1 m for the parent and child domain, respectively. To compare the results with the findings of Klose and Shao (2016), another setup called R20N10 is used, which has a parent resolution of 20 m and a child resolution of 10 m. Both setups are summarized in Table 2. The domain extents along the Cartesian coordinates x -, y -, and z are indicated by L_x , L_y , and L_z , respectively. At the top boundary, a Neumann (zero-gradient) condition is used for the dust mass concentration ($\partial s / \partial z = 0 \text{ kg m}^{-4}$). Note that the surface scalar (or dust) flux is not explicitly set but dynamically calculated as described in Section 2.2. The initial concentration is set to 0.0 g m^{-3} . For both setups, the simulation time t_s is 4 hr. Following Giersch and Raasch (2023), the first 45 min are considered as model spin-up time t_{su} , which is why the actual analysis time is defined as $t_a = t_s - t_{su}$. If not otherwise stated, all results in Section 3 refer to simulation R5N1. R20N10 is discussed in Appendix B. At this point we want to note that the R5N1 setup demands substantial computational resources, with a single simulation requiring approximately 10 days of wall-clock time on 6,900 cores of an Atos/Bull system equipped with Intel Xeon Platinum 9242 processors.

Table 2
 Domain Size and Number of Grid Points for Both Simulated Setups^a

Simulation name	Grid spacing Δ in (m)	Domain size $L_x \times L_y \times L_z$ in (m ³)	Number of grid points
R20N10	20	4,000 × 4,000 × 2,005	200 × 200 × 80
	10	4,000 × 4,000 × 240	400 × 400 × 24
R5N1	5	4,000 × 4,000 × 2,248	800 × 800 × 277
	1	4,000 × 4,000 × 242	4,000 × 4,000 × 242

^aIn the parent domain, vertical grid stretching is applied.

2.4. Detection and Tracking of Vortices

In the following, details of the detection and tracking algorithm of convective vortices are introduced. The algorithm is principally designed as in Giersch and Raasch (2023) with minor changes. Here, a more generalized version is presented that is not explicitly developed for a grid sensitivity study. The algorithm can be split into two parts. The first part takes care of the detection of vortex centers during the simulation. The second part filters and combines the detected centers in a post-processing step, which finally results in dust devil-like vortices that are analyzed.

During the simulation, vortex centers are identified via criteria for the modified perturbation pressure π^* and vertical vorticity ζ at or slightly above an altitude of 10 m (e.g., scalar quantities are defined at 10.5 m in R5N1). The criteria read as follows:

1. A local minimum of $\pi^* < \pi_{th}^* = 3 \text{ std}(\pi^*)$ must be given. Its position defines the location of the vortex core.
2. A local extremum of $|\zeta| > \zeta_{th} = 5 \text{ std}(\zeta)$ must be reached, which is located somewhere within a square of $20 \times 20 \text{ m}^2$ around the π^* -minimum.

The thresholds are based on the standard deviation (std) approach by Nishizawa et al. (2016) and set to $\pi_{th}^* = -3.4 \text{ Pa}$ and $\zeta_{th} = 1.08 \text{ s}^{-1}$ in accordance with the $\Delta = 1 \text{ m}$ simulation of Giersch and Raasch (2023). The square of $20 \times 20 \text{ m}^2$, which limits the spatial offset of the pressure minimum and vorticity extremum, mimics typical extents of intense dust devil-like vortices in the 1 m simulation of Giersch and Raasch (2023). It allows the maximum absolute values of pressure drop and vorticity to be slightly displaced and also ensures that they belong to the same vortex center. For each detected center, the core radius R_c is calculated as the distance at which the tangentially averaged modified perturbation pressure is less than 50% of its peak value at the center for the first time (see also Giersch & Raasch, 2023; Giersch et al., 2019; Kanak, 2005; Raasch & Franke, 2011). This method agrees well with empirical and analytical models of dust devils (Lorenz, 2014), where the core radius defined as above matches the location of the highest tangential velocity.

Regarding the tracking of vortices, the first step is to filter all detected centers when the simulation is finished by the following three criteria (for an explanation see further below):

- A. Vortex centers with core radii R_c larger than 50 m are deleted.
- B. Centers are neglected if a stronger center (rated by π^*) is found within a radius of 20 m at the same time step in order to consider the merging of vortices and to omit counting the same vortex structure with several sub-centers twice or more.

Second, the remaining vortex centers are sequentially processed to generate so-called dust devil tracks, having a certain duration. Centers are assigned to the same track if the following criteria are satisfied:

1. The maximum allowed displacement between two consecutive detections is limited. It is determined by the larger value of (a) 20 m or (b) the distance calculated by a translation speed of 10 m s^{-1} times the time difference Δt from the previous detection of the track.
2. The area-averaged vorticity ζ_{av} (in a square of $20 \times 20 \text{ m}^2$ around the center) must have the same sign.
3. The change in π^* and ζ_{av} must be less than 10% between two consecutive centers.
4. A new vortex track is initiated if no center, satisfying Criteria 1–3, is found within 3 s of simulated time.

Note, we follow the suggestion of Klose and Shao (2016) and remove all short vortex tracks with a duration of less than 30 s to increase the comparability of the data with field measurements (short-lived dust devils are hard to

detect in the field) and to eliminate strong, non-coherent turbulent fluctuations that do not correspond to fully developed vortices. The theoretical and technical foundations for the criteria above (A, B, and 1–4) are well explained in Giersch and Raasch (2023), however, with a special focus on grid sensitivity. For the more generalized algorithm here, we decoupled the algorithm from its focus on the comparability for different grid spacings. The maximum core radius of Criterion A is reduced from 100 to 50 m based on a comprehensive investigation of the data from the R5N1 simulation of Giersch and Raasch (2023). This investigation showed that more than 99% of the dust devil tracks with lifetimes exceeding 30 s have mean core radii of less than 50 m, and that the remaining dust devil tracks with mean radii of more than 50 m show only weak intensities, accumulating at less than 10 Pa (not shown). Thus, we decided to neglect centers with a radius larger than 50 m. Criterion 3 is extended by the plane-averaged vorticity to better ensure that two subsequent detections belong to the same vortex track. Criterion 4 enables gaps in the vortex tracks of up to 3 s that might occur from values of the pressure drop or vorticity, which are temporarily lower than the absolute values of the applied detection thresholds. For time intervals of more than 2 s, Criterion 1 allows a larger displacement between two consecutive centers than 20 m based on the assumed maximum translation speed of 10 m s⁻¹, which is a reasonable value in accordance to measurements (e.g., Murphy et al., 2016).

2.5. Contribution of Dust Devils to the Dust Emission

To estimate the contribution of dust devil-like vortices to the overall dust release, an area must be defined that delimits the vortices' dust emission from the background emission. While the core area can be considered as the visible dust column (e.g., Balme & Greeley, 2006; Luan et al., 2017), the area of the total dust emission by a dust devil-like vortex is not necessarily restricted to its core. We follow the approach of Klose and Shao (2016) and assume that the relevant area for dust emission is equal to a circle of twice the core radius. This ensures that potentially high dust emission fluxes just outside the core region are also assigned to the emission fluxes by dust devils. Hereinafter, these circular regions are termed as dust devil flux areas and denoted by σ , that is, $\sigma(n, t)$ stands for the flux area of the n th dust devil center of the whole sample $N_{\text{dds}}(t)$ detected at time t . The union of all individual dust flux areas at t is denoted as

$$\Omega(t) = \cup_n^{N_{\text{dds}}} \sigma(n, t). \quad (9)$$

Thus, $\Omega(t)$ accounts for all emission flux relevant areas assigned to dust devils. Areas that are covered by more than one vortex (overlapping dust devil flux areas) are counted only once. In the following, $\omega(t) = \Omega(t)/D$ and $\bar{\omega}^t$ describe the instantaneous fractional area covered by dust devils and its time-averaged value, respectively. The horizontal domain is denoted as D and spans $4,000 \times 4,000$ m².

The instantaneous mass flow rate $\dot{M}_x^A(t)$ due to a given mass flux F_x is defined as the mass of lifted dust per unit time (kg s⁻¹). The subscript $x = \{e, t\}$ refers either to the dust emission flux F_e or the vertical dust transport at 10 m altitude F_t . The instantaneous mass flow rate is calculated via spatial integration of the respective flux over a certain area A with the surface elements dA :

$$\dot{M}_x^A(t) = \int_A F_x(t, x, y) dA. \quad (10)$$

The total amount of (emitted/transported) dust mass M_x^A is calculated by the temporal integration of \dot{M}_x^A over the analysis period t_a , that is, from the model's spin-up time t_{su} until the end of the simulation t_s :

$$M_x^A = \int_{t_{\text{su}}}^{t_s} \dot{M}_x^A(t) dt = \int_{t_a} \dot{M}_x^A(t) dt. \quad (11)$$

Both, $\dot{M}_x^A(t)$ and M_x^A can be considered for the n th dust devil ($A = \sigma$), for all dust devils ($A = \Omega$), or for the whole domain ($A = D$). If the vertical dust transport is considered instead of the emission flux at the surface, we neglect the negative values of F_t and consider only the positive values of the vertical dust transport. With this restriction, the values related to F_t can directly be related to the results from field measurements, which consider the positive vertical dust flux as the product of the concentration and positive vertical velocity (e.g., Metzger et al., 2011;

Renno et al., 2004). With $\dot{M}_x^A(t)$ and M_x^A , the contribution by dust devils to the overall dust emission can be calculated. We distinguish between an instantaneous contribution $r_x(t)$, which is calculated via

$$r_x(t) = \frac{\dot{M}_x^\Omega(t)}{\dot{M}_x^D(t)} \quad (12)$$

and a time-integrated contribution R_x defined as:

$$R_x = \frac{M_x^\Omega}{M_x^D}. \quad (13)$$

Lastly, we apply the concept of spectral frequency analysis to investigate the spectral distribution of the friction velocity, as the main simulation parameter for saltation-induced dust emission. Bins of size 10^{-3} m s^{-1} within the interval from 0 to 3.0 m s^{-1} are chosen. During the analysis period, u_{*} -values at each grid point of a considered region are assigned to the corresponding bin. In this way, instantaneous frequency distributions are generated. The time-integrated frequency spectra are finally determined by an accumulation of the instantaneous distributions over the whole simulation time. We calculate both global spectra and dust devil spectra, which show the frequencies of u_{*} over the whole simulated domain D and over the union of all dust devil flux areas Ω , respectively.

3. Results and Discussion

This Section clarifies the question about the contribution of dust devils to the total dust release and transport. For this purpose, we start with a domain-wide analysis of the friction velocity because of its large influence on the simulated surface dust flux. Later on, friction velocities are investigated within the dust devil flux areas. In Section 3.2, saltation-induced dust emission is analyzed in the whole simulated domain. This emission will be found to be caused by large-scale convective patterns and several exceptionally high dust fluxes associated with dust devils. Both phenomena are separately studied in Sections 3.3 and 3.4, respectively. Finally, the dust devils' contribution to the overall dust emission and vertical transport is estimated in Section 3.5.

3.1. Friction Velocities and the Saltation Threshold

Figure 1 illustrates a snapshot of the horizontal cross-section of the friction velocity for the whole simulation domain at an arbitrary time step of the simulation. To separate areas with saltation from areas without saltation, we chose a threshold friction velocity of $u_{*t} = 0.21 \text{ m s}^{-1}$, corresponding to the sixth saltation size bin of the AFWA scheme with an effective diameter of $70 \mu\text{m}$ (see Table 1). This size bin provides the minimum threshold friction velocity above which saltation of particles is possible and can be considered as AFWA's saltation threshold.

It can be seen that intermittent saltation occurs frequently during daytime convection. This conflicts with the opinion that saltation contributes only slightly to the background dust loading and that saltation thresholds are only exceeded during strong wind events like dust storms (e.g., Klose & Shao, 2016; Klose et al., 2016). In our simulation, saltation is organized and arranged along large-scale meandering patterns. These patterns are comprehensively addressed in Section 3.3 in the context of the dust emission field. The threshold friction velocity of 0.21 m s^{-1} is exceeded in roughly half of the horizontal area. The temporally averaged area fraction at which saltation occurs is $\bar{a}_{u_{*t} > u_{*t}}^a \approx 52\%$. In comparison, dust devils, which are visible as small light spots in Figure 1, occupy a much smaller fraction of the total horizontal area. This temporally averaged fraction is determined as $\bar{a}^a = 0.16\%$, utilizing the dust devil flux areas as described in Section 2.5. Combining field observations with the thermodynamic theory about natural convective as a heat engine (Rennó & Ingersoll, 1996), Koch and Renno (2005) estimated the fractional area covered by dust devils to be $\omega_{\text{obs}} = 0.003\% \pm 0.002\%$, which is even smaller than \bar{a}^a . Their fractional area is defined as the region where dust devils are strong enough to produce saltation through perturbations in surface velocity. Thus, we expect more than 99% of the area where saltation is present to be outside of dust devils. This shows that saltation-induced dust emission might not only be important for the dust release of dust devils but also for the continuous, ambient dust emission during convective conditions. Local mechanisms such as strong electric fields or the Δp -effect, which are especially prevalent in dust devils,

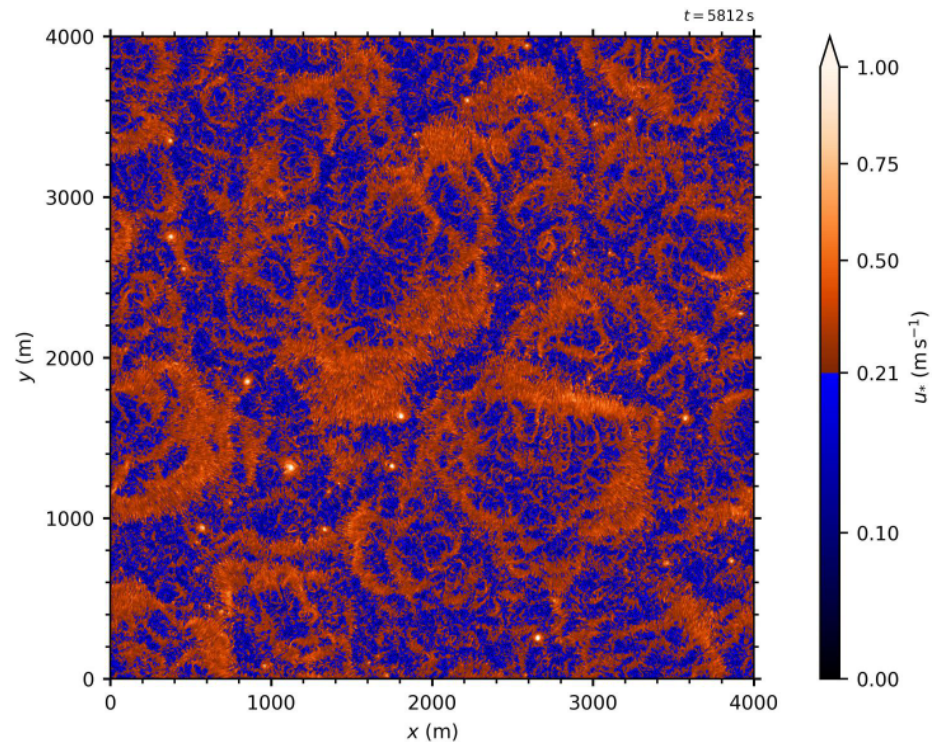


Figure 1. Instantaneous horizontal cross-section of the friction velocity for the whole domain.

could cause a significant decrease of the threshold friction velocity (Balme & Hagermann, 2006; Esposito et al., 2016), resulting in even higher dust emissions than simulated (see Section 4). Contrary, for non-idealized surfaces, soil crusting can increase the threshold friction velocity by a factor of 2 (Pi & Sharratt, 2019), and soil moisture can lead to a further increase (Yang et al., 2019). The soil may also not contain abundant sand particles with diameters of about 70 μm or they may be shielded by larger particles. Consequently, saltation would not be initiated at a friction velocity of 0.21 m s^{-1} but higher.

Considering the variable values of the saltation threshold for different soils and atmospheric conditions, Table 3 summarizes the temporally averaged area fraction at which a certain friction velocity is exceeded. The value of $u_{*t} \approx 0.2 \text{ m s}^{-1}$ corresponds to the minimum value of Equation 3, $u_{*t} \approx 0.21 \text{ m s}^{-1}$ corresponds to the minimum threshold friction velocity of the AFWA scheme, and $u_{*t} = 0.4 \text{ m s}^{-1}$ as well as $u_{*t} = 0.6 \text{ m s}^{-1}$ follow the suggestions of Li et al. (2014) and Ju et al. (2018), respectively, to clearly separate saltation from CTDE.

Under the assumption of a higher friction velocity threshold of $u_{*t} = 0.4 \text{ m s}^{-1}$ to clearly separate intermittent saltation from CTDE (e.g., Li et al., 2014), the area occupied by saltation is $\bar{a}_{u_* > u_{*t}}^a \approx 1.8\%$. In this scenario, roughly 90% (following $\bar{\omega}^a$) or 99.8% (following ω_{obs}) of the saltation area is found outside dust devils. Here, we have assumed that saltation is active throughout the whole dust devil flux areas, which is mostly the case. Otherwise, the fraction of the saltation area outside dust devils (following $\bar{\omega}^a$) would be even higher. Even for an area fraction of 1.8%, the ambient saltation might cause a decisive contribution to the total dust emission because saltation bombardment is considered to produce fluxes an order of magnitude larger than direct entrainment (Shao, 2008).

Table 3

Temporally-Averaged Area Fraction $\bar{a}_{u_* > u_{*t}}^a$ at Which a Given Threshold Friction Velocity for Saltation u_{*t} is Exceeded

u_{*t} (m s^{-1})	0.2	0.21	0.25	0.3	0.35	0.4	0.5	0.6	0.75	1
$\bar{a}_{u_* > u_{*t}}^a$ (%)	56	52	32	14	5.4	1.8	0.23	0.058	0.018	0.0038

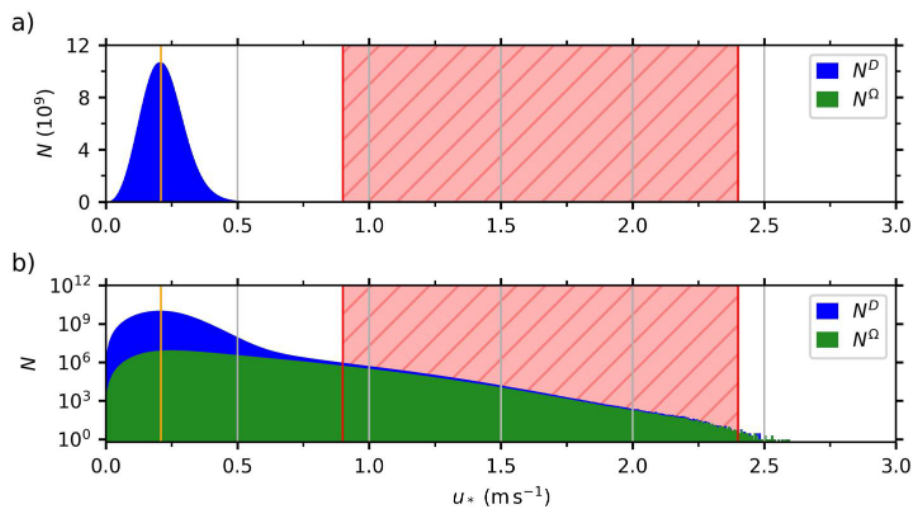


Figure 2. Frequency spectra of the friction velocity based on approximately 10^{12} counts. (a) displays the frequency N by using a linear y-axis, whereas in (b) a logarithmic y-axis is used. Frequencies of the whole domain (D) are displayed in blue, while the frequencies within the dust devil flux areas (Ω) are given in green. The vertical orange line marks the saltation threshold of the Air Force Weather Agency scheme. The red area indicates the interval (0.9 m s^{-1} , 2.4 m s^{-1}) measured by Balme et al. (2003).

To investigate the friction velocity distribution in more detail, we carry out a frequency analysis of u_* (as described in Section 2.5). By this analysis, a better understanding of saltation-induced dust emission in the CBL is achieved. The results are illustrated in Figure 2. The frequency spectrum follows a Gaussian curve with a mean value of approximately 0.22 m s^{-1} and a standard deviation of 0.079 m s^{-1} . The tail of the distribution extends to 2.59 m s^{-1} . Considering the log-scale distribution from Figure 2b, the frequencies for $u_* > 1 \text{ m s}^{-1}$ are mainly located within the dust devil flux areas. However, there is a small portion of very high friction velocity counts which is not assigned to dust devils. This is visible through the slight offset between the global (blue) and the dust devil spectra (green). The offset is caused by the algorithm for vortex identification (see Section 2.4) and the definition of the dust devil flux areas (see Section 2.5). It is discussed in detail in Appendix A. We conclude that almost all strong saltation events are an exclusive feature of dust devils. This would also explain their pronounced visibility in the field. Outside the dust devils, u_* regularly exceeds the saltation threshold of 0.21 m s^{-1} . In some cases, values up to 0.8 m s^{-1} are reached. This once again stresses the important role of saltation for dust emission in the CBL. We therefore expect that observed dusty plumes, as mentioned by Koch and Renno (2005), are related to the saltation-induced dust emission caused by daytime convection and are not solely related to CTDE.

The statistical analysis of all dust devils shows that the instantaneous peak friction velocity (found during the individual dust devil lifetimes and within the dust devil flux areas σ), has a mean value (averaged over all dust devil tracks) of 0.89 m s^{-1} and a maximum of 2.59 m s^{-1} . Both values are in very good agreement with field observations by Balme et al. (2003), who derived near-surface peak friction velocities within 10 dust devils between 0.9 and 2.4 m s^{-1} . The friction velocity, averaged over both the individual dust devil lifetimes and over σ , has a mean of 0.32 m s^{-1} with a maximum of 1.28 m s^{-1} . The relatively low value of 0.32 m s^{-1} is explained by the pressure threshold $|\pi^*| \geq 3.5 \text{ Pa}$ used for the detection of vortex centers (see Section 2.4). If only the most intense dust devils are considered that would be able to lift a sufficient amount of dust to become visible in nature ($|\pi^*| \geq 30 \text{ Pa}$, see Lorenz, 2014), the corresponding average value is 0.60 m s^{-1} . Apart from dust devils, temporal and spatial averaging over the analysis period and the remaining regions ($D \setminus \Omega$) lead to a mean friction velocity of 0.21 m s^{-1} , which roughly corresponds to the mean value of the Gaussian frequency spectrum discussed above. This highlights again that dust devils cover only small areas in the simulated domain and that they do not determine the overall frequency distribution of u_* (except the right tail).

Note that the simulated setup considers a homogeneous roughness length of 0.1 m in agreement with Giersch and Raasch (2023). However, roughness lengths for flat sandy surfaces are generally lower by about one to three orders of magnitude (Chapman et al., 2017; Kurgansky, 2018). Therefore, our simulations might overestimate the friction velocity, whose magnitude is controlled by the roughness length. We suggest performing further

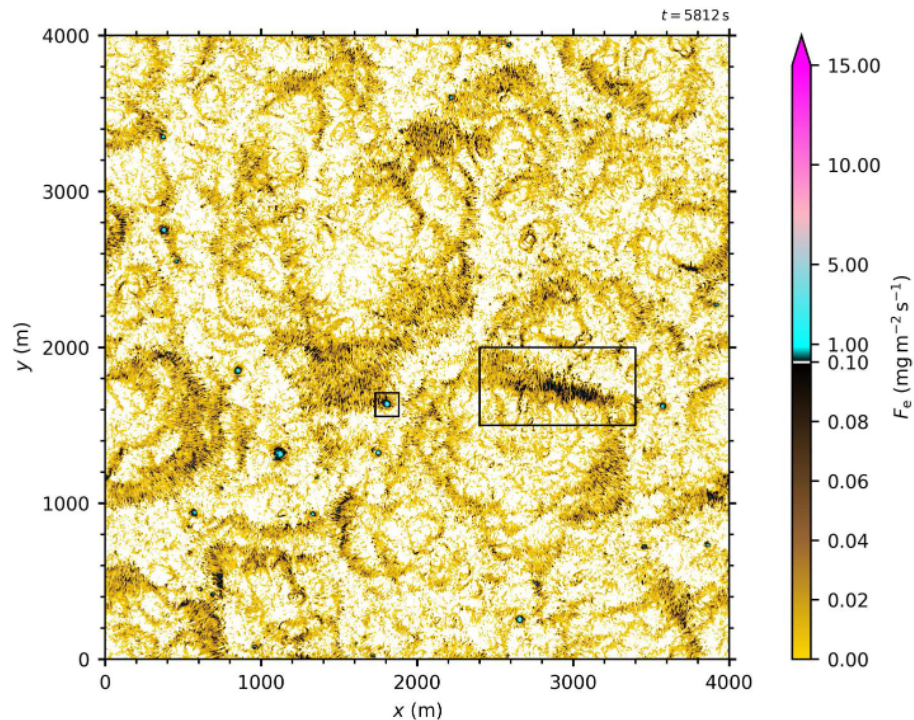


Figure 3. Instantaneous horizontal cross-section of the saltation-based dust emission flux. Areas with a vanishing dust flux are displayed in white. The color scale changes at $F_e = 10^{-1} \text{ mg m}^{-2} \text{ s}^{-1}$ (as marked by the white line). The left black rectangle contains the most intense dust devil at this time step and the right rectangle contains a very strong structure of large-scale ambient dust emission.

simulations to investigate the impact of lower roughness lengths on the simulation results, especially concerning the friction velocity and how often the saltation threshold is exceeded.

3.2. Saltation-Based Dust Emission in the CBL

Figure 3 illustrates a domain-wide horizontal cross-section of the saltation-based dust emission flux computed at the same time as the friction velocities of Figure 1. A comparison of both Figures reveals that the friction velocity mainly controls the dust emission flux, which is the case in almost every existing emission parameterization, regardless of the considered emission mechanism (e.g., Kawamura, 1951; Klose et al., 2014; LeGrand et al., 2019; Loosmore & Hunt, 2000; Shao et al., 2011; Zender et al., 2004). In Figure 3, a very strong dust devil is visible with a peak pressure drop of about $|\pi^*| = 256 \text{ Pa}$. The dust devil is highlighted with the left black rectangle. The right rectangle marks an area with very strong, large-scale dust emission that is not connected to any intense vortex. More detailed illustrations of both areas can be found in Figures 5 and 6a. It can be seen that saltation-induced dust emission is organized along cellular, large-scale patterns distributed all over the domain, similar to the patterns observed for u_* . Because dust emission is directly connected to the flow field, this pattern confirms that the CBL is determined on a large scale by polygonal convection cells as described in Section 1. Averaged over the analysis period, the mean dust emission flux over all locations with $F_e > 0$ and outside of dust devils ($A_{F_e > 0} \Omega$), is $1.06 \times 10^{-2} \text{ mg m}^{-2} \text{ s}^{-1}$. We will refer to $10^{-2} \text{ mg m}^{-2} \text{ s}^{-1}$ as a typical background emission flux. Local peaks along the large-scale emission patterns are in the order of 10^{-1} to $10^0 \text{ mg m}^{-2} \text{ s}^{-1}$, corresponding to a friction velocity of roughly $0.46\text{--}0.82 \text{ m s}^{-1}$. Figure 3 also shows that the highest dust emission fluxes are limited to very small areas. These areas can always be assigned to intense dust devils. Instantaneous peak emission fluxes of intense dust devils reach up to $46.7 \text{ mg m}^{-2} \text{ s}^{-1}$. Therefore, dust devils clearly distinguish themselves from their surroundings with dust fluxes that are one (10^{-1} compared to 10^{-2}) to three (10 compared to 10^{-2}) orders of magnitude larger compared to the typical ambient dust emission.

Note that the application of MOST at the lower boundary is theoretically founded only for horizontally averaged quantities, but the local application has become standard in most of today's LES codes (Maronga, Banzhaf,

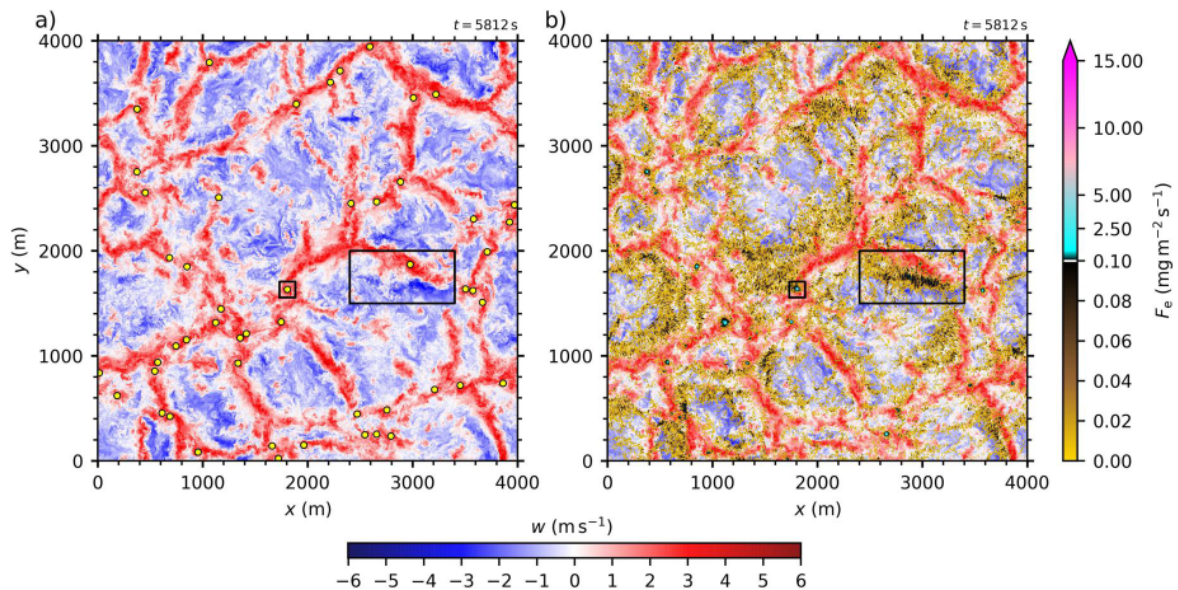


Figure 4. Instantaneous horizontal cross-sections of the vertical velocity at an altitude of 100 m in combination with detected vortex centers (yellow dots) in (a) and with the surface dust emission flux in (b). Only centers with $|\tau^*| \geq 10$ Pa are considered so that dust devils visible in (b) can be clearly assigned to detections in (a). The rectangles are the same as in Figure 3.

et al., 2020). However, it is known that the local application of MOST between the surface and the first grid level causes a systematic overestimation of the averaged wind shear near the surface. Following Maronga, Knigge, and Raasch (2020), this leads to a systematic underestimation of the surface shear stress and surface friction velocity. Consequently, the general level of dust emission in the whole domain might be too small. Unfortunately, no meaningful measurement data exist for the mean background emission in the CBL that would allow a direct comparison to our values.

3.3. Large-Scale Convective Dust Emission

The large-scale patterns of dust emission are closely connected to convective motions of air in the CBL. Figure 4 illustrates both a snapshot of the horizontal cross-section of the vertical velocity w at 100 m altitude in (a), and the dust emission field together with w in (b). It is evident that the dust emission bands are located between adjacent updrafts and downdrafts, where, due to the continuity of the flow, high horizontal velocities occur. Along these regions of high horizontal velocities, we regularly find friction velocities of up to 0.5 m s^{-1} , which is significantly

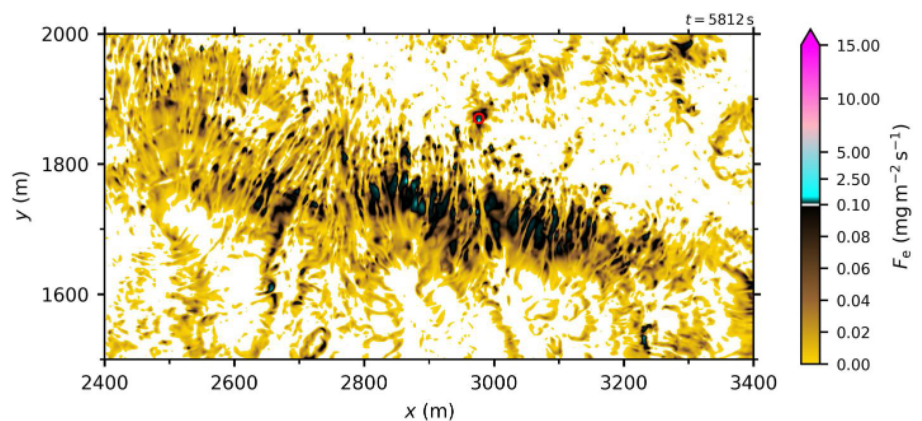


Figure 5. Instantaneous horizontal cross-section of the surface dust emission, focusing on the strong large-scale dust emission pattern, corresponding to the right rectangle of Figure 3. The red circle depicts the dust devil flux area of a vortex with $|\tau^*| \geq 10$ Pa.

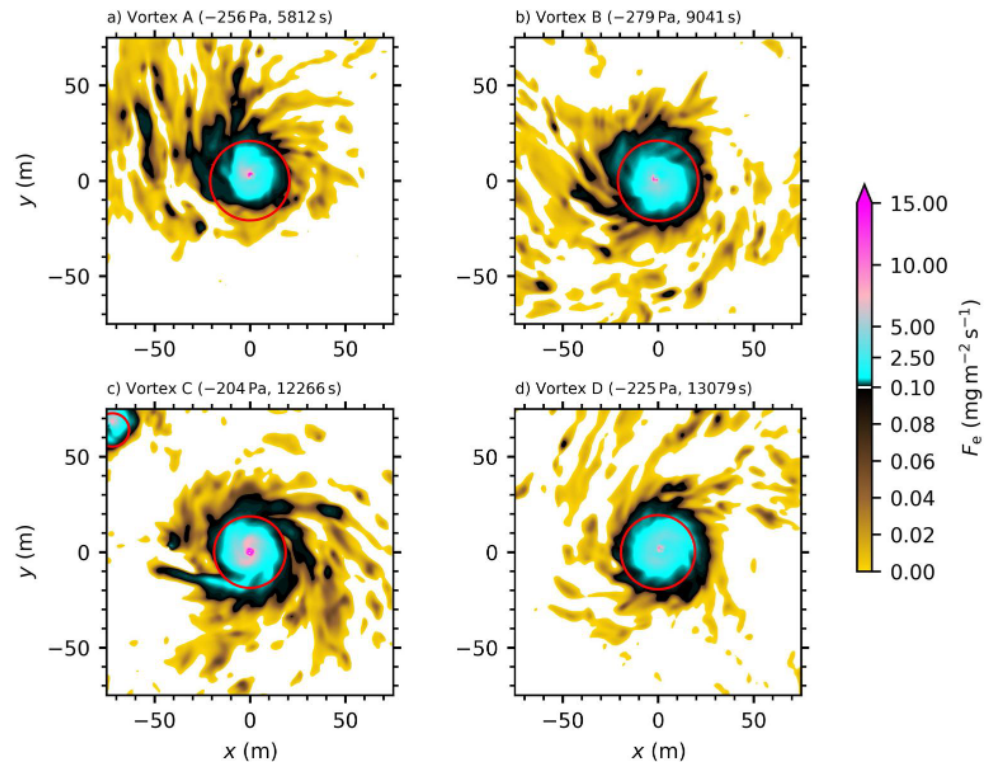


Figure 6. Instantaneous horizontal cross-sections of the surface dust emission flux for the four most intense dust devils at the time of their pressure minima. The red circles indicate the dust devil flux area (sphere with a radius of two times the core radius).

above AFWA's saltation threshold of 0.21 m s^{-1} . As marked by the right black rectangle, dust fluxes are especially high when horizontal gradients of the vertical velocity are strong, that is, when regions of strong up- and downdrafts are close to each other.

Figure 5 displays the dust flux for the very pronounced large-scale emission structure that is highlighted by the right rectangles in Figures 3 and 4. Due to the high resolution of 1 m, details of this band-like emission pattern are well captured, revealing a large variation of F_e from 0 to more than $1 \text{ mg s}^{-1} \text{ m}^{-2}$ even on short distances. The large-scale bands generally extend over several hundred meters and are composed of many, partly parallel, line-like structures of high dust emission, which follow the regions of high near-surface horizontal velocity. These structures are reminiscent of (elongated) streaks in the surface layer that have often been reported in the literature for the velocity field (e.g., Asmuth et al., 2021; Leonardi et al., 2004; Moeng & Sullivan, 1994). Analogous patterns of large-scale dust emission caused by horizontal winds due to turbulent convection were also examined in studies based on direct aerodynamic entrainment and termed as CTDE events (e.g., Ju et al., 2018; Klose & Shao, 2012; Klose et al., 2014; Li et al., 2014). However, the parameterization of CTDE usually assumes the absence of saltation and, consequently, that the respective dust emission is solely governed by direct aerodynamic entrainment. In contrast, our study reveals for the first time that convective motions of air can cause significant intermittent saltation on a large scale. Therefore, saltation should be considered in future CTDE studies. It might be decisive for the overall daytime ambient dust emission in arid and semi-arid regions. The consideration of large-scale convective dust emissions in the calculation of total global dust emissions could also potentially reduce its existing uncertainties. Note that the AFWA dust emission scheme is based on the assumption of quasi-stationary saltation, which may not always be applicable to these large-scale patterns. As this study reports these large-scale emission patterns for the first time, further research on the corresponding dust fluxes and suitable parameterizations is required.

3.4. Dust Fluxes and Concentrations Within Dust Devils

Similar to the large-scale dust emission patterns, dust devils are closely connected to the convective motions in the CBL. Figure 4a illustrates the locations of detected dust devil centers, exceeding $|\pi_*| \geq 10 \text{ Pa}$ at that time. We

excluded weaker detections ($3.5 \text{ Pa} < |\pi^*| < 10 \text{ Pa}$) from the illustration to make sure that the detected vortex centers do not overlap and are visually distinguishable from each other. For illustrations including all dust devil centers at a specific time, the reader is referred to Giersch and Raasch (2023). By comparing Figures 4a and 4b, we find a high correlation between large local emission fluxes (cyan color) and relatively strong vertical vortices in terms of the pressure drop (yellow dots). In addition, vortices are exclusively found at or very close to the updraft regions of the cellular pattern, which is in agreement with previous findings (e.g., Giersch et al., 2019; Kanak, 2005; Raasch & Franke, 2011). The reason is that dust devil-like vortices require strong updrafts and sufficient wind shear for their genesis and maintenance. As stated by Willis and Deardorff (1979) and Raasch and Franke (2011) both requirements are fulfilled at the vertices and branches of the convective cells. Although large-scale dust emission bands might enclose weaker dust devils, very intense ones show a clear spatial offset from these bands. The large-scale emission mainly occurs directly adjacent to the updraft regions, while dust devils are preferentially located within them. The mean value and standard deviation of the area fraction occupied by dust devils is $\bar{\omega}^d = 0.164 \pm 0.039\%$. As already noted in Section 3.1, this value exceeds previous estimates based on field observations and thermodynamics by at least one order of magnitude. For example, Koch and Renno (2005) estimated the fractional area covered by dust devils to be $\omega_{\text{obs}} = 0.003\% \pm 0.002\%$. An extensive statistical analysis by Lorenz and Jackson (2016) showed area fractions between 3×10^{-4} and 4×10^{-6} . The discrepancy to our simulation results is explained as follows: First, it is difficult to obtain good statistics on the occurrence of dust devils during field observations because only very intense dust devils are easily visible. Instead, our simulations capture the whole range of convective vortices, which agrees with the result of significantly higher detection rates in LES compared to observations (Lorenz & Jackson, 2016). Second, the area assigned to a given dust devil is not consistently defined (Klose & Shao, 2016; Koch & Renno, 2005; Lorenz & Jackson, 2016; Lorenz et al., 2021). We recommend to revisit the definition of the dust devil flux area in future studies. Consequences of this definition are addressed in Appendix A.

Figure 6 displays snapshots of horizontal cross-sections of the surface dust emission flux for the four strongest dust devils. Vortex B features the highest pressure drop of almost 280 Pa. Instantaneous peak fluxes in the order of $10 \text{ mg m}^{-2} \text{ s}^{-1}$ at or very close to the vortex center are typical. In addition, it can be seen that the calculated dust devil flux areas capture the highest dust emission fluxes reasonably well. Note that the most intense dust devil in terms of the absolute pressure drop does not necessarily cause the highest dust emission fluxes. Instead, the highest flux is caused by a rather concentrated vortex with a core pressure drop of roughly 150 Pa and a well-developed central downdraft (not shown). We therefore speculate that other factors beside the vortex's intensity, like the strength of the central downdraft and the radius, result in particularly high near-surface horizontal velocities and, consequently, dust emission fluxes. If only intense dust devils are considered that would probably be visible in nature ($|\pi^*| \geq 30 \text{ Pa}$, see Lorenz, 2014), we found typical peak dust emission fluxes during the vortices' lifetimes between 7.80×10^{-1} and $46.7 \text{ mg m}^{-2} \text{ s}^{-1}$. Thus, our peak dust emission fluxes exceed the LES results from Klose and Shao (2016) by 1–2 orders of magnitude. They determined peak fluxes in the order of 10^{-3} to $10^0 \text{ mg m}^{-2} \text{ s}^{-1}$. In laboratory experiments, Neakrase and Greeley (2010) determined sediment fluxes in the range of 4×10^0 – $10^8 \text{ mg m}^{-2} \text{ s}^{-1}$. Our peak values fit into this interval, but are much closer to the lower end than the upper end. The fluxes from the laboratory represent the bulk ranges including all sediment types (dust and sand-sized particles). The experiments further guaranteed that sufficient surface material was available for a continuous particle lifting. In addition, Neakrase and Greeley (2010) conducted their terrestrial experiments with steady horizontal wind speeds of up to 10 m s^{-1} and pressure drops of up to 10 hPa (1% of the Earth's ambient pressure of 1,000 hPa), which corresponds to very intense dust devils only. All this might have caused the large upper limit of $10^8 \text{ mg m}^{-2} \text{ s}^{-1}$. Focusing on dust-sized particles, Neakrase and Greeley (2010) determined the relationship $5.68 \times 10^{-6} |\pi^*|^{2.24}$ for calculating the flux. Assuming a typical pressure drop of 100 Pa for our intense dust devils, this relationship results in a dust flux of $10^5 \text{ mg m}^{-2} \text{ s}^{-1}$, which is still several orders of magnitude larger than our maximum values. Metzger (1999) measured sediment fluxes of approximately 6×10^2 – $5 \times 10^3 \text{ mg m}^{-2} \text{ s}^{-1}$ in the field. Because these fluxes were determined for mixed sediment, including both sand and dust-sized particles, Metzger's flux estimates can be interpreted as an upper bound for our dust fluxes. Newer measurements by Metzger et al. (2011) indicate dust fluxes of 10^0 – $10^2 \text{ mg m}^{-2} \text{ s}^{-1}$, which shows again that Neakrase's lower limit of $4 \times 10^0 \text{ mg m}^{-2} \text{ s}^{-1}$ from the laboratory and, thus, our determined fluxes are much more realistic. Averaged over all detected dust devils, the lifetime- and spatially-averaged (over σ) dust emission flux is $9.35 \times 10^{-2} \text{ mg m}^{-2} \text{ s}^{-1}$. If we apply the same averaging to the most intense dust devils that would probably be visible in nature ($|\pi^*| \geq 30 \text{ Pa}$, see Lorenz, 2014), the corresponding mean value is $5.90 \times 10^{-1} \text{ mg m}^{-2} \text{ s}^{-1}$.

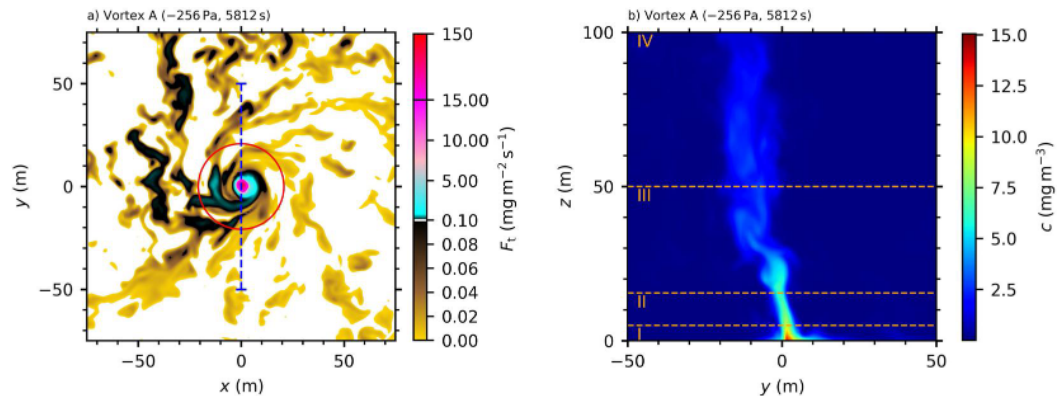


Figure 7. (a) Instantaneous horizontal cross-section of the (positive) vertical dust transport at 10 m height around Vortex A. The red circle depicts the dust devil flux area. The blue dotted line marks the location of the vertical cross-section (yz -plane) of the dust mass concentration field in (b). The orange dashed lines separate different height intervals (see text).

Figure 7a displays the positive vertical dust transport of Vortex A at 10 m height for the same time as in Figure 6a. A comparison of the dust transport and surface dust emission reveals that the area of $F_t > 1 \text{ mg m}^{-2} \text{ s}^{-1}$ is significantly smaller compared to the area with $F_e > 1 \text{ mg m}^{-2} \text{ s}^{-1}$. The peak value of vortex A is $F_t = 118.3 \text{ mg m}^{-2} \text{ s}^{-1}$, which is almost seven times the corresponding peak flux of $F_e = 17.6 \text{ mg m}^{-2} \text{ s}^{-1}$. Averaged over its dust flux area σ , vortex A has an instantaneous mean vertical dust transport of $\bar{F}_t^\sigma = 14.7 \text{ mg m}^{-2} \text{ s}^{-1}$, which is again roughly four times larger than the mean dust emission flux of $\bar{F}_e^\sigma = 4.0 \text{ mg m}^{-2}$. These observations highlight that F_e and F_t are not directly comparable in terms of amplitude and shape and that observed dust fluxes by dust devils are significantly influenced by the considered height.

The large discrepancy between F_e and F_t is further confirmed by a more profound statistical analysis. Averaged over the domain and analysis period, F_t has a mean value of $1.25 \times 10^{-2} \text{ mg m}^{-2} \text{ s}^{-1}$, which is twice the mean of $F_e = 5.77 \times 10^{-3} \text{ mg m}^{-2} \text{ s}^{-1}$. Averaged over all dust devils and their lifetimes, the spatially-averaged (over σ) value of F_t is $4.69 \times 10^{-1} \text{ mg m}^{-2} \text{ s}^{-1}$. This is five times the corresponding value of $F_e = 9.35 \times 10^{-2} \text{ mg m}^{-2} \text{ s}^{-1}$. Applying the same averaging procedure to the peak value within σ , we derive a dust transport of $2.77 \times 10^0 \text{ mg m}^{-2} \text{ s}^{-1}$, which is about 35% more than the corresponding value for $F_e = 2.06 \times 10^0 \text{ mg m}^{-2} \text{ s}^{-1}$. The total maxima of $F_t = 1.61 \times 10^2 \text{ mg m}^{-2} \text{ s}^{-1}$ and $F_e = 46.7 \text{ mg m}^{-2} \text{ s}^{-1}$ differ by a factor of three.

The vertical structure of the dust column, which is, based on field observations, defined as the visible column of a dust devil (e.g., Balme & Greeley, 2006; Luan et al., 2017), can be related to the dust concentration field in numerical setups. Figure 7b shows an instantaneous yz -cross-section of the dust mass concentration through the center of vortex A. The results support the findings of Morton (1966) and Hess and Spillane (1990) that the observed maximum height to maximum width ratio is of order 10 for a wide range of sizes. For vortex A, the width in terms of the diameter is about 5–10 m, which would suggest a (visible) height of 50–100 m. We also find that the dust concentration field significantly tapers from the surface to a height of a few meters (3.5 m for vortex A), where the minimum horizontal extent is reached. This height interval is called Region I in the following. The contraction of the dust column in the first meters above ground agrees well with the observation of a near-surface radial inflow of dust particles (e.g., see Balme & Greeley, 2006; Sinclair, 1966). Above this first region, the dust column is sharply confined with a small, almost constant radius (depicted by Region II). For intense dust devils, Region II usually reaches heights between 10 and 50 m (approximately 17.5 m for vortex A), that is, it includes the detection height of 10 m, where the previously mentioned transports F_t were evaluated. Above Region II, the horizontal extent of the concentration field slightly increase and the dust devils begin to blur. We term this area as Region III. At a certain height, the dust column is fully blurred and the horizontal extension of the visible column would be almost constant (if visible at all). We depict this height interval by Region IV, which often extends beyond elevations of 100 m and can potentially reach the top of the boundary layer. Thus, Figure 7 only captures the lowermost part of this region. The blurring effect agrees well with observations of Renno et al. (2004), who stated that dust devils at 100 m above the surface have no clear core but rather a uniform dust content. All in all, the previously defined regions match well with those established by Sinclair (1966) and revisited by Murphy

Table 4
Peak Values of F_e and F_t Around the Four Strongest Dust Devils at Different Altitudes^a

Altitude (m)	Vortex A	Vortex B	Vortex C	Vortex D
0	17.6	13.2	17.5	11.1
1	40.3	36.9	65	37.2
2	72.5	65.3	113	66.2
3	95.8	85.9	146	88.2
4	110	99.7	168	105
5	119	112	180	116
6	122	121	182	122
8	122	130	168	118
10	118	138	134	113
20	44.5	68.3	44.9	29.6
40	25.6	13.6	9.84	9.42
60	13.8	10.1	8.3	12.6
80	12.3	4.32	6.97	10.8
100	6.26	4.21	9.76	20.2

^aValues are given for an area of $150 \times 150 \text{ m}^2$ at the time where the vortices reach their maximum intensity. The height of 0 m refers to F_e . All other heights show the vertical transports as defined in Section 2.2. Fluxes are given in $\text{mg m}^{-2} \text{ s}^{-1}$.

et al. (2016): Region 1 describes the near-surface, radial inflow zone that is heavily particle-loaded and often has a v-shaped form. Region 2, at an intermediate height, is characterized by strong rotation and uplift. It includes the near-vertical column of rotating dust. In the upper-most Region 3, the structure dissipates, that is, the rotation decays and the dust devil “fades” into the ambient atmosphere. Our classification can be regarded as an extension of these three regions by a fourth one as explained above.

The tapering from Region I to II is also visible in the flux fields. As previously mentioned, the area of high dust fluxes is significantly narrower for F_t than for F_e . Due to continuity of the mass flow, the narrowing of the area of dust fluxes causes the fluxes to increase significantly, which is why F_t is larger for any statistical measure that we have calculated above. Table 4 shows the peak fluxes at different altitudes for the four strongest dust devils. Within the first 20 m, fluxes for each dust devil vary up to one order of magnitude. Particularly the lowest four m show a significant increase. For example, the vertical dust transport of Vortex A increases by a factor of two from 1 to 2 m altitude. Therefore, the height at which the dust flux is determined is critical for both numerical simulations and field observations. This conclusion is also true for the σ -averaged fluxes (not shown). We strongly recommend to use a uniform height in future studies. Note, values referring to an altitude above 10 m might not be located in the dust devil flux areas due to the commonly observed tilting of dust devils (e.g., Kaimal & Businger, 1970).

Lastly, we want to address the influence of dust devils on the dust concentration within the boundary layer. The vertical dust transport by intense dust devils is visible even at altitudes of several hundred meters. Figure 8 illustrates a xz -cross-section of the concentration field averaged along the y -direction.

Through the entire vertical extent of the child domain (240 m), the most intense dust devil-like vortices cause a significant increase of the y -averaged concentration compared to the ambient value. This stresses the important role of dust devils for the dust transport into higher heights.

A statistical analysis of the dust mass concentration at the detection height of 10.5 m shows that if only intense and visible dust devils are considered ($|\pi^*| \geq 30 \text{ Pa}$, see Lorenz, 2014), the mean value (over all detected dust devils) of the instantaneous peak dust mass concentration within σ and during the vortex lifetime is $8.92 \times 10^{-1} \text{ mg m}^{-3}$. The total maximum is 16.2 mg m^{-3} . The mean value (over all dust devils) of the temporally and spatially averaged dust mass concentration (over the individual lifetimes and σ) is $6.02 \times 10^{-1} \text{ mg m}^{-3}$. Due to different definitions of the dust column diameter utilized in field measurement and the dust devil flux areas in simulations, mean concentrations can hardly be compared with observational data. We limit the comparison to the observed peak values. Table 5 summarizes the peak dust mass concentrations within the first 9.5 m of the four strongest dust devils.

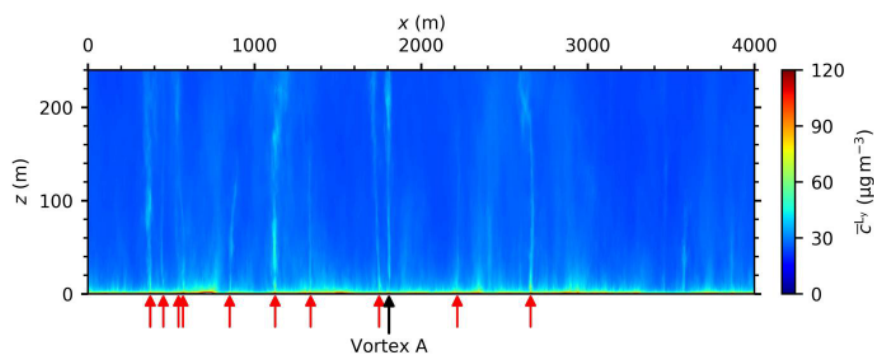


Figure 8. Vertical xz -cross-section of the dust mass concentration at 5,812 s, averaged over the whole domain length L_y perpendicular to the cross-section. Positions of the strongest vortices with $|\pi^*| > 30 \text{ Pa}$ are marked by the red arrows.

Table 5
 Peak Values of the Dust Mass Concentration c Around the Four Strongest Dust Devils at Different Altitudes^a

Vortex	Altitude								
	0.5 m	1.5 m	2.0 m	2.5 m	3.5 m	4.5 m	5.5 m	7.5 m	9.5 m
A	13.3	12.2	11.6	11.0	10.1	9.30	8.69	7.92	7.12
B	13.5	12.2	11.7	11.2	10.6	10.0	9.26	8.54	7.97
C	17.6	16.0	15.3	14.6	13.5	12.8	12.2	11.5	11.0
D	12.3	11.6	11.3	10.9	10.2	9.60	9.09	8.02	7.58

^aValues are given for an area of $150 \times 150 \text{ m}^2$ at the time where the vortices reach their maximum intensity. Concentrations are given in mg m^{-3} . The values at 2.0 m altitude are linearly interpolated from the adjacent grid levels.

Simulated peak dust concentrations decrease with altitude, and the highest values are always found at the first grid level. In contrast to Klose and Shao (2016), who determined a mass concentration of 10^{-3} – 10^0 mg m^{-3} at an altitude of 2 m, our dust devils show values between 11.3 and 15.3 mg m^{-3} , respectively. Thus, our values are closer to the measurements of Metzger et al. (2011), who determined PM10 peaks between 1.3 and 162.0 mg m^{-3} for 21 dust devils in altitudes of 1.14–4.5 m. Renno et al. (2004) measured mass concentrations inside strong dust devils and dusty plumes of 100 mg m^{-3} . However, they did not consider the grain-size distribution of the lifted material. As the dust mass contributes about 10% to the total suspended particles (Metzger et al., 2011), our values are again in very good agreement. Note, because the dust emission flux F_e controls c at the surface and vortex A–D do not cause the simulation's peak dust emission fluxes, we expect the simulation's concentration peaks at 2 m to be even higher.

3.5. Contribution by Dust Devils

Figures 9a and 9b illustrate the instantaneous dust mass flow rates defined in Section 2.5. Both the mass flow rates caused by the dust emission flux and by the vertical dust transport at 10 m height are shown, each for the union of all dust devil flux areas and for the total domain. The instantaneous contribution by all dust devils is also displayed in (c) and (d). A statistical summary of the different mass flow rates and the corresponding contribution of dust devils to these rates is given in Table 6. According to our knowledge, this table provides the most precise and extensive overview of saltation-induced dust mass flow rates and total emitted/transported dust masses in the CBL to date.

The dust emission flux of the total domain fluctuates around 100 g s^{-1} and is approximately 20 times larger than the dust emission flux caused by all dust devils (Figure 9a). Therefore, the (regional) contribution of dust devils to the total dust release amounts to an average of 5%, with instantaneous fluctuations approximately between 1 and 15% (Figure 9c). Note that it remains unclear whether the AFWA dust emission scheme is well-suited for the ambient dust emission flux along the large-scale patterns. AFWA assumes quasi-stationary saltation, which might not always be satisfied along the patterns. In addition, the assumed roughness length of 0.1 m might cause too high friction velocities for flat sandy surfaces and, hence, too high values for the ambient dust emission. Considering a possible overestimation of ambient dust emission and the potential to improve the considered region which are relevant for dust emission by dust devils (see Appendix A), the contribution could increase further. A contribution of 5% is significantly less than previous regional estimates of about 30%–50% that were based on observational data and/or large-scale modeling (Han et al., 2016; Pan et al., 2021; Tang et al., 2018), but it is significantly higher

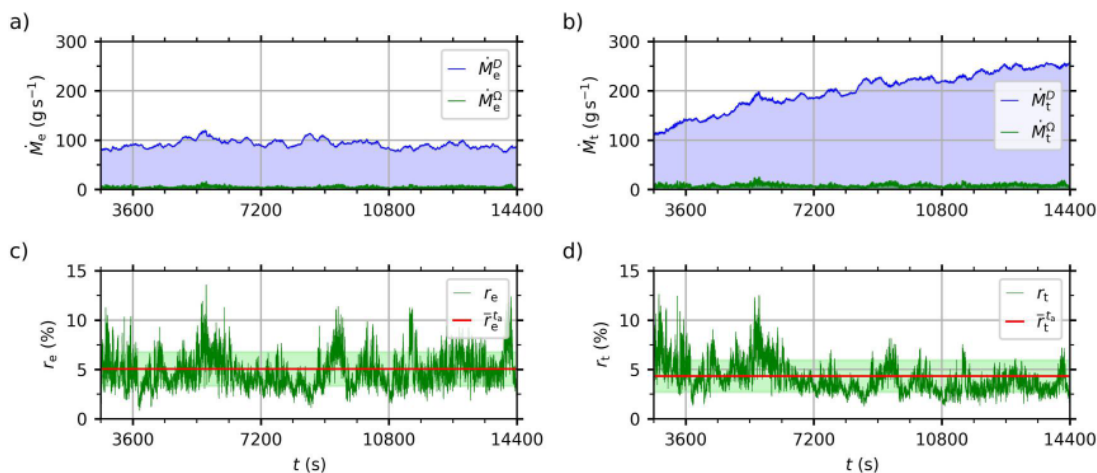


Figure 9. Instantaneous dust mass flow rates caused by (a) the dust emission flux \dot{M}_e and by (b) the positive vertical dust transport \dot{M}_t , each for the union of all dust devil flux areas Ω and for the total domain D . Instantaneous and time-averaged contribution of the dust devils to (c) the total emission flux r_e and (d) the positive vertical dust transport r_t . The areas shaded in light green represent the intervals of \pm the standard deviation.

Table 6
 Statistics of the Mass Flow Rates and the Corresponding Contribution of Dust Devils^a

	Min	Max	Mean	Std		Integrated
\dot{M}_e^Ω (g s ⁻¹)	0.76	15.9	4.67	1.69	M_e^Ω (kg)	53.6
\dot{M}_e^D (g s ⁻¹)	75.6	120	92.3	8.69	M_e^D (kg)	1,080
\dot{M}_t^Ω (g s ⁻¹)	1.91	24.7	8.40	2.75	M_t^Ω (kg)	96.4
\dot{M}_t^D (g s ⁻¹)	110	259	200	39	M_t^D (kg)	2,340
r_e (%)	0.85	13.6	5.05	1.71	R_e (%)	4.97
r_t (%)	1.27	12.6	4.33	1.61	R_t (%)	4.11

^aNotation as in Figure 9.

than the only existing estimate based on LES (0.03%–0.19% for Australia, Klose & Shao, 2016). Reasons for these deviations are diverse. First, the studies of Han et al. (2016), Tang et al. (2018), and Pan et al. (2021) assumed that the total amount of lifted dust aerosols is caused by dust storms, dust devils and dusty plumes. Thus, they completely neglected the background dust emission during daytime convection, which we found to be a main dust emission source but is most likely invisible in the field. Second, all three studies utilized an emission flux of 7.0×10^2 mg m⁻² s⁻¹, as suggested by Koch and Renno (2005). This value is one order of magnitude larger than our highest dust emission flux of 46.7 mg m⁻² s⁻¹, probably because they did not differentiate between dust and sand-sized particles and simply considered all lifted particles as dust. Regarding the fact that roughly 90% (Metzger et al., 2011) to 99% (Raack et al., 2018) of the lifted material is larger than dust-size, Koch and Renno's value is roughly one order of magnitude too large

if it is applied to describe dust fluxes. Third, Klose and Shao (2016) determined a mean dust flux based on a 10 m resolution LES. This is too coarse to generate dust devils of observed intensity (see Appendix B). Therefore, they underestimated the dust fluxes. Moreover, their dust emission scheme is not based on saltation, which is active in dust devils and the dominant dust emission process (Shao, 2008). Both explain their low estimate of contribution compared to our results.

As indicated by Table 6, the dust transport values at 10 m height and the contributions by dust devils to these transports are similar compared to \dot{M}_e . However, during the simulation, a significant accumulation of dust in the atmosphere can be observed. At 10.5 m altitude the domain-averaged concentration increases from 1.82×10^{-2} mg m⁻³ at 2,700 s to 5.96×10^{-2} mg m⁻³ at 14,400 s. This is caused by the net dust surface flux which remains positive because total emission exceeds deposition for the simulated period. Consequently, the (positive) vertical dust transport outside dust devils is enhanced on average because it scales with the concentration c (see Equation 6). This enhancement finally causes a continuous increase of \dot{M}_t^D , as visible in Figure 9b.

Dust devils, however, are not that affected by the background dust concentration increase (see \dot{M}_t^Ω in Figure 9b). Their dust content is mostly governed by the local dust emission rather than the advection of ambient dust (e.g., Gu et al., 2006; Zhao et al., 2004). This in combination with the enhanced vertical dust transport outside dust devils results in an overall negative trend of the dust devils' contribution to the total positive vertical transport with simulated time (see Figure 9d). We observe that the mean contribution averaged over 1 hr is 5.71% and 3.57% for the first and last hour of the analysis period, respectively. For that reason, conclusions regarding the contribution of dust devils to the total vertical dust transport crucially depend on the background concentration of atmospheric dust. For future studies, we suggest to either analyze both positive and negative transports at certain altitudes or to follow a quadrant analysis approach that focuses on the turbulent transports as a deviation from the mean (Y. Zhang et al., 2018). Note, the calculation of the dust devil flux areas is a critical step for the determination of the contribution of dust devils to the total dust emission and transport. Therefore, we address this issue in Appendix A in more detail.

4. Summary and Conclusion

In this study, saltation-induced dust emission fluxes in the dry atmospheric CBL were simulated, focusing on terrestrial dust devil-like vortices. The local and regional contribution of dust devils to the overall dust release of PM10 particles was estimated, which might have strong consequences for the consideration of dust devils in the dust budget of the climate system (Klose et al., 2016).

The numerical simulations were performed with the PALM model system, utilizing the LES approach. The model core was extended with a dust physics scheme to consider the emission, passive advection, gravitational settling, and dry deposition of dust. With the help of PALM's nesting technique, very high resolution LES were performed. For the first time, grid spacings down to the meter scale were used to simulate the saltation-induced dust emission in a simultaneously large domain of about $4 \times 4 \times 2$ km⁻³. Such grid spacings follow the resolution guidelines of Giersch and Raasch (2023) for simulating dust devils in the CBL. So far, similar studies (e.g., Ito et al., 2010; Klose & Shao, 2016) have used too coarse grid spacings of 10 m or more and have not applied a dust emission

parameterization based on saltation bombardment, which is one of the key processes for the release of soil particles into the atmosphere (Shao, 2008).

The simulated friction velocity, as the main simulation parameter that controls saltation and, consequently, dust entrainment into the atmosphere, agrees well with measurements. Balme et al. (2003) derived peak near-surface friction velocities in dust devils of 0.9–2.4 m s⁻¹. We showed that peak values of up to 2.59 m s⁻¹ can occur. Typical maxima of the friction velocity during the vortices' lifetimes amounted to 0.89 m s⁻¹. However, the threshold friction velocity above which saltation can occur is much more often exceeded outside dust devils. Assuming a threshold of 0.21 m s⁻¹, we showed that more than 99% of the area where saltation was present was not covered by dust devils. This relatively high proportion could partly be caused by the friction velocity assumed in the simulation, which is rather at the upper limit for typical desert-like conditions.

The simulated dust emission fluxes of dust devils fit very well to the most extensive terrestrial field measurements of dust fluxes to date, which indicated values in the range of 10⁰–10² mg m⁻² s⁻¹. Our fluxes were simulated in a range between 10⁻¹ and 10 mg m⁻² s⁻¹, while in the surroundings mean emission fluxes of 10⁻² mg m⁻² s⁻¹ occurred. Thus, the local contribution of dust devils to the dust release can be significant but also varies strongly, which is in agreement with the conclusions of Klose et al. (2016). The maximum flux of 46.7 mg m⁻² s⁻¹ was caused by a dust devil with an instantaneous pressure drop of approximately 150 Pa and a maximum tangential wind velocity of 7.4 m s⁻¹. Averaged over all dust devils, the mean dust emission maxima during the vortices' lifetimes amounted to 2.06 mg m⁻² s⁻¹ and the temporally as well as spatially averaged (over the lifetime and the horizontal vortex sphere) dust emission fluxes showed a mean value of 9.35 × 10⁻² mg m⁻² s⁻¹. To the best knowledge of the authors, this was the first comprehensive statistical evaluation of dust emission fluxes by dust devils. Moreover, the values above indicate that previous LES studies significantly underestimated dust fluxes of dust devils, like the study from Klose and Shao (2016) (10⁻³–10⁰ mg m⁻² s⁻¹) or Ito et al. (2010) (10⁻³–10⁻¹ mg m⁻² s⁻¹). For future studies that rely on dust fluxes by dust devils, we suggest to use the value of 5.90 × 10⁻¹ mg m⁻² s⁻¹ as the typical dust emission flux for intense dust devil-like vortices that would also be visible in the field. This value corresponds to the mean temporal and spatial average (over the vortex lifetime and horizontal sphere) of all detected dust devils with $|\Delta p| \geq 30$ Pa and a minimum duration of 30 s.

Finally, we estimated the mean contribution of dust devils to the total dust emission for desert-like regions on Earth to be approximately 5%. This is much less than previous estimates from regional studies for North Africa (38%; Pan et al., 2021), Western China (53% including dusty plumes; Han et al., 2016), or East Asia (30.4%; Tang et al., 2018), but much larger than the estimate of Klose and Shao (2016) for Australia (0.03%–0.19%). The resolution in numerical simulations and the considered dust emission phenomena in the individual studies are the main uncertainty factors that cause this variety. The rather low contribution in our case could be attributed to large-scale patterns of relatively strong dust emission, which are tightly connected to the cellular convection pattern of the CBL and dominate the overall dust release. As we did not investigate cases with prescribed background winds caused by, for example, dust storms triggered by synoptic lows, the simulated ambient dust emission might be underestimated. Similarly, the consideration of direct aerodynamic entrainment as a further dust emission process might also enhance the ambient dust emission. Both background winds and the inclusion of direct aerodynamic entrainment could reduce the relative contribution of dust devils to the overall dust release. On the other hand, our setup utilized a roughness length of 0.1 m, which is relatively high for desert-like conditions. Consequently, the resulting ambient friction velocity and, hence, the background dust emissions might be overestimated, potentially resulting in a higher relative contribution of dust devils.

In future work, all relevant dust release processes should be implemented into the simulation. Apart from the saltation-based emission, this includes aggregate disintegration and direct aerodynamic entrainment (Shao, 2008). More advanced environmental conditions should also be incorporated. Especially effects of surface properties, heterogeneities, and background winds on dust emission and transport need to be investigated because these parameters strongly influence the simulated intensity of dust devils (Giersch et al., 2019) and the ambient dust emission. Besides, the consideration of the so-called Δp -effect (Balme & Hagermann, 2006) and electrical fields (Esposito et al., 2016; Franzese et al., 2018; Kok & Renno, 2006) in dust devils could significantly modify the simulated dust fluxes. A more technical study about the dust emission area attributed to dust devils is also missing. We followed the procedure by Klose and Shao (2016) to define this area as a circle of twice the core radius. However, there is neither a theoretical foundation for this approach nor measurements or simulations that support the application of such a circle. Therefore, we highly recommend to investigate the emission area relevant for dust

devils for different vortex features in more detail because it significantly determines the emission contribution by dust devils.

Appendix A: Emission Region of Dust Devils

The dust devil flux area, as the relevant area for dust emission, is a critical quantity, especially for determining the fractional area covered by dust devils, their spatially averaged dust fluxes and concentrations, and the contribution of dust devils to the overall dust release and transport. In this study, we follow the approach of Klose and Shao (2016) and choose a circle of twice the core radius as the area that is considered for dust emission. This way, most of the very high dust emission fluxes above $10^{-1} \text{ mg m}^{-2} \text{ s}^{-1}$ are well-captured, which can be seen in Figure 6. However, for some very intense dust devils, small areas just outside the dust devil flux areas with emission fluxes exceeding $10^{-1} \text{ mg m}^{-2} \text{ s}^{-1}$ are not captured. Moreover, we observe narrow bands with relatively high fluxes, protruding from the central region (e.g., the third dust devil of Figure 6). These bands are also not captured by the circular area. They were first reported by Giersch and Raasch (2023) for the pressure and velocity field and are referred to as dust devil tails. Our results indicate that they are also present in the dust emission and concentration fields of some particularly strong dust devils.

The method to determine the radius that is needed to calculate the dust devil flux area might also be improved for the near-surface region of dust devils. In previous LES studies, this (core) radius was estimated as the distance at which the tangentially averaged modified perturbation pressure is less than 50% of its peak value at the center for the first time (e.g., Giersch et al., 2019; Kanak, 2005; Raasch & Franke, 2011). This method agrees well with empirical and analytical models of dust devils, where the core radius is defined at the same location as the highest tangential velocity (Lorenz, 2014), which is why we also follow this approach. However, our core radius is determined at the vortex detection height of 10.5 m but the dust devil flux area that is calculated based on this radius is defined at the surface. Our results suggest that the calculation of the core radius is well suited for the vertical region 2 of intense dust devils (see Section 3.4), which contains the near-vertical column of rotating dust. However, the lowest vertical region of dust devils, which is the near-surface, radial inflow zone and crucial for dust emission, might require a different approach because it shows completely different flow features. Further research is required, whether the extent of the near-surface inflow zone can be directly related to the core radius of the vertical column above.

Overall, the calculation of the dust devil flux areas might be optimized in future studies. We suggest the development of an algorithm that directly refers to the surface dust fluxes around the center rather being based on the pressure field at a height close to the surface.

Appendix B: Grid Resolution Dependence

Results from LES of dust devils vary significantly for different grid resolution (Giersch & Raasch, 2023). In order to better classify the results of Klose and Shao (2016), the only LES study that systematically determined dust fluxes from dust devils before our investigations, we investigate the grid sensitivity of the friction velocity and the dust emission flux for grid spacings ranging from $\Delta = 10 \text{ m}$, as utilized by Klose and Shao (2016), to $\Delta = 1 \text{ m}$, as recommended for quantitative studies by Giersch and Raasch (2023). We analyze the friction velocity because it is a major parameter of almost every dust emission parameterization. Figure B1 illustrates the global frequency spectra of u_* for different resolutions, utilizing a linear (left) and logarithmic scale (right) on the y-axis. Note that the total frequency increases with higher resolutions because the number of surface grid points and the number of time steps increase by orders of magnitude.

For all resolutions, the frequency spectra follow a Gaussian-like distribution, as can be seen in Figure B1a. The mean values and standard deviations of this Gaussian-like spectra are given by 0.209 ± 0.068 , 0.210 ± 0.071 , 0.214 ± 0.074 , and $0.218 \pm 0.079 \text{ m s}^{-1}$ for the 10, 5, 2.5, and 1 m resolution, respectively. Thus, the means and standard deviations show no significant grid sensitivity and only a minor increase with higher resolution. In contrast, the tail of large values of the Gaussian distribution is strongly affected by the grid (Figure B1b). Peak values of u_* , which are exclusively found inside the dust devil flux areas, are given by 0.69, 0.94, 1.42, and 2.59 m s^{-1} for the 10, 5, 2.5, and 1 m resolution, respectively. In field observations of Balme et al. (2003), maximum near-surface friction velocities were measured in the interval of (0.9 m s^{-1} , 2.4 m s^{-1}). Thus, the 1 m

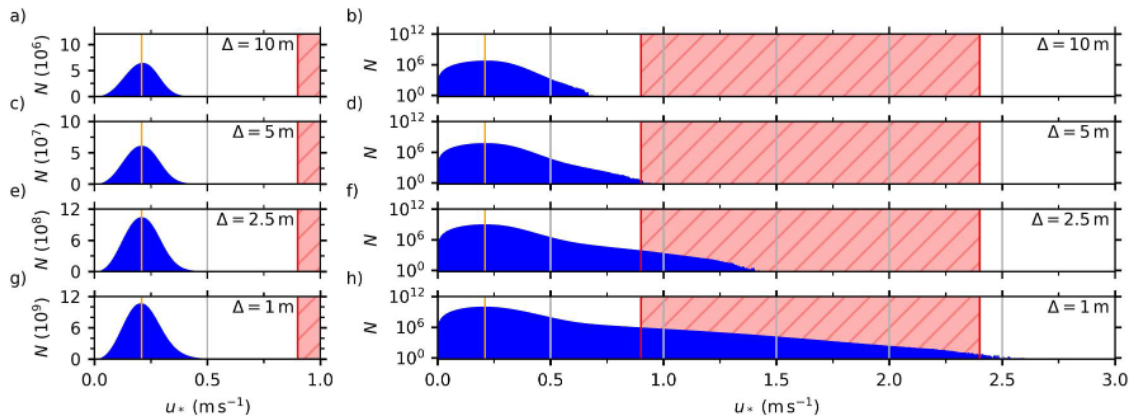


Figure B1. Frequency distribution of the simulated friction velocity u_* for a resolution of 10, 5, 2.5, and 1 m. Graphs (a), (c), (e), and (g) show the frequency N with a linear scale, while (b), (d), (f), and (h) utilize a logarithmic scale. For the vertically nested simulations, that is, P20N10 ($\Delta = 10$ m) and R5N1 ($\Delta = 1$ m), only the high-resolution inner nest is considered. The orange line marks AFWA's saltation threshold of $u_{*c} = 0.21$ m s⁻¹. The red area indicates the interval (0.9 m s⁻¹, 2.4 m s⁻¹) measured by Balme et al. (2003).

simulation performs best in replicating the entire range of observed peak values. Similarly, the 2.5 m simulation produces peak friction velocities within the observed range, albeit primarily toward the lower end. Coarser resolutions than 2.5 m significantly underestimate the peak values. Particularly the resolution of 10 m, as applied by Klose and Shao (2016), underestimates the maximum observed friction velocities by a factor of about 3.5 (2.4/0.69). We assume that the significantly lower values for the coarser resolutions are caused by the reduced peak dust devil intensities with increasing grid spacing, as discussed in Giersch and Raasch (2023). Overall, the above findings confirm the grid requirements of Giersch and Raasch (2023) to use a resolution on the meter scale if quantitative dust devil analysis shall be performed with LES.

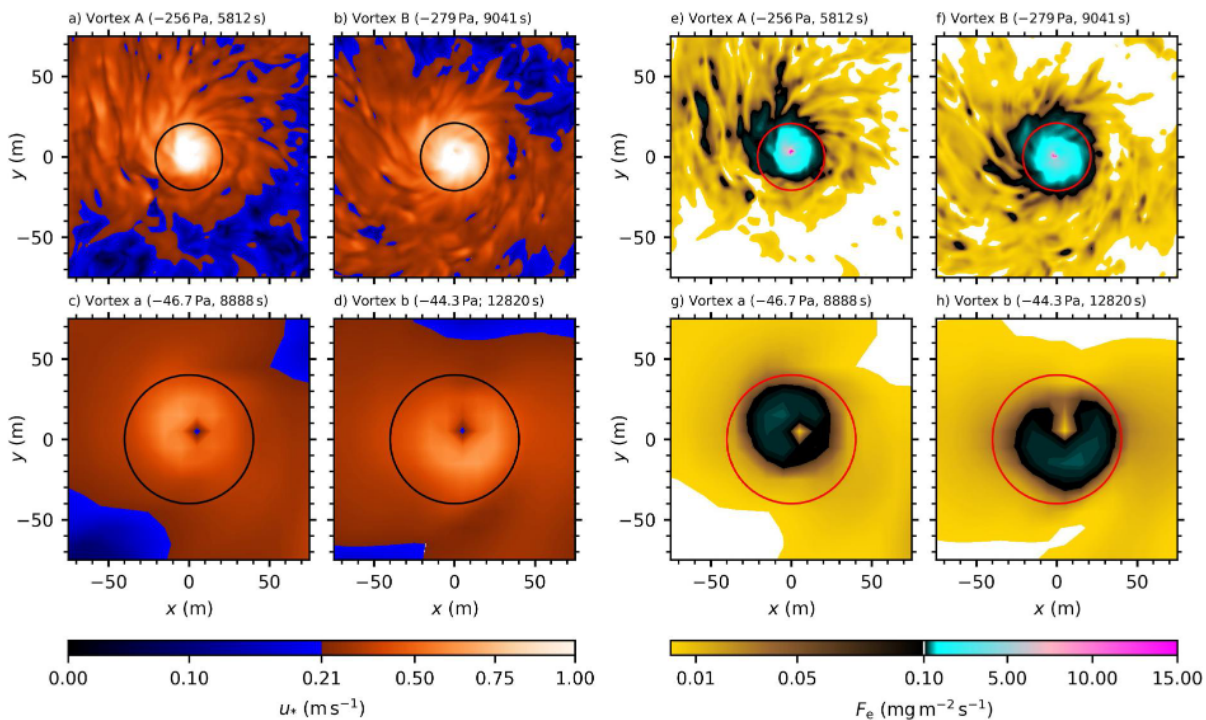


Figure B2. Friction velocity (left) and dust emission flux (right) within a square of 150×150 m² around the two strongest dust devil centers observed in P20N10 and R5N1. The black (red) circles indicate the dust devil flux area defined as a sphere with a radius of two times the core radius.

The resolution dependence of the highest values of the friction velocities has far-reaching consequences for the simulated dust emission of the most intense dust devils. To illustrate this, we compared the two strongest dust devils of R5N1 ($|\pi_A^*| = 256$ Pa and $|\pi_B^*| = 279$ Pa) with the two strongest dust devils of R20N10 ($|\pi_A^*| = 46.7$ Pa and $|\pi_B^*| = 44.3$ Pa). Figure B2 shows the friction velocity fields (left) and the dust emission flux fields (right) in a square of $150 \times 150 \text{ m}^2$ around these dust devils when they reached their peak pressure drops. First, it can be seen that more small-scale structures are resolved in R5N1 for both u_* and F_e . Second, the regions considered as dust devil flux areas are significantly smaller for higher resolutions (black and red circles). Decreasing horizontal vortex sizes with better resolution were also reported by Giersch and Raach (2023). Third, the friction velocities increase by a factor of three while the dust emission fluxes of the core region increase by approximately one order of magnitude. We conclude that quantitative results from $\Delta = 10$ m are not reliable. The 10 m simulation can neither reproduce realistic friction velocities nor realistic dust emission fluxes (see also discussion in Section 3.4). For that reason, we strongly believe that the estimate of the contribution of dust devils to the overall dust release in Australia, $R_c = 0.03\%–0.19\%$ (Klose & Shao, 2016), which was derived from a $\Delta = 10$ m LES, is too low.

Appendix C: Visual Appearance of Mass Concentration Fields

To the best knowledge of the authors, it has never been investigated numerically whether the concentration fields within dust devils differ for different grain-size categories, namely clay-sized ($D_p \leq 4 \mu\text{m}$), silt-sized ($4 \mu\text{m} < D_p \leq 63 \mu\text{m}$) and sand-sized particles ($D_p > 63 \mu\text{m}$). Vertically, the particle size distribution was studied by Raack et al. (2018), who collected particles of two dust devils at different heights and found that the mean particle size is decreasing with height. However, not a single study addressed the horizontal distribution of particle sizes. To investigate the three-dimensional structure for the different size categories, we utilize the AFWA scheme and distribute the bulk dust emission flux F_e onto different bins i with individual dust emission fluxes $F_e(i)$. In total, 9 size bins are utilized, which are chosen equally to the study of Raack et al. (2018). Effective diameters $d_{\text{eff}}(i)$ range from 1 to 375 μm . Table C1 summarizes the dust emission bins and their associated properties. For all emission bins i , the physics described in Section 2.2 is applied. Settling velocities for the sand-sized particles, that are out of the continuum regime, are calculated based on the semi-empirical equation of Ferguson and Church (2004). Bin-specific emission fluxes $F_e(i)$ are determined by multiplying the total bulk flux F_e with bin specific weighting factors $dS_{\text{rel}}(i)$. These weighting factors are derived from the mass distribution of the second dust devil DD #2 analyzed in Raack et al. (2018). Note, the AFWA scheme is designed for estimating the bulk flux of dust-sized particles. Therefore, F_e is distributed among all dust-sized bins (bins 1–6). The sand-sized particles (bin 7–9) are not included in the bulk flux F_e . We derive their weighting factors by an extrapolation according to the mass contributions measured by Raack et al. (2018).

Following this approach, we visualized a well-developed dust devil-like vortex for the different particle categories clay, silt and sand based on a simulation with 5 m resolution. The visualization can be found under <https://doi.org/10.5446/62786>. The clay mass is rather equally distributed over the whole volume and the concentration within the vortex does not clearly separate from the ambient region. Contrary, both the masses of silt and sand-sized particles are more restricted to the region of the dust devil. Especially the mass concentration field of sand-sized particles is in good agreement with the visual impressions of dust devils in the field. We conclude that sand-sized particles require the strong updrafts within the dust devil core region to be lifted, as they have high settling velocities. This indicates that the visual feedback of dust devils in the field is related to the mass concentration field of the coarser sand-sized particles rather than to the finer dust-sized particles. Field measurements also show only a small fraction of 1 (Raack

Table C1
Size Distribution of All Lifted Particles Used for Vortex Visualization

Category size bin i	Clay		Silt				Sand		
	1	2	3	4	5	6	7	8	9
Diameter range (μm)	<2	2–4	4–8	8–16	16–31	31–63	63–125	125–250	250–500
d_{eff} (μm)	1	3.0	6.0	12.0	23.5	47.0	94.0	187.5	375.0
dS_{rel}	0.000078	0.000595	0.0039	0.0259	0.1551	0.8145	11.015	63.062	23.438

et al., 2018) to 10% (Metzger et al., 2011) of the total lifted particle mass to be in the regime of fine dust-sized particles. According to Raack et al. (2018), the mass distribution within dust devils is dominated by coarser sand-sized particles. However, we plan to repeat the grain-size-resolved simulation utilizing a grid spacing of 1 m.

Acronyms

AFWA	Air Force Weather Agency
CBL	convective boundary layer
CTDE	convective turbulent dust emission
DEAD	mineral dust entrainment and deposition
DNS	direct numerical simulation
ECMWF	European Center for Medium-Range Weather Forecasts
LES	large-eddy simulation
MOST	Monin-Obukhov Similarity Theory
WRF	Weather Research and Forecasting Model

Data Availability Statement

The raw model output, user-specific code, model steering files and post-processing scripts used for creating the results and figures can be accessed under the CC BY 3.0 license via (<https://doi.org/10.25835/pa564r7y>; Klamt et al., 2024). The PALM model system (revision number 4732, <http://palm.muk.uni-hannover.de/trac/browser/?rev=4732>) used for the numerical simulations of this study is free software. It can be redistributed and/or modified under the terms of the GNU General Public License (v3) and is currently developed at GitLab (https://gitlab.palm-model.org/releases/palm_model_system/-/releases).

Acknowledgments

The work by Sebastian Giersch was partly funded by the German Research Foundation (DFG) under Grant RA 617/31-1. In addition, all authors supported the work as part of their employment at the Leibniz University Hannover. The authors gratefully acknowledge the computing time granted by the Resource Allocation Board and provided on the supercomputers Lise and Emmy at NHR@ZIB and NHR@Göttingen as part of the NHR infrastructure. Open access funding enabled and organized by Projekt DEAL.

References

- Asmuth, H., Janßen, C. F., Olivares-Espinosa, H., & Ivanell, S. (2021). Wall-modeled lattice Boltzmann large-eddy simulation of neutral atmospheric boundary layers. *Physics of Fluids*, 33(10), 105111. <https://doi.org/10.1063/5.0065701>
- Balme, M., & Greeley, R. (2006). Dust devils on earth and mars. *Reviews of Geophysics*, 44(3), RG3003. <https://doi.org/10.1029/2005RG000188>
- Balme, M., & Hagermann, A. (2006). Particle lifting at the soil-air interface by atmospheric pressure excursions in dust devils. *Geophysical Research Letters*, 33(19), L19S01. <https://doi.org/10.1029/2006GL026819>
- Balme, M., Metzger, S., Towner, M., Ringrose, T., Greeley, R., & Iversen, J. (2003). Friction wind speeds in dust devils: A field study. *Geophysical Research Letters*, 30(16), 1830. <https://doi.org/10.1029/2003GL017493>
- Barcan, R., Kassis, Z. R., Teaf, C. M., Danley-Thomson, A., Covert, D. J., & Missimer, T. M. (2023). Dry and wet atmospheric deposition composition in southwest Florida: Environmental and health implications. *Atmosphere*, 14(1), 102. <https://doi.org/10.3390/atmos14010102>
- Bergametti, G., Marticorena, B., & Laurent, B. (2007). Key processes for dust emissions and their modeling. In *Regional climate variability and its impacts in the mediterranean area* (Vol. 79, pp. 63–81). Springer. https://doi.org/10.1007/978-1-4020-6429-6_5
- Chapman, R., Lewis, S., Balme, M., & Steele, L. (2017). Diurnal variation in Martian dust devil activity. *Icarus*, 292, 154–167. <https://doi.org/10.1016/j.icarus.2017.01.003>
- Darmenova, K., Sokolik, I. N., Shao, Y., Marticorena, B., & Bergametti, G. (2009). Development of a physically based dust emission module within the weather research and forecasting (WRF) model: Assessment of dust emission parameterizations and input parameters for source regions in central and East Asia. *Journal of Geophysical Research*, 114(D14), D14201. <https://doi.org/10.1029/2008JD011236>
- Deardorff, J. W. (1980). Stratocumulus-capped mixed layers derived from a three-dimensional model. *Boundary-Layer Meteorology*, 18(4), 495–527. <https://doi.org/10.1007/BF00119502>
- Esposito, F., Molinaro, R., Popa, C. I., Molfese, C., Cozzolino, F., Marty, L., et al. (2016). The role of the atmospheric electric field in the dust-lifting process. *Geophysical Research Letters*, 43(10), 5501–5508. <https://doi.org/10.1002/2016GL068463>
- Farrell, E. J., & Sherman, D. J. (2015). A new relationship between grain size and fall (settling) velocity in air. *Progress in Physical Geography*, 39(3), 361–387. <https://doi.org/10.1177/0309133314562442>
- Ferguson, R. I., & Church, M. (2004). A simple universal equation for grain settling velocity. *Journal of Sedimentary Research*, 74(6), 933–937. <https://doi.org/10.1306/051204740933>
- Franzese, G., Esposito, F., Lorenz, R., Silvestro, S., Popa, C. I., Molinaro, R., et al. (2018). Electric properties of dust devils. *Earth and Planetary Science Letters*, 493, 71–81. <https://doi.org/10.1016/j.epsl.2018.04.023>
- Giersch, S., Brast, M., Hoffmann, F., & Raasch, S. (2019). Toward large-eddy simulations of dust devils of observed intensity: Effects of grid spacing, background wind, and surface heterogeneities. *Journal of Geophysical Research: Atmospheres*, 124(14), 7697–7718. <https://doi.org/10.1029/2019jd030513>

- Giersch, S., & Raasch, S. (2021). Evolution and features of dust devil-like vortices in turbulent Rayleigh-Bénard convection—A numerical study using direct numerical simulation. *Journal of Geophysical Research: Atmospheres*, 126(7), e2020JD034334. <https://doi.org/10.1029/2020JD034334>
- Giersch, S., & Raasch, S. (2023). How do dust devil-like vortices depend on model resolution? A grid convergence study using large-eddy simulation. *Boundary-Layer Meteorology*, 187(3), 703–742. <https://doi.org/10.1007/s10546-023-00792-3>
- Gillette, D. A., & Sinclair, P. C. (1990). Estimation of suspension of alkaline material by dust devils in the United States. *Atmospheric Environment, Part A: General Topics*, 24(5), 1135–1142. [https://doi.org/10.1016/0960-1686\(90\)90078-2](https://doi.org/10.1016/0960-1686(90)90078-2)
- Gu, Z., Zhao, Y., Li, Y., Yu, Y., & Feng, X. (2006). Numerical simulation of dust lifting within dust devils—Simulation of an intense vortex. *Journal of the Atmospheric Sciences*, 63(10), 2630–2641. <https://doi.org/10.1175/JAS3748.1>
- Han, Y., Wang, K., Liu, F., Zhao, T., Yin, Y., Duan, J., & Luan, Z. (2016). The contribution of dust devils and dusty plumes to the aerosol budget in western China. *Atmospheric Environment*, 126, 21–27. <https://doi.org/10.1016/j.atmosenv.2015.11.025>
- Hellsten, A., Ketelsen, K., Sühling, M., Auvinen, M., Maronga, B., Knigge, C., et al. (2021). A nested multi-scale system implemented in the large-eddy simulation model palm model system 6.0. *Geoscientific Model Development*, 14(6), 3185–3214. <https://doi.org/10.5194/gmd-14-3185-2021>
- Hess, G. D., & Spillane, K. T. (1990). Characteristics of dust devils in Australia. *Journal of Applied Meteorology and Climatology*, 29(6), 498–507. [https://doi.org/10.1175/1520-0450\(1990\)029<0498:CODDIA>2.0.CO;2](https://doi.org/10.1175/1520-0450(1990)029<0498:CODDIA>2.0.CO;2)
- Huneus, N., Schulz, M., Balkanski, Y., Griesfeller, J., Prospero, J., Kinne, S., et al. (2011). Global dust model intercomparison in aerocom phase I. *Atmospheric Chemistry and Physics*, 11(15), 7781–7816. <https://doi.org/10.5194/acp-11-7781-2011>
- Ito, J., Niino, H., & Nakanishi, M. (2010). Large eddy simulation on dust suspension in a convective mixed layer. *SOLA*, 6, 133–136. <https://doi.org/10.2151/sola.2010-034>
- Ito, J., Niino, H., & Nakanishi, M. (2013). Formation mechanism of dust devil-like vortices in idealized convective mixed layers. *Journal of the Atmospheric Sciences*, 70(4), 1173–1186. <https://doi.org/10.1175/JAS-D-12-085.1>
- Ives, R. L. (1947). Behavior of dust devils. *Bulletin of the American Meteorological Society*, 28(4), 168–174. <https://doi.org/10.1175/1520-0477-28.4.168>
- Jemmett-Smith, B. C., Marsham, J. H., Knippertz, P., & Gilkeson, C. A. (2015). Quantifying global dust devil occurrence from meteorological analyses. *Geophysical Research Letters*, 42(4), 1275–1282. <https://doi.org/10.1002/2015GL063078>
- Jones, S. L., Adams-Selin, R., Hunt, E. D., Creighton, G. A., & Cetola, J. D. (2012). Update on modifications to WRF-CHEM GOCART for fine-scale dust forecasting at AFWA. In *American geophysical union fall meeting 2012 abstracts* (p. A33D-0188). American Geophysical Union.
- Jones, S. L., Creighton, G. A., Kuchera, E. L., & Rentschler, S. A. (2011). Adapting WRF-CHEM GOCART for fine-scale dust forecasting. In *American geophysical union fall meeting 2011 abstracts* (p. U14A-06). American Geophysical Union.
- Ju, T., Li, X., Zhang, H., Cai, X., & Song, Y. (2018). Parameterization of dust flux emitted by convective turbulent dust emission (CTDE) over the Horqin Sandy Land area. *Atmospheric Environment*, 187, 62–69. <https://doi.org/10.1016/j.atmosenv.2018.05.043>
- Kaestner, C., Schneider, J. D., & du Puits, R. (2023). Evolution and features of dust devil-like vortices in turbulent Rayleigh-Bénard convection—An experimental study. *Journal of Geophysical Research: Atmospheres*, 128(2), e2022JD037466. <https://doi.org/10.1029/2022JD037466>
- Kaimal, J. C., & Businger, J. A. (1970). Case studies of a convective plume and a dust devil. *Journal of Applied Meteorology*, 9(4), 612–620. [https://doi.org/10.1175/1520-0450\(1970\)009<0612:csocap>2.0.co;2](https://doi.org/10.1175/1520-0450(1970)009<0612:csocap>2.0.co;2)
- Kanak, K. M. (2005). Numerical simulation of dust devil-scale vortices. *Quarterly Journal of the Royal Meteorological Society*, 131(607), 1271–1292. <https://doi.org/10.1256/qj.03.172>
- Kanak, K. M., Lilly, D. K., & Snow, J. T. (2000). The formation of vertical vortices in the convective boundary layer. *Quarterly Journal of the Royal Meteorological Society*, 126(569), 2789–2810. <https://doi.org/10.1002/qj.49712656910>
- Kawamura, R. (1951). Study on sand movement by wind. *Report*, 5(3), 95–112.
- Klamt, J., Giersch, S., & Raasch, S. (2024). Data for “Saltation-induced dust emission of dust devils in the convective boundary” [Dataset]. *LUIS*. <https://doi.org/10.25835/pa564r7y>
- Klose, M. R. (2014). *Convective turbulent dust emission: Process, parameterization, and relevance in the earth system (PhD Thesis)*. University of Cologne.
- Klose, M. R., Jemmett-Smith, B. C., Kahanpää, H., Kahre, M., Knippertz, P., Lemmon, M. T., et al. (2016). Dust devil sediment transport: From lab to field to global impact. *Space Science Reviews*, 203(1–4), 377–426. <https://doi.org/10.1007/s11214-016-0261-4>
- Klose, M. R., & Shao, Y. (2012). Stochastic parameterization of dust emission and application to convective atmospheric conditions. *Atmospheric Chemistry and Physics*, 12(16), 7309–7320. <https://doi.org/10.5194/acp-12-7309-2012>
- Klose, M. R., & Shao, Y. (2016). A numerical study on dust devils with implications to global dust budget estimates. *Aeolian Research*, 22, 47–58. <https://doi.org/10.1016/j.aeolia.2016.05.003>
- Klose, M. R., Shao, Y., Li, X., Zhang, H., Ishizuka, M., Mikami, M., & Leys, J. F. (2014). Further development of a parameterization for convective turbulent dust emission and evaluation based on field observations. *Journal of Geophysical Research: Atmospheres*, 119(17), 10441–10457. <https://doi.org/10.1002/2014JD021688>
- Knippertz, P., & Stuut, J.-B. (2014). *Mineral dust: A key player in the earth system* (1st ed.). Springer. <https://doi.org/10.1007/978-94-017-8978-3>
- Koch, J., & Renno, N. O. (2005). The role of convective plumes and vortices on the global aerosol budget. *Geophysical Research Letters*, 32(18), L18806. <https://doi.org/10.1029/2005GL023420>
- Kok, J. F., & Renno, N. O. (2006). Enhancement of the emission of mineral dust aerosols by electric forces. *Geophysical Research Letters*, 33(19), L19S10. <https://doi.org/10.1029/2006GL026284>
- Kurgansky, M. (2018). To the theory of particle lifting by terrestrial and Martian dust devils. *Icarus*, 300, 97–102. <https://doi.org/10.1016/j.icarus.2017.08.029>
- LeGrand, S. L., Polashenski, C., Letcher, T. W., Creighton, G. A., Peckham, S. E., & Cetola, J. D. (2019). The AFWA dust emission scheme for the GOCART aerosol model in WRF-CHEM v3.8.1. *Geoscientific Model Development*, 12(1), 131–166. <https://doi.org/10.5194/gmd-12-131-2019>
- Leonardi, S., Orlandi, P., Djenidi, L., & Antonia, R. A. (2004). Structure of turbulent channel flow with square bars on one wall. *International Journal of Heat and Fluid Flow*, 25(3), 384–392. <https://doi.org/10.1016/j.ijheatfluidflow.2004.02.022>
- Li, X. L., Klose, M. R., Shao, Y., & Zhang, H. S. (2014). Convective turbulent dust emission (CTDE) observed over Horqin Sandy Land area and validation of a CTDE scheme. *Journal of Geophysical Research: Atmospheres*, 119(16), 9980–9992. <https://doi.org/10.1002/2014JD021572>
- Liu, D., Ishizuka, M., Mikami, M., & Shao, Y. (2018). Turbulent characteristics of saltation and uncertainty of saltation model parameters. *Atmospheric Chemistry and Physics*, 18(10), 7595–7606. <https://doi.org/10.5194/acp-18-7595-2018>
- Loosmore, G. A., & Hunt, J. R. (2000). Dust resuspension without saltation. *Journal of Geophysical Research*, 105(D16), 20663–20671. <https://doi.org/10.1029/2000JD900271>

- Lorenz, R. D. (2014). Vortex encounter rates with fixed barometer stations: Comparison with visual dust devil counts and large-eddy simulations. *Journal of the Atmospheric Sciences*, *71*(12), 4461–4472. <https://doi.org/10.1175/JAS-D-14-0138.1>
- Lorenz, R. D., & Jackson, B. K. (2016). Dust devil populations and statistics. *Space Science Reviews*, *203*(1–4), 277–297. <https://doi.org/10.1007/s11214-016-0277-9>
- Lorenz, R. D., & Lanagan, P. D. (2014). A barometric survey of dust-devil vortices on a desert playa. *Boundary-Layer Meteorology*, *153*(3), 555–568. <https://doi.org/10.1007/s10546-014-9954-y>
- Lorenz, R. D., Spiga, A., Lognonné, P., Plasman, M., Newman, C. E., & Charalambous, C. (2021). The whirlwinds of Elysium: A catalog and meteorological characteristics of “dust devil” vortices observed by InSight on Mars. *Icarus*, *355*, 114119. <https://doi.org/10.1016/j.icarus.2020.114119>
- Luan, Z., Han, Y., Zhao, T., Liu, F., Liu, C., Rood, M. J., et al. (2017). Dust opacities inside the dust devil column in the Taklimakan Desert. *Atmospheric Measurement Techniques*, *10*(1), 273–279. <https://doi.org/10.5194/amt-10-273-2017>
- Maronga, B., Banzhaf, S., Burmeister, C., Esch, T., Forkel, R., Fröhlich, D., et al. (2020). Overview of the palm model system 6.0. *Geoscientific Model Development*, *13*(3), 1335–1372. <https://doi.org/10.5194/gmd-13-1335-2020>
- Maronga, B., Gryscha, M., Heinze, R., Hoffmann, F., Kanani-Sühring, F., Keck, M., et al. (2015). The parallelized large-eddy simulation model (palm) version 4.0 for atmospheric and oceanic flows: Model formulation, recent developments, and future perspectives. *Geoscientific Model Development*, *8*(8), 2515–2551. <https://doi.org/10.5194/gmd-8-2515-2015>
- Maronga, B., Knigge, C., & Raasch, S. (2020). An improved surface boundary condition for large-eddy simulations based on Monin–Obukhov similarity theory: Evaluation and consequences for grid convergence in neutral and stable conditions. *Boundary-Layer Meteorology*, *174*(2), 297–325. <https://doi.org/10.1007/s10546-019-00485-w>
- Marticoirena, B., & Bergametti, G. (1995). Modeling the atmospheric dust cycle: 1. Design of a soil-derived dust emission scheme. *Journal of Geophysical Research*, *100*(D8), 16415–16430. <https://doi.org/10.1029/95JD00690>
- Marticoirena, B., Bergametti, G., Aumont, B., Callot, Y., N'Doumé, C., & Legrand, M. (1997). Modeling the atmospheric dust cycle: 2. Simulation of Saharan dust sources. *Journal of Geophysical Research*, *102*(D4), 4387–4404. <https://doi.org/10.1029/96JD02964>
- Mason, J. P., Patel, M. R., & Lewis, S. R. (2014). The retrieval of optical properties from terrestrial dust devil vortices. *Icarus*, *231*, 385–393. <https://doi.org/10.1016/j.icarus.2013.12.013>
- Metzger, S. M. (1999). *Dust devils as aeolian transport mechanisms in southern Nevada and the mars pathfinder landing site (PhD Thesis)*. University of Nevada.
- Metzger, S. M., Balme, M. R., Townner, M. C., Bos, B. J., Ringrose, T. J., & Patel, M. R. (2011). In situ measurements of particle load and transport in dust devils. *Icarus*, *214*(2), 766–772. <https://doi.org/10.1016/j.icarus.2011.03.013>
- Miller, R. L., Knippertz, P., García-Pando, C. P., Perlwitz, J. P., & Tegen, I. (2014). Impact of dust radiative forcing upon climate. In P. Knippertz & J.-B. W. Stuut (Eds.), *Mineral dust: A key player in the earth system* (1st ed., pp. 327–357). Springer. https://doi.org/10.1007/978-94-017-8978-3_13
- Moeng, C.-H., & Sullivan, P. P. (1994). A comparison of shear-and buoyancy-driven planetary boundary layer flows. *Journal of the Atmospheric Sciences*, *51*(7), 999–1022. [https://doi.org/10.1175/1520-0469\(1994\)051\(0999:ACOSAB\)2.0.CO;2](https://doi.org/10.1175/1520-0469(1994)051(0999:ACOSAB)2.0.CO;2)
- Moeng, C.-H., & Wyngaard, J. C. (1988). Spectral analysis of large-eddy simulations of the convective boundary layer. *Journal of the Atmospheric Sciences*, *45*(23), 3573–3587. [https://doi.org/10.1175/1520-0469\(1988\)045\(3573:SAOLES\)2.0.CO;2](https://doi.org/10.1175/1520-0469(1988)045(3573:SAOLES)2.0.CO;2)
- Monin, A. S., & Obukhov, A. M. (1954). Basic laws of turbulent mixing in the surface layer of the atmosphere. *Tr. Akademii Nauk SSSR Geophys. Inst.*, *24*(151), 163–187.
- Morman, S. A., & Plumlee, G. S. (2014). Dust and human health. In *Mineral dust: A key player in the earth system* (1st ed., pp. 385–409). Springer. https://doi.org/10.1007/978-94-017-8978-3_15
- Morton, B. R. (1966). Geophysical vortices. *Progress in Aerospace Sciences*, *7*, 145–194. [https://doi.org/10.1016/0376-0421\(66\)90008-X](https://doi.org/10.1016/0376-0421(66)90008-X)
- Mullen, J. B., & Maxworthy, T. (1977). A laboratory model of dust devil vortices. *Dynamics of Atmospheres and Oceans*, *1*(3), 181–214. [https://doi.org/10.1016/0377-0265\(77\)90006-9](https://doi.org/10.1016/0377-0265(77)90006-9)
- Murphy, J., Steakley, K., Balme, M., Deprez, G., Esposito, F., Kahanpää, H., et al. (2016). Field measurements of terrestrial and Martian dust devils. *Space Science Reviews*, *203*(1–4), 39–87. <https://doi.org/10.1007/s11214-016-0283-y>
- Neakrase, L. D. V., Balme, M. R., Esposito, F., Kelling, T., Klose, M. R., Kok, J. F., et al. (2016). Particle lifting processes in dust devils. *Space Science Reviews*, *203*(1–4), 347–376. <https://doi.org/10.1007/s11214-016-0296-6>
- Neakrase, L. D. V., & Greeley, R. (2010). Dust devil sediment flux on earth and mars: Laboratory simulations. *Icarus*, *206*(1), 306–318. <https://doi.org/10.1016/j.icarus.2009.08.028>
- Nenes, A., Murray, B., & Bougiatioti, A. (2014). Mineral dust and its microphysical interactions with clouds. In *Mineral dust: A key player in the earth system* (1st ed., pp. 287–325). Springer. https://doi.org/10.1007/978-94-017-8978-3_12
- Nishizawa, S., Odaka, M., Takahashi, Y. O., Sugiyama, K.-i., Nakajima, K., Ishiwatari, M., et al. (2016). Martian dust devil statistics from high-resolution large-eddy simulations. *Geophysical Research Letters*, *43*(9), 4180–4188. <https://doi.org/10.1002/2016GL068896>
- Pan, L., Han, Y., Lu, Z., Li, J., Gao, F., Liu, Z., et al. (2021). Integrative investigation of dust emissions by dust storms and dust devils in North Africa. *Science of the Total Environment*, *756*, 144128. <https://doi.org/10.1016/j.scitotenv.2020.144128>
- Patrinos, A. A. N., & Kistler, A. L. (1977). A numerical study of the Chicago lake breeze. *Boundary-Layer Meteorology*, *12*(1), 93–123. <https://doi.org/10.1007/BF00116400>
- Pérez, C., Haustein, K., Janjic, Z., Jorba, O., Huneeus, N., Baldasano, J. M., et al. (2011). Atmospheric dust modeling from meso to global scales with the online NMMB/BSC-dust model—Part 1: Model description, annual simulations and evaluation. *Atmospheric Chemistry and Physics*, *11*(24), 13001–13027. <https://doi.org/10.5194/acpd-11-17551-2011>
- Pi, H., & Sharratt, B. (2019). Threshold friction velocity influenced by the crust cover of soils in the Columbia Plateau. *Soil Science Society of America Journal*, *83*(1), 232–241. <https://doi.org/10.2136/sssaj2018.06.0230>
- Raack, J., Reiss, D., Balme, M. R., Taj-Eddine, K., & Ori, G. G. (2018). In situ sampling of relative dust devil particle loads and their vertical grain size distributions. *Astrobiology*, *18*(10), 1305–1317. <https://doi.org/10.1089/ast.2016.1544>
- Raasch, S., & Franke, T. (2011). Structure and formation of dust devil-like vortices in the atmospheric boundary layer: A high-resolution numerical study. *Journal of Geophysical Research*, *116*(D16), D16120. <https://doi.org/10.1029/2011JD016010>
- Raasch, S., & Schröter, M. (2001). Palm: A large-eddy simulation model performing on massively parallel computers. *Meteorologische Zeitschrift*, *10*(5), 363–372. <https://doi.org/10.1127/0941-2948/2001/0010-0363>
- Renno, N. O., Abreu, V. J., Koch, J., Smith, P. H., Hartogensis, O. K., De Bruin, H. A. R., et al. (2004). Matador 2002: A pilot field experiment on convective plumes and dust devils. *Journal of Geophysical Research*, *109*(E7), E07001. <https://doi.org/10.1029/2003JE002219>
- Rennó, N. O., & Ingersoll, A. P. (1996). Natural convection as a heat engine: A theory for cape. *Journal of the Atmospheric Sciences*, *53*(4), 572–585. [https://doi.org/10.1175/1520-0469\(1996\)053\(0572:NCAAHE\)2.0.CO;2](https://doi.org/10.1175/1520-0469(1996)053(0572:NCAAHE)2.0.CO;2)

- Saiki, E. M., Moeng, C.-H., & Sullivan, P. P. (2000). Large-eddy simulation of the stably stratified planetary boundary layer. *Boundary-Layer Meteorology*, 95, 1–30. <https://doi.org/10.1023/A:1002428223156>
- Schmidt, H., & Schumann, U. (1989). Coherent structure of the convective boundary layer derived from large-eddy simulations. *Journal of Fluid Mechanics*, 200, 511–562. <https://doi.org/10.1017/S0022112089000753>
- Shao, Y. (2008). *Physics and modelling of wind erosion* (2nd ed.). Springer. <https://doi.org/10.1007/978-1-4020-8895-7>
- Shao, Y., Ishizuka, M., Mikami, M., & Leys, J. F. (2011). Parameterization of size-resolved dust emission and validation with measurements. *Journal of Geophysical Research*, 116(D8), D08203. <https://doi.org/10.1029/2010JD014527>
- Shao, Y., & Lu, H. (2000). A simple expression for wind erosion threshold friction velocity. *Journal of Geophysical Research*, 105(D17), 22437–22443. <https://doi.org/10.1029/2000JD900304>
- Shao, Y., Raupach, M. R., & Findlater, P. A. (1993). The effect of saltation bombardment on the entrainment of dust by wind. *Journal of Geophysical Research*, 98(D7), 12719–12726. <https://doi.org/10.1029/93JD00396>
- Sinclair, P. C. (1964). Some preliminary dust devil measurements. *Monthly Weather Review*, 92(8), 363–367. [https://doi.org/10.1175/1520-0493\(1964\)092<0363:SPDDM>2.3.CO;2](https://doi.org/10.1175/1520-0493(1964)092<0363:SPDDM>2.3.CO;2)
- Sinclair, P. C. (1966). *A quantitative analysis of the dust devil* (PhD Thesis). University of Arizona.
- Spiga, A., Barth, E., Gu, Z., Hoffmann, F., Ito, J., Jemmett-Smith, B., et al. (2016). Large-eddy simulations of dust devils and convective vortices. *Space Science Reviews*, 203(1–4), 245–275. <https://doi.org/10.1007/s11214-016-0284-x>
- Stout, J. E., & Zobeck, T. M. (1997). Intermittent saltation. *Sedimentology*, 44(5), 959–970. <https://doi.org/10.1046/j.1365-3091.1997.d01-55.x>
- Tang, Y., Han, Y., & Liu, Z. (2018). Temporal and spatial characteristics of dust devils and their contribution to the aerosol budget in East Asia—An analysis using a new parameterization scheme for dust devils. *Atmospheric Environment*, 182, 225–233. <https://doi.org/10.1016/j.atmosenv.2018.03.050>
- Tian, R., Ma, X., & Zhao, J. (2021). A revised mineral dust emission scheme in GEOS-chem: Improvements in dust simulations over China. *Atmospheric Chemistry and Physics*, 21(6), 4319–4337. <https://doi.org/10.5194/acp-21-4319-2021>
- Tingting, J., Li, X., Hongsheng, Z., Cai, X., & Song, Y. (2018). Comparison of two different dust emission mechanisms over the Horqin Sandy Land area: Aerosols contribution and size distributions. *Atmospheric Environment*, 176, 82–90. <https://doi.org/10.1016/j.atmosenv.2017.12.017>
- Wang, K., Zhang, Y., Nenes, A., & Fountoukis, C. (2012). Implementation of dust emission and chemistry into the community multiscale air quality modeling system and initial application to an Asian dust storm episode. *Atmospheric Chemistry and Physics*, 12(21), 10209–10237. <https://doi.org/10.5194/acp-12-10209-2012>
- White, B. R. (1979). Soil transport by winds on mars. *Journal of Geophysical Research*, 84(B9), 4643–4651. <https://doi.org/10.1029/JB084iB09p04643>
- Wicker, L. J., & Skamarock, W. C. (2002). Time-splitting methods for elastic models using forward time schemes. *Monthly Weather Review*, 130(8), 2088–2097. [https://doi.org/10.1175/1520-0493\(2002\)130<2088:TSMFEM>2.0.CO;2](https://doi.org/10.1175/1520-0493(2002)130<2088:TSMFEM>2.0.CO;2)
- Williamson, J. H. (1980). Low-storage runge-kutta schemes. *Journal of Computational Physics*, 35(1), 48–56. [https://doi.org/10.1016/0021-9991\(80\)90033-9](https://doi.org/10.1016/0021-9991(80)90033-9)
- Willis, G., & Deardorff, J. (1979). Laboratory observations of turbulent penetrative-convection planforms. *Journal of Geophysical Research*, 84(C1), 295–302. <https://doi.org/10.1029/JC084iC01p00295>
- Yang, X., Zhou, C., Huo, W., Yang, F., Liu, X., & Mamtimin, A. (2019). A study on the effects of soil moisture, air humidity, and air temperature on wind speed threshold for dust emissions in the Taklimakan desert. *Natural Hazards*, 97(3), 1069–1081. <https://doi.org/10.1007/s11069-019-03686-1>
- Yuan, T., Chen, S., Huang, J., Zhang, X., Luo, Y., Ma, X., & Zhang, G. (2019). Sensitivity of simulating a dust storm over Central Asia to different dust schemes using the WRF-CHEM model. *Atmospheric Environment*, 207, 16–29. <https://doi.org/10.1016/j.atmosenv.2019.03.014>
- Zender, C. S., Miller, R., & Tegen, I. (2004). Quantifying mineral dust mass budgets: Terminology, constraints, and current estimates. *Eos, Transactions American Geophysical Union*, 85(48), 509–512. <https://doi.org/10.1029/2002JD002775>
- Zeng, Y., Wang, M., Zhao, C., Chen, S., Liu, Z., Huang, X., & Gao, Y. (2020). WRF-CHEM v3.9 simulations of the East Asian dust storm in May 2017: Modeling sensitivities to dust emission and dry deposition schemes. *Geoscientific Model Development*, 13(4), 2125–2147. <https://doi.org/10.5194/gmd-13-2125-2020>
- Zhang, L., Gong, S., Padro, J., & Barrie, L. (2001). A size-segregated particle dry deposition scheme for an atmospheric aerosol module. *Atmospheric Environment*, 35(3), 549–560. [https://doi.org/10.1016/S1352-2310\(00\)00326-5](https://doi.org/10.1016/S1352-2310(00)00326-5)
- Zhang, Y., Hu, R., & Zheng, X. (2018). Large-scale coherent structures of suspended dust concentration in the neutral atmospheric surface layer: A large-eddy simulation study. *Physics of Fluids*, 30(4), 046601. <https://doi.org/10.1063/1.5022089>
- Zhao, Y. Z., Gu, Z. L., Yu, Y. Z., Ge, Y., Li, Y., & Feng, X. (2004). Mechanism and large eddy simulation of dust devils. *Atmosphere-Ocean*, 42(1), 61–84. <https://doi.org/10.3137/ao.420105>

Chapter 7

Conclusions

This chapter summarizes the main results of the previously presented studies. A special focus is on the research questions from Section 1.5. Answers to these questions are given and discussed. Concluding remarks and an outlook finish this thesis. The outlook reveals future perspectives of the numerical investigation of Dust Devil (DD) based on the results that were achieved.

7.1 Summary and Discussion

In this thesis, DD-like vortices that frequently occur in Convective Boundary Layers (CBLs) were numerically investigated with the help of Large-Eddy Simulation (LES) and Direct Numerical Simulation (DNS). The following main research questions were motivated and addressed in four different studies presented in Chapters 3–6:

1. What causes the quantitative discrepancy between simulated and observed DD-like vortices and how can realistic values be reproduced in LES?
2. Is DNS able to generate DD samples for a comprehensive statistical analysis and if so what are the main control parameters in these setups?
3. What are differences and similarities between convective vortices in DNS of Rayleigh-Bénard convection and LES of the atmospheric CBL?
4. Do DD-like vortices in DNS of Rayleigh-Bénard convection preferentially occur at the vertices and branches of the polygonal convective cells like it can be expected from LES and if so, what are possible mechanisms for their formation and maintenance?
5. What is the dependence of different DD features on the grid spacing and what is the required resolution in LES to capture the whole range of atmospheric DDs realistically?
6. How much do DD-like vortices contribute to the particle release and transport in the atmospheric CBL and what are typical particle concentrations within these vortices?

The first LES study (Chapter 3) investigated the effects of the grid spacing, background wind, and surface heat flux heterogeneities on the simulated vortex strength. Results from this investigation can be used to answer the first question. In agreement with previous studies like that from Raasch and Franke (2011), it could be shown that an increased resolution and moderate background winds cause the vortices to be more numerous and intense. Additionally, heterogeneously heated surfaces, that were considered for the first time in numerical simulations of DDs, also led to an intensification due to a secondary circulation

that developed. This circulation caused additional wind shear and flow convergence – two main factors that influence the formation and development of vortices. The combination of a fine resolution (2 m), moderate background wind (5 m s^{-1}), and a 1-D striped heating pattern finally produced intense DDs with central pressure drops of several hundred pascals. This agreed well with field observations but had never been achieved before with LES. In summary, the quantitative discrepancy (especially in the intensity) between simulated and observed DD-like vortices is caused by very idealized numerical setups compared to reality with too coarse resolutions to capture convective vortices appropriately. For a simulation of realistic quantitative DD features, it is beneficial to consider surface heterogeneities, different vorticity sources (e.g., obstacles or secondary circulations), and large-scale weather impacts like those from a geostrophic wind. All this is also present in nature.

Chapter 4 showed for the first time that DD-like vortices frequently occur in DNS of turbulent Rayleigh-Bénard convection with Rayleigh numbers up to 10^{11} , which is much smaller than the atmospheric value of 10^{18} . Convective vortices preferentially occurred at the cell vertices and branches of the polygonal convective cells, which are an inherent feature of Rayleigh-Bénard convection (question 4). This was already noticed in LES of the atmospheric CBL performed by Kanak (2005) and Raasch and Franke (2011). Moreover, the results from Chapter 4 supported the initial vortex formation mechanism derived from LES results of Raasch and Franke (2011): The flow converges at the cell vertices due to the strong updrafts located at these positions. Also, several convergence branches are present around the strong updrafts, merging at the vertex. As a result, the flow around a vertex has a velocity component toward the vertex itself but also toward the branches. Due to turbulence, the strength of the velocity at each side of the branches is not uniformly distributed, which can lead to initial vertical vorticity (see Fig. 15a in Raasch and Franke, 2011). Vortex intensification mechanisms like the general flow convergence and twisting of horizontal vorticity at the vertex can eventually result in a DD-like vortex.

However, the limited domain size in DNS could not capture the cellular pattern for the whole simulation time due to a broadening of structure size. After the convective cells vanished, DD-like vortices were found at wide band-like structures of high vertical velocities where near-surface flow convergence was strong. These bands often extended over the entire horizontal domain similar to LES results of Raasch and Franke (2011), who also performed simulations with a horizontal domain that was too small to allow for an undisturbed development of the polygonal convective cells. Also along the bands of high vertical velocity, flow convergence is irregularly shaped with a wind component parallel to the convergence line. If this wind happens to be opposite on both sides, an initial rotation is created, which might also explain the DD occurrence at the cell branches far away from the vertices when the cellular pattern is still present.

The DD samples simulated with DNS were large enough for a comprehensive statistical analysis once the Rayleigh number, the model domain's aspect ratio, and the velocity boundary condition were set appropriately (question 2). Generally, the Rayleigh number significantly influenced the appearance of flow properties and structures, which includes DD-like vortices. Only for Rayleigh numbers of 10^7 or larger, convective vortices occurred. However, for the calculation of meaningful statistics, Rayleigh numbers of at least 10^9 were necessary. Higher numbers produced higher translation speeds and more intense DDs in terms of increased pressure drops, vertical vorticities, and velocities. However, the sample-averaged lifetime decreased because more and more short-lived vortices were simulated with higher Rayleigh numbers. Unlike the Rayleigh number, the domain's aspect ratio (var-

ied between 2 and 4) did not show a significant effect on most of the vortex characteristics. As already mentioned before, the horizontal model extent was not large enough to capture the increasing width of the cellular convective pattern with simulation time. Limitations of computational resources prohibited larger aspect ratios than 4. Interestingly, no statistically significant effect of the broadening of structure size on the vortex properties could be observed. The velocity boundary condition was the last main control parameter that was modified in the DNS setups. A free-slip boundary condition (no friction) increased the number of detected vortices drastically. In addition, translation speeds and tangential velocities were higher but lifetimes, radii, and intensities expressed by the pressure drop were much smaller. Thus, a certain level of surface friction is essential for strengthening and maintaining DD-like vortices.

The comparison of convective vortices in DNS of Rayleigh-Bénard convection with those in LES of the atmospheric CBL revealed almost no qualitative difference (question 3). The vortices were very similar with respect to their three-dimensional flow structure, which shows that there is no strong need in LES to explicitly resolve the small-scale turbulence near the ground and that the effects of surface layer parameterizations on the simulated DD-like vortices are not that large, at least, if a sufficiently small grid spacing is used in LES (see below). However, a quantitative analysis of the vortex properties (e.g., size, lifetime or intensity) in DNS showed values several orders of magnitude smaller compared to LES because of the differences in the underlying setups and simulated scales. Kaestner et al. (2023) recently studied DD-like vortices in an experimental setup under very similar top and bottom boundary and initial conditions as explained in Chapter 4. They were able to choose a much larger measuring time of 22 hr compared to the vortex analysis time of 70 s in the DNS. This allowed them to extend the DD statistics for rare events such as very long-lived or large vortices but their setup prohibited to detect vortices less than 0.1 m. However, Chapter 4 showed that the typical spatial scale of DD-like vortices in DNS is smaller than 0.1 m, which is why the data of Kaestner et al. (2023) should be considered as a complementary rather than comparative data set. It might be that the larger scale convective vortices detected in the Rayleigh-Bénard convection experiments can be interpreted as the large-scale rotating atmospheric updrafts in which natural DD-like vortices are sometimes embedded and which penetrate the whole CBL. Nevertheless, the simulated and measured vortices showed a good agreement of maximum pressure drops (~ 100 mPa) and lifetimes (~ 10 s), which was, to the best knowledge of the author, the first direct experimental validation of numerically simulated DD properties.

While conducting the first two studies of this thesis, it was still unclear what resolution must be chosen to adequately resolve DD-like vortices with LES. Therefore, the third study (Chapter 5) investigated the resolution dependent convergence of various DD features (question 5). Grid spacings between 10 and 0.625 m were chosen while simulating a domain of approximately $4 \times 4 \times 2 \text{ km}^{-3}$ to capture the large-scale cellular pattern of the CBL. Resolutions less than 2 m had never been used before to simulate terrestrial DDs in such large domains. The results regarding the general flow in the CBL agreed well with previous studies (e.g., Sullivan and Patton, 2011), that is, for the boundary layer interior, grid spacings of the order of 10 m are sufficient to capture the mean flow and low-order moment statistics. Instead, no convergence could be found for near-surface properties and the peak values in the flow, like maximum wind velocities. Peak values could mostly be attributed to the occurrence of DD-like vortices in combination with the very thin super-adiabatic layer close to the ground that was drawn into and stretched within the vortex core.

The convergence of most of the mean (lifetime- and additionally sample-averaged) vortex properties and a detailed comparison of the simulated vortex sample with field data indicated a necessary grid resolution of less than 2 m to get good quantitative estimates of DD characteristics. Converged DD occurrence rates and mean intensities in terms of the pressure drop amounted to $19 \text{ km}^{-2} \text{ h}^{-1}$ and 14 Pa, respectively. Typical lifetimes, radii and temperature deviations from the background conditions were in a range of 4–5 min, 6–8 m, and 3–4 K. Maximum pressure drops and temperature deviations showed values of several hundred pascal and 8 K, respectively. Plane-averaged vertical vorticities around the vortex core typically ranged from 0.1 to 1 s^{-1} . Mean tangential and radial velocities were converged at approximately 2.1 m s^{-1} and 1.35 m s^{-1} , respectively, with maximum values of 13 m s^{-1} for the tangential and 4 m s^{-1} for the radial component. This shows that the tangential velocity is usually higher than the radial velocity, as already stated in Subsection 1.2.2. In case of the vertical velocity, no convergence was observed neither for the mean values nor for the maxima. At the finest resolution, peak vertical velocities of almost 20 m s^{-1} were simulated, which is already very close to the maximum measured wind velocities in the field of 25 m s^{-1} (Balme and Greeley, 2006). The results further suggested that a convergence for the whole DD statistics can be expected at resolutions of just less than 0.5 m, even for the peak values. These resolutions might be affordable within the next years.

The derived statistics of terrestrial DDs from above are probably the most precise and comprehensive that have ever been determined from LES of the atmospheric CBL. If the three-dimensional flow structure is of interest, qualitative results are already realistic for grid spacings of 2.5 m or smaller. With these resolutions, all basic vortex features are captured, like central downdrafts, subvortices, and the near-surface convergent flow that turns into a spiraling predominantly upward motion near the center. Also the simulated, vertically-thin, super-adiabatic layer with high temperature lapse rates of $\sim 1 \text{ K m}^{-1}$ agreed well with measured environmental conditions in which DDs usually develop. Instantaneous pressure fields revealed tail-like structures for the first time, where the low pressure region is extended at one side of the vortex and protrudes from the core region. The tail always separates strong updrafts near the center from downdrafts further away, thus, the horizontal shear of the vertical velocity is large in that region. The grid convergence study also stressed that the vortex detection and analysis algorithm must be clearly defined in numerical simulations, similar to the features of the DD population for which the results are valid. For example, the previously mentioned values are representative for a population with vortex lifetimes of at least 120 s and lifetime-averaged radii of 5 m or more.

Finally, Chapter 6 focused on surface dust emission fluxes, near-surface dust transports, and dust concentrations of DDs that were simulated in LES of the atmospheric CBL (question 6). Dust emission was provoked by a parameterization for saltation bombardment and resolution requirements described above were taken into account, resulting in the first LES simulation of saltation-based dust emission in the CBL on the meter scale. Other dust physics than saltation bombardment was also considered, like passive advection, gravitational settling, and dry deposition. Simulated friction velocities, as the main control parameter of saltation, were in very good agreement with the measured values of Balme et al. (2003), who derived peak friction velocities in DDs between 0.9 - 2.4 m s^{-1} . However, more than 99 % of the area where saltation was present was not covered by dust devils but occurs in form of large-scale patterns of several hundred meters in size. These patterns were tightly connected to the cellular flow pattern of the CBL and were the main mechanism for dust release. The magnitude of the simulated dust emission fluxes ranged from 10^{-1}

to $10 \text{ mg m}^{-2} \text{ s}^{-1}$, which is consistent with field measurements by Metzger et al. (2011) but which is higher than previous values derived from LES studies (10^{-3} to $1 \text{ mg m}^{-2} \text{ s}^{-1}$). Compared to the emission fluxes at the surface, the dust fluxes or dust transports at 10 m height were five times higher on average. Within the strongest simulated DDs, a peak dust mass concentration of 10 mg m^{-3} was typical. Ultimately, it was concluded that DDs are a significant phenomenon for the local atmospheric dust content with severe consequences for air quality and visibility. However, they seem to be less important on the regional scale because they contribute only 5 % to the total simulated dust emissions of desert-like regions.

7.2 Outlook

This thesis showed that the erratic occurrence of DDs is not only challenging for field observations but also to a certain extent for numerical simulations due to the limited computational resources. Good statistics of DD features that also contain the strongest and therefore rarest DDs require large model domains and/or long simulation times with relatively high resolutions. Another approach to improve the statistics would be to create a simulation ensemble, where the same simulation is repeated several times. This high demand for computing power must be taken into account for future studies.

A fundamental DD feature that was not considered in the statistics of this thesis but is still important is the vortex height. Because dust is often not regarded in numerical simulations of DDs, the dust column can not be used to estimate the height. Instead, a quantitative criterion based on distinct vortex feature needs to be developed. One possibility is to use the spatial distribution of the pressure around the vortex center, an approach that was successfully used in this thesis for determining the horizontal extent of DDs. It should be noted here that each future DD study requires a clear definition of what is interpreted as a DD, for example, whether non-visible vortices are equally considered as visible ones. Otherwise, comparisons between different numerical DD studies or comparisons with field measurements become difficult.

Beside these statistical and conceptual questions, follow-up studies should try to simulate the environmental conditions in which DDs preferentially occur more realistically. This was already noted by Spiga et al. (2016), who stated that LES of DDs are still idealized numerical experiments. This is also true for the setups of this thesis. Although surface heat flux heterogeneities and background winds were considered, other influencing factors like heterogeneities in the topography or roughness length were not investigated. The numerical model PALM, which was applied in this thesis, offers various model components to better approach the reality, for example to simulate a more complex natural terrain. The land surface model provides the ability to avoid prescribed surface conditions (e.g., surface fluxes or temperatures) that were used in the previous chapters. Instead, surface conditions are calculated locally based on different land surface types (e.g., water or vegetation), the surface radiation budget, which additionally requires the radiation model to be active, and atmospheric conditions. Because the (local) heat flux or temperature at the surface is an essential parameter for the development of DDs, results might significantly change if the land surface model is applied for regions with a more complex surface structure than flat deserts. If vegetation is assumed, various vegetation types with predefined physical properties can be set (e.g. a bare soil or desert). In addition, the surface is coupled to a one-dimensional soil model, for which different soil types can be chosen. These soil types vary in their grain size and, consequently, in their physical behavior regarding moisture so that even the effects of

soil moisture on the DD occurrence can be investigated. The plant canopy model of PALM is another option to consider more complex natural terrain in the simulation of DDs. It is used to study the turbulent flow inside, above, and around vegetation canopies, which can be a source for additional vorticity. Also, simulations over heterogeneous and complex urban terrain would provide additional insights into the dynamics and characteristics of DDs. These simulations would especially complement measurement studies in urban areas (e.g., Fujiwara et al., 2011; Inagaki and Kanda, 2022). To simulate an urban setting, PALM's Cartesian topography implementation together with the urban surface model could be used. The latter solves the energy balance for different urban surfaces (e.g., green roofs or bare walls).

Non-stationary boundary layer processes that were totally neglected in the numerical setups of this thesis can also be considered to make the simulations more realistic, for example, by using a so-called offline nesting, where large-scale weather information is incorporated into the simulation. The offline nesting is especially designed for realistic heterogeneous domains under evolving synoptic conditions that are prescribed as initial and boundary conditions. As noticed by Spiga et al. (2016), the coupling of LES with a global or regional climate model is probably a very promising method to explore effects of varying large-scale and regional meteorological conditions on the vortex development. By prescribing a daily heat flux time series or by using the land surface model together with the radiation model, more idealized diurnal cycles can be simulated without the application of the offline nesting but with simple cyclic boundary conditions. In this way, the vortex occurrence rates and properties can be studied for different times of the day. This would help, for example, to better define the period of "strong DD activity", which is usually assumed to be 4 h (Lorenz, 2014).

Apart from the physical characteristics of the setups, also the numerical features and the turbulence closure of the LES model might influence the simulated vortices in an unknown way. Therefore, results from different resolutions, advection schemes, and Subfilter-Scale (SFS) models should be compared in the future. The previous chapters showed that the resolution is a very critical numerical parameter in LES of DDs because many vortices show radii only slightly larger than typical LES grid spacings. While a convergence for the mean quantities could be achieved for grid spacings of about 1 m or less, maxima and near-surface properties still vary with resolution. Thus, the grid convergence behavior for the extreme flow events need to be studied in the future to test the hypothesis of Chapter 5 that also maximum values will be converged at grid spacings of just less than 0.5 m. Beside the resolution-dependence of DD statistics, this thesis highlighted potential effects of numerical diffusion and dispersion provoked by the model's advection scheme. It was observed that a second-order scheme (schemes of even order are typically dominated by numerical dispersion) caused the DDs to be weaker and less persistent compared to a high-order and less dispersive advection scheme. The difference in intensity reached approximately 10 % on average (see also Spiga et al., 2016). Therefore, investigations regarding the numerical schemes are highly recommended for any other numerical DD study. Moreover, the DNS results of this thesis indicated that the significance of the exact formulation of the SFS model in LES might be low for the three-dimensional flow structure of DDs. However, further analysis is necessary here. For example, DD statistics from LES utilizing different SFS models could be compared. Another numerical uncertainty is induced by the local application of the Monin-Obukhov Similarity Theory (MOST) for defining the surface boundary conditions. This approach is theoretically questionable, although it is often used in practice as in

this thesis. MOST assumes horizontal homogeneity of the surface and a steady-state flow, which is in more realistic setups not the case. Moreover, it actually defines mean quantities but is assumed here to be valid also for a local application at each time step. The theory is especially limited with regard to very high resolutions, where the grid spacing is close to the roughness length. Basu and Lacser (2017) strongly advocated to place the lowest grid level above 50 times the roughness length if MOST is applied. Because this rule was frequently violated in this thesis, the effects of different lower boundary conditions for the surface-atmosphere exchange should be tested in LES of DDs.

A further follow-up challenge is to enable LES to consider both radiative effects as well as particle lifting and transport. Only in these simulations, a potential radiative effect on the DD dynamics by the particles' absorption of solar radiation or the shading of the ground could be studied. Instead of using an Eulerian approach for the particles, they could also be simulated with a Lagrangian method, for example, to study the causes for DD formation. Although the DNS results of this thesis were able to support the suggested initial DD formation mechanism by Raasch and Franke (2011), details are still unclear and the origin of vertical vorticity needs to be further investigated in future studies. Especially other existing formation theories (e.g., Rennó et al., 2004; Kanak, 2005; Ito et al., 2013) could not be totally refuted in the previous chapters. To do so, passive tracers could be injected into the flow, while tracking their position and flow information at this position. Their trajectories and time series information might help to identify where the vorticity actually comes from and how a vortex forms. Interestingly, no LES study exists so far that focused on the reasons for the decay of terrestrial DDs. New insights into this particular time of the vortex life cycle would help to better understand the large range of DD lifetimes from a few tens of seconds to hours.

Another goal of this thesis was to generate DNS data of DDs that enable a direct validation and comparison with laboratory investigations, that is, DNS and the experimental setup consider the same spatial scales. However, it was noticed that direct comparisons with laboratory studies are quite challenging because they are currently unable to reproduce a DD population similar to that from DNS. The numerical results were strongly limited in the simulation time (~ 100 s) but could capture the mean horizontal vortex size of less than 10 mm, utilizing high-resolutions runs (~ 1 mm). In the laboratory, it already requires great technical effort to detect dust devil-like vortices of the order of 100 mm (Kaestner et al., 2023). Smaller vortices could not be captured in these large-scale experimental setups of ~ 100 m³. The advantage of the experiments is the much higher detection time. Therefore, bringing numerical simulations and experiments further together remains an up-to-date topic.

The last study of this thesis quantified the dust emission, transport and concentration of DDs. Future LES studies regarding this topic should include a dust emission parameterization that is able to simulate different particle classes (e.g., clay, silt, and sand) and emission mechanisms (e.g., saltation bombardment, direct aerodynamic entrainment). Additionally, resolutions of 1 m or even below should be used. Also more advanced environmental conditions like background winds and surface heterogeneities should be incorporated in these simulations. Only in this way, more precise quantitative estimations of the local, regional, or global contribution of DDs to the atmospheric aerosol input can be achieved. However, apart from the dust flux and transport, a precise quantification of the vertical momentum and heat transport by DDs is still missing, although this information is principally easy accessible in numerical simulations. Measurements of a single DD and plume showed that the heat flux within a dust devil is an order of magnitude larger than in a convective plume (Kaimal

and Businger, 1970). Moreover, Kaimal and Businger (1970) granted the dust devil a quite severe influence on the momentum transport but not an overwhelming effect on the 5-min averaged heat transport. Rennó et al. (2004) observed heat fluxes two orders of magnitude larger than the background ambient flux. All of this must still be verified and discussed using LES.

Acknowledgements

I would like to express my deepest gratitude to those people who have supported me throughout my journey of completing this PhD thesis. Your encouragement, guidance, and contributions have been invaluable, and I am truly grateful for your continuous support.

First and foremost, I would like to express my heartfelt appreciation to my supervisor, Siegfried Raasch. Your mentorship, expertise, and dedication to my research have been essential in shaping the direction and quality of this thesis. Your insightful feedback, patience, and constant encouragement have been very useful, and I am deeply grateful for the opportunity to learn from you. Above all, the frequent discussions about the manuscripts to be published helped me a lot to develop further. Last but not least, I am very grateful for the various opportunities for a worldwide scientific exchange in form of workshops and conferences.

I would also like to express my sincere appreciation to my academic committee members, Siegfried Raasch, Björn Maronga, and Peter Knippertz. Your valuable feedback, constructive criticism, and scholarly insights have greatly enriched my work and helped me refine my research to the highest standards. Thank you also for the willingness to evaluate this work.

My heartfelt thanks also go to my colleagues, fellow researchers, and friends who have provided valuable discussions, feedback, and support during the course of my research. Your intellectual input, camaraderie, and encouragement have been a source of inspiration and motivation. I would like to give special thanks to Alice Loesch and Janis Klamt. The joint project work motivated me a lot and made things easier. In addition, special thanks goes to Manuel Dröse, Johannes Schwenkel, and Micha Gryschka for the proofreading of this thesis.

I am grateful to my family and wife for their unwavering support, love, and encouragement throughout my academic journey. Your belief in me, sacrifices, and understanding have been my pillar of strength, and I am deeply thankful for your constant motivation. Especially my wife helped me a lot with her patience and sympathy.

Special thanks also go to the Deutsche Forschungsgemeinschaft (DFG, German Research Foundation), which funded most of the work in this thesis under Grant RA 617/31-1.

Last but not least, I would like to express my heartfelt appreciation to all the participants who willingly participated in my research. Without their contribution, this thesis would not have been possible, and I am grateful for their time, effort, and willingness to share their insights, ideas and experiences.

Bibliography

- Alekseenko, S. V., Kuibin, P. A., and Okulov, V. L.: Theory of Concentrated Vortices, Springer, Berlin, Germany, 1 edn., doi:10.1007/978-3-540-73376-8, 2007.
- Ansmann, A., Tesche, M., Knippertz, P., Bierwirth, E., Althausen, D., Müller, D., and Schulz, O.: Vertical profiling of convective dust plumes in southern Morocco during SAMUM, *Tellus B: Chem. Phys. Meteorol.*, **61**, 340–353, doi:10.1111/j.1600-0889.2008.00384.x, 2009.
- Arakawa, A. and Lamb, V. R.: General Circulation Models of the Atmosphere, vol. 17 of *Methods in Computational Physics: Advances in Research and Applications*, chap. Computational design of the basic dynamical processes of the UCLA general circulation model, pp. 173–265, Academic Press, New York, NY, USA, doi:10.1016/B978-0-12-460817-7.50009-4, 1977.
- Argyropoulos, C. D. and Markatos, N. C.: Recent advances on the numerical modelling of turbulent flows, *Appl. Math. Model.*, **39**, 693–732, doi:10.1016/j.apm.2014.07.001, 2015.
- Baddock, M. C., Strong, C. L., Leys, J. F., Heidenreich, S. K., Tews, E. K., and McTainsh, G. H.: A visibility and total suspended dust relationship, *Atmos. Environ.*, **89**, 329–336, doi:10.1016/j.atmosenv.2014.02.038, 2014.
- Bailon-Cuba, J., Emran, M. S., and Schumacher, J.: Aspect ratio dependence of heat transfer and large-scale flow in turbulent convection, *J. Fluid Mech.*, **655**, 152–173, doi:10.1017/S0022112010000820, 2010.
- Balme, M. and Greeley, R.: Dust devils on Earth and Mars, *Rev. Geophys.*, **44**, RG3003, doi:10.1029/2005RG000188, 2006.
- Balme, M. and Hagermann, A.: Particle lifting at the soil-air interface by atmospheric pressure excursions in dust devils, *Geophys. Res. Lett.*, **33**, L19S01, doi:10.1029/2006GL026819, 2006.
- Balme, M., Metzger, S., Towner, M., Ringrose, T., Greeley, R., and Iversen, J.: Friction wind speeds in dust devils: A field study, *Geophys. Res. Lett.*, **30**, 1830, doi:10.1029/2003GL017493, 2003.
- Balme, M., Pathare, A., Metzger, S. M., Towner, M. C., Lewis, S. R., Spiga, A., Fenton, L. K., Renno, N., Elliott, H. M., Saca, F. A., Michaels, T. I., Russell, P., and Verdasca, J.: Field measurements of horizontal forward motion velocities of terrestrial dust devils: Towards a proxy for ambient winds on Mars and Earth, *Icarus*, **221**, 632–645, doi:10.1016/j.icarus.2012.08.021, 2012.
- Bangert, M., Nenes, A., Vogel, B., Vogel, H., Barahona, D., Karydis, V. A., Kumar, P., Kottmeier, C., and Blahak, U.: Saharan dust event impacts on cloud formation and radiation over Western Europe, *Atmos. Chem. Phys.*, **12**, 4045–4063, doi:10.5194/acp-12-4045-2012, 2012.

- Basu, S. and Lacser, A.: A Cautionary Note on the Use of Monin–Obukhov Similarity Theory in Very High-Resolution Large-Eddy Simulations, *Boundary-Layer Meteorol.*, **163**, 351–355, doi:10.1007/s10546-016-0225-y, 2017.
- Bluestein, H. B., Weiss, C. C., and Pazmany, A. L.: Doppler radar observations of dust devils in Texas, *Mon. Weather Rev.*, **132**, 209–224, doi:10.1175/1520-0493(2004)132<0209:DROODD>2.0.CO;2, 2004.
- Bristow, C. S., Hudson-Edwards, K. A., and Chappell, A.: Fertilizing the Amazon and equatorial Atlantic with West African dust, *Geophys. Res. Lett.*, **37**, L14 807, doi:10.1029/2010GL043486, 2010.
- Broersen, T.: Quantification of soil erosion by dust devil in the Jordan Badia, Master's thesis, Utrecht University, Utrecht, The Netherlands, 2013.
- Burgers, J. M.: A Mathematical Model Illustrating the Theory of Turbulence, *Adv. Appl. Mech.*, **1**, 171–199, doi:10.1016/S0065-2156(08)70100-5, 1948.
- Cantor, B. A., Kanak, K. M., and Edgett, K. S.: Mars Orbiter Camera observations of Martian dust devils and their tracks (September 1997 to January 2006) and evaluation of theoretical vortex models, *J. Geophys. Res. Planets*, **111**, E12 002, doi:10.1029/2006JE002700, 2006.
- Cao, Z.: Dynamics of Absolute Vorticity in the Boussinesq Fluid, *Adv. Atmos. Sci.*, **16**, 482–485, doi:10.1007/s00376-999-0025-0, 1999.
- Cao, Z. and Cho, H.-R.: Generation of Moist Potential Vorticity in Extratropical Cyclones, *J. Atmos. Sci.*, **52**, 3263–3282, doi:10.1175/1520-0469(1995)052<3263:GOMPVI>2.0.CO;2, 1995.
- Carroll, J. J. and Ryan, J. A.: Atmospheric vorticity and dust devil rotation, *J. Geophys. Res. Oceans Atmos.*, **75**, 5179–5184, doi:10.1029/JC075i027p05179, 1970.
- Chaibou, A. A. S., Ma, X., and Sha, T.: Dust radiative forcing and its impact on surface energy budget over West Africa, *Sci. Rep.*, **10**, 12 236, doi:10.1038/s41598-020-69223-4, 2020.
- Clark, T. L. and Farley, R. D.: Severe Downslope Windstorm Calculations in Two and Three Spatial Dimensions Using Anelastic Interactive Grid Nesting: A Possible Mechanism for Gustiness, *J. Atmos. Sci.*, **41**, 329–350, doi:10.1175/1520-0469(1984)041<0329:SDWCIT>2.0.CO;2, 1984.
- Cooley, J. R.: Dust Devil Meteorology, Technical Memorandum NWS CR-42, NOAA, Kansas City, MO, USA, 1971.
- Cormen, T. H., Leiserson, C. E., Rivest, R. L., and Stein, C.: Introduction to Algorithms, MIT Press, Cambridge, MA, USA, 3 edn., 2009.
- Cortese, T. and Balachandar, S.: Vortical nature of thermal plumes in turbulent convection, *Phys. Fluids A Fluid Dyn.*, **5**, 3226–3232, doi:10.1063/1.858679, 1993.

- Crozier, W. D.: Dust devil properties, *J. Geophys. Res. Oceans Atmos.*, **75**, 4583–4585, doi:10.1029/2006JE002700, 1970.
- Deardorff, J. W.: Stratocumulus-capped mixed layers derived from a three-dimensional model, *Boundary-Layer Meteorol.*, **18**, 495–527, doi:10.1007/BF00119502, 1980.
- DeMott, P. J., Sassen, K., Poellot, M. R., Baumgardner, D., Rogers, D. C., Brooks, S. D., Prenni, A. J., and Kreidenweis, S. M.: African dust aerosols as atmospheric ice nuclei, *Geophys. Res. Lett.*, **30**, 1732, doi:10.1029/2003GL017410, 2003.
- Dörenkämper, M., Witha, B., Steinfeld, G., Heinemann, D., and Kühn, M.: The impact of stable atmospheric boundary layers on wind-turbine wakes within offshore wind farms, *J. Wind. Eng. Ind. Aerodyn.*, **144**, 146–153, doi:10.1016/j.jweia.2014.12.011, 2015.
- Ellehoj, M. D., Gunnlaugsson, H. P., Taylor, P. A., Kahanpää, H., Bean, K. M., Cantor, B. A., Gheynani, B. T., Drube, L., Fisher, D., Harri, A.-M., Holstein-Rathlou, C., Lemmon, M. T., Madsen, M. B., Malin, M. C., Polkko, J., Smith, P. H., Tamppari, L. K., Weng, W., and Whiteway, J.: Convective vortices and dust devils at the Phoenix Mars mission landing site, *J. Geophys. Res. Planets*, **115**, E00E16, doi:10.1029/2009JE003413, 2010.
- Esposito, F., Molinaro, R., Popa, C. I., Molfese, C., Cozzolino, F., Marty, L., Taj-Eddine, K., Achille, G. D., Franzese, G., Silvestro, S., and Ori, G. G.: The role of the atmospheric electric field in the dust-lifting process, *Geophys. Res. Lett.*, **43**, 5501–5508, doi:10.1002/2016GL068463, 2016.
- Farrell, W. M., Smith, P. H., Delory, G. T., Hillard, G. B., Marshall, J. R., Catling, D., Hecht, M., Tratt, D. M., Renno, N., Desch, M. D., Cummer, S. A., Houser, J. G., and Johnson, B.: Electric and magnetic signatures of dust devils from the 2000–2001 MATADOR desert tests, *J. Geophys. Res. Planets*, **109**, E03 004, doi:10.1029/2003JE002088, 2004.
- Fenton, L., Reiss, D., Lemmon, M., Marticorena, B., Lewis, S., and Cantor, B.: Orbital Observations of Dust Lofted by Daytime Convective Turbulence, *Space Sci. Rev.*, **203**, 89–142, doi:10.1007/s11214-016-0243-6, 2016.
- Fiedler, B. H. and Kanak, K. M.: Rayleigh-Bénard convection as a tool for studying dust devils, *Atmos. Sci. Lett.*, **2**, 104–113, doi:10.1006/asle.2001.0043, 2001.
- Fisher, J. A., Richardson, M. I., Newman, C. E., Szwast, M. A., Graf, C., Basu, S., Ewald, S. P., Toigo, A. D., and Wilson, R. J.: A survey of Martian dust devil activity using Mars Global Surveyor Mars Orbiter Camera images, *J. Geophys. Res. Planets*, **110**, E03 004, doi:10.1029/2003JE002165, 2005.
- Frigo, M. and Johnson, S. G.: The Design and Implementation of FFTW3, in: Proceedings of the IEEE, vol. 93, pp. 216–231, IEEE, doi:10.1109/JPROC.2004.840301, 2005.
- Fröhlich, J. and von Terzi, D.: Hybrid LES/RANS methods for the simulation of turbulent flows, *Prog. Aerosp. Sci.*, **44**, 349–377, doi:10.1016/j.paerosci.2008.05.001, 2008.
- Fuerstenau, S. D.: Solar heating of suspended particles and the dynamics of Martian dust devils, *Geophys. Res. Lett.*, **33**, L19S03, doi:10.1029/2006GL026798, 2006.

- Fujiwara, C., Yamashita, K., Nakanishi, M., and Fujiyoshi, Y.: Dust Devil–Like Vortices in an Urban Area Detected by a 3D Scanning Doppler Lidar, *J. Appl. Meteorol. Climatol.*, **50**, 534–547, doi:10.1175/2010JAMC2481.1, 2011.
- García-Risueño, P. and Ibáñez, P. E.: A Review of High Performance Computing Foundations for Scientists, *Int. J. Mod. Phys. C*, **23**, 1230 001, doi:10.1142/S0129183112300011, 2012.
- Garrison, V. H., Shinn, E. A., Foreman, W. T., Griffin, D. W., Holmes, C. W., Kellogg, C. A., Majewski, M. S., Richardson, L. L., Ritchie, K. B., and Smith, G. W.: African and Asian Dust: From Desert Soils to Coral Reefs, *Bioscience*, **53**, 469–480, doi:10.1641/0006-3568(2003)053[0469:AAADFD]2.0.CO;2, 2003.
- Geissler, P. E.: Three decades of Martian surface changes, *J. Geophys. Res. Planets*, **110**, E02 001, doi:10.1029/2004JE002345, 2005.
- Gheynani, B. T. and Taylor, P. A.: Large-Eddy Simulations of Vertical Vortex Formation in the Terrestrial and Martian Convective Boundary Layers, *Boundary-Layer Meteorol.*, **137**, 223–235, doi:10.1007/s10546-010-9530-z, 2010.
- Giersch, S. and Raasch, S.: Evolution and Features of Dust Devil-Like Vortices in Turbulent Rayleigh–Bénard Convection — A Numerical Study Using Direct Numerical Simulation, *J. Geophys. Res. Atmos.*, **126**, e2020JD034 334, doi:10.1029/2020JD034334, 2021.
- Giersch, S. and Raasch, S.: How Do Dust Devil-Like Vortices Depend On Model Resolution? A Grid Convergence Study Using Large-Eddy Simulation, *Bound.-Layer Meteorol.*, **187**, 703–742, doi:10.1007/s10546-023-00792-3, 2023.
- Giersch, S., Brast, M., Hoffmann, F., and Raasch, S.: Toward Large-Eddy Simulations of Dust Devils of Observed Intensity: Effects of Grid Spacing, Background Wind, and Surface Heterogeneities, *J. Geophys. Res. Atmos.*, **124**, 7697–7718, doi:10.1029/2019JD030513, 2019.
- Greeley, R., Whelley, P. L., Arvidson, R. E., Cabrol, N. A., Foley, D. J., Franklin, B. J., Geissler, P. G., Golombek, M. P., Kuzmin, R. O., Landis, G. A., Lemmon, M. T., Neakrase, L. D. V., Squyres, S. W., and Thompson, S. D.: Active dust devils in Gusev crater, Mars: Observations from the Mars Exploration Rover Spirit, *J. Geophys. Res. Planets*, **111**, E12S09, doi:10.1029/2006JE002743, 2006.
- Gronemeier, T., Kanani-Sühring, F., and Raasch, S.: Do Shallow Cumulus Clouds have the Potential to Trigger Secondary Circulations Via Shading?, *Boundary-Layer Meteorol.*, **162**, 143–169, doi:10.1007/s10546-016-0180-7, 2017.
- Gropp, W., Lusk, E., and Skjellum, A.: Using MPI: Portable parallel programming with the Message Passing Interface, MIT Press, Cambridge, MA, USA, 2 edn., doi:10.7551/mitpress/7056.001.0001, 1999.
- Gu, Z., Zhao, Y., Y.Li, Yu, Y., and Feng, X.: Numerical Simulation of Dust Lifting within Dust Devils—Simulation of an Intense Vortex, *J. Atmos. Sci.*, **63**, 2630–2641, doi:10.1175/JAS3748.1, 2006.

- Gu, Z., Qiu, J., Zhao, Y., and LI, Y.: Simulation of Terrestrial Dust Devil Patterns, *Adv. Atmos. Sci.*, **25**, 31–42, doi:10.1007/s00376-008-0031-7, 2008.
- Hall, F. F.: Visibility reductions from soil dust in the Western U.S., *Atmos. Environ.*, **15**, 1929–1933, doi:10.1016/0004-6981(81)90227-4, 1981.
- Han, Y., Wang, K., Liu, F., Zhao, T., Yin, Y., Duan, J., and Luan, Z.: The contribution of dust devils and dusty plumes to the aerosol budget in western China, *Atmos. Environ.*, **126**, 21–27, doi:10.1016/j.atmosenv.2015.11.025, 2016.
- Harlow, F. H. and Welch, J. E.: Numerical Calculation of Time-Dependent Viscous Incompressible Flow of Fluid with Free Surface, *Phys. Fluids*, **8**, 2182, doi:10.1063/1.1761178, 1965.
- Heifetz, E., Maor, R., and Guha, A.: On the opposing roles of the Boussinesq and non-Boussinesq baroclinic torques in surface gravity wave propagation, *Q. J. R. Meteorol. Soc.*, **146**, 1056–1064, doi:10.1002/qj.3719, 2019.
- Hellsten, A., Ketelsen, K., Sührling, M., Auvinen, M., Maronga, B., Knigge, C., Barmpas, F., Tsegas, G., Moussiopoulos, N., and Raasch, S.: A nested multi-scale system implemented in the large-eddy simulation model PALM model system 6.0, *Geosci. Model Dev.*, **14**, 3185–3214, doi:10.5194/gmd-14-3185-2021, 2021.
- Hess, G. D. and Spillane, K. T.: Characteristics of dust devils in Australia, *J. Appl. Meteorol. Clim.*, **29**, 498–507, doi:10.1175/1520-0450(1990)029<0498:CODDIA>2.0.CO;2, 1990.
- Hess, G. D., Spillane, K. T., and Lourensz, R. S.: Atmospheric Vortices in Shallow Convection, *J. Appl. Meteorol.*, **27**, 305–317, 1988.
- Inagaki, A. and Kanda, M.: Use of Thermal Image Velocimetry to Measure a Dust-Devil-Like Vortex Within a Sports Ground in a Residential Area, *Boundary-Layer Meteorol.*, **183**, 125–141, doi:10.1007/s10546-021-00674-6, 2022.
- Ito, J., Niino, H., and Nakanishi, M.: Large Eddy Simulation on Dust Suspension in a Convective Mixed Layer, *SOLA*, **6**, 133–136, doi:10.2151/sola.2010-034, 2010a.
- Ito, J., Tanaka, R., Niino, H., and Nakanishi, M.: Large Eddy Simulation of Dust Devils in a Diurnally-Evolving Convective Mixed Layer, *J. Meteorol. Soc. Jpn.*, **88**, 63–77, doi:10.2151/jmsj.2010-105, 2010b.
- Ito, J., Niino, H., and Nakanishi, M.: Formation mechanism of dust devil-like vortices in idealized convective mixed layers, *J. Atmos. Sci.*, **70**, 1173–1186, doi:10.1175/JAS-D-12-085.1, 2013.
- Ives, R. L.: Behavior of Dust Devils, *Bull. Am. Meteorol. Soc.*, **28**, 168–174, doi:10.1175/1520-0477-28.4.168, 1947.
- Jackson, B., Lorenz, R., Davis, K., and Lipple, B.: Using an Instrumented Drone to Probe Dust Devils on Oregon’s Alvord Desert, *Remote Sens.*, **10**, 65, doi:10.3390/rs10010065, 2018.

- Jackson, B., Crevier, J., Szurgot, M., Battin, R., Perrin, C., and Rodriguez, S.: Inferring Vortex and Dust Devil Statistics from InSight, *Planet. Sci.*, **2**, 206, doi:10.3847/PSJ/ac260d, 2021.
- Jackson, T. L. and Farrell, W. M.: Electrostatic fields in dust devils: an analog to Mars, *IEEE Trans. Geosci. Remote Sens.*, **44**, 2942–2949, doi:10.1109/TGRS.2006.875785, 2006.
- Jemmett-Smith, B. C., Marsham, J. H., Knippertz, P., and Gilkeson, C. A.: Quantifying global dust devil occurrence from meteorological analyses, *Geophys. Res. Lett.*, **42**, 1275–1282, doi:10.1002/2015GL063078, 2015.
- Kaestner, C., Schneider, J. D., and du Puits, R.: Evolution and Features of Dust Devil-Like Vortices in Turbulent Rayleigh-Bénard Convection – An Experimental Study, *J. Geophys. Res. Atmos.*, **128**, e2022JD037466, doi:10.1029/2022JD037466, 2023.
- Kahanpää, H., Newman, C., Moores, J., Zorzano, M.-P., Martín-Torres, J., Navarro, S., Lepinette, A., Cantor, B., Lemmon, M. T., Valentín-Serrano, P., Ullán, A., and Schmidt, W.: Convective vortices and dust devils at the MSL landing site: Annual variability, *J. Geophys. Res. Planets*, **121**, 1514–1549, doi:10.1002/2016JE005027, 2016.
- Kahre, M. A., Murphy, J. R., and Haberle, R. M.: Modeling the Martian dust cycle and surface dust reservoirs with the NASA Ames general circulation model, *J. Geophys. Res. Planets*, **111**, E06008, doi:10.1029/2005JE002588, 2006.
- Kaimal, J. C. and Businger, J. A.: Case Studies of a Convective Plume and a Dust Devil, *J. Appl. Meteorol. Clim.*, **9**, 612–620, doi:10.1175/1520-0450(1970)009<0612:CSOACP>2.0.CO;2, 1970.
- Kanak, K. M.: Numerical simulation of dust devil-scale vortices, *Q. J. R. Meteorol. Soc.*, **131**, 1271–1292, doi:10.1256/qj.03.172, 2005.
- Kanak, K. M.: On the numerical simulation of dust devil-like vortices in terrestrial and martian convective boundary layers, *Geophys. Res. Lett.*, **33**, L19S05, doi:10.1029/2006GL026207, 2006.
- Kanak, K. M., Lilly, D. K., and Snow, J. T.: The formation of vertical vortices in the convective boundary layer, *Q. J. R. Meteorol. Soc.*, **126**, 2789–2810, doi:10.1002/qj.49712656910, 2000.
- Kanda, M., Inagaki, A., Miyamoto, T., Gryschka, M., and Raasch, S.: A New Aerodynamic Parametrization for Real Urban Surfaces, *Boundary-Layer Meteorol.*, **148**, 357–377, doi:10.1007/s10546-013-9818-x, 2013.
- Kellogg, C. A. and Griffin, D. W.: Aerobiology and the global transport of desert dust, *Trends Ecol. Evol.*, **21**, 638–644, doi:10.1016/j.tree.2006.07.004, 2006.
- Klamt, J., Giersch, S., and Raasch, S.: Saltation-Induced Dust Emission of Dust Devils in the Convective Boundary Layer - An LES Study on the Meter Scale, *J. Geophys. Res. Atmos.*, **129**, e2023JD040058, doi:10.1029/2023JD040058, 2024.
- Klose, M. and Shao, Y.: A numerical study on dust devils with implications to global dust budget estimates, *Aeolian Res.*, **22**, 47–58, doi:10.1016/j.aeolia.2016.05.003, 2016.

- Klose, M., Jemmett-Smith, B. C., Kahanpää, H., Kahre, M., Knippertz, P., Lemmon, M. T., Lewis, S. R., Lorenz, R. D., Neakrase, L. D. V., Newman, C., Patel, M. R., Reiss, D., Spiga, A., and Whelley, P. L.: Dust Devil Sediment Transport: From Lab to Field to Global Impact, *Space Sci. Rev.*, **203**, 377–426, doi:10.1007/s11214-016-0261-4, 2016.
- Koch, J. and Renno, N. O.: The role of convective plumes and vortices on the global aerosol budget, *Geophys. Res. Lett.*, **32**, L18 806, doi:10.1029/2005GL023420, 2005.
- Kok, J. F. and Renno, N. O.: Enhancement of the emission of mineral dust aerosols by electric forces, *Geophys. Res. Lett.*, **33**, L19S10, doi:10.1029/2006GL026284, 2006.
- Kurgansky, M. V.: Size distribution of dust devils in the atmosphere, *Izv. Atmos. Ocean. Phys.*, **42**, 319–325, doi:10.1134/S0001433806030054, 2006.
- Kurgansky, M. V., Montecinos, A., Villagran, V., and Metzger, S. M.: Micrometeorological Conditions for Dust-Devil Occurrence in the Atacama Desert, *Boundary-Layer Meteorol.*, **138**, 285–298, doi:10.1007/s10546-010-9549-1, 2011.
- Kurgansky, M. V., Lorenz, R. D., Rennó, N. O., Takemi, T., Gu, Z., and Wei, W.: Dust Devil Steady-State Structure from a Fluid Dynamics Perspective, *Space Sci. Rev.*, **203**, 209–244, doi:10.1007/s11214-016-0281-0, 2016.
- Lamberth, R. L.: on the measurement of dust devil parameters, *Bull. Am. Meteorol. Soc.*, **47**, 522–526, doi:10.1175/1520-0477-47.7.522, 1966.
- Leslie, F. W.: Surface Roughness Effects on Suction Vortex Formation: A Laboratory Simulation, *J. Atmos. Sci.*, **34**, 1022–1027, doi:10.1175/1520-0469(1977)034<1022:SREOSV>2.0.CO;2, 1977.
- Lilly, D. K.: The Representation of Sall-Scale Turbulence In Numerical Simulation Experiments, Technical Memorandum 281, NCAR, Boulder, CO, USA, doi:10.5065/D62R3PMM, 1966.
- Loesch, A. and du Puits, R.: The Barrel of Ilmenau: A large-scale convection experiment to study dust devil-like flow structures, *Meteorol. Zeitschrift*, **30**, 89–97, doi:10.1127/metz/2020/1046, 2021.
- Lorenz, R. D.: On the statistical distribution of dust devil diameters, *Icarus*, **215**, 381–390, doi:10.1016/j.icarus.2011.06.005, 2011.
- Lorenz, R. D.: Observing desert dust devils with a pressure logger, *Geosci. Instrum. Methods Data Syst.*, **1**, 209–220, doi:10.5194/gi-1-209-2012, 2012.
- Lorenz, R. D.: The longevity and aspect ratio of dust devils: Effects on detection efficiencies and comparison of landed and orbital imaging at Mars, *Icarus*, **226**, 964–970, doi:10.1016/j.icarus.2013.06.031, 2013.
- Lorenz, R. D.: Vortex Encounter Rates with Fixed Barometer Stations: Comparison with Visual Dust Devil Counts and Large-Eddy Simulations, *J. Atmos. Sci.*, **71**, 4461–4472, doi:10.1175/JAS-D-14-0138.1, 2014.

- Lorenz, R. D.: Heuristic estimation of dust devil vortex parameters and trajectories from single-station meteorological observations: Application to InSight at Mars, *Icarus*, **271**, 326–337, doi:10.1016/j.icarus.2016.02.001, 2016.
- Lorenz, R. D. and Jackson, B. K.: Dust devils and dustless vortices on a desert playa observed with surface pressure and solar flux logging, *GeoResJ*, **5**, 1–11, doi:10.1016/j.grj.2014.11.002, 2015.
- Lorenz, R. D. and Jackson, B. K.: Dust Devil Populations and Statistic, *Space Sci. Rev.*, **203**, 277–297, doi:10.1007/s11214-016-0277-9, 2016.
- Lorenz, R. D. and Lanagan, P. D.: A Barometric Survey of Dust-Devil Vortices on a Desert Playa, *Boundary-Layer Meteorol.*, **153**, 555–568, doi:10.1007/s10546-014-9954-y, 2014.
- Lorenz, R. D. and Myers, M. J.: DUST DEVIL HAZARD TO AVIATION A REVIEW OF UNITED STATES AIR ACCIDENT REPORTS, *J. Meteorol.*, **30**, 178–184, 2005.
- Lorenz, R. D., Balme, M. R., Gu, Z., Kahanpää, H., Klose, M., Kurgansky, M. V., Patel, M. R., Reiss, D., Rossi, A. P., Spiga, A., Takemi, T., and Wei, W.: History and Applications of Dust Devil Studies, *Space Sci. Rev.*, **203**, 5–37, doi:10.1007/s11214-016-0239-2, 2016.
- Luan, Z., Han, Y., Zhao, T., Liu, F., Liu, C., Rood, M. J., Yang, X., He, Q., and Lu, H.: Dust opacities inside the dust devil column in the Taklimakan Desert, *Atmos. Meas. Tech.*, **10**, 273–279, doi:10.5194/amt-10-273-2017, 2017.
- Lyons, T. J., Nair, U. S., and Foster, I. J.: Clearing enhances dust devil formation, *J. Arid Environ.*, **72**, 1918–1928, doi:10.1016/j.jaridenv.2008.05.009, 2008.
- Maronga, B. and Raasch, S.: Large-Eddy Simulations of Surface Heterogeneity Effects on the Convective Boundary Layer During the LITFASS-2003 Experiment, *Boundary-Layer Meteorol.*, **146**, 17–44, doi:10.1007/s10546-012-9748-z, 2013.
- Maronga, B., Gryschka, M., Heinze, R., Hoffmann, F., Kanani-Sühring, F., Keck, M., Ketelsen, K., Letzel, M. O., Sühring, M., and Raasch, S.: The Parallelized Large-Eddy Simulation Model (PALM) version 4.0 for atmospheric and oceanic flows: model formulation, recent developments, and future perspectives, *Geosci. Model Dev.*, **8**, 2515–2551, doi:10.5194/gmd-8-2515-2015, 2015.
- Maronga, B., Banzhaf, S., Burmeister, C., Esch, T., Forkel, R., Fröhlich, D., Fuka, V., Gehrke, K. F., Geletic, J., Giersch, S., Gronemeier, T., Groß, G., Heldens, W., Hellsten, A., Hoffmann, F., Inagaki, A., Kadasch, E., Kanani-Sühring, F., Ketelsen, K., Khan, B. A., Knigge, C., Knoop, H., Krc, P., Kurppa, M., Maamari, H., Matzarakis, A., Mauder, M., Pallasch, M., Pavlik, D., Pfafferott, J., Resler, J., Rissmann, S., Russo, E., Salim, M., Schrempf, M., Schwenkel, J., Seckmeyer, G., Schubert, S., Sühring, M., von Tils, R., Vollmer, L., Ward, S., Witha, B., Wurps, H., Zeidler, J., and Raasch, S.: Overview of the PALM model system 6.0, *Geosci. Model Dev.*, **13**, 1335–1372, doi:10.5194/gmd-13-1335-2020, 2020a.
- Maronga, B., Knigge, C., and Raasch, S.: An Improved Surface Boundary Condition for Large-Eddy Simulations Based on Monin–Obukhov Similarity Theory: Evaluation and

- Consequences for Grid Convergence in Neutral and Stable Conditions, *Bound.-Layer Meteorol.*, **174**, 297–325, doi:10.1007/s10546-019-00485-w, 2020b.
- Mason, P. J.: Large-Eddy Simulation of the Convective Atmospheric Boundary Layer, *J. Atmos. Sci.*, **46**, 1492–1516, doi:10.1175/1520-0469(1989)046<1492:LESOTC>2.0.CO;2, 1989.
- Mellado, J. P.: Direct numerical simulation of free convection over a heated plate, *J. Fluid Mech.*, **712**, 418–450, doi:10.1017/jfm.2012.428, 2012.
- Mellado, J. P., Bretherton, C. S., Stevens, B., and Wyant, M. C.: DNS and LES for Simulating Stratocumulus: Better Together, *J. Adv. Model. Earth Syst.*, **10**, 1421–1438, doi:10.1029/2018MS001312, 2018.
- Metzger, S. M., Carr, J. R., Johnson, J. R., Parker, T. J., and Lemmon, M. T.: Dust devil vortices seen by the Mars Pathfinder Camera, *Geophys. Res. Lett.*, **26**, 2781–2784, doi:10.1029/1999GL008341, 1999.
- Metzger, S. M., Balme, M. R., Towner, M. C., Bos, B. J., Ringrose, T. J., and Patel, M. R.: In situ measurements of particle load and transport in dust devils, *Icarus*, **214**, 766–772, doi:10.1016/j.icarus.2011.03.013, 2011.
- Miller, R. L., Knippertz, P., García-Pando, C. P., Perlwitz, J. P., and Tegen, I.: Mineral Dust, chap. Impact of Dust Radiative Forcing upon Climate, pp. 327–357, Springer, Dordrecht, The Netherlands, doi:10.1007/978-94-017-8978-3_13, 2014.
- Moeng, C.-H. and Wyngaard, J. C.: Spectral Analysis of Large-Eddy Simulations of the Convective Boundary Layer, *J. Atmos. Sci.*, **45**, 3573–3587, doi:10.1175/1520-0469(1988)045<3573:SAOLES>2.0.CO;2, 1988.
- Mortan, B. R.: Geophysical vortices, *Prog. Aerosp. Sci.*, **7**, 145–194, doi:10.1016/0376-0421(66)90008-X, 1966.
- Mullen, J. B. and Maxworthy, T.: A laboratory model of dust devil vortices, *Dyn. Atmos. Oceans*, **1**, 181–214, doi:10.1016/0377-0265(77)90006-9, 1977.
- Murphy, J., Steakley, K., Balme, M., Deprez, G., Esposito, F., Kahanpää, H., Lemmon, M., Lorenz, R., Murdoch, N., Neakrase, L., Patel, M., and Whelley, P.: Field Measurements of Terrestrial and Martian Dust Devils, *Space Sci. Rev.*, **203**, 39–87, doi:10.1007/s11214-016-0283-y, 2016.
- Neakrase, L. D. V. and Greeley, R.: Dust devils in the laboratory: Effect of surface roughness on vortex dynamics, *J. Geophys. Res. Planets*, **115**, E05 003, doi:10.1029/2009JE003465, 2010.
- Newman, C. E., Lewis, S. R., Read, P. L., and Forget, F.: Modeling the Martian dust cycle, 1. Representations of dust transport processes, *J. Geophys. Res. Planets*, **107**, 6–1–6–18, doi:10.1029/2002JE001910, 2002.
- Nishizawa, S., Odaka, M., Takahashi, Y. O., Sugiyama, K., Nakajima, K., Ishiwatari, M., Takehiro, S., Yashiro, H., Sato, Y., Tomita, H., and Hayashi, Y.-Y.: Martian dust devil statistics from high-resolution large-eddy simulations, *Geophys. Res. Lett.*, **43**, 4180–4188, doi:10.1002/2016GL068896, 2016.

- Noh, Y., Min, H. S., and Raasch, S.: Large Eddy Simulation of the Ocean Mixed Layer: The Effects of Wave Breaking and Langmuir Circulation, *J. Phys. Oceanogr.*, **34**, 720–735, doi:10.1175/1520-0485(2004)034<0720:LESOTO>2.0.CO;2, 2004.
- Ohno, H. and Takemi, T.: Mechanisms for intensification and maintenance of numerically simulated dust devils, *Atmos. Sci. Lett.*, **11**, 27–32, doi:10.1002/asl.249, 2010a.
- Ohno, H. and Takemi, T.: Numerical Study for the Effects of Mean Wind on the Intensity and Evolution of Dust Devils, *SOLA*, **6A**, 5–8, doi:10.2151/sola.6A-002, 2010b.
- Oke, A. M. C., Tapper, N. J., and Dunkerley, D.: Willy-willies in the Australian landscape: The role of key meteorological variables and surface conditions in defining frequency and spatial characteristics, *J. Arid Environ.*, **71**, 201–215, doi:10.1016/j.jaridenv.2007.03.008, 2007.
- Oncley, S. P., Hartogensis, O., and Tong, C.: Whirlwinds and Hairpins in the Atmospheric Surface Layer, *J. Atmos. Sci.*, **73**, 4927–4943, doi:10.1175/JAS-D-15-0368.1, 2016.
- Onishchenko, O., Fedun, V., Horton, W., Pokhotelov, O., and Verth, G.: Dust Devils: Structural Features, Dynamics and Climate Impact, *Climate*, **7**, 12, doi:10.3390/cli7010012, 2019.
- Onishchenko, O., Fedun, V., Horton, W., Pokhotelov, O., Astafieva, N., Skirvin, S. J., and Verth, G.: The Stationary Concentrated Vortex Model, *Climate*, **9**, 39, doi:10.3390/cli9030039, 2021.
- Pan, L., Han, Y., Lu, Z., Li, J., Gao, F., Liu, Z., Liu, W., and Liu, Y.: Integrative investigation of dust emissions by dust storms and dust devils in North Africa, *Sci. Total Environ.*, **756**, 144 128, doi:10.1016/j.scitotenv.2020.144128, 2021.
- Pandey, A., Scheel, J. D., and Schumacher, J.: Turbulent superstructures in Rayleigh-Bénard convection, *Nat. Commun.*, **9**, 2118, doi:10.1038/s41467-018-04478-0, 2018.
- Patrinos, A. A. N. and Kistler, A. L.: A numerical study of the Chicago lake breeze, *Boundary-Layer Meteorol.*, **12**, 93–123, doi:10.1007/BF00116400, 1977.
- Piacsek, S. A. and Williams, G. P.: Conservation properties of convection difference schemes, *J. Comput. Phys.*, **6**, 392–405, doi:10.1016/0021-9991(70)90038-0, 1970.
- Pope, S. B.: *Turbulent Flows*, Cambridge University Press, New York, NY, USA, 1 edn., doi:10.1017/CBO9780511840531, 2000.
- Raasch, S. and Franke, T.: Structure and formation of dust devil-like vortices in the atmospheric boundary layer: A high-resolution numerical study, *J. Geophys. Res. Atmos.*, **116**, D16 120, doi:10.1029/2011JD016010, 2011.
- Raasch, S. and Schröter, M.: PALM - A large-eddy simulation model performing on massively parallel computers, *Meteorol. Zeitschrift*, **10**, 363–372, doi:10.1127/0941-2948/2001/0010-0363, 2001.
- Rafkin, S., Jemmett-Smith, B., Fenton, L., Lorenz, R., Takemi, T., Ito, J., and Tyler, D.: Dust Devil Formation, *Space Sci. Rev.*, **203**, 183–207, doi:10.1007/s11214-016-0307-7, 2016.

- Rankine, W. J. M.: A Manual of Applied Mechanics, Charles Griffin and Company, London, United Kingdom, 4 edn., 1868.
- Reiss, D.: First Observations of Terrestrial Dust Devils in Orbital Image Data: Comparison with Dust Devils in Amazonis Planitia, Mars, in: 47th Lunar and Planetary Science Conference, Abstract 2912, The Woodlands, TX, USA, 21–25 March, 2016.
- Reiss, D., Fenton, L., Neakrase, L., Zimmerman, M., Statella, T., Whelley, P., Rossi, A. P., and Balme, M.: Dust Devil Tracks, *Space Sci. Rev.*, **203**, 143–181, doi:10.1007/s11214-016-0308-6, 2016.
- Rennó, N. O. and Ingersoll, A. P.: Natural Convection as a Heat Engine: A Theory for CAPE, *J. Atmos. Sci.*, **53**, 572–585, doi:10.1175/1520-0469(1996)053<0572:NCAAHE>2.0.CO;2, 1996.
- Rennó, N. O., Burkett, M. L., and Larkin, M. P.: A Simple Thermodynamical Theory for Dust Devils, *J. Atmos. Sci.*, **55**, 3244–3252, doi:10.1175/1520-0469(1998)055<3244:ASTTFD>2.0.CO;2, 1998.
- Rennó, N. O., Nash, A. A., Lunine, J., and Murphy, J.: Martian and terrestrial dust devils: Test of a scaling theory using Pathfinder data, *J. Geophys. Res. Planets*, **105**, 1859–1865, doi:10.1029/1999JE001037, 2000.
- Rennó, N. O., Abreu, V. J., Koch, J., Smith, P. H., Hartogensis, O. K., Bruin, H. A. R. D., Burose, D., Delory, G. T., Farrell, W. M., Watts, C. J., Garatuza, J., Parker, M., and Carswell, A.: MATADOR 2002: A pilot field experiment on convective plumes and dust devils, *J. Geophys. Res. Planets*, **109**, E07 001, doi:10.1029/2003JE002219, 2004.
- Rott, N. R.: On the viscous core of a line vortex, *Z. Angew. Math. Phys.*, **9**, 543–553, doi:10.1007/BF02424773, 1958.
- Ryan, J. A.: Relation of dust devil frequency and diameter to atmospheric temperature, *J. Geophys. Res. Oceans Atmos.*, **77**, 7133–7137, doi:10.1029/JC077i036p07133, 1972.
- Ryan, J. A. and Carroll, J. J.: Dust devil wind velocities: Mature state, *J. Geophys. Res. Oceans Atmos.*, **75**, 531–541, doi:10.1029/JC075i003p00531, 1970.
- Ryan, J. A. and Lucich, R. D.: Possible dust devils, vortices on Mars, *J. Geophys. Res. Oceans*, **88**, 11 005–11 011, doi:10.1029/JC088iC15p11005, 1983.
- Saiki, E. M., Moeng, C.-H., and Sullivan, P. P.: Large-eddy simulation of the stably stratified planetary boundary layer, *Boundary-Layer Meteorol.*, **95**, 1–30, doi:10.1023/A:1002428223156, 2000.
- Sarkar, S.: 50 Years of CFD in Engineering Sciences, chap. Large Eddy Simulation of Flows of Engineering Interest: A Review, pp. 363–400, Springer, Singapore, Republic of Singapore, doi:10.1007/978-981-15-2670-1_11, 2020.
- Schepanski, K.: Transport of Mineral Dust and Its Impact on Climate, *Geosci.*, **8**, 151, doi:10.3390/geosciences8050151, 2018.

- Scherer, D., Fehrenbach, U., Grassmann, T., Holtmann, A., Meier, F., Scherber, K., Pavlik, D., Höhne, T., Kanani-Sühring, F., Maronga, B., Ament, F., Banzhaf, S., Langer, I., Halbig, G., Kohler, M., Queck, R., Stratbücker, S., Winkler, M., Wegener, R., and Zeeman, M.: [UC]² Data Standard "Urban Climate under Change", Technical Report 1.4.1, Federal Ministry of Education and Research, Berlin, Germany, 2020.
- Schlichting, H. and Gersten, K.: *Grenzschicht-Theorie*, Springer, Berlin, Germany, 10 edn., doi:10.1007/3-540-32985-4, 2006.
- Schmidt, H. and Schumann, U.: Coherent structure of the convective boundary layer derived from large-eddy simulations, *J. Fluid Mech.*, **200**, 511–562, doi:10.1017/S0022112089000753, 1989.
- Schumann, U.: Subgrid scale model for finite difference simulations of turbulent flows in plane channels and annuli, *J. Comput. Phys.*, **18**, 376–404, doi:10.1016/0021-9991(75)90093-5, 1975.
- Schumann, U. and Sweet, R. A.: Fast Fourier transforms for direct solution of poisson's equation with staggered boundary conditions, *J. Comput. Phys.*, **75**, 123–137, doi:10.1016/0021-9991(88)90102-7, 1988.
- Shao, Y., Wyrwoll, K.-H., Chappell, A., Huang, J., Lin, Z., McTainsh, G. H., Mikami, M., Tanaka, T. Y., Wang, X., and Yoon, S.: Dust cycle: An emerging core theme in Earth system science, *Aeolian Res.*, **2**, 181–204, doi:10.1016/j.aeolia.2011.02.001, 2011.
- Shinn, E. A., Smith, G. W., Prospero, J. M., Betzer, P., Hayes, M. L., Garrison, V., and Barb, R. T.: African Dust and the Demise of Caribbean Coral Reefs, *Geophys. Res. Lett.*, **27**, 3029–3032, doi:10.1029/2000GL011599, 2000.
- Sinclair, P. C.: Some preliminary dust devil measurements, *Mon. Weather Rev.*, **92**, 363–367, doi:10.1175/1520-0493(1964)092<0363:SPDDM>2.3.CO;2, 1964.
- Sinclair, P. C.: General Characteristics of Dust Devils, *J. Appl. Meteorol. Clim.*, **8**, 32–45, doi:10.1175/1520-0450(1969)008<0032:GCODD>2.0.CO;2, 1969.
- Sinclair, P. C.: The Lower Structure of Dust Devils, *J. Atmos. Sci.*, **30**, 1599–1619, doi:10.1175/1520-0469(1973)030<1599:TLSODD>2.0.CO;2, 1973.
- Smagorinsky, J.: GENERAL CIRCULATION EXPERIMENTS WITH THE PRIMITIVE EQUATIONS, *Mon. Weather Rev.*, **91**, 99–164, doi:10.1175/1520-0493(1963)091<0099:GCEWTP>2.3.CO;2, 1963.
- Snow, J. T. and McClelland, T. M.: Dust devils at White Sands Missile Range, New Mexico: 1. Temporal and spatial distributions, *J. Geophys. Res. Atmos.*, **95**, 13 707–13 721, doi:10.1029/JD095iD09p13707, 1990.
- Souza, E. P., Rennó, N. O., and Dias, M. A. F. S.: Convective Circulations Induced by Surface Heterogeneities, *J. Atmos. Sci.*, **57**, 2915–2922, doi:10.1175/1520-0469(2000)057<2915:CCIBSH>2.0.CO;2, 2000.

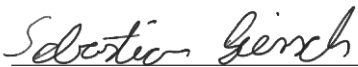
- Spiga, A., Barth, E., Gu, Z., Hoffmann, F., Ito, J., Jemmett-Smith, B., Klose, M., Nishizawa, S., Raasch, S., Rafkin, S., Takemi, T., Tyler, D., and Wei, W.: Large-Eddy Simulations of Dust Devils and Convective Vortices, *Space Sci. Rev.*, **203**, 245–275, doi:10.1007/s11214-016-0284-x, 2016.
- Steakley, K. and Murphy, J.: A year of convective vortex activity at Gale crater, *Icarus*, **278**, 180–193, doi:10.1016/j.icarus.2016.06.010, 2016.
- Stull, R. B.: An Introduction to Boundary Layer Meteorology, Kluwer Academic Publishers, Dordrecht, The Netherlands, 1 edn., doi:10.1007/978-94-009-3027-8, 1988.
- Sullivan, P. P. and Patton, E. G.: The Effect of Mesh Resolution on Convective Boundary Layer Statistics and Structures Generated by Large-Eddy Simulation, *J. Atmos. Sci.*, **68**, 2395–2415, doi:10.1175/JAS-D-10-05010.1, 2011.
- Sultanian, B.: Gas Turbines - Internal Flow Systems Modeling, chap. Appendix E - Thomas Algorithm for Solving a Tridiagonal System of Linear Algebraic Equations, pp. 337–339, Cambridge University Press, New York, NY, USA, doi:10.1017/9781316755686.012, 2018.
- Tang, Y., Han, Y., and Liu, Z.: Temporal and spatial characteristics of dust devils and their contribution to the aerosol budget in East Asia—An analysis using a new parameterization scheme for dust devils, *Atmos. Environ.*, **182**, 225–233, doi:10.1016/j.atmosenv.2018.03.050, 2018.
- Thorne, S. N., Johnson, C. L., Mittelholz, A., Langlais, B., Lorenz, R., Murdoch, N., Spiga, A., Smrekar, S. E., and Banerdt, W. B.: Investigation of magnetic field signals during vortex-induced pressure drops at InSight, *Planet. Space Sci.*, **217**, 105487, doi:10.1016/j.pss.2022.105487, 2022.
- Toigo, A. D., Richardson, M. I., Ewald, S. P., and Gierasch, P. J.: Numerical simulation of Martian dust devils, *J. Geophys. Res. Planets*, **108**, 5047, doi:10.1029/2002JE002002, 2003.
- Tratt, D. M., Hecht, M. H., Catling, D. C., Samulon, E. C., and Smith, P. H.: In situ measurement of dust devil dynamics: Toward a strategy for Mars, *J. Geophys. Res. Planets*, **108**, 5116, doi:10.1029/2003JE002161, 2003.
- Tsinober, A., ed.: An Informal Conceptual Introduction to Turbulence, chap. Introduction, pp. 1–33, Fluid Mechanics and Its Applications, vol 92, Springer, Dordrecht, The Netherlands, doi:10.1007/978-90-481-3174-7_1, 2009.
- Vatistas, G. H., Kozel, V., and Mih, W. C.: A simpler model for concentrated vortices, *Exp. Fluids*, **11**, 73–76, doi:10.1007/BF00198434, 1991.
- von Hardenberg, J., Parodi, A., Passoni, G., Provenzale, A., and Spiegel, E. A.: Large-scale patterns in Rayleigh–Bénard convection, *Phys. Lett. A*, **13**, 2223–2229, doi:10.1016/j.physleta.2007.10.099, 2008.
- Wakimoto, R. M. and Liu, C.: The Garden City, Kansas, Storm during VORTEX 95. Part II: The Wall Cloud and Tornado, *Mon. Weather Rev.*, **126**, 393–408, doi:10.1175/1520-0493(1998)126<0393:TGCKSD>2.0.CO;2, 1998.

- Wicker, L. J. and Skamarock, W. C.: Time-Splitting Methods for Elastic Models Using Forward Time Schemes, *Mon. Weather Rev.*, **130**, 2088–2097, doi:10.1175/1520-0493(2002)130<2088:TSMFEM>2.0.CO;2, 2002.
- Wilkins, E. M., Sasaki, Y., and Johnson, H. L.: Surface Friction Effects on Thermal Convection in a Rotating Fluid: A Laboratory Simulation, *Mon. Weather Rev.*, **103**, 305–317, doi:10.1175/1520-0493(1975)103<0305:SFEOTC>2.0.CO;2, 1975.
- Williams, N. R.: Development of Dust Whirls and Similar Small-Scale Vortices, *Bull. Am. Meteorol. Soc.*, **29**, 106–117, doi:10.1175/1520-0477-29.3.106, 1948.
- Williamson, J. H.: Low-storage Runge-Kutta schemes, *J. Comput. Phys.*, **35**, 48–56, doi:10.1016/0021-9991(80)90033-9, 1980.
- Wyett, R. E.: PRESSURE DROP IN A DUST DEVIL, *Mon. Weather Rev.*, **82**, 7–8, doi:10.1175/1520-0493(1954)082<0007:PDIADD>2.0.CO;2, 1954.
- Wyngaard, J. C.: Turbulence in the Atmosphere, Cambridge University Press, New York, NY, USA, 1 edn., doi:10.1017/CBO9780511840524, 2010.
- Xie, Z. and Castro, I. P.: LES and RANS for Turbulent Flow over Arrays of Wall-Mounted Obstacles, *Flow Turbul. Combust.*, **76**, 291–312, doi:10.1007/s10494-006-9018-6, 2006.
- Zhang, M., Luo, X., Li, T., Zhang, L., Meng, X., Kase, K., Wada, S., Yu, C. W., and Gu, Z.: From Dust Devil to Sustainable Swirling Wind Energy, *Sci. Rep.*, **5**, 8322, doi:10.1038/srep08322, 2015.
- Zhao, Y. Z., Gu, Z. L., Yu, Y. Z., Ge, Y., Li, Y., and Feng, X.: Mechanism and large eddy simulation of dust devils, *Atmos.-Ocean*, **42**, 61–84, doi:10.3137/ao.420105, 2004.

Declaration

I hereby declare that

1. I am familiar with and have complied with the rules of the applicable doctoral regulations and agree to be examined in accordance with the provisions of the doctoral regulations,
2. I have written the dissertation myself, that I have not taken over any text sections from third parties or from my own examination papers without marking them, and that I have indicated all aids and sources used in the work,
3. the scientific work has not been acquired or procured in whole or in part by third parties in return for payment or other consideration,
4. the dissertation has not yet been submitted as a paper for any other examination,
5. the same or a substantially similar thesis has not been submitted as a dissertation to another faculty or to another university, and that another paper has not been submitted as a dissertation elsewhere,
6. the dissertation is being subjected to a review of compliance with generally accepted scientific standards.



Sebastian Giersch
PhD candidate

Hannover, 4. April 2024

Curriculum Vitae

This CV contains all the information about the scientific career.

Personal Details

Name	Sebastian Giersch
Place of residence	Gerstenweg 2, 31867 Lauenau
Date of Birth	05.04.1992
Birthplace	Bielefeld, Germany
Nationality	German

Career

2017 – 2024	Research associate at Leibniz University Hannover, Hannover, Germany.
2013 – 2017	Student assistant at Leibniz University Hannover, Hannover, Germany.
2015	Student internship at Meteorological Observatory Lindenberg (German Weather Service), Lindenberg, Germany.
2013	Student internship at Meteomedia GmbH Bochum, Bochum, Germany.

Education

2018 – 2023	Ph.D. student, Leibniz University Hannover, Germany.
2014 – 2017	M.Sc. in Meteorology (1,2), Leibniz University Hannover, Germany.
2011 – 2014	B.Sc. in Meteorology (1,5), Leibniz University Hannover, Germany.

Scholarships

2016	Japan Student Services Organization (JASSO) scholarship for a short-term study program at the National Institute of Technology in Gifu, Japan.
------	--

Awards and Certificates

- 2021 University Didactic Certificate Program Pro Lehre - Professional planning, design and implementation of courses, Leibniz University Hannover, Hannover, Germany.
- 2019 Promotion plus+ qualifiziert - Obtaining Management Competencies for Careers Outside of Academia, Leibniz University Hannover, Hannover, Germany.
- 2017 Karl-Doetsch-Nachwuchspreis (an award for junior scientists) issued by the Aeronautics Research Centre Niedersachsen, 22 November 2017, Braunschweig, Germany.
- 2016 Best oral presentation at the Fifth International Education Forum on Environment and Energy Science, 15 – 19 December 2016, San Diego, CA, USA.

Publications and Academic Work

Journals

- Klamt, J., and Giersch, S., and Raasch, S.: Saltation-Induced Dust Emission of Dust Devils in the Convective Boundary Layer - An LES Study on the Meter Scale, *J. Geophys. Res. Atmos.*, **129**, e2023JD040058, doi:10.1029/2023JD040058, 2024.
- Giersch, S., and Raasch, S.: How Do Dust Devil-Like Vortices Depend On Model Resolution? A Grid Convergence Study Using Large-Eddy Simulation, *Bound.-Layer Meteorol.*, **187**, 703–742, doi:10.1007/s10546-023-00792-3, 2023.
- Giersch, S., El Guernaoui, O., Raasch, S., Sauer, M., and Palomar, M.: Atmospheric flow simulation strategies to assess turbulent wind conditions for safe drone operations in urban environments, *J. Wind. Eng. Ind.*, **229**, 105136, doi:10.1016/j.jweia.2022.105136, 2022.
- Giersch, S., and Raasch, S.: Evolution and Features of Dust Devil-Like Vortices in Turbulent Rayleigh-Bénard Convection — A Numerical Study Using Direct Numerical Simulation, *J. Geophys. Res. Atmos.*, **126**, e2020JD034334, doi:10.1029/2020JD034334, 2021.
- Maronga, B., Banzhaf, S., Burmeister, C., Esch, T., Forkel, R., Fröhlich, D., Fuka, V., Gehrke, K. F., Geletic, J., Giersch S., Gronemeier, T., Groß, G., Heldens, W., Hellsten, A., Hoffmann, F., Inagaki A., Kadasch, E., Kanani-Sühring, F., Ketelsen, K., Khan, B. A., Knigge, C., Knoop, H., Krc, P., Kurppa, M., Maamari H., Matzarakis, A., Mauder, M., Pallasch, M., Pavlik, D., Pfafferott, J., Resler, J., Rissmann, S., Russo, E., Salim, M., Schrempf, M., Schwenkel, J., Seckmeyer, G., Schubert, S., Sühring, M., von Tils, R., Vollmer, L., Ward, S., Witha, B., Wurps, H., Zeidler, J., and Raasch, S.: Overview of the PALM model system 6.0, *Geosci. Model Dev.*, **13**, 1335–1372, doi:10.5194/gmd-13-1335-2020, 2020.

Giersch, S., Brast, M., Hoffmann, F., and Raasch, S.: Toward Large-Eddy Simulations of Dust Devils of Observed Intensity: Effects of Grid Spacing, Background Wind, and Surface Heterogeneities, *J. Geophys. Res. Atmos.*, **124**, 7697–7718, doi:10.1029/2019JD030513, 2019.

Conference and Workshop Contributions

Giersch, S., and Raasch, S.: Resolution Requirements for the Numerical Simulation of Atmospheric Dust Devil-like Structures in Convective Boundary Layers Using Large-Eddy Simulation - a Grid Convergence Study (talk), AMS2023 103rd Annual Meeting, 8–12 January 2023, Denver, CO, USA, 2023.

Bechina, A. A. A., Cabañas, E. N., Güldal, S., Dahle, O. H., Bueno, J., Dullweber, M., Giersch, S., and Coyne, M.: A Model for a Safer Drone's Operation in an Urban Environment (abstract), in: Proceedings of the 2022 International Conference on Unmanned Aircraft Systems, 21–24 June 2022, Dubrovnik, Croatia, doi:10.1109/ICUAS54217.2022.9835715, 2022.

Giersch, S., and Raasch, S.: Staubteufelähnliche Wirbel in turbulenter Rayleigh-Bénard Konvektion – Eine Studie unter Verwendung der direkten numerischen Simulation (talk), DACH2022, 21–25 March 2022, DACH2022-42, Leipzig, Germany, doi:10.5194/dach2022-42, 2022.

Giersch, S., and Raasch, S.: Die Entstehung, Entwicklung und Eigenschaften staubteufelähnlicher Wirbel in konvektiven Grenzschichten - Eine numerische Studie mittels LES und DNS (talk), ExtremWetterKongress 2021, 22–24 September 2021, Hamburg, Germany, 2021.

Giersch, S., and Raasch, S.: Genesis and Features of Dust Devil-Like Vortices in Convective Boundary Layers – A Numerical Study Using LES and DNS (talk), EGU General Assembly 2020, Online, 4–8 May 2020, EGU2020-1579, doi:10.5194/egusphere-egu2020-1579, 2020.

Giersch, S., and Lösch, A.: Genesis and Features of Dust Devil-Like Vortices in Convective Boundary Layers - A Comparative Study Using DNS/LES and Laboratory Experiments (talk), 2nd Annual Meeting of the Priority Programme SPP 1881 Turbulent Superstructures, 10–11 December 2019, Ilmenau, Germany, 2019.

Giersch, S., Brast, M., Hoffmann, F., and Raasch, S.: Toward Large-Eddy Simulations of Dust Devils of Observed Intensity: Effects of Grid Spacing, Background Wind, and Surface Heterogeneities (talk), European Postgraduate Fluid Dynamics Conference, 16–19 July 2019, Ilmenau, Germany, 2019.

Giersch, S., Brast, M., Hoffmann, F., and Raasch, S.: Large-Eddy Simulationen von Staubteufeln mit beobachtbarer Intensität: Auswirkungen von Gitterweite, Hintergrundwind und Oberflächenheterogenitäten (talk), DACH2019, 18–22 March 2019, DACH2019-61-1, Garmisch-Partenkirchen, Germany, 2019.

Giersch, S., and Raasch, S.: Flight simulations in near-surface turbulent wind fields as generated by LES (talk), AVT 39th Panel Business Meeting Week, 15–19 May 2017, Vilnius, Lithuania, 2017.

Giersch, S., and Raasch, S.: Flight simulations in near-surface turbulent wind fields as generated by LES (talk), The Fifth International Education Forum on Environment and Energy Science, 15–19 December 2016, San Diego, CA, USA, 2016.

Theses

Giersch, S.: Flugsimulationen in mit LES generierten bodennahen turbulenten Windfeldern, Master's thesis, Supervisor: Prof. Dr. S. Raasch, Leibniz University Hannover, Hannover, Germany, 134 pp., 2017.

Giersch, S.: Aufstellung eines Modellgleichungssystems auf Basis der anelastischen Approximation und Bestimmung der Auswirkungen auf die PALM-Modellnumerik, Bachelor's thesis, Supervisor: Prof. Dr. S. Raasch, Leibniz University Hannover, Hannover, Germany, 80 pp., 2014.

Other Projects

- | | |
|-------------|---|
| 2021 – 2022 | USEPE - U-space Separation in Europe, https://usepe.eu/ . |
| 2019 – 2022 | MOSAİK-2 - Second phase of the project "Model-based city planning and application in climate change", https://palm.muk.uni-hannover.de/mosaik . |
| 2019 – 2021 | Drone WAVES - Weather and Artificial Vision-Enabled Safety, https://www.meteo.uni-hannover.de/en/research/boundary-layer-meteorology/research-projects/drone-waves/ . |

Miscellaneous

Brassat, J., Giersch, S., and Klamt, J.: Computer Animation: Visualization of a Dust Devil-Like Vortex in a Large-Eddy Simulation of the Atmospheric Convective Boundary Layer, doi:10.5446/62785, 2023.

Brassat, J., Giersch, S., and Klamt, J.: Computer Animation: Visualization of a Dust Devil-Like Vortex in a Large-Eddy Simulation of the Atmospheric Convective Boundary Layer - Visual Feedback of Different Grain Sizes, doi:10.5446/62786, 2023.

Giersch, S., and Raasch, S.: Dataset: Data for How Do Dust Devil-Like Vortices Depend On Model Resolution? A Grid Convergence Study Using Large-Eddy Simulation, doi:10.25835/x81j6gj2, 2022.

Giersch, S., El Guernaoui, O., Raasch, S., Sauer, M., and Palomar, M.: Dataset: Data for Atmospheric Flow Simulation Strategies to Assess Turbulent Wind Conditions for Safe Drone Operations in Urban Environments, doi:10.25835/727jszhs, 2022.

- Giersch, S.: Computer Animation: Visualization of a Dust Devil-Like Vortex in a Direct Numerical Simulation of Rayleigh-Bénard Convection Between Two Plates, doi:10.5446/60619, 2021.
- Giersch, S., and Raasch, S.: Dataset: Evolution and Features of Dust Devil-Like Vortices in Turbulent Rayleigh-Bénard Convection - A Numerical Study using Direct Numerical Simulation, doi:10.25835/0071502, 2020.
- Giersch, S., Brast, M., Hoffmann, F., and Raasch, S.: Dataset: Toward Large-Eddy Simulations of Dust Devils of Observed Intensity: Effects of Grid Spacing, Background Wind, and Surface Heterogeneities, doi:10.25835/0095133, 2019.